

Robust Close-Proximity Trajectory Design around Small  
Solar System Bodies:  
Application to the Hera Mission.

PhD Thesis

Iosto Fodde

Aerospace Centre of Excellence  
Mechanical and Aerospace Engineering  
University of Strathclyde, Glasgow

March 21, 2024

This thesis is the result of the author's original research. It has been composed by the author and has not been previously submitted for examination which has led to the award of a degree.

The copyright of this thesis belongs to the author under the terms of the United Kingdom Copyright Acts as qualified by University of Strathclyde Regulation 3.50. Due acknowledgement must always be made of the use of any material contained in, or derived from, this thesis.

The research presented in this thesis is co-funded by the European Space Agency's Open Space Innovation Platform, under contract number: 4000130259/20/NL/MH/ac "Bounded stability of motions around minor bodies". It is further co-funded by the University of Strathclyde Student Excellence Award (SEA) Studentship.

# Abstract

The exploration of small Solar System bodies is a major topic for various space programs due to their scientific potential, relevance to planetary defence, and resource utilization possibilities. Designing the spacecraft's close proximity operations for these types of missions is extremely challenging mainly due to two factors. First, the dynamics of the spacecraft are highly complex and non-linear due to the bodies' irregular shape and significant influence of the Solar radiation pressure. Second, the large distance to the Earth and the small size of the bodies result in difficulties in the observational process and brings about significant uncertainties in the modeling of the dynamics. Besides the uncertainty due to Earth based observations, the difficulty in navigating around an asteroid brings about uncertainties in the state of the spacecraft as well. These issues can lead to higher risk of impact with the target body, reduced scientific return, and increased planning and operational costs. This thesis presents novel methods and algorithms for the design of close-proximity orbits and trajectories around small bodies, which are capable of dealing with these issues. ESA's Hera mission to binary asteroid Didymos is considered as a test case throughout this thesis, to show the applicability of these methods to real-life scenarios. First, two novel dynamics indicators are introduced and used to characterise the uncertain orbital dynamics around Didymos. These uncertain dynamical indicators are able to relate initial conditions to the sensitivity of the state over time to different realisation of the uncertain parameters. Maps of these indicators are made to determine the various orbits which are robust stable and thus good options for a spacecraft. Additionally, as the two CubeSats on-board Hera plan to perform a ballistic landing on Dimorphos, this thesis also develops a novel method for the robust design of these landings. The previously defined uncertain dynamics

indicators are applied to this case to constrain the impact velocity and angle to values which allow for successful settling on the surface. This information is then used to optimize the trajectory itself for minimal dispersion of the landing footprint. Finally, the very-close flyby of Dimorphos by Hera is designed by developing a technique that is able to combine the nominal trajectory design and navigation analysis steps to create a trajectory which directly takes the uncertainties and navigation performance into account. It is shown that this significantly reduces the impact risk of the flown trajectory, while obtaining long periods of good observability of Dimorphos. The results presented in this thesis regarding the robust trajectory design of the different phases of the Hera mission, show the importance of taking the uncertainties directly into consideration, and present novel algorithms that are capable of doing this efficiently. It is therefore extremely relevant for improving the performance and reducing the risks of future small Solar System body missions.

# Acknowledgements

This thesis was not possible without the support of many different people, to whom I would like to express my deepest gratitude. First of all, I am very grateful to my supervisor, Dr. Jinglang Feng, who has taught me an immense amount about asteroids, astrodynamics, and academics in general. Her help and supervision throughout my PhD journey has influenced and inspired me greatly. Furthermore, a special thanks goes to Prof. Massimiliano Vasile, who has been a major help throughout my PhD and has influenced my research in many positive ways. His immense knowledge in many different fields and enthusiasm about research has helped and inspired me tremendously.

For the great six months I spent at the Hera office in ESTEC, I would like to thank Ian Carnelli and the rest of the Hera team. They were extremely welcoming and helpful, and showed me the true dedication and hard work necessary to engineer a mission like Hera. Specifically, I want to thank Jesús Gil-Fernández. His expertise in trajectory design and optical navigation helped me greatly in my research, but also his life and career advice during our post-lunch coffee and Patxaran breaks were incredibly helpful to me and my career. Thanks as well to everyone from the Deimos Madrid team for welcoming me to their office and showing me around Madrid.

Of course a huge thanks as well to all the PhD students at the University of Strathclyde: Luis, Simao, Yirui, Gianluca, Marianna, Catarina, Fabio, Paul, and everyone else. My time working in Glasgow was a great success because of you! To the J-men: Aurelio and Wail, I couldn't have imagined better people as PhD colleagues. Thanks for the good times during all the conferences we attended together, the British gold, the Carbonara dinners, Ukelele concerts, and all the stupid jokes I've had to endure.

A lot of gratitude goes towards all my friends back in the Netherlands who have

supported me, kept in contact with me, or even took the time to visit me during my time away: Rutger, Sjoerd, Boudewijn, Job, Camiel, Steven, Sven, and everyone else! A specific word of thanks to the best housemates, remote working colleagues, pandemic survivors, Scottish roadtrip companions, and just great friends: Misha and Mischa.

Finally, I want to give a heartfelt mention to my family, who have supported me unconditionally and have given me all the tools to successfully complete my thesis: my parents Monique and Riccardo, my brother Marco, everyone in Italy and Greece, and of course my grandparents: Oma en Opa and Nonna e Nonno. To Camille, thank you for going on this adventure with me and always being there to support me, regardless of all the flights, self-quarantines, Covid tests, and airport goodbyes. Without you I would not have been able to do this.

# Contents

<b>List of Figures</b>	<b>ix</b>
<b>List of Tables</b>	<b>xvii</b>
<b>List of Acronyms</b>	<b>xx</b>
<b>1 Introduction</b>	<b>2</b>
1.1 Small Solar System Bodies and their Exploration . . . . .	2
1.1.1 Orbital and Physical Characteristics . . . . .	3
1.1.2 Small Body Exploration . . . . .	8
1.1.3 Didymos and the Hera Mission . . . . .	9
1.2 Uncertainties . . . . .	11
1.2.1 Uncertainties in Astrodynamics . . . . .	12
1.2.2 Small Solar System Body Mission Uncertainties . . . . .	14
1.3 Thesis Overview . . . . .	16
1.3.1 Limitations and Challenges . . . . .	16
1.3.2 Objective and Methodologies . . . . .	18
1.3.3 Structure . . . . .	19
1.3.4 List of Publications . . . . .	20
<b>2 Dynamical Environment around Asteroids</b>	<b>23</b>
2.1 Reference Frames . . . . .	24
2.1.1 Quasi-inertial Didymos Equatorial Reference Frame . . . . .	25
2.1.2 Synodic Reference Frame . . . . .	26

## Contents

2.1.3	Body-fixed Reference Frame . . . . .	27
2.2	Force Models . . . . .	27
2.2.1	Gravitational Force . . . . .	28
2.2.2	Solar Radiation Pressure . . . . .	36
2.2.3	Third Body Perturbations . . . . .	38
2.3	Equations of Motion . . . . .	39
2.3.1	Generalised Inertial Form . . . . .	39
2.3.2	Circular Restricted Three Body Problem . . . . .	40
2.3.3	Lagrange Planetary Equations . . . . .	43
2.3.4	Uncertain Dynamics . . . . .	44
2.4	Solution Stability and Dynamical Indicators . . . . .	45
2.4.1	Equilibrium Points and (Quasi-)Periodic Orbits . . . . .	45
2.4.2	Averaging and Frozen Orbits . . . . .	49
2.4.3	Dynamical Indicators . . . . .	50
2.5	Chapter Summary . . . . .	53
<b>3</b>	<b>Uncertainty Propagation and Quantification</b>	<b>55</b>
3.1	Uncertainty Propagation . . . . .	57
3.1.1	Generalised Intrusive Polynomial Algebra . . . . .	59
3.1.2	Non-Intrusive Chebyshev Interpolation . . . . .	66
3.1.3	Numerical Results . . . . .	67
3.2	Uncertainty Quantification . . . . .	75
3.2.1	Uncertain Dynamics Indicators . . . . .	76
3.2.2	Expectation Estimation . . . . .	90
3.3	Chapter Summary . . . . .	92
<b>4</b>	<b>Uncertainty Dynamical Maps of Orbital Motion around Didymos</b>	<b>94</b>
4.1	Didymos Mass Uncertainty . . . . .	95
4.2	Didymos High-Fidelity Model . . . . .	101
4.2.1	Robust Stability . . . . .	104
4.2.2	Mission Performance . . . . .	118

Contents

4.3	Chapter Summary . . . . .	122
<b>5</b>	<b>Ballistic Landing Trajectory Design under Uncertainty</b>	<b>123</b>
5.1	Surface Motion . . . . .	125
5.1.1	Surface Impact . . . . .	126
5.1.2	Surface Rocks . . . . .	131
5.2	Minimum Touchdown Velocity . . . . .	135
5.3	Robust Trajectory Optimization . . . . .	139
5.4	Chapter Summary . . . . .	145
<b>6</b>	<b>Robust Crater Fly-by Trajectory Design</b>	<b>147</b>
6.1	Experimental Phase . . . . .	149
6.1.1	Nominal Trajectory Design . . . . .	149
6.1.2	GNC System Design . . . . .	154
6.2	Trajectory Optimization under Uncertainty . . . . .	158
6.2.1	Problem Definition . . . . .	158
6.2.2	Transcription Method . . . . .	163
6.3	Results . . . . .	167
6.3.1	Optimised Trajectory . . . . .	169
6.4	Chapter Summary . . . . .	172
<b>7</b>	<b>Conclusion</b>	<b>173</b>
7.1	Summary and Contributions . . . . .	173
7.2	Limitations and Future Work . . . . .	178
	<b>Bibliography</b>	<b>179</b>

# List of Figures

1.1	A collage of 20 of the 22 asteroids and comets that have been imaged by a spacecraft. Adapted from original montage 'Asteroids and comets visited by spacecraft' by Emily Lakdawalla of The Planetary Society, ©ESA, 2019. Updated 2022 by The Planetary Society. Data from NASA / JPL / JHUAPL / SwRI / ESA / OSIRIS / ISAS / JAXA / Russian Academy of Sciences / UMD / China National Space Agency / Goddard / University of Arizona. Processed by Emily Lakdawalla, Daniel Machacek, Ted Stryk, Gordan Ugarkovic, Thomas Appere. Image link: <a href="https://planetary.s3.amazonaws.com/web/assets/pictures/small-asteroids-and-comets-visited-by-spacecraft-2022.jpg">https://planetary.s3.amazonaws.com/web/assets/pictures/small-asteroids-and-comets-visited-by-spacecraft-2022.jpg</a> , date accessed: March 21, 2024. . . . .	4
1.2	The rotational speed versus the size of a large group of asteroids taken from various populations. The theoretical spin barrier can be clearly seen to correspond with observations. Adapted from [1]. . . . .	6
1.3	Timeline for the Hera mission. Image credit: ©ESA, ESA – Science Office, image link: <a href="https://www.esa.int/ESA_Multimedia/Images/2019/01/Hera_mission_timeline">https://www.esa.int/ESA_Multimedia/Images/2019/01/Hera_mission_timeline</a> , accessed: March 21, 2024. . . . .	11

List of Figures

1.4	A visual explanation of how uncertainties affect the operations. The target orbit is shown as a dashed circle around the asteroid. First, during the orbit determination (OD) arc, the knowledge of where the spacecraft is located and its velocity is improved. Then, according to the measured difference between the mean estimated state and the nominal state $\Delta\mathbf{r}$ , a correctional manoeuver $\Delta\mathbf{v}$ is executed. The uncertain state is then propagated over time under the different forces and their uncertainties, the uncertainty propagation (UP) arc, until the start of the following OD arc. . . . .	13
2.1	Didymos' orbit in the J2000 reference frame. . . . .	25
2.2	The quasi-inertial Didymos equatorial reference frame and its orientation with respect to the J2000 reference frame and the difference between Dimorphos' orbit and the Sun direction . . . . .	26
2.3	Representation of the influence of different degree and order SH coefficients on modelling the mass distribution. The color on the spheres represent the normalised value of the potential $U_g$ at that location if only that coefficient is included, darker regions represent higher values and vice versa. . . . .	30
2.4	The ZVS plotted for four different Jacobi constant values. . . . .	42
3.1	A diagram explaining the general process of GIPA. . . . .	59
3.2	The error distribution of the two different GIPA bases as a function of the location in the set. The top figure shows the spatial distribution of the differences, where the bottom figure shows the differences between the two bases. Below the zero line signifies better Chebyshev performance, whereas above the line shows better Taylor performance. . . . .	61
3.3	The accuracy after 10 days of propagation for different polynomial degree expansions and coefficient range estimation algorithms. The horizontal line represent the MC runtime. . . . .	70
3.4	The change in accuracy over time for various GIPA settings. . . . .	71

List of Figures

3.5	Grid of several initial set sizes and the corresponding RMSE and maximum error (norm over whole state vector) at the final time. . . . .	71
3.6	The influence of the starting semi-major axis on the accuracy development over time. The green lines are for the Taylor basis and the red lines for the Chebyshev basis. . . . .	73
3.7	The influence of the starting eccentricity on the accuracy development over time at a semi-major axis of 7 km. . . . .	74
3.8	Monte Carlo versus Taylor basis GIPA of the $e = 0.3$ orbit for 5 points in time. The order in time for the different steps is represented by the number next to it. . . . .	74
3.9	LHS sampling accuracy compared against the Smolyak sparse grid accuracy. The RMSE and max error are taken of the norm of the full state. The zoomed in part of the figure is the time epoch when the landing occurs. Both the RMSE and max error are given in the dimensionless values of the CR3BP. . . . .	76
3.10	Diagram showing two sets being propagated. The gray shaded area is where the actual trajectories are located and the black square represents the range of the set. Set A represent the propagation through more non-linear dynamics while set B has larger variance but is less non-linear.	84
3.11	Phase plot of two trajectories (dashed green and solid blue lines) for the Duffing oscillator with slightly different initial conditions. The system parameters are as follows: $\gamma = 0.4$ , $\omega = 1.0$ , $\delta = 0.25$ , $\alpha = -1.0$ , $\beta = 1.0$ .	86
3.12	The uncertain dynamics indicators maps for the Duffing oscillator with state uncertainty at $T = 8$ . The letters in the maps correspond to several sample trajectories shown in figure 3.13. . . . .	87
3.13	Sample trajectories from the uncertain dynamics indicator maps propagated until $T = 16$ for the Duffing oscillator. . . . .	89
3.14	The polynomial coefficients at the final epoch from test trajectories A and C. . . . .	89

List of Figures

3.15	Samples taken from the resulting polynomial and translated to be centered around $(0, 0)$ for initial conditions A and C at the final epoch. . . . .	90
4.1	The maps of the uncertain dynamics indicator for the SH-CR3BP with model uncertainties at $T = 3$ with $C = 3.1$ . The red area contains the secondary, therefore no initial conditions appear there. . . . .	96
4.2	Sample trajectories from the uncertain dynamics indicator maps propagated until $T = 6$ . The ZVS are shown from the nominal system parameters. . . . .	98
4.3	The polynomial coefficients at the final epoch from test trajectories A and C from figure 4.1a. . . . .	99
4.4	Samples taken from the resulting polynomial and translated to be centered around $(0, 0)$ for initial conditions A and C at the final epoch for figure 4.1a. . . . .	100
4.5	The uncertain dynamics indicator maps for the SH-CR3BP with model uncertainty at $T = 3$ with velocities set to zero. . . . .	100
4.6	Sample trajectories from the uncertain dynamics indicator maps of the zero velocity initial conditions propagated until $T = 6$ . . . . .	102
4.7	The uncertain dynamics indicators for grid 1. The colormaps represent the value of the respective indicator, thus the amount of variance and non-linearity. The letters indicate the set of sample orbits that are used to verify this grid, which are shown in Figure 4.8. . . . .	107
4.8	Sample trajectories from the uncertain dynamics indicator maps propagated until $t_f = 8$ periods. . . . .	108
4.9	The uncertain dynamics indicators for grid 2. The colormaps represent the value of the respective indicator, thus the amount of variance and non-linearity. . . . .	109
4.10	Sample trajectories from the uncertain dynamics indicator maps propagated until $t_f = 8$ periods for grid 2 and 3. . . . .	110

List of Figures

4.11 The distance  $r$  from the centre of Didymos and velocity  $v$  of different trajectories over time for sample orbits E and F. . . . . 111

4.12 The uncertain dynamics indicators for grid 3. The colormaps represent the value of the respective indicator, thus the amount of variance and non-linearity. . . . . 112

4.13 The variance in the semi-major axis  $a$  and squared orbital eccentricity  $e^2$  at the final time for grid 1. The letters indicate the set of sample orbits that are used to verify this grid, which are shown in Figure 4.8. . 113

4.14 Maximum and minimum values for the semi-major axis and eccentricity of the different initial conditions and the sample orbits shown for C. . . 114

4.15 The variance in the semi-major axis  $a$  and squared orbital eccentricity  $e^2$  at the final time for grid 2. The dotted line represents the theoretical frozen orbit condition from Eq. (4.2) . . . . . 115

4.16 The orbital elements over time for two different test trajectories from grid 2. In 4.16a the bounds are shown, and in 4.16b the results for E are shown in more detail. . . . . 116

4.17 The variance in the semi-major axis  $a$  and squared orbital eccentricity  $e$  at the final time for grid 3. . . . . 117

4.18 Maximum and minimum values for the semi-major axis and eccentricity of the sample orbits from grid 3. . . . . 118

4.19 Minimum and maximum observability, shown in percentage of the trajectory for which Dimorphos is observable for grid 1. . . . . 120

4.20 Minimum and maximum observability, shown in percentage of the trajectory for which Dimorphos is observable for grid 2. . . . . 121

4.21 Minimum and maximum observability, shown in percentage of the trajectory for which Dimorphos is observable for grid 3. . . . . 121

5.1 2D representation of the geometry during landing. . . . . 127

5.2  $\tilde{\gamma}$  for CoR only model at DART crater location. . . . . 129

List of Figures

5.3 A set of the trajectories plotted from the example MC analyses performed for the case of an uncertainty in the CoR and spherical harmonics coefficients only. . . . . 130

5.4 Distribution of the final locations of the MC analyses performed for the case of an uncertainty in the CoR and spherical harmonics coefficients only. . . . . 131

5.5 Distribution of the angles with respect to the local surface normal for different rock shapes. . . . . 132

5.6  $\tilde{\gamma}$  for different rock models at DART crater location. . . . . 133

5.7 A set of the trajectories plotted from the example MC analyses performed for the case of an uncertainty in the CoR, spherical harmonics coefficients, and with stochastic perturbation of the normal vector. . . . 134

5.8 Distribution of the final locations of the MC analyses performed for the case of an uncertainty in the CoR, spherical harmonics coefficients, and with stochastic perturbation of the normal vector. . . . . 135

5.9 Diagram showing the process of finding the minimum landing velocity when considering uncertainties. . . . . 136

5.10 Minimum landing velocity for different landing areas, considering also uncertainty in the mass of both bodies and the  $C_{20}$  and  $C_{22}$  coefficients of Dimorphos. It is important to note that the colors are plotted according to a power law to allow for more detail in the low velocity areas. . . . . 139

5.11 Minimum landing velocity for different landing vector orientations at the DART impact crater, considering also uncertainty in the mass of both bodies and the  $C_{20}$  and  $C_{22}$  coefficients of Dimorphos. . . . . 140

5.12 Diagram explaining how the robust landing trajectory optimization works using the NCI uncertainty propagation method. The grey areas represent the actual area which the trajectories occupy whereas the squares represent the total propagated area using NCI. . . . . 141

5.13 The distributions of landing location and geometry of both the robust optimization method and the nominal point-wise method. . . . . 144

List of Figures

5.14 The distributions of landing geometry of both the robust optimization method and the nominal point-wise method projected on the  $\tilde{\gamma}$  maps. . . 145

6.1 A diagram of Hera’s experimental phase. . . . . 150

6.2 Definition of the various angles that influence the lighting conditions during close approach. . . . . 151

6.3 The semi-analytically designed nominal VCFB trajectory and its observation parameters given over time. The time of closest approach with respect to the crater is given by the black cross, and the shaded regions in the observation parameter plots are the desired constraint regions. Furthermore, the vertical dashed lines show when the periapsis lowering manoeuvres are executed. . . . . 152

6.4 The evolution of the position knowledge variance based on the analytical model. The red areas are the blackout periods where Dimorphos is not visible. . . . . 157

6.5 The results for the Monte Carlo analysis of the semi-analytically determined trajectory. The B-plane distribution for Didymos is shown on the left, where the ellipse is the  $3\text{-}\sigma$  region. And the evolution of the different observation parameter mean (solid line) and  $3\text{-}\sigma$  region (dotted lines) on the right. . . . . 159

6.6 Diagram showing an example two-variable system in the case of a deterministic OCP (above) and an uncertain OCP (below). The shaded green areas represent the probability distribution of  $u^*$  and  $\mathbf{x}_0$ , and in 6.6b the solid lines represent realisations of the uncertainties. . . . . 160

6.7 The different steps that are performed at each segments to solve the UOCP. In figure 6.7a and 6.7c a large number of samples are shown, however the knowledge distribution and its propagation is only shown for a subset of points for clarity. Thus, it is important to keep in mind that these steps are performed for all points. . . . . 163

List of Figures

6.8	The trajectory obtained from the uncertain optimization procedure, for which the NLP is given by (6.24). The MC results for this trajectory in Cartesian space is given on the left and the observation parameter mean and $3\text{-}\sigma$ regions are given on the right. . . . .	170
6.9	The B-plane distribution of both the semi-analytical and robust trajectory for the Didymos flyby section. . . . .	171
6.10	The distribution of observation times, which is defined to be the time spent within the observation parameter requirements, including resolutions higher than 10 cm/pixel. . . . .	171

# List of Tables

1.1	A summary of the taxonomy of asteroids. There are other classes outside these main ones, and there are other characteristics of these classes that are not discussed here, but can be important when considering newly discovered asteroids. . . . .	7
1.2	A summary of different uncertainties, the categorization of them, and in which references they are discussed in more detail. . . . .	15
2.1	Physical parameters of the Didymos system, taken from [3] and the post impact parameters are taken from [4]. . . . .	24
2.2	Comparison of the three main gravitational models used in the study of the dynamics around small Solar system bodies. . . . .	35
4.1	The initial conditions for the three different maps. . . . .	105
5.1	The results of the optimization of the landing trajectory. . . . .	142
6.1	Uncertainties considered for the VCFB, taken from [5]. . . . .	157



# List of Acronyms

<b>AIDA</b>	Asteroid Impact and Deflection Assessment
<b>COM</b>	Centre-of-Mass
<b>COP</b>	Close Observation Phase (Hera mission)
<b>CR3BP</b>	Circular Restricted 3-Body Problem
<b>C/A</b>	Close-Approach
<b>DCP</b>	Detailed Characterisation Phase (Hera mission)
<b>DSN</b>	Deep Space Network
<b>ECP</b>	Early Characterisation Phase (Hera mission)
<b>ESA</b>	European Space Agency
<b>EXP</b>	Experimental Phase (Hera mission)
<b>FLI</b>	Fast Lyapunov Indicator
<b>FPE</b>	Fokker-Planck Equation
<b>FTLE</b>	Finite-time Lyapunov Exponent
<b>GHQ</b>	Gauss-Hermite Quadrature
<b>GIPA</b>	Generalised Intrusive Polynomial Algebra
<b>GNC</b>	Guidance, Navigation, and Control
<b>ISL</b>	Inter-Satellite Link
<b>JAXA</b>	Japan Aerospace Exploration Agency
<b>KBO</b>	Kuiper Belt Objects
<b>LCE</b>	Lagrange Characteristic Exponent
<b>LCS</b>	Lagrange Coherent Structure
<b>LD</b>	Lagrangian Descriptor
<b>LHS</b>	Latin Hypercube Sampling
<b>LPE</b>	Lagrange Planetary Equations
<b>MBA</b>	Main Belt Asteroid
<b>MC</b>	Monte Carlo
<b>MEGNO</b>	Mean Exponential Growth Factor
<b>NASA</b>	National Aeronautics and Space Administration
<b>NCI</b>	Non-Intrusive Chebyshev Interpolation
<b>NEO</b>	Near Earth Objects
<b>NLP</b>	Non-Linear Programming
<b>OCP</b>	Optimal Control Problem
<b>OD</b>	Orbit Determination
<b>PDF</b>	Probability Density Function
<b>PDP</b>	Payload Deployment Phase (Hera mission)
<b>UOCP</b>	Uncertain Optimal Control Problem

## List of Acronyms

<b>PO</b>	Periodic Orbit
<b>POMDP</b>	Partially Observable Markov Decision Process
<b>QPO</b>	Quasi-Periodic Orbit
<b>RMSE</b>	Root Mean Square Error
<b>SH</b>	Spherical Harmonics
<b>SRP</b>	Solar Radiation Pressure
<b>SSB</b>	Small Solar System Body
<b>UP</b>	Uncertainty Propagation
<b>VCFB</b>	Very-Close Fly-by
<b>ZVS</b>	Zero-velocity surfaces

## List of Acronyms

# Chapter 1

## Introduction

### 1.1 Small Solar System Bodies and their Exploration

Besides the eight planets, there are a large amount of different objects that reside in various regions of the Solar System. These so called Small Solar System bodies (SSB), or small bodies in short, consists of objects like asteroids, comets, Kuiper Belt Objects (KBO), minor planets, and planetary moons.

These SSBs are early remnants of the Solar System [1], thus studying them can provide vital information regarding fundamental scientific questions concerning: the evolution of the Solar System, the formation of the planets, and the origin of life [6]. For example, initial samples returned from asteroid Ryugu by the Hayabusa 2 mission has already revealed various organic compounds, which can be compared with meteorites that impacted Earth to investigate how materials like water were transported through the early Solar system [7]. Besides their scientific potential, an impact of the Earth with an asteroid, or other type of SSB, can have devastating consequences. The impact of asteroid Chicxulub roughly 65 million years ago led to devastating atmospheric shock waves, tsunamis around the globe, and large heat pulses. Furthermore, over the following years the Earth's surface was cooled as dust and debris was ejected into the atmosphere. This event lead to a mass extinction of around 60 % of species that lived on the Earth at that moment in time [8]. Understanding the properties of asteroids [9] and testing method to deflect them [4] is thus of great importance to avoid future events.

Finally, these asteroids and comets can contain several valuable resources, which can be mined and brought back to Earth or used for in-situ resource utilization [10]. The mining of valuable resources on SSBs can potentially have beneficial impacts on human rights and reduces their environmental impact.

For these reasons, missions to SSBs have received a lot of interest in the past decades. This section goes into the characteristics of the SSBs, and the missions that have already visited several of these bodies. One upcoming mission called Hera is highlighted, as this mission will be as an example and test case throughout the thesis.

### 1.1.1 Orbital and Physical Characteristics

Most of the SSBs reside in the dynamically most stable regions of the Solar System [1], like the region between Mars and Jupiter (the Main Asteroid Belt), the region beyond Neptune (the Kuiper belt and Oort cloud), and the Trojan asteroids in the region near Jupiter's triangular Lagrange points (which are stable equilibrium points found in the three-body problem, which will be explained in section 2.3.2). An important class of objects that do not reside in a particularly stable region are the Near-Earth Objects (NEO), which have orbits that come close to the Earth's orbit.

The Main Belt Asteroids (MBA) all reside within 2.1 and 3.3 Astronomical Units (AU), have low average inclination of roughly between zero and 15 degrees, and mean eccentricity of  $\sim 0.14$ . When looking at the distribution of semi-major axes of these MBAs, there are several prominent gaps where there are little asteroids. These regions are called the Kirkwood gaps, and exist due to the fact these semi-major axes are in resonance with the orbit of Jupiter, the most prominent ones being the 4:1, 3:1, 7:3, and 2:1 resonances. These resonances can increase the eccentricities of the bodies' orbit over time until it crosses the planetary orbit of Mars and/or Earth, which can cause their removal due to gravitational interactions and/or collision. Not all the resonances with Jupiter are destabilizing, specifically the ones located closer to Jupiter can actually protect the asteroids from its own large gravitational perturbation and cause these orbits to remain stable. For example, this happens for the Hilda class of asteroids, which are in a 3:2 resonance with Jupiter.

## Chapter 1. Introduction

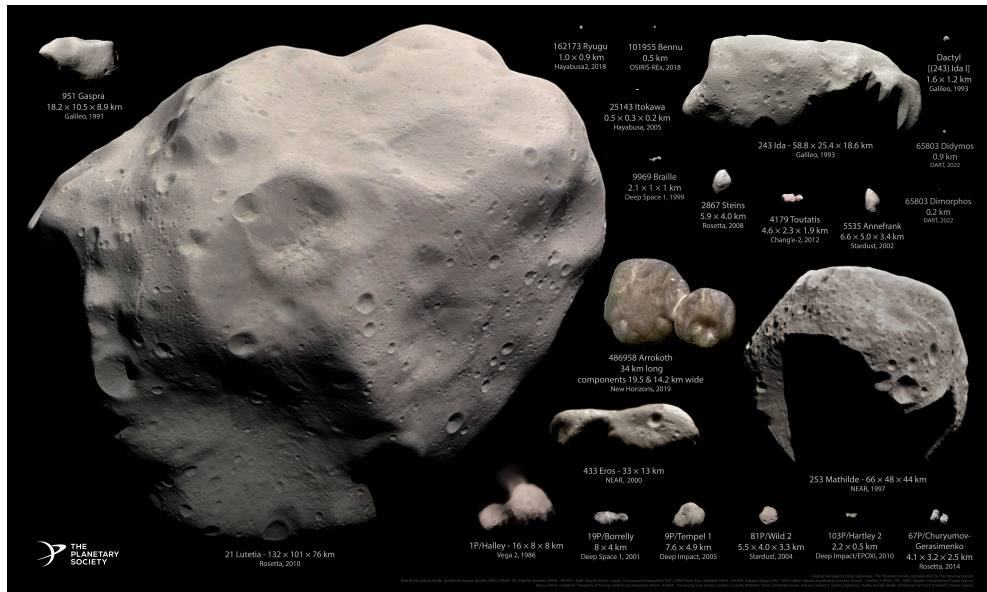


Figure 1.1: A collage of 20 of the 22 asteroids and comets that have been imaged by a spacecraft. Adapted from original montage 'Asteroids and comets visited by spacecraft' by Emily Lakdawalla of The Planetary Society, ©ESA, 2019. Updated 2022 by The Planetary Society. Data from NASA / JPL / JHUAPL / SwRI / ESA / OSIRIS / ISAS / JAXA / Russian Academy of Sciences / UMD / China National Space Agency / Goddard / University of Arizona. Processed by Emily Lakdawalla, Daniel Machacek, Ted Stryk, Gordan Ugarkovic, Thomas Appere. Image link: <https://planetary.s3.amazonaws.com/web/assets/pictures/small-asteroids-and-comets-visited-by-spacecraft-2022.jpg>, date accessed: March 21, 2024.

The locations near Earth, where NEOs reside, are generally much less stable than the region of the MBAs. NEOs have a relatively short lifespan of around  $10^7$  years [1], which thus requires a constant resupply from other regions of the Solar System. Numerical studies have shown that the most likely source of NEOs are the previously mentioned Kirkwood gaps. This also requires that asteroids are constantly moved in the asteroid belt to these gaps, which occurs likely due to collisions between asteroids creating fragments that move to these gaps after the impact occurs. NEOs are one of the most important class of objects as they are more easily studied from Earth and a small but significant fraction of these objects end their life impacting the Earth, which can cause significant harm to its inhabitants.

Impacts between asteroids can create another class of asteroids called rubble piles, which consist of a large amount of rocky fragments with possibly large internal voids. These rubble pile asteroids are likely a relatively large fraction of the total asteroid population, and many binary, or many-body, systems are also formed from these collisional fragments [11]. Based on samples taken from the rubble pile asteroid Itokawa, visited by JAXA's Hayabusa mission, it is also hypothesized that these rubble pile asteroids can absorb shocks created by impacts much better compared to monolithic asteroids, and thus also have a relatively longer lifetime [12].

Due to their small size, most small bodies are not spherical in shape. This results in various different shapes and sizes for these bodies, as can be seen in figure 1.1, where the various bodies that have been imaged by a spacecraft are shown. Besides the location and morphology of the body, its spin state is also an important factor in determining its dynamical history and evolution [13]. Roughly three different classes can be defined: uniform rotators, tumblers, and synchronous rotators [14]. Uniform rotators rotate around a single axis of rotation with a near constant rotational rate. This is also the expected rotational state of most bodies as it is the minimum energy state after all energy is lost due to tidal forces. Tumblers have a complex, non-periodic or quasi-periodic, rotational state. This does not necessarily mean that all tumblers are rotating chaotically. The number of observed tumblers is relatively low, however this can also be due to the fact that these types of rotations might be hard to verify

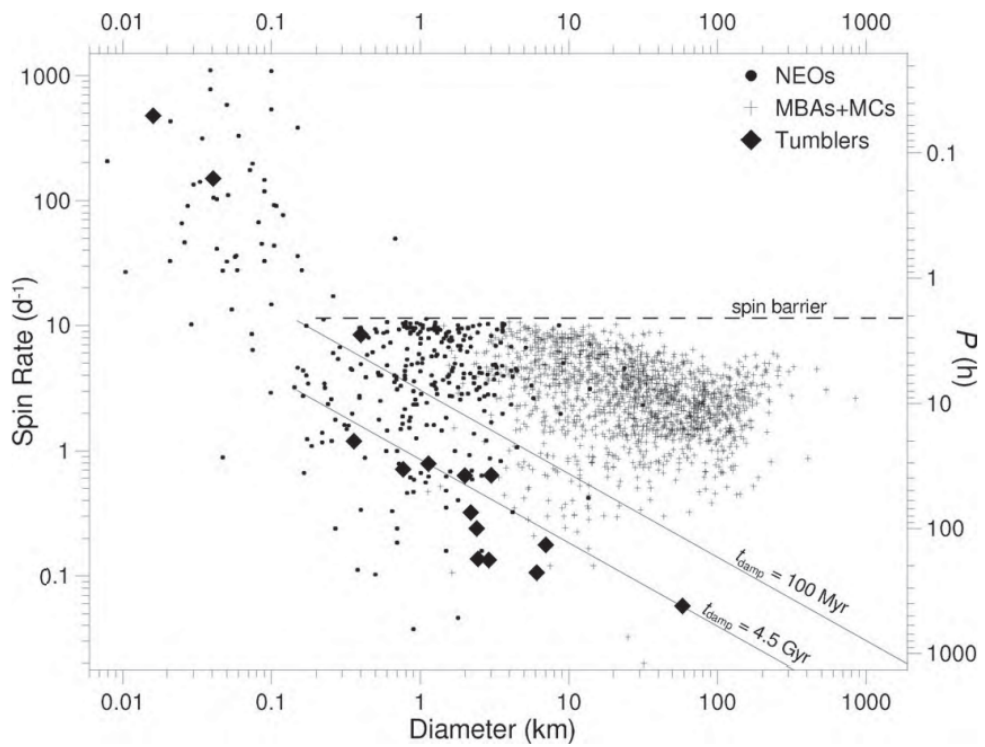


Figure 1.2: The rotational speed versus the size of a large group of asteroids taken from various populations. The theoretical spin barrier can be clearly seen to correspond with observations. Adapted from [1].

Taxonomy	Description	Albedo	Abundance
C	Carbonaceous; Flat spectra; Have undergone little to no heating; Abundant in outer belt	0.04 - 0.06	~ 40 %
S	Stony; Fairly bright; Mostly in inner belt	0.14 - 0.17	30 - 35 %
D/P	Quite dark; Reddish colour; Extreme outer belt and Trojans	0.02 - 0.07	5 - 10 %
M/W	Stony-iron; W when they have a water feature in their spectra; Undergone lots of thermal evolution.	0.1 - 0.2	~ 5 %

Table 1.1: A summary of the taxonomy of asteroids. There are other classes outside these main ones, and there are other characteristics of these classes that are not discussed here, but can be important when considering newly discovered asteroids.

through light curve observations [14]. The class of synchronous rotators only exists in systems where they are orbiting a parent body. They are defined by having a orbital period equal to their rotational rate. This state of rotation occurs frequently as non-synchronous rotation often evolves into synchronous rotation due to tidal interaction with the parent body. There is a clear relationship between the size of asteroids and their spin rate [1], the smaller the asteroid the faster it can spin. Furthermore, a clear upper limit can be observed for certain size ranges, as is shown in figure 1.2. This upper limit exists due to the fact that a large part of the asteroid population is a rubble pile, for which there is a theoretical limit of how fast they can spin before the centrifugal force overcomes the cohesion of the internal fragments.

A final important characteristic of SSBs, and more specifically here asteroids, is their composition. As these bodies are preserved remnants of the early Solar system, their composition can reveal a lot regarding the formation of the Solar system. The taxonomy of asteroids is mostly based of their albedos and spectra, and a short summary of the main types is shown in table 1.1. This taxonomy is still used as of today, however it is acknowledged that space weathering has an effect on the observation of an asteroids spectra and reflectance, and thus the true composition of the interior may differ from what is observed.

### 1.1.2 Small Body Exploration

One of the first missions to orbit an asteroid was the NEAR Shoemaker mission that visited asteroid 433 Eros in 2000 [15]. It remained in a bound orbit around the asteroid for around 1.5 years, requiring at the time novel mission design techniques to deal with Eros' complex shape and high spin rate [14]. Most of the orbit design and navigation was done on-ground [16], relying on data from NASA's Deep Space Network (DSN), laser ranging, and optical images taken from the spacecraft. As the ground based observation offered little knowledge about Eros' physical properties, only after an initial flyby a suitable orbit was selected, which fulfilled safety and observation requirements. After this initial orbit, increasingly precise models for the asteroid were developed, which allowed for lowering the orbit, which in turn resulted in more detailed observations of the asteroid [17].

After the NEAR mission, another asteroid orbiter was developed by JAXA to visit rubble pile asteroid Itokawa and return a sample from its surface in 2005 [18]. The Hayabusa mission applied a hovering solution instead of inserting the spacecraft into a gravitationally bound orbit around the asteroid, due to Itokawa's low mass and thus low gravitational attraction [19]. The spacecraft returned to Earth with a sample of regolith taken from Itokawa's surface in 2010. A second version of this mission, called Hayabusa 2, visited another rubble pile asteroid Ryugu, deployed a lander called Mascot on its surface, and returned a sample from the surface [20]. Its trajectory design is relatively similar to the first Hayabusa mission, with a hovering strategy employed to maintain a favourable position with respect to the surface features it wanted to investigate.

Besides visits to asteroids, another mission called Rosetta was developed by the European Space Agency to visit a comet called 67P/Churyumov-Gerasimenko. As with the NEAR mission, the uncertainty in the shape and gravitational model during initial analysis did not allow for orbit design prior to arrival [21]. Thus, several "pyramid" trajectories were designed where the spacecraft performed short arc flybys (with velocities above the systems escape velocity) at around 100 - 50 km to develop more accurate comet models. Afterwards, an initial orbit at a distance of 29 km was selected, which was lowered to 9 km for the final orbital phase. One of the challenges for the dynamics

close to the surface of the comet was the interaction between the outgassing plume and the spacecraft [22].

NASA's Dawn spacecraft visited two SSBs called Vesta and Ceres. The difference with previous missions is the fact that the size of these bodies is much larger than previous missions, namely 530 km (Vesta) and 960 km (Ceres) in diameter compared to 17 km for Eros, 313 m for Itokawa, and 4 km for 67P. This allowed for more detailed orbital design with more stringent requirements before arrival. For example, the initial orbit around Ceres was designed to have a minimal lifetime of 20 years under worst case gravity field model [23].

OSIRIS-Rex is a recent mission developed by NASA. Its goal is to collect a sample from the asteroid Bennu. The orbits around the asteroid are designed with the requirement that over 21 days, no maintenance manoeuvres are required to diminish ground operations [24]. One of the special design considerations for the orbit around Bennu is that the solar radiation pressure is relatively high compared to the gravitational attraction. For these types of systems, there exist a special class of stable orbits that are located in the Sun-terminator plane (orbit normal pointing towards the Sun), which are discussed more in detail in chapter 4. The OSIRIS-REx mission used these orbits to remain in a bounded trajectory around Bennu for long periods of time, showing that these theoretically derived orbits are also practically stable [25].

### 1.1.3 Didymos and the Hera Mission

The main mission that will be used as a test case throughout this thesis is ESA's Hera mission, part of the Asteroid Impact and Deflection Assessment (AIDA) program. AIDA is a collaborative mission between ESA and NASA to test the effectiveness of a kinetic impactor, by impacting the secondary of binary asteroid system (65803) Didymos, consisting of the primary body Didymos and smaller moon Dimorphos. ESA's contribution to AIDA, the Hera mission, will visit the asteroid in late 2026 after NASA's DART spacecraft successfully impacted Dimorphos in September 2022. Hera aims to characterize the physical properties of the binary system and investigate the consequence of the impact in more detail [2].

The impact by DART demonstrated the technical capability of a spacecraft to impact an asteroid [26], and successfully demonstrated the viability of the kinetic impactor technique as an option for asteroid deflection. Following the impact, observations of the system by several telescopes and the accompanying CubeSat LICIACube found that the impact changed the secondary's orbital period around the primary by 33 minutes [27], and that the momentum of the spacecraft impact was enhanced due to the ejecta of the impact by a factor of  $\sim 3.6$  [4]. This impact caused some other interesting changes to the system as well, e.g. 37 boulders of up to 7 meters in diameter were ejected from the system due to the impact [28], and a large tail of smaller ejecta could be observed for months after the impact [29].

The goals of Hera related to the AIDA collaboration are as follows [2]: infer the masses of Didymos (the primary) and Dimorphos (the secondary), observe the crater created by DART, characterise the spin state of Dimorphos, and characterise the surface and interior of Dimorphos. Several other scientific goals, which are separate to the impact measurements, are set as well, focusing on low gravity geophysics, the formation of binary systems, and comparing Didymos and Dimorphos with other asteroids and their properties. On board Hera there is an optical camera, hyperspectral imager, LIDAR, and infrared imager. Besides the larger Hera mother spacecraft, two CubeSats (called Milani [30] and Juventas [31]) will be released into orbits around the system as well. They carry separate instruments to investigate the two asteroids, allowing for riskier operations without compromising the main mission. An inter-satellite link (ISL) will also be present to communicate between all the spacecrafts and perform radio science, allowing for high resolution observations of the binary asteroid's gravity field.

Hera will arrive in December 2026, and will fly in hyperbolic arcs around the system, similarly to Rosetta. It will also perform several technology demonstration tests, mainly concerning close proximity operations, autonomy, and optical navigation [32]. A summary of the timeline of Hera is given in Figure 1.3. The mission starts with an Early Characterisation Phase (ECP) of six weeks, where the initial properties of the asteroid are estimated. Then, the Payload Deployment Phase (PDP) of two weeks starts where the CubeSats are released and commissioned, followed by the two week

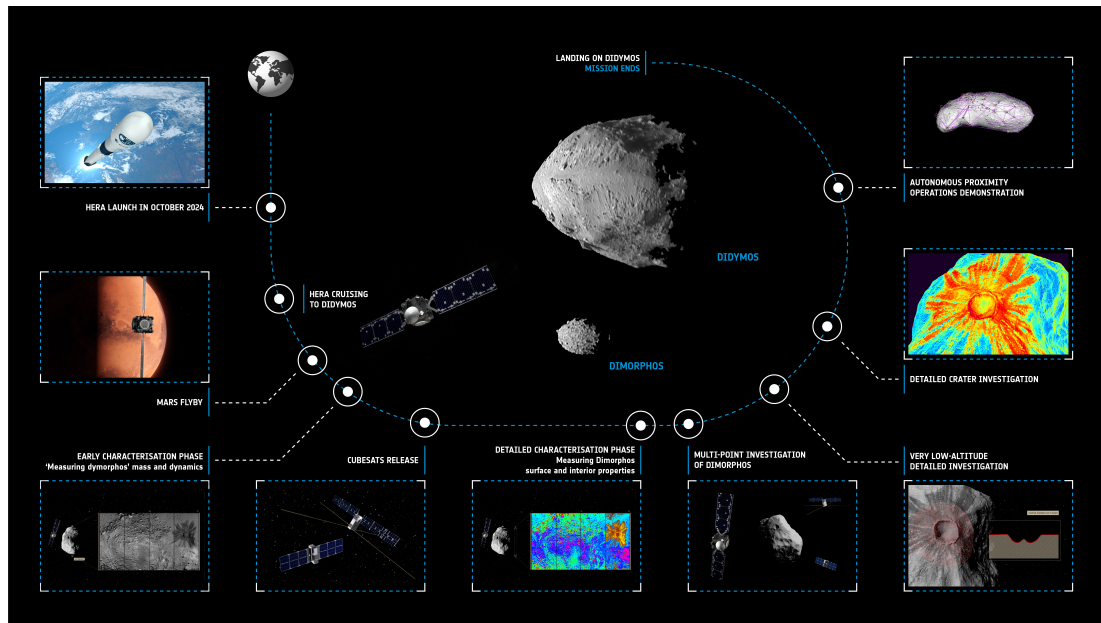


Figure 1.3: Timeline for the Hera mission. Image credit: ©ESA, ESA – Science Office, image link: [https://www.esa.int/ESA\\_Multimedia/Images/2019/01/Hera\\_mission\\_timeline](https://www.esa.int/ESA_Multimedia/Images/2019/01/Hera_mission_timeline), accessed: March 21, 2024.

Detailed Characterisation Phase (DCP), improving the initial asteroid property estimates by flying closer to the system. The main bulk of scientific requirements are met during the 6 week Close Observation Phase (COP), followed by the Experimental Phase (EXP) where additional science and technology demonstration objectives can be met. Finally, both CubeSats and Hera plan to end their mission with a landing on either Didymos or Dimorphos, which could significantly improve the scientific gain of the mission.

## 1.2 Uncertainties

Uncertainties play an important role in astrodynamics as a whole, and especially in small body missions. These uncertainties can come from several different sources, and can represent random phenomena or uncertain quantities. Depending on the specific subject, there are several ways to classify uncertainties. One general classification is between aleatoric and epistemic uncertainties [33]. Aleatoric uncertainties are irreducible uncertainties, meaning that they are part of the system and cannot be diminished. An

engineer has to deal with these uncertainties in their designs and cannot reduce their effects, only mitigate them. Epistemic uncertainties, on the other hand, are reducible and stem from the lack of knowledge of the system, and/or the numerical errors that stem from modeling the system. Even though with increased effort these types of uncertainties can be reduced, or even removed entirely, it might still require intensive processes to do so and thus it might still be beneficial to design around them instead of trying to reduce them.

There are several reasons for mission designers to try to reduce the impacts of uncertainties: they can reduce the scientific performance of a mission [34], reduce the accuracy of positioning systems for satellite-navigation applications [35], and possibly cause catastrophic failure of a mission [36]. An especially important field where uncertainties play a role is in the tracking of space debris [37], as continuous tracking of all pieces of debris is not possible and thus the evolution of the probability density function of the state of the different pieces of debris needs to be estimated to make sure the debris does not interfere with active missions.

### 1.2.1 Uncertainties in Astrodynamics

For astrodynamics, the uncertainties can originate from three types of sources: dynamic, actuation, and navigation. Dynamic uncertainties come from the imperfect modelling of the forces acting on the spacecraft, and from forces that are by nature stochastic. Actuation uncertainties come from the improper execution of thrusters, reaction wheels, or other devices that exert a force or torque on the spacecraft. Finally, navigation uncertainties stem from the errors that come from estimating the state of the spacecraft, and result in an uncertain position and velocity at certain instants of time.

The full process of how all these uncertainties affect the operations and performance of space missions is shown in Figure 1.4 and are as follows: first at some instant in time an orbit determination (OD) arc starts, which can either be performed by ground or autonomously on-board. During this arc measurements like range, range-rate, and/or optical landmark tracking are taken, and a filter is used to process these measurements



sphere plays an important dynamical role. This region of the atmosphere is affected by space weather and is hard to model, hence it contains large uncertainties [39].

An important difficulty that arises in the uncertainty propagation (UP) process for satellites and space debris, is the non-linearity of the dynamics. The main gravitational force, with its  $1/r$  term, causes the distribution to evolve non-linearly. This non-linearity affects both the ability to predict the deterministic evolution of the spacecraft and it causes an initial Gaussian probability distribution to lose its Gaussian nature over time. For Gaussian random variables, the full distribution can be characterised by the first two moments of the probability density function and simple techniques are available to propagate them [33]. Most non-Gaussian distributions do not have this property and thus require more complex techniques to propagate and quantify the uncertainties.

## 1.2.2 Small Solar System Body Mission Uncertainties

The problem of uncertainties is made worse in the case of small body missions due to the highly non-linear dynamics and imprecise dynamical modelling. First, the dynamics become even more non-linear as perturbations like the non-spherical shape of the body (sinusoidal terms) and Solar radiation pressure ( $1/r$ ), are much more important. Second, as in most cases before arrival only measurements from ground based observations are available, the knowledge about the dynamical environment contains large uncertainties [40]. A summary of the various sources of uncertainties that affect a small body orbiter during its operations is given in table 1.2.

Before arrival, in most cases the environment parameters are known with uncertainties  $> 10\%$  [3]. Only after arrival can the uncertainties be lowered. For this, long periods at the start of the mission are planned to perform in-depth investigations of the physical characteristics of the body [53] [2]. The approach for most small body missions to estimate the dynamical model parameters, like the gravitational parameter and shape based gravity coefficients, is to use radiometric tracking of the spacecraft as it moves around the body [56]. This mainly allows for the estimation of the gravity based forces, and requires close proximity and free flight around the body.

Source	Type	Notes	References
Mass and gravity parameters	Epistemic	<ul style="list-style-type: none"> <li>- Different uncertainties for different phases of the mission: radar observations, flyby observations, close-proximity measurements</li> <li>- Highest uncertainty radar (<math>\sim 10</math> percent).</li> <li>- Uncertainty of converting shape to gravity can be calculated.</li> </ul>	[41], [42], [18], [43], [44], [45], [46]
SRP	Epistemic	<ul style="list-style-type: none"> <li>- Uncertainties depend on model and measured mass-to-area ratio.</li> <li>- Rosetta experienced 5 to 10 percent error during heliocentric phase.</li> </ul>	[47], [48]
Outgassing	Epistemic	<ul style="list-style-type: none"> <li>- Only Rosetta visited outgassing comet, thus not a lot of information on the uncertainty.</li> </ul>	[49], [50]
Navigation	Aleatory	<ul style="list-style-type: none"> <li>- Most navigation uncertainties come from ground based estimation.</li> <li>- Error in estimation changes with altitude.</li> <li>- Generally, in initial orbit around 50 m uncertainty.</li> <li>- Shape model is needed, which contains non-Gaussian uncertainties.</li> </ul>	[51], [52], [41], [53]
Actuators	Aleatory	<ul style="list-style-type: none"> <li>- Mainly errors considered when performing trajectory corrections or during momentum dumping from translational components.</li> <li>- <math>\pm 0.6</math> mm/s for Rosetta (single momentum dumping manoeuvre) and between 0.2 and 4 mm/s for Bepi-Colombo.</li> </ul>	[54], [55]

Table 1.2: A summary of different uncertainties, the categorization of them, and in which references they are discussed in more detail.

This was a problem for the Hayabusa spacecraft, as it mainly performed a controlled hovering motion and the influence of Solar radiation pressure (SRP) was relatively high compared to the gravitational force because of Itokawa's small size. To remedy this problem, the spacecraft performed several ballistic descents towards the surface, which resulted in a mass estimate with an uncertainty of around 1.3% [57]. For Rosetta, different challenges arose as the mass and gravity field was continuously estimated as it moved from 100 km to 10 km from the body. At 30 km, the shape coefficients could already be determined due to the complex shape of 67p, however between 10 and 20 km the gas and dust cloud around the comet caused drag and reduced the impact from the gravitational force, reducing the accuracy of the gravity field estimation [58]. For the estimation of the gravity field of Bennu, again close distances were needed due to its small size [59]. Another approach was formulated in this case where ejected particles from the surface of Bennu were tracked to estimate the gravity field, resulting in a highly accurate estimation of the shape based gravity coefficients [60].

### 1.3 Thesis Overview

#### 1.3.1 Limitations and Challenges

As discussed in the previous sections, during the design and execution of small body missions, engineers have to account for the highly non-linear and complex dynamics during close proximity operations, and the large uncertainties that exist due to limited information regarding the environment and complex navigational system. In dealing with these problems, the following limitations in current approaches can be identified:

1. **Simplified dynamical models.** Outside of small body missions, Keplerian dynamics is mostly assumed where the motion of the spacecraft can be described by conical sections. There are several methods to then patch these orbits together using impulsive thrusts, leading to a simple design of the mission. Most orbiters of SSBs experience large perturbations that make the dynamics non-Keplerian and highly non-linear, which means that there are no closed-form solutions of the dynamics, significantly complicating the mission design process. Furthermore,

for other processes like uncertainty propagation and control/navigation system design, the dynamical models are often linearised. However, for most small body missions these linear dynamical models are not accurate anymore. In NASA's GNC Assessment for Future Planetary Science Mission report <sup>1</sup>, the following recommendation is made: "*To increase the effectiveness of mission design in the future, increasingly more complex dynamical models must be used to perform preliminary designs*".

**2. Intensive ground operations.** Most larger missions to small bodies take long periods of time at the start of the mission to perform preliminary characterisation of the body and reduce the uncertainties in the environment parameters. The mission designers then use this new information to validate and/or update the current mission plan. For example, Hera's Early Characterisation Phase lasts approximately six weeks, allowing for preparation for the following phases [2]. The current trend in spaceflight is to move to smaller low-cost missions involving CubeSats [61] [62]. These types of missions can significantly reduce the cost of small body missions due to their smaller size, use of off-the-shelf components, and shorter completion times. However, one segment that does not scale with size in both cost and complexity is the ground based operations segment [63]. Requiring large amounts of time at the start of the mission where the ground segment needs to constantly interpret data, update the environment models, and iterate on the mission plan, significantly limits the transition to small-scale and low cost small body missions.

**3. Decoupled Approach to Uncertainty Analysis.** The chaotic dynamics, large uncertainties, and long communication delays between the ground and spacecraft can cause significant problems as small perturbations from the nominal state can cause unexpected behaviour. This requires rapid response from ground to

---

<sup>1</sup>[https://solarsystem.nasa.gov/system/downloadable\\_items/156\\_GNC\\_Tech\\_Assess\\_Part\\_I\\_Onboard\\_and\\_Ground\\_NMD\\_130117\\_soo.pdf](https://solarsystem.nasa.gov/system/downloadable_items/156_GNC_Tech_Assess_Part_I_Onboard_and_Ground_NMD_130117_soo.pdf), accessed 03-08-2023.

counteract, otherwise there is a significant possibility of the spacecraft escaping the system or impacting the body. This rapid response is often not possible due to the long distances involved and limited communication availability. This problem is mostly tackled by performing a so-called navigation analysis after the nominal design is done. This analysis determines the sensitivity of the trajectory to uncertainties coming from navigation and control system performances, and system parameter uncertainties. Based on this analysis, the nominal design is updated by adding margins, implementing large amounts of trajectory correction manoeuvres, and/or increasing distances with respect to the body [64] [65] [66]. These factors reduce the scientific gain of the mission, complicate the design, and as this cycle is often repeated, the development time is also significantly increased.

### 1.3.2 Objective and Methodologies

Two approaches to improve upon the current limitations of designing low-cost, scalable, and high performance small body missions can be identified: i) *increasing the autonomy of spacecrafts*, ii) *designing with uncertainties and robustness in mind*. Autonomy mitigates the problems of intensive ground operations, and recent efforts have shown that incorporating medium to high fidelity models in the autonomous decision making process is possible [67]. However, an autonomous spacecraft still has to deal with uncertainties in an efficient manner. Changing the mission design paradigm to focus on implementing the uncertainty/navigation analysis from the start allows for reduced operational costs during the execution of the mission, and potentially improved reliability and scientific performance as the scientific goals can be met immediately after arrival, in turn reducing the total mission lifetime. Furthermore, these two approaches are not mutually exclusive, as an uncertainty focused mission design allows for better formulation of the objectives and performance of an autonomous system, and improves its reliability. This leads to the following thesis statement:

#### **Thesis Statement**

*Combining efficient uncertainty propagation and quantification techniques with trajectory design methods using high fidelity dynamical models, and applying them*

*throughout the whole close-proximity operations design process, significantly improves the robustness and performance of missions to small Solar System bodies.*

To support this statement, several objectives are formulated which will be addressed through the research presented in this thesis. These objectives are based on developing new techniques regarding the quantification of the effect of uncertainties on the evolution of the spacecraft trajectory over time, and on novel approaches to apply these techniques to different scenarios that are often present in SSB missions. These objectives are as follows:

1. Determine the applicability and efficiency of different uncertainty propagation techniques for trajectories around a binary asteroid, and develop an indicator that can be used to quantify the sensitivity of a trajectory to the uncertainties present in the system.
2. Use the previously developed indicators to determine robust stable orbits around the binary asteroid system considering the full dynamical model.
3. Design ballistic landing trajectories on an asteroid that are reliable and have low sensitivity to uncertainties in both the landing conditions and deployment execution.
4. Develop a method to combine the navigation analysis and nominal trajectory design to obtain robust trajectories for the very close flyby of an asteroid.

### **1.3.3 Structure**

The thesis is structured as follows: at first the necessary background information regarding the modeling and analysis of the environment around a SSB is discussed in Chapter 2. In this chapter, the various reference frames, force models, equations of motion, and solution analysis methods are discussed. The following chapter, Chapter 3, then goes into the two uncertainty propagation methods that will be used throughout this thesis: generalised intrusive polynomial algebra and non-intrusive Chebyshev interpolation. This chapter also presents the novel ideas of the uncertain dynamical

indicators that are used throughout this work, addressing objective 1. Chapter 4 starts with the first application of these methods, namely the orbital motion around binary asteroid Didymos. Mainly analysing the sensitivity to uncertainties of certain initial conditions and the robust stability of specific orbits, focusing on fulfilling objective 2. In chapter 5 the design of landing trajectories considering uncertainties is presented, introducing how the ideas of the previous chapters can be applied to improve the reliability and performance of landing on Dimorphos, addressing objective 3. The application of uncertainty propagation methods within trajectory optimization schemes to combine the navigation analysis and nominal trajectory design is then discussed in Chapter 6, where the very close flyby of the DART crater on Dimorphos is used as a test case, which thus discusses objective 4. Finally, Chapter 7 presents the conclusions of this work and recommends future directions to continue this research.

### 1.3.4 List of Publications

Below is a list of publications which are a result of the work performed during the PhD process.

#### **Journal**

##### *Published*

- **Fodde, I.**, Feng, J., Riccardi, A., & Vasile, M. (2023). Robust stability and mission performance of a CubeSat orbiting the didymos binary asteroid system. *Acta Astronautica*, 203, 577-591. <https://doi.org/10.1016/j.actaastro.2022.12.021>
- **Fodde, I.**, Feng, J., & Vasile, M. (2022). Uncertainty maps for motion around binary asteroids. *Celestial Mechanics and Dynamical Astronomy*, 134(5), [41]. <https://doi.org/10.1007/s10569-022-10096-2>
- Casini, S., **Fodde, I.**, Monna, B., Cervone, A., & Gill, E. (2020). Novel 3U stand-alone CubeSat architecture for autonomous Near Earth Asteroid fly-by. *Aerospace*, 8(1), [9]. <https://doi.org/10.3390/aerospace8010009>

##### *In-review*

## Chapter 1. Introduction

- **Fodde, I.**, Feng, J., Vasile, M., & Gil-Fernández, J. (2023). Design and Analysis of Robust Ballistic Landings on the Secondary of a Binary Asteroid. *Journal of Guidance, Control, and Dynamics*

### *In-development*

- **Fodde, I.**, Feng, J., Vasile, M., & Gil-Fernández, J. (2023). Chance-Constrained Trajectory Design for Hera’s Experimental Phase using Polynomial Algebra.

### **Conference**

- **Fodde, I.**, Feng, J., Gil-Fernández, J., & Vasile, M. (2023). Combined Trajectory Design and Navigation Analysis for Hera’s Very-Close Flyby of Dimorphos. Paper presented at 74th International Astronautical Congress 2023, Baku, Azerbaijan.
- **Fodde, I.**, Boumchita, W., Kaluthantrige, A., Savitski, V., Feng, J., & Vasile, M. (2023). The LASERS Mission Concept for Active Debris Removal using Laser Ablation by a Swarm of CubeSats. Paper presented at 74th International Astronautical Congress 2023, Baku, Azerbaijan.
- **Fodde, I.**, Feng, J., Gil-Fernández, J., & Vasile, M. (2022). Binary asteroid landing trajectory design from a self-stabilized terminator orbit considering parametric uncertainties. Paper presented at 73rd International Astronautical Congress 2022, Paris, France.
- Marlin, T. C., Gentgen, C., **Fodde, I.**, Groshaus, J., Hennig, A., Hudson, B., Lin, A., Pabarcus, L., Smith, E., Vilchis Lagunes, N., Wall, M., Jiang, R., Mahendrakar, T., Shimane, Y., Christuraj, E., & Gammill, M. E. (2022). ORACLE: A sample-return mission to Titan. In ASCEND 2022 [4372] American Institute of Aeronautics and Astronautics Inc. (AIAA). <https://doi.org/10.2514/6.2022-4372>
- **Fodde, I.**, Feng, J., Gil-Fernández, J., & Vasile, M. (2022). Binary asteroid landing trajectory design from a self-stabilized terminator orbit considering parametric uncertainties. Paper presented at 73rd International Astronautical Congress 2022, Paris, France.

## Chapter 1. Introduction

- Kaluthantrige, M., **Fodde, I.**, Feng, J., & Gil-Fernández, J. (2022). Autonomous navigation around didymos using CNN-based image processing. Paper presented at AAS/AIAA Astrodynamics Specialist Conference 2022, Charlotte, United States.
- **Fodde, I.**, Feng, J., & Vasile, M. (2022). Landing area analysis for ballistic landing trajectories on the secondary of a binary asteroid. Paper presented at AAS/AIAA Astrodynamics Specialist Conference 2022, Charlotte, United States.
- **Fodde, I.**, Feng, J., & Vasile, M. L. (2022). Robust trajectory design for ballistic landings on Dimorphos. Paper presented at American Institute of Aeronautics and Astronauts SCITECH 2022 Forum, San Diego, United States. <https://doi.org/10.2514/6.2022-1476>
- **Fodde, I.**, Feng, J., Riccardi, A., & Vasile, M. (2021). Analysis of the robustness and mission performance of a CubeSat orbiting a binary asteroid system. Paper presented at 72nd International Astronautical Congress, Dubai, United Arab Emirates.
- **Fodde, I.**, Feng, J., & Vasile, M. (2021). Uncertainty propagation for orbital motion around an asteroid using generalized intrusive polynomial algebra: application to didymos system. Paper presented at 8th International Conference on Astrodynamics Tools and Techniques.

## Chapter 2

# Dynamical Environment around Asteroids

Two of the main challenges for the design of small body missions are the complex dynamics of the spacecraft's motion around the system and the uncertainties in the small body environment. The main system considered in this thesis is the Didymos (68503) binary asteroid, target of NASA's DART and ESA's Hera mission. This chapter discusses the environment the spacecraft will encounter and the dynamics that govern its motion around the asteroids.

The two bodies part of the Didymos (68503) binary asteroid system are the main asteroid Didymos with a diameter of around 780 meters, and the secondary asteroid Dimorphos of around 164 meters. An interesting challenge with this system is that the DART spacecraft impacted Dimorphos in September 2022, changing some of its properties. As this happened while this research was conducted, both pre- and post-impact parameters are used at different stages of this research, mainly in chapter 4 the pre-impact parameters are used and in chapter 5 and 6 the post-impact ones. The physical parameters determined from the pre- and post-impact observations of the system can be found in Table 2.1. The effect of the DART impact on Dimorphos is mainly seen in the change of orbital period of 32 minutes, and thus a change in the semi-major axis of 48 meters [4]. The eccentricity is also slightly increased, to a value of around 0.03. As this value is low enough to not alter the dynamics of the system

Table 2.1: Physical parameters of the Didymos system, taken from [3] and the post impact parameters are taken from [4].

System mass	$5.28 (\pm 0.54) \cdot 10^{11}$ kg
Mass ratio	$0.0093 \pm 0.0013$
Heliocentric eccentricity	$0.38 \pm 7.7 \cdot 10^{-9}$
Heliocentric semimajor axis	$1.64 \text{ AU} \pm 9.8 \cdot 10^{-9} \text{ AU}$
Heliocentric inclination	$3.41 \text{ +/- } 2.4 \cdot 10^{-6} \text{ deg}$
Binary Orbit Obliquity	$175 \text{ +/- } 9 \text{ deg}$
<i>Primary</i>	
Diameter	$780 \text{ m} \pm 3 \text{ m}$
Rotational Period	$2.26 \text{ h} \pm 0.0001 \text{ h}$
Ellipsoid semi-axes (a, b, c)	399, 392, 380 m
<i>Secondary</i>	
Diameter	$164 \text{ m} \pm 18 \text{ m}$
Ellipsoid semi-axes (a, b, c)	103, 79, 66 km
Binary eccentricity	0.03 (upper limit)
Binary semimajor axis	$1.19 \pm 0.035 \text{ km}$
Binary inclination	0.0 deg
<i>Post impact</i>	
Dimorphos Orbital Period	$11.372 \pm 0.0055 \text{ hrs}$
Binary semimajor axis	$1.144 \pm 0.07 \text{ km}$

significantly for the problem considered in this work, a circular orbit will be assumed for Dimorphos. Changes to the shape and mass of Dimorphos are also expected due to the impact [68]. However, these changes can only be measured once the Hera spacecraft arrives at the system, thus the shape and mass of Dimorphos used here is based on the pre-impact measurements.

## 2.1 Reference Frames

This section describes the main reference frames that are used in this thesis. The orbit of the small body with respect to the Sun is described in the heliocentric J2000 reference frame (for brevity, this frame is referred to here as just the J2000 frame). This reference frame is located at the center of the Sun, where the z-axis is normal with respect to the

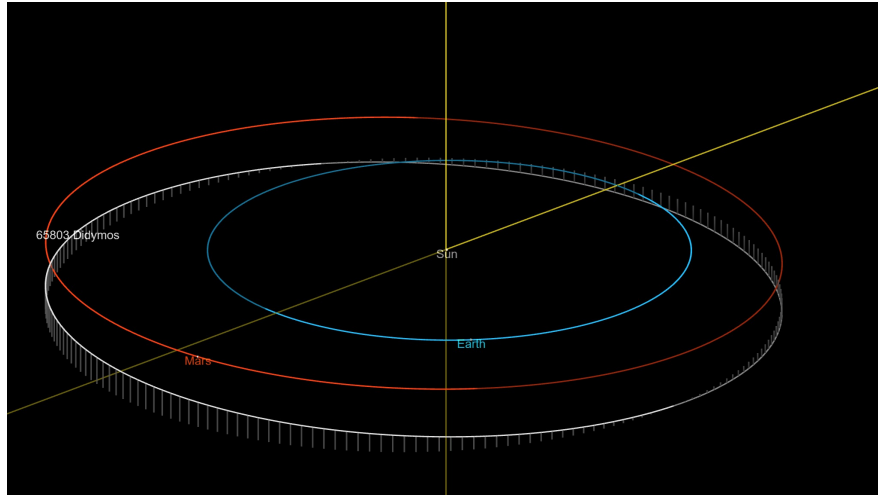


Figure 2.1: Didymos' orbit in the J2000 reference frame.

ecliptic plane, the  $x$ -axis points to the location of the vernal equinox at the beginning of the year 2000, and the  $y$ -axis completes the right-handed orthogonal reference frame. This reference frame is mainly used to define the position of the small body with respect to the Sun. The orbit of Didymos (68503) in the J2000 frame is shown in figure 2.1.

### 2.1.1 Quasi-inertial Didymos Equatorial Reference Frame

A quasi-inertial Didymos equatorial reference frame (see figure 2.2) is used to describe the motion of the orbiter with respect to the asteroid system. The quasi-inertial description in this case refers to the fact that the heliocentric motion of the Didymos system is not taken into account, as the time frames of the simulations discussed here are significantly shorter than the dynamical timescales of the motion of the system around the Sun. Under this assumption the reference frame can be interpreted as inertial, even though in reality there is a small rotation happening, hence quasi-inertial. It is also assumed that the motion of Dimorphos around Didymos is described by a Keplerian orbit (with orbital parameters shown in table 2.1). The  $x - y$  plane of the reference frame is defined to be in the binary's orbital plane, where the  $x$ -axis points in the direction of the Sun. The  $z$ -axis is parallel to the binary orbit normal. The rotational motion of both bodies is described by a uniform rotation around the reference frame's  $z$ -axis, and coincides with the inertial frame at time  $t = 0$ . Didymos rotates

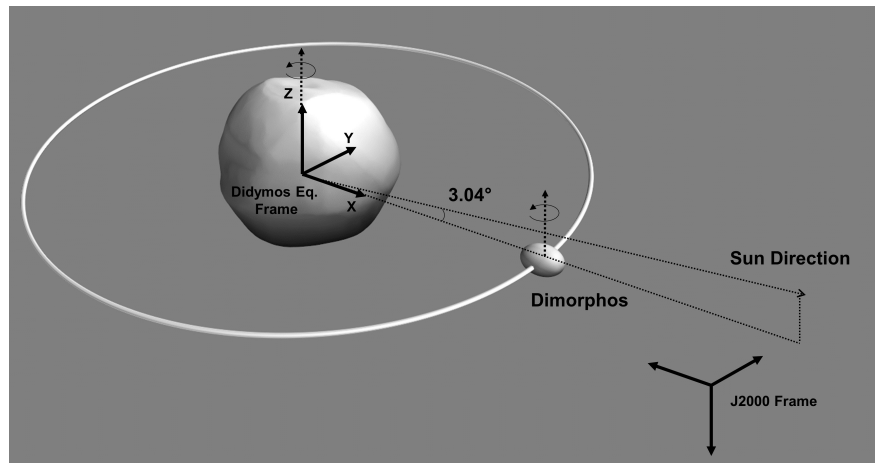


Figure 2.2: The quasi-inertial Didymos equatorial reference frame and its orientation with respect to the J2000 reference frame and the difference between Dimorphos' orbit and the Sun direction

at a speed of 0.0442 deg/s, whereas Dimorphos is tidally locked with the primary and thus rotates at the same speed as the mean motion of its orbit around the primary. As the obliquity of the binary orbit is around 175 degrees with respect to the heliocentric orbit, the reference frame is flipped with respect to the  $J2000$  frame, and the Sun is located 5 degrees above the Dimorphos orbit plane and thus 5 degrees above the  $x$ -axis of the quasi-inertial reference frame.

### 2.1.2 Synodic Reference Frame

A rotating reference frame centered at the barycentre of the binary system is also considered, called the synodic reference frame. This reference frame rotates together with the orbital period of the system. This results in both bodies being stationary in this reference frame, where the  $x$ -axis is defined to be pointing in the direction of Dimorphos, the  $z$ -axis in the direction of the orbit normal, and the  $y$ -axis completing the right-handed frame. The advantage of this reference frame is the fact that the equations of motion do not depend on time in this frame. The transformation between the Didymos equatorial reference frame and the synodic reference frame is given as follows:

$$\mathbf{r}^I = R_{S^I}^I \mathbf{r}^S = \begin{pmatrix} \cos \omega_{orb} t & -\sin \omega_{orb} t & 0 \\ \sin \omega_{orb} t & \cos \omega_{orb} t & 0 \\ 0 & 0 & 1 \end{pmatrix} \begin{pmatrix} x^S \\ y^S \\ z^S \end{pmatrix}, \quad (2.1)$$

where  $\omega_{orb}$  is the angular rate at which Dimorphos moves around Didymos, the superscript of the vectors denote the reference frame in which it is taken, and for the reference frame transformation  $R$  the subscript is the original frame and the superscript denotes the target frame. It is important to note for the velocity components the transport theorem needs to be used to perform the frame transformations.

### 2.1.3 Body-fixed Reference Frame

Finally, both bodies have an associated body-fixed reference frame. The origin of these frames is located at the centre-of-mass (COM) of the body, and the axes align with the constant density principal axes of the body, ensuring a diagonal moment of inertia in this frame. As the body's z-axes both align with the Didymos equatorial reference frame z-axis, the transformation between them consists of only a rotation around the z-axis:

$$R_B^I = \begin{pmatrix} \cos \omega_b t & -\sin \omega_b t & 0 \\ \sin \omega_b t & \cos \omega_b t & 0 \\ 0 & 0 & 1 \end{pmatrix}, \quad (2.2)$$

where  $\omega_b$  is the body spin rate.

## 2.2 Force Models

To model the different forces acting on a body in this system, various different models are needed. In this thesis, the (non-spherical) gravitational forces of Didymos and Dimorphos are considered, together with the Solar radiation pressure (SRP) force, and the perturbing force from the gravitational influence of a "third" body. The models that are often used for these various forces are discussed in more detail in this section.

### 2.2.1 Gravitational Force

One of the key differences between modelling the gravity of a planetary body and a small Solar System body is their non-spherical mass distribution. This means that using Newton's law of Gravity is not possible, and therefore most of the results from the two-body problem do not hold anymore. Hence, a different way of expressing the gravitational force that the small body is exerting on an orbiter is needed.

A set of basic facts can be used to derive a condition that the gravitational model needs to fulfill [14]. First, the gravitational force is conservative, which leads to the fact that a potential  $U$  can be defined as follows:  $F = -\nabla U$ . Second, the gravitational attraction between two different masses follows the inverse square law:  $F \propto 1/r^2$ . Finally, the principle of superposition holds, i.e. the gravitational potential of a sum of masses is equal to the sum of the gravitational potential of the different masses:  $U = \int_V \frac{Gdm}{r}$ . It can be shown that from these three facts one of the most important conditions can be derived, namely Laplace's equation [69]:

$$\nabla^2 U = 0. \quad (2.3)$$

Thus, any gravitational model that is a solution of Laplace's equation and represents the mass distribution of the small body well can be used. In this section, several of the most common and relevant options are discussed.

#### 2.2.1.1 Spherical Harmonics

One solution of Laplace's equation can be found in terms of the spherical coordinates:  $r$  the radial distance from the center of the body,  $\delta$  the latitude, and  $\lambda$  the longitude. This solution is called the spherical harmonics (SH) series and for modelling the gravitational field of a non-spherical body the general expression is [38]:

$$U_g(r, \delta, \lambda) = \frac{\mu_g}{r} \sum_{l=0}^{\infty} \sum_{m=0}^l \left(\frac{R}{r}\right)^l P_{lm}(\sin \delta) [C_{lm} \cos m\lambda + S_{lm} \sin m\lambda] \quad (2.4)$$

where  $\mu_g$  is the gravitational coefficient of the body,  $R$  is a normalizing radius which is taken as the maximum radial size of the body,  $P_{lm}$  are the Associated Legendre

Functions (their expressions can be found in [14]), and  $C_{lm}$  and  $S_{lm}$  are the Stokes coefficients which represent the mass distribution of the body.

There are various different solutions to Laplace's equation, the reason this specific solution is often used is due to several factors, most importantly is its functional orthogonality. To show why this is important and useful in modelling the gravitational field, first two functions are defined:

$$R_l^m(\delta, \lambda) = P_{lm}(\sin \delta) \cos m\lambda \quad (2.5)$$

$$S_l^m(\delta, \lambda) = P_{lm}(\sin \delta) \sin m\lambda \quad (2.6)$$

When these functions are integrated over the unit sphere  $S$ , it gives the following orthogonality relations:

$$\iint_S R_l^m R_p^q dS = \iint_S S_l^m S_p^q dS = 0, \text{ if } m \neq q \text{ or } n \neq p, \quad (2.7)$$

$$\iint_S (R_l^0)^2 dS = \frac{4\pi}{2l+1}, \quad (2.8)$$

$$\iint_S (R_l^m)^2 dS = \iint_S (S_l^m)^2 dS = \frac{2\pi}{2l+1} \frac{(l+m)!}{(l-m)!}. \quad (2.9)$$

This orthogonality can be exploited to obtain an expression for the Stokes coefficients by multiplying the potential with  $R_l^m$  or  $S_l^m$  and integrate it over a sphere with radius  $R$  as follows:

$$\iint_S U_g(R, \delta, \lambda) R_l^m dS = C_{lm} \frac{\mu}{R} \iint_S (R_l^m)^2 dS \quad (2.10)$$

$$\iint_S U_g(R, \delta, \lambda) S_l^m dS = S_{lm} \frac{\mu}{R} \iint_S (S_l^m)^2 dS. \quad (2.11)$$

To make sure that the Stokes coefficients do not vary significantly as a function of

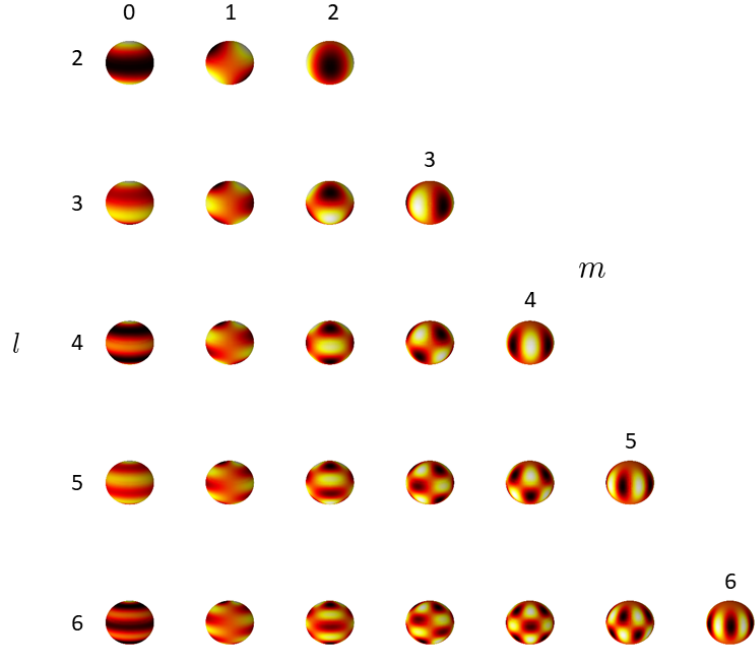


Figure 2.3: Representation of the influence of different degree and order SH coefficients on modelling the mass distribution. The color on the spheres represent the normalised value of the potential  $U_g$  at that location if only that coefficient is included, darker regions represent higher values and vice versa.

$l$  and  $m$ , a normalization is also applied. This normalization is selected to make sure that the right hand side of Eqs. (2.8) and (2.9) are equal to 1, i.e.:

$$N_{lm} = \sqrt{2(2l+1) \frac{(l+m)!}{(l-m)!}}. \quad (2.12)$$

This also simplifies Eqs. (2.10) and (2.11) to:

$$\iint_S U_g(R, \delta, \lambda) R_l^m dS = \bar{C}_{lm} \frac{\mu}{R} \quad (2.13)$$

$$\iint_S U_g(R, \delta, \lambda) S_l^m dS = \bar{S}_{lm} \frac{\mu}{R}. \quad (2.14)$$

These equations basically show that if  $U_g$  is known at the different points of the sphere  $S$ , i.e. the mass distribution of the body is known, the Stokes coefficients can

be used to model this mass distribution and the gravitational potential it produces, which is a direct result from the orthogonality of the SH series. This is one of the main reasons the SH series is often used to model the gravitational field of non-spherical bodies. A graphical representation of how the different coefficients influence the shape of the gravitational field around the body is shown in Figure 2.3.

It can be shown from these integrals that there are several relations between the Stokes coefficients and the higher order mass moments of an arbitrary body [14]. First of all, the zeroth order cosine coefficient is always the same:  $C_{00} = 1$ . Then,  $C_{10}$ ,  $C_{11}$ , and  $S_{11}$  are all directly proportional to the position of the centre of mass of the body. As  $U_g$  is always defined in the body fixed frame and, as stated in section 2.1, the centre of this frame is located at the centre of mass of the body, all these coefficients can be set to 0. The second order coefficients are all related to the different mass moments of inertia ( $I_{xx}$ ,  $I_{yy}$ ,  $I_{zz}$ ,  $I_{xy}$ ,  $I_{xz}$ , and  $I_{yz}$ ). As the body fixed reference frame is chosen to have its axis aligned with the constant density principal axes of the body, i.e.  $I_{xy} = I_{xz} = I_{yz} = 0$ , this directly means that  $C_{21} = S_{21} = S_{22} = 0$ . This means that for a second order and degree gravity field only the  $C_{20}$  and  $C_{22}$  coefficients remain. It is important to note that the coefficients which are equal to zero are set to this value because of the assumption of homogeneous density within the body. As during the orbit determination process the coefficients are estimated from the path of an orbiter (spacecraft or natural body), if it is found that these coefficients are non-zero, it is a direct result of the non-homogeneous density distribution [14].

One significant disadvantage of the spherical harmonics model is that there is a possibility of the model diverging for  $r < R$ , also known as the Brillouin sphere. This significantly limits the use of the SH model for close proximity motion and landings on the body itself. However, in the case that the bodies shape is sufficiently close to a sphere or triaxial ellipsoid, there is a certain condition for the eccentricities of the ellipsoidal shape which guarantees global convergence, namely that  $a < c\sqrt{2}$  [70], where  $a > b > c$  are the ellipsoid axes. Therefore, if the body used fulfills this condition, the SH model can be used for every phase of the mission.

Another advantage for when the body is close in shape to an ellipsoid, is that there

exists an analytical expression for the Stokes coefficients, assuming a constant density body [70]:

$$R = \sqrt{\frac{3}{\frac{1}{a^2} + \frac{1}{b^2} + \frac{1}{c^2}}} \quad (2.15)$$

$$C_{20} = \frac{1}{5R^2}(c^2 - \frac{1}{2}(a^2 + b^2)), \quad (2.16)$$

$$C_{22} = \frac{1}{20R^2}(a^2 - b^2), \quad (2.17)$$

$$C_{40} = \frac{15}{7}(C_{20}^2 + 2C_{22}^2), \quad (2.18)$$

$$C_{42} = \frac{5}{7}C_{20}C_{22}, \quad (2.19)$$

$$C_{44} = \frac{5}{28}C_{22}^2, \quad (2.20)$$

where  $a$ ,  $b$ , and  $c$  are the ellipsoid axes, ordered such that  $a > b > c$ .

There are several methods to calculate the acceleration from Eq. (2.4). In this work, the representation of the spherical harmonics acceleration of [71] is used.

### 2.2.1.2 Polyhedron Model

Werner and Scheeres [72] developed a closed-form expression for bodies with arbitrary shape, assuming constant density, using a polyhedron model. This model has been used extensively in different studies and has been used for several missions, including NEAR. The expression is as follows:

$$U(\mathbf{r}) = \frac{G\sigma}{2} \left( \sum_{e \in \text{edges}} \mathbf{r}_e \cdot \mathbf{E}_e \cdot \mathbf{r}_e L_e - \sum_{f \in \text{faces}} \mathbf{r}_f \cdot \mathbf{F}_f \cdot \mathbf{r}_f \omega_f \right), \quad (2.21)$$

where  $\sigma$  is the constant density of the body,  $G$  is the Cavendish constant,  $\mathbf{r}_e$  is the vector between edge  $e$  and  $\mathbf{r}$ , and  $\mathbf{r}_f$  is the vector between face  $f$  and  $\mathbf{r}$ . The expressions for  $\mathbf{E}_e$  (edge dyad),  $\mathbf{F}_f$  (face dyad),  $L_e$  (potential of edge  $e$ ), and  $\omega_f$  (projected area of face  $f$ ) are all given in [14].

This method is computationally heavy, as many polyhedron shape models have a large number of facets. The Euler-Descartes formula can give the amount of faces  $f$  and

edges  $e$  necessary for a polyhedron specified by  $v$  vectors:  $f = 2v - 4$  and  $e = 3(v - 2)$ . This shows that the sums of equation (2.21) can grow in numerical complexity quickly as more detail is added to the polyhedron model. Furthermore, inherent to the model is the need for a high resolution shape model, which is not available during all phases of the mission. Finally, this model assumes a constant density body, as for each facet the same density is assumed. This is often not close to reality as voids and density variations are often found in the interior of asteroids, significantly affecting the exterior gravity field.

### 2.2.1.3 Mascon model

The mass concentration, or mascon, model is a simple and easily interpretable method that uses a set of point mass gravitation models placed inside the body and adds them together to create a gravity field of an irregular body [72]. The total gravity field at an exterior point becomes:

$$U_g(\mathbf{r}) = G \sum_{i=1}^{N_m} \frac{\rho_i V_i}{|\mathbf{r} - \mathbf{R}_i|}, \quad (2.22)$$

where  $N_m$  the number of mascons,  $\rho_i$  and  $V_i$  are the density and volume of mascon  $i$  respectively, and  $\mathbf{R}_i$  is the location of mascon  $i$ .

As simple as this model is, the amount of parameters that can be changed to form the desired distribution, can make the use of these models quite complex [73]. Either point mass or spherical mascons can be used, and several different ways of packing the spherical mascons within the body are available: simple packing where all the mascons are equally sized and space within a square grid, face centered packing where the mascons are placed at the faces of a polyhedral model, or large packing where a single large mascon is used together with smaller ones in a shell around it to represent the density variations.

The mascon model has a similar problem as the polyhedron model, where to get an accurate representation of the gravity field a shape model of the body is needed. Furthermore, the discontinuous nature of the density distribution within the body can

lead to inaccuracies and model divergence when close to the individual mascons [74].

#### 2.2.1.4 Model Comparison

The models discussed here all have their own strengths and weaknesses, and there is no clear choice for a model that can be used for a large variety of applications. Therefore, it is important to consider first the application and from there select the desired model based on their specific properties. In this section, a short comparison is made between the different models and a summary is made of when which model is preferable.

For applications where highly non-spherical bodies are considered and a high amount of accuracy is needed, e.g. close-proximity trajectory design, the polyhedron gravity model is favourable. As this requires a reasonably accurate shape model of the body, the use of this method is mainly advantageous post-arrival or post-flyby. Additionally, the computational complexity of this method eliminates its use for early orbit and/or trajectory design as this requires large amounts of evaluations, e.g. inside a trajectory optimization scheme. Even though the polyhedron model is extremely accurate if a high resolution shape model is available, the assumed homogeneous density can still result in reduced accuracy. It was shown for asteroid 433 Eros, target of the NEAR spacecraft, that even on a local scale the differences in gravity field can be in the order of 1 % at the surface [56].

Even though the mascon model also requires large amounts of mascons to be used to represent the shape of an asteroid, it does reduce the computational complexity of the potential calculation compared to the polyhedron model, due to the simplicity of the potential formulation. It was shown in [73] that a 1000 facet polyhedron model has the same computational cost as for a model that uses 90,000 mascons. The same study, however, found that the accuracy of this model does converge slowly, requiring 100,000 mascons to reach a 1 % accuracy. Furthermore, the various different packing methods and tunable parameters like mascon sizes and locations can make this model difficult to implement. The main application of this model can be found for near-spherical bodies with large mass anomalies, e.g. the Moon [75], where a model with 1241 Mascons was equivalent to a SH model of order 60 in terms of accuracy, and showed 2 to 8 times

Model	Advantages	Drawbacks
Spherical Harmonics	<ul style="list-style-type: none"> <li>• Direct relationship of coefficients with mass distribution of body.</li> <li>• Can be easily used in orbit determination process to estimate coefficients.</li> <li>• Numerically efficient for (near) ellipsoidal shaped bodies.</li> <li>• No shape model (necessarily) needed.</li> </ul>	<ul style="list-style-type: none"> <li>• Possible divergence below the Brillouin sphere.</li> <li>• For highly non-spherical bodies a significant amount of terms are needed.</li> </ul>
Polyhedron Model	<ul style="list-style-type: none"> <li>• Depending on available data, can be highly accurate.</li> <li>• Can be used for landing, close orbital motion, and far orbital motion.</li> </ul>	<ul style="list-style-type: none"> <li>• Computationally inefficient for high resolution shape models.</li> <li>• Assumes homogeneous density distribution.</li> <li>• Hard to include shape and mass distribution uncertainties.</li> </ul>
Mascon Model	<ul style="list-style-type: none"> <li>• Easily interpretable and implementable.</li> <li>• Efficiently model density perturbations on near spherical/ellipsoidal bodies.</li> <li>• Various different customization options in terms of mascon size, shape, and location distribution to fit various different types of bodies.</li> </ul>	<ul style="list-style-type: none"> <li>• Computationally inefficient for highly irregular bodies requiring large amount of mascons.</li> <li>• Discontinuous density distribution.</li> <li>• Requires high effort fine tuning of the various parameters to get acceptable accuracy.</li> </ul>

Table 2.2: Comparison of the three main gravitational models used in the study of the dynamics around small Solar system bodies.

computational speed increase.

The spherical harmonics model is the main model used in preliminary orbit design and analysis applications due to its computational speed and direct relationship between the coefficients and the bodies' mass distribution. Furthermore, the simplicity of the expression allows for the use of this model in analytical frameworks [76]. The main drawbacks can be found when using this model for extreme close-proximity operations like landings, where the distance to the body is often below the Brillouin radius (as mentioned before, this is not a problem for close to ellipsoidal bodies). Furthermore, for applications where a high degree of accuracy during close-proximity operations is needed, highly non-spherical bodies require a large degree and order model. This can be problematic as even post-arrival the orbit determination process can only give information up to a certain degree. For NEAR, it was shown that the coefficients could only be found up until degree and order 10 as beyond this, the signal of these coefficients would be below the noise level [56].

As can be seen from this analysis, there is no gravitational model that is always preferable to others, and the specific model used depends highly on the application and mission phase. Both Didymos and Dimorphos (the bodies considered mainly in this work) are close to ellipsoidal in shape. Furthermore, the pre-arrival mission design process is mainly considered in this work, where no highly accurate shape model is available and the mass distribution uncertainties are high. Hence, the spherical harmonics model is mainly used in this thesis.

It is noted that recently other gravitational models have been developed like hybrid models [74] or machine learning based models [77], which are able to mitigate several of the drawbacks seen in the models mentioned here. As these models have only been developed recently and have not yet been extensively investigated and applied, they are not considered here and are left for future work.

### 2.2.2 Solar Radiation Pressure

Solar radiation pressure (SRP) is the force acting on a spacecraft that is produced by the impact of Sunlight on the surface of the spacecraft. The momentum produced by

this impact imparts a small acceleration which over longer periods of time can influence the trajectory of an object. In general, this force is quite small, but in specific cases it can have a significant impact on the motion, e.g. for high area-to-mass ratio objects, in libration point orbits, and for small body orbiters. Specifically, as the gravitational force around small bodies is quite low, the SRP can be at the same order of magnitude as the gravitational force, significantly affecting its trajectory.

To model the SRP, both the photons that are absorbed and that are reflected need to be considered, where the reflection can be either specular or diffusive. As this force depends on several factors (e.g. the material properties, spacecraft shape, spacecraft attitude, and distance to the Sun) it can become quite complex to model. Three main approaches are generally used for small body orbiters [78], which are (in order of least to most complex): the cannonball model, the N-plate model, and the finite element technique.

The most commonly used method of modelling the SRP is the cannonball model, where it is assumed that a constant surface is shown to the incoming photon stream. The acceleration for this model is given by the following formula:

$$a_{SRP} = -(1 + \kappa_s) \frac{P_0}{\beta} \cdot \frac{\mathbf{r} - \mathbf{r}_\odot}{|\mathbf{r} - \mathbf{r}_\odot|^3} \quad (2.23)$$

where  $\kappa_s$  is the specular reflection coefficient of the spacecraft,  $P_0$  is the solar constant,  $\beta$  the mass-to-area ratio of the spacecraft,  $\mathbf{r}$  the vector between the small-body and the spacecraft, and  $\mathbf{r}_\odot$  the vector between the small-body and the Sun. The cannonball model provides a simple method of analysing the influence of SRP, but does not provide the highest fidelity possible as more generally, no constant area is shown towards the Sun (but this is often still a reasonable approximation as for most missions the solar panels are pointed towards the Sun for a large part of the mission).

The N-plate model is a higher fidelity method, and is used when the shape of the spacecraft becomes more complex and the attitude motion needs to be taken into account. The spacecraft can then be modelled using a number of flat plates each with different properties:

$$a_{SRP} = \frac{P(d)}{m} \sum_i^N \left( A_i \cos \theta_i \left[ (1 - \kappa_s^i) \frac{\mathbf{r} - \mathbf{r}_\odot}{|\mathbf{r} - \mathbf{r}_\odot|} + 2(\kappa_s^i \cos \theta_i + \kappa_d^i/3) \hat{\mathbf{n}}_i \right] H(\theta_i) \right), \quad (2.24)$$

where  $P(d)$  is the SRP at distance  $d$  from the Sun,  $m$  the mass of the satellite,  $A_i$  the surface area of plate  $i$ ,  $\theta_i$  the angle between the incoming photon stream and the plate normal  $\hat{\mathbf{n}}_i$ ,  $\kappa_s^i$  and  $\kappa_d^i$  are the specular and diffusive reflection coefficient respectively, and  $H(\theta_i)$  is the illumination function which is one if plate  $i$  is illuminated and 0 if not. This model requires more input from the design of the spacecraft and is computationally more expensive, but gives higher fidelity results and should be considered if the attitude of the spacecraft with respect to the Sun changes significantly over time [40].

For even higher accuracy, a finite element technique can be used to include occultation and reflection by simulating the paths of rays of photons. The application of this technique is, however, not suitable for inclusion in (faster than) real-time simulations concerning the full dynamics of the environment. They can, however, be combined with other techniques which are able to fit the results from these types of simulations, to obtain less computationally expensive solutions. In [47] a new analytical model was developed based on a Fourier expansion of the finite element SRP model, as the force is periodic over its attitude angles. This model was applied to the OSIRIS-Rex spacecraft and showed a reasonably high fidelity while minimizing the computational burden.

### 2.2.3 Third Body Perturbations

In general, when considering the gravitational force of a planetary body or the Sun acting on a small body orbiter, the gravitational force will be equal to  $-\mu_p/|\mathbf{r} - \mathbf{d}|^3 \cdot (\mathbf{r} - \mathbf{d})$ , where  $\mathbf{r}$  is the position of the orbiter with respect to the small body (system) centre of mass, and  $\mathbf{d}$  is the position of the small body (system) centre of mass with respect to the perturbing body. This expression can be used when an inertial reference frame is considered, where the acceleration of the small body due to the perturbing body is also taken into account. As the main interest here is the orbiter's motion around the small body, the acceleration of interest is with respect to the small body. Hence,

the small body's acceleration due to the perturbing body needs to be subtracted, giving the perturbing acceleration as follows [38]:

$$a_p = -\mu_p \left[ \frac{\mathbf{r} - \mathbf{d}}{|\mathbf{r} - \mathbf{d}|^3} + \frac{\mathbf{d}}{|\mathbf{d}|^3} \right]. \quad (2.25)$$

The position of the perturbing body can either be taken from a simple two-body solution, or from a pre-computed ephemeris.

## 2.3 Equations of Motion

Using the previously discussed force models, the equations of motion can be formulated. The specific manner in which these equations are formulated is non-trivial as it depends on various factors like the selected force models, specific use case, and the selected reference frame. Hence, in this section the different options are discussed.

### 2.3.1 Generalised Inertial Form

In its most general form, the equations of motion of an orbiter are described in the Didymos equatorial quasi-inertial reference frame  $I$  as follows:

$$\mathbf{F}_{tot}^I = \mathbf{F}_{g,prim}^I + \mathbf{F}_{g,sec}^I + \mathbf{F}_{SRP}^I + \mathbf{F}_{g,Sun}^I, \quad (2.26)$$

where the specific forces of influence are the primary's gravity  $\mathbf{F}_{g,prim}^I$ , the secondary's gravity  $\mathbf{F}_{g,sec}^I$ , the SRP  $\mathbf{F}_{SRP}^I$ , and the gravity of the Sun  $\mathbf{F}_{g,Sun}^I$ . The specific force model used depends on the specific dynamical regime considered. Ferrari et al. [79] performed an analysis of the different dynamical regimes and which effects are most important in those different regimes. It was found that the SRP needs to be included for most of the dynamical regimes due to the low gravitational influence of the asteroids. For distances reaching 10 km and beyond, the third body effect of the Sun becomes significant and needs to be included as well. Below this distance, the separate influence of the two asteroids become significant, and as the distances to the bodies decrease to below 1 km, the shape of the asteroids needs to be incorporated as well. It is important

to note that this analysis was performed for the purpose of spacecraft trajectory design, and thus different applications might require more or less accurate force calculations. However, this does provide a good starting point for determining the most significant forces for each dynamical regime.

### 2.3.2 Circular Restricted Three Body Problem

As Dimorphos is observed to be in a nearly circular orbit around the primary, and the mass of the spacecraft is negligible compared to the two asteroids, the circular restricted three-body problem (CR3BP) can be applied to model the system. In the CR3BP, the synodic reference frame that rotates together with the orbit of Dimorphos is considered. The dynamics of the third body, given in the synodic frame, can be written as follows [78]:

$$\ddot{x} - 2\dot{y} = \frac{\partial U}{\partial x}, \quad (2.27)$$

$$\ddot{y} + 2\dot{x} = \frac{\partial U}{\partial y}, \quad (2.28)$$

$$\ddot{z} = \frac{\partial U}{\partial z}. \quad (2.29)$$

Here, the mass parameter  $\mu = m_2/(m_1 + m_2)$ , the body separation distance  $R$ , and the time constant  $1/n$  (where  $n$  is the mean motion of Dimorphos) are used to obtain dimensionless parameters and simplify the equations to only include  $\mu$  and the dimensionless coordinates  $x$ ,  $y$ , and  $z$ . The potential  $U$  includes the rotational terms, and other forces acting on the third body. The potential  $U$  in this case is given by:

$$U = \frac{1}{2}(x^2 + y^2) + U_{g,1}(x, y, z) + U_{g,2}(x, y, z), \quad (2.30)$$

where  $U_{g,1}$  and  $U_{g,2}$  represent the gravitational potential of the primary and secondary respectively.

There are five equilibrium points, called the Lagrange points, which can be found in this dynamical system by solving the following equation:

$$\frac{\partial U}{\partial x} = \frac{\partial U}{\partial y} = \frac{\partial U}{\partial z} = 0. \quad (2.31)$$

All of these points lie in the x-y plane, where there are three colinear equilibrium points on the x-axis ( $L_1, L_2, L_3$ ), and 2 equilateral points ( $L_4, L_5$ ) [78]. The location of the colinear points in the Didymos system (assuming point mass gravity) is shown in figure 2.4.

The CR3BP allows an integral of motion called Jacobi's constant, given by [78]:

$$C = 2U - V^2, \quad (2.32)$$

where  $V$  is the velocity of the 3rd body. This variable can be seen as an energy measure, where lower values correspond to higher energy spacecraft trajectories. Constant values of  $C = 2U$  give surfaces where the velocity of the spacecraft is zero and are called zero-velocity surface (ZVS). The ZVS restricts the motion of the spacecraft to certain regions in space, as is shown by the black lines in Figure 2.4. For high values of  $C$ , the ZVS blocks transport between the region around the two bodies, and between the inner regions and the region outside of the system (Figure 2.4a). As the energy of trajectories increases (decreasing value of  $C$ ), the region near the first Lagrange point  $L_1$  opens up to allow transport between the two bodies (Figure 2.4b). Increasing the energy even further opens up the  $L_2$  point, which then allows for a spacecraft to enter the inner region of the binary system (Figure 2.4c). Then, as  $C$  decreases more, the ZVS opens at the  $L_3$  point (Figure 2.4d).

Analysing the phase space near the Lagrange points for values of  $C$  that correspond to the ZVS opening around the Lagrange point can be of interest as the dynamical structures in these regions can be exploited for mission design purposes [80]. Determining the eigenstructure of the linearized dynamics around the Lagrange point results in the following general solution for planar motion:

$$\mathbf{x}(t) = \alpha_1 e^{\lambda t} \mathbf{v}_\lambda + \alpha_2 e^{-\lambda t} \mathbf{v}_{-\lambda} + 2\mathbf{Re}(\beta e^{i\nu t} \mathbf{w}_\nu), \quad (2.33)$$

where  $\lambda$  and  $\nu$  are the eigenvalues of the linearized dynamics around the Lagrange

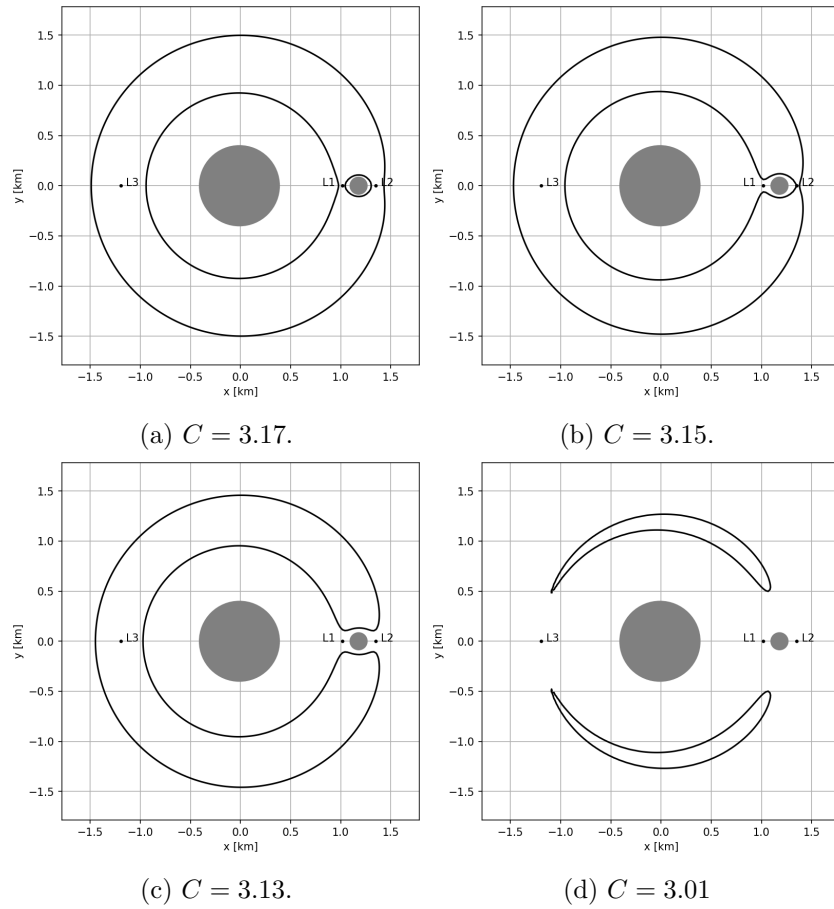


Figure 2.4: The ZVS plotted for four different Jacobi constant values.

point,  $\mathbf{v}$  and  $\mathbf{w}$  their corresponding eigenvectors, and  $\alpha_1$ ,  $\alpha_2$ , and  $\beta$  are constants defining the specific solution. The state vector  $\mathbf{x}(t)$  here is translated to be centered at the chosen Lagrange point. This solution has three main components: an unstable manifold in the direction of  $\mathbf{v}_\lambda$ , a stable manifold in the direction of  $\mathbf{v}_{-\lambda}$ , and a center manifold projected on the phase space by  $\mathbf{w}_\nu$ . Depending on the signs of the constants  $\alpha_i$  and  $\beta$ , the ZVS region in which the trajectory will end up in as  $t \rightarrow \pm\infty$  is determined by the sign of  $\alpha_i$ . Thus, for example, by selecting the proper values of these constants, one can design trajectories that come from the exterior region and enter through the  $L_2$  point into the interior region, moving towards  $L_2$  along the stable manifold and moving away again along the unstable manifold. This can be an extremely powerful tool in designing low energy trajectories that transport a spacecraft to specific desired

regions in phase space. For example, in [81] and [82], these hyperbolic manifolds were used to design ballistic landings on the secondary of a binary asteroid.

### 2.3.3 Lagrange Planetary Equations

A particularly useful way of formulating the equations of motion are the Lagrange Planetary Equations (LPE), formulated in an inertial frame. The idea behind these equations is that if a problem is taken that is integrable in terms of its constants of motion, the Variation of Parameters method can be used to obtain the perturbed solution where the constants of motion are now time varying parameters. However, the transformation between the original constants of motion and the solution of the problem still holds, thus these time varying parameters now describe the perturbed solution as well [14]. For describing the motion around an asteroid, the original two-body problem is used with its constants of motion being the standard orbital elements: semi-major axis  $a$ , eccentricity  $e$ , inclination  $i$ , argument of periapsis  $\omega$ , right-ascension of the ascending node  $\Omega$ , and  $\sigma = -n\tau_0$  (where  $n$  is the mean motion and  $\tau_0$  is the time of periapsis passage), for which the physical meaning is explained in more detail in [78]. If the perturbing forces can be formulated as a potential  $\mathcal{R}$ , the LPE then take the following form:

$$\dot{a} = \frac{2}{na} \frac{\partial \mathcal{R}}{\partial \sigma} \quad (2.34)$$

$$\dot{e} = \frac{1}{na^2 e} \left[ (1 - e^2) \frac{\partial \mathcal{R}}{\partial \sigma} - \sqrt{1 - e^2} \frac{\partial \mathcal{R}}{\partial \omega} \right] \quad (2.35)$$

$$\dot{i} = \frac{1}{na^2 \sqrt{1 - e^2}} \left[ \cot i \frac{\partial \mathcal{R}}{\partial \omega} - \csc i \frac{\partial \mathcal{R}}{\partial \Omega} \right] \quad (2.36)$$

$$\dot{\omega} = \frac{\sqrt{1 - e^2}}{na^2 e} \frac{\partial \mathcal{R}}{\partial e} - \frac{\cot i}{na^2 \sqrt{1 - e^2}} \frac{\partial \mathcal{R}}{\partial i} \quad (2.37)$$

$$\dot{\Omega} = \frac{\csc i}{na^2 \sqrt{1 - e^2}} \frac{\partial \mathcal{R}}{\partial i} \quad (2.38)$$

$$\dot{\sigma} = -\frac{1 - e^2}{na^2 e} \frac{\partial \mathcal{R}}{\partial e} - \frac{2}{na} \frac{\partial \mathcal{R}}{\partial a} \quad (2.39)$$

This set of equations can accurately describe how a regular two-body orbit is chang-

ing over time due to a particular (combination) of perturbing forces. As the orbital elements are useful for mission designers in the sense of giving a geometric interpretation of an orbit of a spacecraft, having an idea of how these elements change over time can allow for improved design choices.

### 2.3.4 Uncertain Dynamics

This thesis is mainly concerned with how uncertainties affect the motion of a spacecraft around an asteroid. Therefore, it is important to have a framework and set of definitions to use when working with these uncertain dynamical systems.

In general, a dynamical system which is governed by fluctuating random forces and/or random variables is called a stochastic system and is described by a so-called Itô process [83]:

$$d\mathbf{x} = \mathbf{f}(\mathbf{x}, t)dt + \boldsymbol{\sigma}(\mathbf{x}, t)dW(t), \quad (2.40)$$

where  $\mathbf{x}$  is a state vector consisting of  $n$  random variables,  $\mathbf{f}$  the the drift of the system (i.e. the deterministic dynamics),  $W$  a Wiener process (also know as Brownian motion process), and  $\boldsymbol{\sigma}$  the  $n \times n$  diffusion matrix of the Itô process which describes the specific stochastic forces of the dynamics. For a given dynamical system that satisfies Eq. (2.40), the probability density function (PDF)  $p(\mathbf{x}, t)$  of the state random variable  $\mathbf{X}$  evolves over time according to the Fokker-Planck (FPE) equation [33]:

$$\frac{\partial p(\mathbf{x}, t)}{\partial t} = - \sum_{i=1}^d \frac{\partial}{\partial x^i} [p(\mathbf{x}, t) f_i(\mathbf{x}, t)] + \frac{1}{2} \sum_{i=1}^d \sum_{j=1}^d \frac{\partial^2}{\partial x^i \partial x^j} [D_{ij}(\mathbf{x}, t) p(\mathbf{x}, t)], \quad (2.41)$$

where  $x^k$  represents the  $k$ th state variable and  $D$  is the diffusion tensor defined as:  $D = 1/2 \boldsymbol{\sigma} \boldsymbol{\sigma}^T$ . Thus, given an initial PDF  $p(\mathbf{x}_0, t_0)$  this partial differential equation can be solved to obtain the evolution over time of the PDF due to an uncertain parameter like the initial state and/or environment variables, and due to a stochastic process characterised by  $\boldsymbol{\sigma}$ .

The system described in Eq. (2.40) describes when there is a stochastic pertur-

bative force present in the system. However, another important class of uncertain dynamical systems are the systems with initial state and model parameter uncertainty, i.e. parametric uncertainty, which is especially relevant for small body missions as the environment around the body is often poorly characterized. In this case the diffusion term of Eq. (2.40) disappears and the drift term now contains the uncertain variables. The equations of motion can be described by a Cauchy problem as follows:

$$\begin{cases} \dot{\boldsymbol{x}} = \boldsymbol{f}(\boldsymbol{x}(t), \boldsymbol{\beta}, t) \\ \boldsymbol{x}(t_0) = \boldsymbol{x}_0 \end{cases} \quad (2.42)$$

where  $t$  is the time,  $\boldsymbol{x}$  the state vector, and  $\boldsymbol{\beta}$  a set of model parameter. Here,  $\boldsymbol{x}_0$  and/or  $\boldsymbol{\beta}$  are uncertain and independent. In this work, parametric uncertainties are mainly considered as these are the main sources of uncertainties for small body missions [40]. There are certain cases for which stochastic perturbations are important, e.g. the coupling of rotational state and SRP force for small particles [84] or the effect of undesired translational thrusts from momentum dumping manoeuvres [85], which should be studied in future work.

## 2.4 Solution Stability and Dynamical Indicators

In the previous sections the reference frames in which dynamics of an orbiter are described were discussed, the different models for the forces have been outlined, and the different setups for the equations of motion have been mentioned. This section will go into how the different solutions to the equations of motion can now be found, and how these solutions can be analysed from a stability standpoint. The discussion of the methods presented in this section, together with chapter 3, will be used as a starting point for the robust stability indicators presented in chapters 4 and 5.

### 2.4.1 Equilibrium Points and (Quasi-)Periodic Orbits

In general, the assumption is made here that the equations of motion are non-integrable for all cases considered. This means that there is no closed-form solution to the equa-

tions of motions, which is a key difference compared to the unperturbed two-body system. If the dynamical evolution of a generic initial condition is desired, a numerical integrator is used to obtain the future states. The solution obtained through numerical integration has a finite timespan over which the solution is obtained, and always has a limited precision. However, there are special solutions of the dynamics which are exceptions to this, namely equilibrium points and periodic orbits, which are important solutions to analyse as they represent important structures in the phase space of the system.

Equilibrium points are states that satisfy the following equation:  $\dot{\boldsymbol{x}}^* = \mathbf{0}$ . Examples of these types of points are the Lagrangian points of section 2.3.2, or the 1:1 mean motion resonance when considering the dynamics around an asteroid in the body-fixed reference frame [86] [87]. An equilibrium point is considered stable if any point in a certain region around  $\boldsymbol{x}^*$  stays "near"  $\boldsymbol{x}^*$  for an infinite amount of time. An even stronger form of stability, called asymptotic stability, is defined for when all points in the vicinity of  $\boldsymbol{x}^*$  converge towards  $\boldsymbol{x}^*$  over time. This form of stability is also known as Lyapunov stability, or stability in the sense of Lyapunov [88]. By performing a Taylor approximation around  $\boldsymbol{x}^*$ , the dynamics of a small perturbation  $\delta\boldsymbol{x}_0$  at time  $t_0$  is given by:  $\delta\boldsymbol{x}(t) = \Phi(t, t_0)\delta\boldsymbol{x}_0$ , where  $\Phi(t, t_0)$  is called the state transition matrix. This state transition matrix has its own dynamics given by [14]:

$$\dot{\Phi}(t, t_0) = A|_{\boldsymbol{x}^*}\Phi(t, t_0) \quad (2.43)$$

$$A = \frac{\partial \boldsymbol{x}(t)}{\partial \boldsymbol{x}_0} \quad (2.44)$$

As this is a first order Taylor expansion, in general this state transition matrix is only accurate close to the equilibrium point.

By analysing the eigenvalues and eigenvectors of  $\Phi$ , the motion around an equilibrium point can be analysed. For Hamiltonian systems,  $\Phi$  is a symplectic matrix [14], which means that if  $\sigma$  is an eigenvalue, then so is its inverse, its complex conjugate, and the inverse of the complex conjugate. This already provides the first observation

regarding these types of systems, which is that no asymptotic stability is possible as this requires negative real eigenvalues, which is not possible as for any negative real eigenvalue, an inverse positive eigenvalue will also exist. It can also be shown that there is a direct relation between the eigenvalues of  $\Phi$  and  $A$ , which means that by just analysing the eigenvalues of  $A$  (a much easier matrix to obtain), the motion near the equilibrium due to  $\Phi$  can be characterised.

From these properties of  $\Phi$ , three different cases can be considered for the motion near an equilibrium point. First, if a pure real eigenvalue is found, there will be one positive and one negative eigenvalue (due to the symplectic nature), which results in asymptotic stable and unstable motion near the equilibrium point. As was already shown in Eq. (2.33) for the CR3BP system, this leads to a pair of manifolds in phase space characterised by the corresponding eigenvectors, called the stable and unstable manifold. The second case is when the eigenvalues are purely imaginary, which relates to an oscillatory motion around the equilibrium point. This is a weak form of Lyapunov stability, which does not guarantee any form of nonlinear stability. These eigenvalues and eigenvectors define a 2D plane around the equilibrium point in which this periodic motion is constrained, called the center manifold. The third case is for a complex eigenvalue, which describes a combination of oscillation and attraction/expansion. The associated manifold is similar to the central one, but instead of periodic motion it consists of spiralling trajectories. In general, the motion near the equilibrium point is described by a combination of all the different manifolds described before.

Besides equilibrium points, there is also another type of special solution to consider: periodic orbits. A periodic orbit (PO) is a type of solution where the state repeats itself after a period  $T$ , i.e.  $\mathbf{x}^*(t) = \mathbf{x}^*(t + T)$  for any  $t$ . For a time-invariant system, this condition is sufficient, however for time-variant systems it is also necessary that the dynamics are periodic. Another difference between time-variant and time-invariant systems is that for time-invariant dynamics there exists a large amount of possible periods for the POs. This means that if a certain period is found for an orbit, it is likely that there is a continuous family of POs in its neighbourhood with slightly different periods. For time-periodic systems, the limiting period is the time-period of

the dynamics, thus only isolated POs exist which are commensurable with the period of the dynamics. Relating this back to small bodies, for uniformly rotating bodies with perturbing forces that are not dependent on time there exist various families of POs. For the Didymos system, in [89] several different periodic orbits were identified (under the assumption that the rotation of the primary, SRP, and third-body effects can be neglected), like direct and retrograde interior/exterior orbits, circum-secondary retrograde orbits, and terminator orbits. In the case that the body is tumbling, and/or there are time dependent perturbing forces, the POs cease to exist or they become isolated if the dynamics are periodic [90].

The stability of POs can be analysed using Floquet's theorem, which shows that the stability can be determined from the eigenvalues of the state transition matrix taken over one period, also called the monodromy matrix. If these eigenvalues have unit magnitude, the periodic orbit is stable, and if the magnitude is not equal to one the orbit is unstable. Similar to equilibrium points, one can define manifolds associated with the different eigenvalues and eigenvectors of the PO. However, in this case the manifolds have one additional dimension. This comes from the fact that along the PO the eigenvalues remain constant but the eigenvectors not. Hence, from each point along the PO a manifold emerges associated with either the stable, unstable, or center eigenvectors and eigenvalues. The center manifold of a PO is especially important, as it creates a torus around the PO on which quasi-periodic orbits (QPO) might exist. These QPOs are interesting options for mission designers as they occupy large volumes in phase space due to their high-dimensional manifolds, which allows for more trajectory options in case there are stringent requirements on the orbit design. The difficulty lies in the method to find general families of QPOs, and the computation of their stability. These QPOs have been studied for small body missions in e.g. [91] and [92], where they are shown to be excellent alternatives to periodic orbits due to their observation characteristics.

### 2.4.2 Averaging and Frozen Orbits

From a mission design perspective, it is often preferable to use orbital elements to define initial conditions for the spacecraft and then derive how these elements evolve over time due to the perturbations. As during a single orbital period the orbital elements can evolve in a periodic manner, it is useful to instead only focus on the secular change of the orbital elements to determine how the orbit changes over longer periods of time. Specifically, it is desirable to find so-called frozen orbits where (a subset of) the orbital elements stay constant [93]. This type of preliminary orbit design has been previously applied to small body missions, e.g. for OSIRIS-REx a terminator orbit was chosen as these types of orbits remain frozen in SRP dominated environments [25].

Several different techniques are used to find these types of orbits. The LPE are used from Eqs. (2.34) - (2.39) to obtain the influence of the perturbations on the orbital elements. As the secular dynamics are of interest, the LPE can be averaged over a single period of the orbit to eliminate short-period dynamics. As the LPE have the form of:  $\mathbf{f}(\mathbf{x}, t) = G(\mathbf{x}) \frac{\partial \mathcal{R}}{\partial \mathbf{x}}$ , it is possible to just average the perturbation over a single period [14]:

$$\bar{\mathcal{R}}(\mathbf{x}) = \frac{1}{2\pi} \int_0^{2\pi} \mathcal{R}(\mathbf{x}, M) dM, \quad (2.45)$$

where the mean anomaly  $M$  is often used as the independent time variable. It is important that if there are multiple time scales or frequencies of interest, these frequencies have to be separated sufficiently so that one of them can be kept constant in the averaged equations. For this reason, this technique is often applied to slow rotating asteroids [94], where the orbital period is much smaller than the rotation period. Otherwise, a doubly averaged perturbation can be considered, where the integral in Eq. (2.45) is replaced by a double integral over both periods. The frozen orbits can then be found by setting (a subset of) the LPE to zero and determining the initial orbital elements that fulfill those equations. As these frozen orbits are basically equilibrium points of the LPE, their stability can be determined using the methods described in section 2.4.1 [94].

### 2.4.3 Dynamical Indicators

The previous sections all considered special solutions (e.g. equilibrium points or periodic orbits) or specific cases (e.g. frozen orbits). These solutions represent important structures in phase space and their (linear) stability can be readily determined. However, they only represent a small number of possibilities for mission designers and when considering real world objectives and constraints, other orbits and trajectories need to be considered. The main problem with analysing trajectories in general is that there are no dynamical constraints that can help predict their behaviour over all time spans. For example, for a trajectory on a stable manifold the time evolution is known as  $t \rightarrow \infty$ , whereas for a trajectory starting from a generic initial condition (in the case of a non-integrable system) there is no closed form solution for the time evolution and the behaviour of neighbouring trajectories cannot be analysed in the same manner.

For this reason, several different types of indicators have been developed that measure how for a general solution nearby trajectories behave. These indicators are then used to create maps that relate certain initial conditions to the value of the indicator. These maps can characterize large areas of phase space and can be used to differentiate between different types of motion (e.g. chaotic or regular, stable or unstable, periodic or aperiodic, etc.). Several large reviews and comparisons of these indicators have been performed (see e.g. [95] and [96]). This section will give a short overview of the most frequently used indicators and their theoretical background, which in turn supports the reasoning behind the uncertain dynamics indicators developed in this work and introduced in section 3.2.1. For a more detailed description and comparison of these indicators, readers are referred to the review papers mentioned previously. In this thesis, three main categories of indicators are discussed: variational based indicators, frequency based indicators, and Lagrangian descriptors.

The variational based indicators are derived from the equations describing how small perturbations  $\delta\mathbf{x}_0$  with respect to a nominal initial condition  $\mathbf{x}_0$  evolve over time, i.e. the variational equations. The variational equations for a time-invariant dynamical system  $f(\mathbf{x})$  are given as follows:

$$\dot{\mathbf{v}} = \frac{\partial f}{\partial \mathbf{x}}(\mathbf{x}(t))\mathbf{v}, \quad (2.46)$$

where  $\mathbf{v}$  represents the evolution of a vector  $\mathbf{v}_0$  tangent to  $\mathbf{x}_0$  at the initial time  $t_0$ . The original indicator that was based on this equation was the Lyapunov Characteristic Exponent (LCE), which is given as follows [97]:

$$\text{LCE} = \lim_{t \rightarrow \infty} \frac{1}{t} \ln \frac{|\mathbf{v}(t)|}{|\mathbf{v}_0|}. \quad (2.47)$$

Thus, the LCE measures the exponential divergence of small perturbations at the initial condition as time goes to infinity. This quantity is hard to measure as the limit only converges after a large amount of time [98]. It was argued that the computation of these tangent vectors over short timespans is much easier and still contain a lot of information. This led to the development of the Fast Lyapunov Indicator (FLI) [99], which is defined as follows:

$$\text{FLI} = \max_{0 \leq t \leq T} \log_{10} \frac{|\mathbf{v}(t)|}{|\mathbf{v}_0|}. \quad (2.48)$$

This indicator is easier to compute and allows for fast computation of the indicator maps. It was used initially to characterize the motion of asteroids in the Solar System [99], and has also been used to characterize the dynamics around small bodies [100]. The FLI can also be interpreted as the loss of precision digits due to the numerical computation of the solution in this time interval [98], i.e. for chaotic regions small numerical errors can lead to large differences in the computed state at time  $T$ . The other popular indicator in this category is the mean exponential growth factor of nearby orbits (MEGNO) [101]:

$$\text{MEGNO} = \frac{2}{t} \int_0^t \frac{|\dot{\mathbf{v}}(\tau)|}{|\mathbf{v}(\tau)|} \tau d\tau. \quad (2.49)$$

It can be shown that the MEGNO can be related to the FLI as follows [102]:

$$\text{MEGNO} = 2[\text{FLI} - \bar{\text{FLI}}], \quad (2.50)$$

where the bar denotes the average. The characteristic of the MEGNO is that it is able to not only measure the exponential divergence of the trajectories, but also able to distinguish certain types of periodic motion. This is done as it subtracts the mean FLI up to that point from the instantaneous FLI. The Finite-time Lyapunov Exponent (FTLE) is another indicator based on variational equations, however in this case defined for a time dependent system  $f(\mathbf{x}, t)$ , with flow map  $F_{t_0}^t(\mathbf{x}_0)$  which brings the state from time  $t_0$  to  $t$ . This flow map is used to produce the Cauchy-Green strain tensor, defined as follows [103]:

$$C_{t_0}^t(\mathbf{x}_0) = [D_x F_{t_0}^t(\mathbf{x}_0)]^T D_x F_{t_0}^t(\mathbf{x}_0), \quad (2.51)$$

where  $D_x$  is the gradient operator with respect to  $\mathbf{x}$ . The FTLE is then defined as follows:

$$\text{FTLE} = \frac{1}{t - t_0} \ln \sqrt{\lambda_{\max}(C_{t_0}^t(\mathbf{x}_0))}, \quad (2.52)$$

where  $\lambda_{\max}(C_{t_0}^t(\mathbf{x}_0))$  is the largest eigenvalue of the Cauchy-Green strain tensor. Again, this indicator is able to measure what happens with small deviations with respect to  $\mathbf{x}_0$ , but needs to be calculated at each time step. This indicator allows for the discovery of material surfaces which separate regions of different behaviour. These surfaces are called Lagrangian Coherent Structures (LCS), and are a generalization of the invariant manifolds for time-dependent dynamical systems. The main weakness of the FTLE indicator is the fact that it requires numerical discretization for the derivatives which leads to noisiness in the FTLE maps. This noisiness requires smoothing which can remove information from the FTLE maps [104].

The second class of indicators are the frequency based methods that are all based on the analysis of the base frequencies of a dynamical system [105]. These types of indicators measure the frequency vector  $\boldsymbol{\nu}$  of a trajectory, obtained using the Fourier analysis of its time-series, and analyse how this changes over different time spans. It

is argued that for quasi-periodic, regular, solutions in non-integrable systems  $\nu$  stays constant as different time spans are taken. Whereas for chaotic or non-regular solutions, the Fourier approximation reveals different quasi-periodic solutions for different time spans, and thus  $\nu$  changes over time. Different indicators can then be used, like the first- or second-order derivatives of the frequencies over time, and various methods of performing the Fourier analysis can be chosen [96]. These methods are especially useful for characterizing high dimensional systems like planetary systems and particle beam accelerators.

Finally, the Lagrangian descriptors are a set of indicators which measure the arc-length, or any other positive bounded quantity that characterizes the system [104]. If this positive bounded physical quantity is given by  $|\mathcal{F}(\mathbf{x}(t))|$ , then the Lagrangian descriptor at time  $t$  with time span  $\tau$  is given by:

$$\text{LD} = \int_{t-\tau}^{t+\tau} |\mathcal{F}(\mathbf{x}(T))|^\gamma dT, \quad (2.53)$$

where  $\gamma$  represent the specific norm taken, e.g.  $\gamma = 2$  is the classic Euclidean length. There is no mathematical definition for why this indicator works, and the heuristic argument given is that across separating surfaces like the LCS, this quantity (for a properly chosen  $\mathcal{F}$ ) changes rapidly for neighbouring initial conditions. Thus, by observing the transversal change of the LD across different initial conditions, these material surfaces can be found. Even though it has been shown that there are several cases where this heuristic argument fails [106], various successful use cases have been found for this type of indicator, including in the dynamics of rubble pile asteroids [13] and in searching for regions of bounded motion in the Didymos system [107].

## 2.5 Chapter Summary

This chapter provides the theoretical background necessary for the understanding and modelling of the environment and dynamics around a small Solar system body. First, the various reference frames used in this thesis were presented: the J2000 frame, the quasi-inertial Didymos equatorial reference frame, the synodic reference frame, and

## Chapter 2. Dynamical Environment around Asteroids

the body-fixed reference frame. The various gravitational models were discussed as well, where the Spherical Harmonics model was determined to be most applicable to the work in this thesis, due to its numerical efficiency and parametrization of the mass distribution through the Stokes Coefficients, which aids in the model uncertainty analysis performed later in this thesis. The different available setups for the equations of motion were presented, and the methods used to analyse several special solutions to these equations, e.g. equilibrium points, periodic orbits, and frozen orbits, were also mentioned. Finally, dynamical indicators were introduced to allow for the analysis of general solution of the equations of motion, which will form the basis for the motivation behind the uncertain dynamical indicators introduced later in this thesis.

## Chapter 3

# Uncertainty Propagation and Quantification

This chapter is based on the work published in:

Fodde, I., Feng, J., & Vasile, M. (2022). Uncertainty maps for motion around binary asteroids. *Celestial Mechanics and Dynamical Astronomy*, 134(5), [41]. <https://doi.org/10.1007/s10569-022-10096-2>

Fodde, I., Feng, J., & Vasile, M. (2021). Uncertainty propagation for orbital motion around an asteroid using generalized intrusive polynomial algebra: application to didymos system. Paper presented at 8th International Conference on Astrodynamics Tools and Techniques.

As discussed in Chapter 1, uncertainties play an important role in space missions as a whole as the spacecraft state and environment can never be known with perfect certainty [108]. The mathematical techniques to deal with these uncertainties are thus incredibly important in space mission design. This is especially the case for small body missions, as ground based observations cannot accurately characterise the operating environment due to the small size of the bodies, leading to large uncertainties in the model parameters [109] (as can be seen in the observation results for Didymos in table 2.1). Furthermore, the techniques to perform relative navigation with respect to these bodies are quite complex, leading to large uncertainties in the state itself [110].

Uncertainty propagation aims to describe the evolution of the uncertain spacecraft

state over time. Usually, this process starts with a description of the stochastic force and/or the uncertainty in the initial state and model parameters. This description can consist of a full probability density function (PDF), uncertainty bounds, or a set of moments (e.g. the mean and covariance). The Fokker-Planck Equation (FPE), Eq. (2.41), can be solved to obtain the full statistical information at any point in time, however this can only be done for certain low-dimensional systems like the linear Langevin equation [111] and zero pressure incompressible fluids [112]. Otherwise, for higher dimensional systems only local solutions using numerical techniques are available [113]. Often, instead of solving the FPE, just the moments are propagated as this can be done more easily. In some cases, the nonlinear dynamical system can be linearized using a first-order Taylor expansion, which then results in simple analytical relations for propagating the first two moments of a Gaussian distribution. This linearization using a Taylor expansions can become problematic as the uncertainties grow [114] and/or when the dynamical system is highly non-linear [115]. Therefore, the other method often used is the Monte Carlo (MC) method, where a fully non-linear computational model of the system can be used to propagate a set of samples and obtain the sample based moments. One of the main problems with this method is that the approximation error scales with a factor of  $1/\sqrt{N}$  where  $N$  is the amount of samples. For computationally complex models, propagating these samples with sufficient accuracy can become numerically expensive. For these reasons, various semi-analytic uncertainty propagation techniques have been proposed. An in-depth overview of these different methods can be found in several surveys, e.g. [33] and [40].

These techniques can be broadly placed into two different categories: intrusive and non-intrusive methods. The intrusive methods use the dynamical equations to obtain the evolution of the uncertainties over time. The linearization approach is an example of this type of method as it uses an analytically derived first-order polynomial expansion of the system, but other more accurate methods, e.g. state transition tensors [115] or differential algebra [116], are also frequently used. Their analytical nature makes them generally numerically faster [117], but this also makes them not applicable to all types of systems. The non-intrusive methods treat the dynamics as a black-box

and can create an analytical representation of the dynamics using a set of samples by numerically propagating them through the system and analysing the outputs. The MC method is the most often used technique in this category. However, methods like non-intrusive polynomial chaos [118] or the unscented transform [119] can be much more efficient as much less samples are needed to obtain similar accuracy. As the dynamics can be treated as a black-box, these methods are especially attractive for dynamics which have complex, non-linear, equations of motion with uncertain and/or stochastic elements [120].

Once the evolution of the state uncertainty is obtained, there are various different types of analyses that can be done, e.g. analysing the effect of individual uncertain parameters on the state uncertainty [121], or analysing the evolution of the moments over time. Recently, newly developed indicators, related to the ones discussed in section 2.4.3, have been developed for uncertain systems ( see e.g. [122] [123] [124]). These uncertain dynamics indicators (as they will be called here) use various different techniques to quantify different properties, and are thus useful in understanding the underlying structures of uncertain dynamical systems.

This chapter reviews the methodology behind the different uncertainty propagation and quantification techniques that are used in this thesis. Several different tests are performed to evaluate their numerical accuracy and efficiency. Furthermore, this chapter introduces novel uncertain dynamical indicators which were developed as part of this thesis. The application and effectiveness of these techniques will then be further evaluated in chapters 4, 5, and 6.

### 3.1 Uncertainty Propagation

Consider again the parametric uncertainty dynamical system given by the Cauchy problem from section 2.3.4:

$$\begin{cases} \dot{\mathbf{x}} = \mathbf{f}(\mathbf{x}(t), \boldsymbol{\beta}, t) \\ \mathbf{x}(t_0) = \mathbf{x}_0 \end{cases} \quad (3.1)$$

where  $t$  is the time,  $\mathbf{x}$  the state vector, and  $\boldsymbol{\beta}$  a set of model parameters, and assume that  $\mathbf{x}_0$  and  $\boldsymbol{\beta}$  are uncertain and independent. Now take a set of  $N$  independent realisations  $[\mathbf{x}_{1,0}, \boldsymbol{\beta}_1, \mathbf{x}_{2,0}, \boldsymbol{\beta}_2, \dots, \mathbf{x}_{i,0}, \boldsymbol{\beta}_i, \dots, \mathbf{x}_{N,0}, \boldsymbol{\beta}_N]$ . Each realisation corresponds to a trajectory  $\phi_i(\mathbf{x}_{i,0}, \boldsymbol{\beta}_i, t)$ , which are solutions of problem (3.1). The corresponding state vector at time  $t_k$  is  $\mathbf{x}_i(t_k) = \phi(\mathbf{x}_{i,0}, \boldsymbol{\beta}_i, t_k)$ .

Now, consider a set of states at time  $t_0$  defined as follows:

$$\Omega_{\mathbf{x}_0} = \{\mathbf{x}_0(\boldsymbol{\xi}) \mid \forall \boldsymbol{\xi} \in \Omega_{\boldsymbol{\xi}}\}, \quad (3.2)$$

where  $\boldsymbol{\xi}$  is the vector containing all the uncertain variables defined over the uncertainty set  $\Omega_{\boldsymbol{\xi}}$ , e.g. in the case of purely parametric uncertainty  $\boldsymbol{\xi} = [\mathbf{x}_0, \boldsymbol{\beta}]$ . In the following we will assume that  $\Omega_{\boldsymbol{\xi}}$  is bounded. A bounded set can be defined also when  $\boldsymbol{\xi}$  is distributed according to a function  $\rho(\boldsymbol{\xi})$  with infinite support by taking  $\Omega_{\boldsymbol{\xi}}$  so that  $\int_{\Omega_{\boldsymbol{\xi}}} \rho(\boldsymbol{\xi}) d\boldsymbol{\xi} < \varepsilon$  with  $\varepsilon$  a given percentile. The set of all possible states at the given time  $T$  induced by the realisations of  $\boldsymbol{\xi}$  can be defined as follows:

$$\Omega_T(\boldsymbol{\xi}) = \{\mathbf{x}(T, \boldsymbol{\xi}) \mid \mathbf{x}(T, \boldsymbol{\xi}) = \mathbf{x}_0 + \int_{t_0}^T \mathbf{f}(\boldsymbol{\xi}, \tau) d\tau \forall \boldsymbol{\xi} \in \Omega_{\boldsymbol{\xi}}\}. \quad (3.3)$$

If  $\mathbf{x}_t$  is continuous in  $\boldsymbol{\xi}$  and the set is compact,  $\Omega_T(\boldsymbol{\xi})$  can be approximated using a polynomial function:

$$\tilde{\Omega}_T(\boldsymbol{\xi}) = P_{n,d}(\boldsymbol{\xi}) = \sum_{i=0}^{\mathcal{N}} c_i(T) \alpha_i(\boldsymbol{\xi}) = \sum_{\mathbf{i}, |\mathbf{i}| \leq n} c_{\mathbf{i}}(T) \alpha_{\mathbf{i}}(\boldsymbol{\xi}), \quad (3.4)$$

where  $n$  is the degree of the polynomial,  $d$  is the number of variables of the polynomial,  $\mathbf{i} \in [0, n]^d \subset \mathbb{N}^d$ ,  $|\mathbf{i}| = i = \sum_{r=1}^d i_r$ ,  $c_{\mathbf{i}}(t_0)$  are a set of coefficients, and  $\alpha_{\mathbf{i}}(\boldsymbol{\xi}) = \alpha_{i_0}(\xi_0) \cdot \alpha_{i_1}(\xi_1) \cdot \dots \cdot \alpha_{i_d}(\xi_d)$  are multivariate basis functions generated using a tensor product of univariate functions, which determine the numerical characteristics of the approximation. The size, i.e. number of terms of the polynomial, is given by  $\binom{n+d}{d}$ . The formulation of the indices in the second summation of Eq. (3.4) allows for a more efficient implementation. The ordering and manipulation of these indices is discussed in more detail in [125]. A polynomial model can have its accuracy and nu-

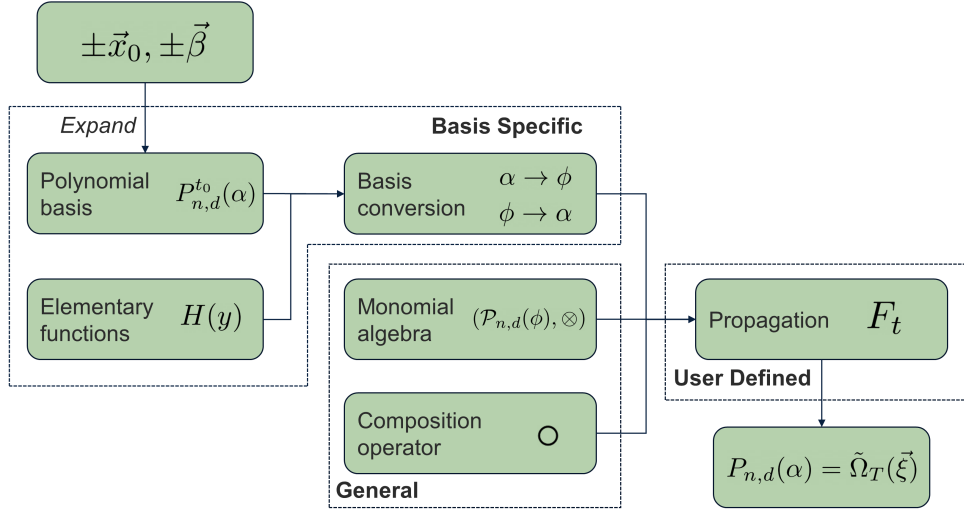


Figure 3.1: A diagram explaining the general process of GIPA.

merical efficiency tuned using the polynomial order of the fitted model. Furthermore, the final model is fully characterised by just its coefficients, allowing for easier analysis of the model as will be shown in section 3.2.1. Several different approaches to obtaining these polynomials are available. This thesis explores two specific methods, one intrusive (Generalised Intrusive Polynomial Algebra) and one non-intrusive (Non-intrusive Chebyshev Interpolation).

### 3.1.1 Generalised Intrusive Polynomial Algebra

The Generalised Intrusive Polynomial Algebra (GIPA) method is a generalisation of various methods like differential algebra [116], Jet transport [123], and Chebyshev polynomial algebra [126]. These methods all obtain  $\tilde{\Omega}_T(\xi)$  by approximating the initial uncertain parameters using polynomial  $P_{n,d}(\alpha)$  with basis functions  $\alpha$ , creating an algebra over the space of these polynomial consisting of elementary operations  $\oplus = \{+, -, \cdot, \text{etc.}\}$  plus composition among polynomials  $P_{n,d}(\alpha)$ . The floating point algebra normally used to obtain the solution  $\mathbf{x}_t = \phi(\mathbf{x}_0, \beta, t)$  for a single deterministic trajectory is then substituted with this polynomial algebra and all the elementary functions in  $\phi$  (e.g.  $1/x$ ,  $\sin(x)$ ,  $\cos(x)$ , etc.) are substituted as well with their respective polynomial expansion. The previously mentioned methods focus on a single

polynomial basis  $\alpha$ , but GIPA introduces a method to generalise this process for any choice of polynomial. These steps and the generalisation introduced by GIPA is shown in figure 3.1 and explained in detail in the following section.

The choice of basis determines the specific properties that the polynomial approximation will have. The two bases that will be discussed in this work are the Taylor polynomial basis and the Chebyshev polynomial basis. Taylor polynomials offer a good approximation near the expansion point and provide analytic expressions for elementary functions, which results in more efficient computation. However, the accuracy of a Taylor polynomial quickly drops off further away from the expansion point (as can be seen in figure 3.2), and requires the function that is approximated to be  $n + 1$  times differentiable. The Chebyshev polynomial approximation is uniformly convergent across the expansion interval, and is able to handle discontinuities in the dynamics better compared to a Taylor expansion [127]. The downside of a Chebyshev basis is the fact that no general expression for elementary functions exist, which can decrease the accuracy in certain cases and increase the computation time.

To graphically show the differences in error distribution between the two bases, a simple propagation of one single orbit around Didymos is performed using the two different bases. The distributions are then sampled using the resulting polynomial and compared with numerically propagated trajectories (in figure 3.2 labeled as MC points). The error as a function of the sampled location, labeled as  $x_1$  in adimensionalized units  $-$ , within the set is shown in more detail in figure 3.2. The Taylor approximation is more accurate near the central point whereas the Chebyshev approximation behaves better near the ends of the distribution, as expected. There is still an increase in the error away from the central point for the Chebyshev basis, which comes as a result of the specific application of the GIPA method, as explained in more detail in this section and reference [117]. There are other bases like the Newton basis and the Hermite basis that might be more applicable to certain other types of problems, and can be implemented and tested in a similar manner to the bases described here.

Once the basis is chosen, the next step of GIPA is to add a set of arithmetic operations  $\otimes$ , which correspond to the commonly known arithmetic operations  $\oplus \in$

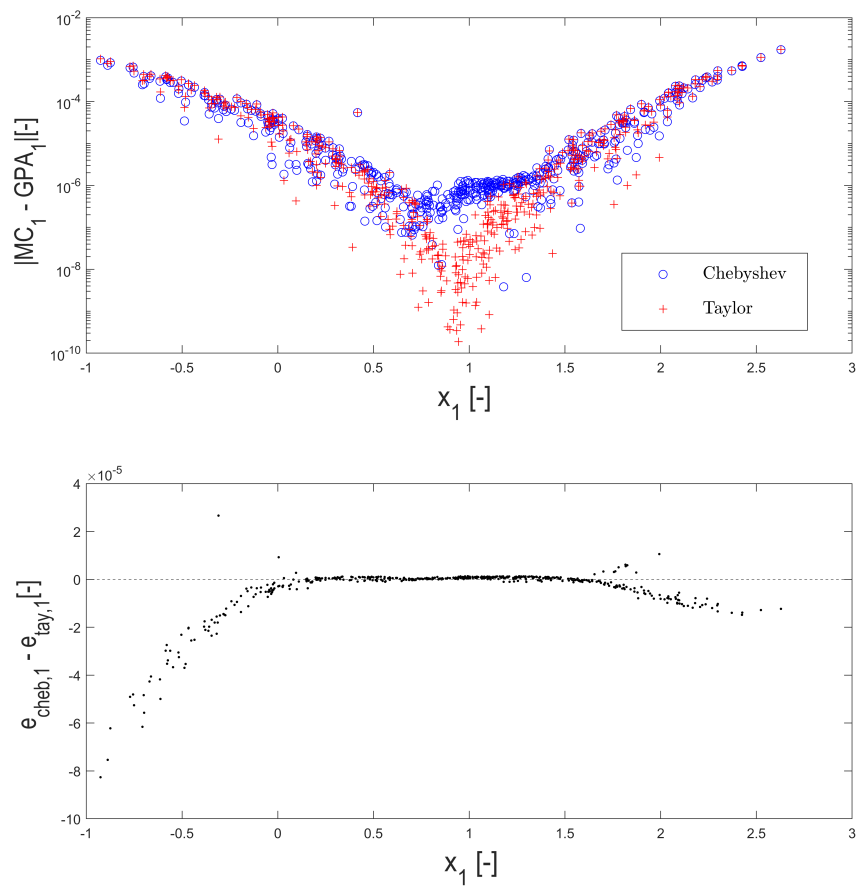


Figure 3.2: The error distribution of the two different GIPA bases as a function of the location in the set. The top figure shows the spatial distribution of the differences, where the bottom figure shows the differences between the two bases. Below the zero line signifies better Chebyshev performance, whereas above the line shows better Taylor performance.

$\{+, -, \cdot, /\}$ . Then, for any operation between two functions  $f_a$  and  $f_b$ , the corresponding operations for their polynomial approximations,  $F_A$  and  $F_B$ , is given as follows:

$$f_a \oplus f_b \sim F_A \otimes F_B. \quad (3.5)$$

The polynomial space  $\mathcal{P}_{n,d}(\alpha)$  and the operations on that space together form an algebra  $(\mathcal{P}_{n,d}(\alpha), \otimes)$  of size  $\mathcal{N} = \binom{n+d}{d}$ , for which any polynomial part of this algebra is completely defined by its coefficients  $c = \{c_i : |\mathbf{i}| < n\}$ .

Ref. [117] argued that for any polynomial basis, it is beneficial to transform the basis to the monomial basis, given by  $\phi$ , after the expansion of the initial set as this will reduce the computational cost and only requires one set of operations to be implemented. The downside is that the coefficients can get much larger compared to other bases and the change of basis operation can be ill-conditioned. However, it was shown that despite this, the monomial basis can still give accurate results [128]. The final order of operations is as follows: first, the initial set is expanded in the desired polynomial basis. Second, the basis is transformed to the monomial basis (if possible) by:

$$\nu : \mathcal{P}_{n,d}(\alpha) \rightarrow \mathcal{P}_{n,d}(\phi). \quad (3.6)$$

Finally, the monomial algebra is constructed to propagate the initial set  $\Omega_{\mathbf{x}_0}$  to the desired final set  $\Omega_{\mathbf{x}_t}$ .

The "general" part of GIPA is due the fact that irregardless of the choice of polynomial basis, the operations remain the same due to the fact that a change of basis to monomials is used after the initial expansion. These operations are further discussed here.

The operations of subtraction and addition for the monomial algebra are as follows: given two polynomials  $A(\mathbf{x})$  and  $B(\mathbf{x})$ , with coefficients  $a$  and  $b$  respectively, the result of addition and subtraction are:

$$c = a \pm b. \quad (3.7)$$

Where the resulting polynomial  $C(\mathbf{x})$  can then be constructed from the coefficients

c. The multiplication operation is given by:

$$A(\mathbf{x}) \cdot B(\mathbf{x}) = \left( \sum_{i, |i| \leq n} a_i \mathbf{x}^i \right) \cdot \left( \sum_{i, |i| \leq n} b_i \mathbf{x}^i \right), \quad (3.8)$$

where all the resulting monomials with orders higher than  $n$  are truncated by setting them to zero to keep the resulting polynomial order equal to the order of  $A(\mathbf{x})$  and  $B(\mathbf{x})$ .

The composition operator can be used to create a set of elementary functions, and is defined as follows: given a multivariate function  $g(\mathbf{y})$  and a  $d$ -dimensional multivariate function  $\mathbf{y}(\mathbf{x})$ , with their respective polynomial approximations  $G(\mathbf{y})$  and  $\mathbf{Y}(\mathbf{x})$ , the composition operator is given by:

$$g(\mathbf{y}(\mathbf{x})) \sim G(\mathbf{y}) \circ \mathbf{Y}(\mathbf{x}). \quad (3.9)$$

Thus, a general definition is given by:

$$\circ : \mathcal{P}_{v,\delta}(\phi) \times [\mathcal{P}_{n,d}(\phi)]^\delta \rightarrow \mathcal{P}_{n,d}(\phi). \quad (3.10)$$

To be able to use the elementary functions given by  $h(y)$  in the polynomial algebra, the composition operator is used as follows:

$$h(\mathbf{f}(\mathbf{x})) \sim H(y) \circ \mathbf{F}(\mathbf{x}). \quad (3.11)$$

where  $H(y)$  is the univariate polynomial approximation of  $h(y)$  and  $\mathbf{f}(\mathbf{x})$  a multivariate function with  $\mathbf{F}(\mathbf{x})$  its polynomial approximation. In this case:

$$\circ : \mathcal{P}_{n,1}(\phi) \times \mathcal{P}_{n,d}(\phi) \rightarrow \mathcal{P}_{n,d}(\phi). \quad (3.12)$$

The way in which  $H(y) \sim h(y)$  is approximated has a large impact on the accuracy and functionality of the polynomial algebra. For the Taylor algebra, the functions are expanded using the well known order- $n$  MacLaurin expansion, which expands around a central point and does not require information about the interval over which it is

approximated. For the Chebyshev algebra, an expansion on the interval  $I = [\underline{y}, \bar{y}]$  is performed using an order 100 Chebyshev interpolation. The Chebyshev series is then obtained by truncating the interpolation to a certain order, and converting it to the monomial basis. A problem with this is that a good estimation of  $I$  is needed to perform the approximation of  $h(y)$  over this interval, which can give an overestimation of the range for certain algorithms. This problem is discussed in more detail in [117]. If a certain dynamics expression has a lot of elementary functions, this range overestimation can become a large problem.

The difference in computational complexity for the expansion of the elementary functions is relatively large between the two different bases. Following the analysis in Ref. [117], the Taylor approach has a complexity of  $O(n)$ , whereas for the Chebyshev basis it is  $O(\mathcal{N}_{n,d} + n^3)$ , where  $\mathcal{N}_{n,d} = \binom{n+d}{d}$  is the size of the algebra. However, besides the function expansion, for both bases the composition operation needs to be performed as well when evaluating these elementary functions. This composition has a computational complexity of  $O(d2^{n+1}\mathcal{N}_{n,d}^2)$ , which has a much larger contribution compared to the elementary function expansion complexity of both bases and needs to be performed regardless of the basis choice. This means that the final runtime is dominated by the composition operator, and thus close to equal between the two bases.

To summarise, consider now a numerical propagation scheme that can propagate the state through the dynamical system given in Eq. (3.1), given by:

$$\psi(\mathbf{x}_k) \rightarrow \mathbf{x}_{k+1}. \quad (3.13)$$

The basic idea is to represent all the elements of the state vector  $\mathbf{x}$  and model parameters  $\beta$  as elements of the polynomial algebra  $(\mathcal{P}_{n,d}(\phi), \otimes)$ , then all operations and elementary functions used in  $\psi$ , which consists of the dynamics Eq. (3.1), are also represented using the algebra. Finally,  $\psi$  is used to propagate the system in time using the same methods for a single state vector  $\mathbf{x}$ , but now propagating the full set represented by  $\mathbf{X}$ .

An example can be given using the Euler scheme, given by:

$$\mathbf{x}_{k+1} = \mathbf{x}_k + \mathbf{f}(\mathbf{x}_k, \beta, t)\Delta t. \quad (3.14)$$

All the elements of the initial state vector  $\mathbf{x}_0$  are expanded in the algebra to give  $\mathbf{X}_0$ .  $\mathbf{f}(\mathbf{x}_k)$  then has all its arithmetic operations and elementary functions changed to the corresponding operations in the polynomial algebra to give at each timestep:

$$\mathbf{X}_{k+1} = \mathbf{X}_k + \mathbf{F}_k\Delta t. \quad (3.15)$$

where  $\mathbf{F}_k$  is the dynamics function represented in the polynomial algebra, evaluated using  $\mathbf{X}_k$ . This is done at each timestep until the final desired time is reached, at which point  $\mathbf{X}_{k_f}$  represents the approximation of the set of final states resulting from the set of initial states, given by Eq.(3.4).

An often discussed disadvantage of intrusive methods is that they require large adaptations to existing software and methods. However, for GIPA it is possible to use the same orbit propagators and dynamical models found in most astrodynamics applications, and only change the underlying elementary functions and arithmetic operations. This can often be done using templates and overloading, which is possible in a range of modern coding languages. The implementation of the algebra for this work uses the open-source SMART-UQ software package [129]. Referring to figure 3.1, the basis specific methods of: expanding the initial state and model parameters in the polynomial basis, representation of elementary functions, and basis conversion are implemented in SMART-UQ for several different bases, including both Taylor and Chebyshev basis. The general methods for the monomial algebra (the elementary operations and composition operator) are then also implemented such that the user defined propagation can be performed by specifying the type of the state and model parameters that are used as input for the dynamics function as a polynomial instead of floating-point and overloading the operations and functions inside the dynamics using the SMART-UQ operators and functions.

### 3.1.2 Non-Intrusive Chebyshev Interpolation

As was mentioned previously, the non-intrusive methods use a set of samples from the initial uncertainty set and propagate them through the dynamical system. Based on the samples after propagation, an approximation of this input-output relationship is made, which can be done in several different manners. This work follows a similar approach as [126] and [130], and uses a Chebyshev polynomial basis together with a Smolyak sparse grid sampling approach to obtain the polynomial from Eq. (3.4), which is hereafter called the non-intrusive Chebyshev Interpolation (NCI) method.

The Smolyak sparse grid was developed in [131], and selects a set of input points based on the extrema of Chebyshev polynomials. An important aspect is that they do not suffer the curse of dimensionality, as the number of points grow polynomially with the dimension of the problem instead of exponentially. A more in depth explanation of this method for uncertainty propagation is given in [126].

Given the propagated samples, the coefficients of the polynomial can be obtained by inverting the following system:

$$HC = Y, \quad (3.16)$$

where:

$$H = \begin{bmatrix} T_{i_1}(\boldsymbol{\xi}_1) & \dots & T_{i_s}(\boldsymbol{\xi}_1) \\ \vdots & \ddots & \vdots \\ T_{i_1}(\boldsymbol{\xi}_s) & \dots & T_{i_s}(\boldsymbol{\xi}_s) \end{bmatrix}, C = \begin{bmatrix} c_{i_1} \\ \vdots \\ c_{i_s} \end{bmatrix}, Y = \begin{bmatrix} y_1 \\ \vdots \\ y_s \end{bmatrix} \quad (3.17)$$

where  $s = \mathcal{N} = \binom{n+d}{d}$ ,  $\boldsymbol{\xi}_1, \dots, \boldsymbol{\xi}_s$  are the Smolyak sparse grid points, and  $Y$  the vector containing all the corresponding propagated samples  $y_i = \phi_i(\boldsymbol{\xi}_i, t)$ .

This method is significantly less complex than the GIPA method, and allows for the dynamics to be used as a black box, which makes this method interesting for dynamics where the derivatives of the equations of motion are difficult to obtain.

In Ref. [117] the theoretical computational complexity of both the NCI and GIPA method were compared. It was shown that if a similar final accuracy is assumed, the

NCI method is much more efficient for systems where there is a low dimensionality but high amount of evaluations of the dynamics. The GIPA, on the other hand, is more efficient in the case of high-dimensional (generally  $d > 3$ ) problem with less dynamics evaluations. As in this thesis the main choice between NCI and GIPA is due to the approach in which they are able to handle different numerical properties (as will be explained in more detail in the following section), the efficiency is less of a factor.

Both the GIPA and NCI technique are used to obtain the same result: a polynomial representation of the uncertainties that can be used to propagate the PDF/uncertainty bounds through the dynamics. The difference in approach between the two methods makes them each more applicable to different problems. As was said before, the GIPA approach is more efficient whereas the NCI can be more easily implemented and handles complex dynamical systems better. Therefore, the GIPA method will be used in the numerically intensive applications discussed in chapter 4 and 6, whereas the NCI will be used for the complex dynamics discussed in chapter 5.

### 3.1.3 Numerical Results

Some numerical results for both methods are discussed in this section. As the GIPA method is used for the orbital motion discussed in chapters 4 and 6, the numerical tests will focus on these scenarios. On the other hand, the main use of the NCI method is to model the complex dynamics of the ballistic landing on Dimorphos discussed in chapter 5, hence the numerical tests performed for this method just focuses on its ability to handle those dynamics.

#### 3.1.3.1 GIPA

To determine the effectiveness of GIPA with a Taylor and Chebyshev basis, several simulation settings have to be considered. These tests are performed for the generalised inertial form of the equations of motion, where the force models used are: a SH model of degree and order 4 for both bodies, a cannonball model for the SRP, and the third body perturbation of the Sun. The rotation model for both Didymos and Dimorphos mentioned in section 2 are also included.

### Chapter 3. Uncertainty Propagation and Quantification

First, for the nominal trajectory a terminator orbit will be chosen, as this has been known to be a stable choice for situations where the SRP has a significant impact on the dynamics [132]. The requirements for the initial conditions for a circular terminator orbit are as follows [76]:

$$\Omega_s = 90^\circ / 270^\circ + \nu_h, \quad (3.18)$$

$$i_s = 90^\circ - i_h, \quad (3.19)$$

$$a_s < \frac{1}{4} \sqrt{\frac{\mu\beta}{G_1}}, \quad (3.20)$$

where  $\Omega_s$  is the right ascension of the ascending node of the spacecraft,  $\nu_h$  is the true anomaly of the heliocentric orbit,  $i_s$  the inclination of the spacecraft,  $i_h$  the inclination of the heliocentric orbit,  $a_s$  the spacecraft's semi-major axis,  $\mu$  the asteroids gravitational parameter,  $\beta$  the mass-to-area ratio of the spacecraft, and  $G_1$  a constant equal to  $1 \cdot 10^8 \frac{kg \cdot km^3}{s^2 \cdot m^2}$ . The resulting maximum semi-major axis is equal to 8.13 km, thus initially orbits with a semi-major axis of 7 km will be considered to ensure no escape (considering no state uncertainties). Most of the simulations will be run for 10 days as this is significantly longer than the time in between planned  $\Delta V$  manoeuvres (3-4 days [133]) and thus can give results on how the orbit will evolve due to its natural dynamics in those time spans, and what the risk is if those manoeuvres cannot be executed. A Runge-Kutta 4 fixed step-size integrator is used to integrate the equations of motion, with 1 hour steps. The initial uncertainties first considered have a magnitude of 1% on the initial semi-major axis and orbital velocity (i.e. upper/lower bound of the position  $x_i$  will be  $x_i \pm 0.01a$ , where  $a$  is the semi-major axis, and of the velocity  $v_i$  will be  $v_i \pm 0.01\sqrt{\mu/a}$ ). The effect of larger uncertainties will be shown later in this section. All the values are adimensionalized and scaled by dividing by the position and velocity of Dimorphos.

Two metrics will be used to determine the accuracy of the GIPA: the root mean square error (RMSE) and the maximum error, defined as follows:

$$RMSE = \sqrt{\frac{1}{N_s} \sum_{i=1}^{N_s} (\hat{x}_i - x_i)^2}, \quad (3.21)$$

$$E_m = \max_{1 \leq i \leq N_s} |\hat{x}_i - x_i|, \quad (3.22)$$

where  $\hat{x}_i$  is the GIPA calculated state and  $x$  is the true state at the same point in time. This requires a large sample of "true" trajectories to be generated, which will be done by first randomly sampling a set of  $N_s = 1000$  initial conditions, and then propagating them using a Runge-Kutta 87 adaptive step-size integrator. In the rest of this thesis, this method is referred to as a Monte Carlo simulation, even though no comparison is necessarily made with the probability distribution or moments of the MC simulation, which is the usual application of the MC method.

The degree of the polynomial expansion is an important factor that firstly needs to be investigated for this specific problem. Figure 3.3 shows both the RMSE and maximum error as a function of the polynomial degree. Furthermore, it shows the runtime for the application on a computer with an Intel<sup>®</sup> 8th generation core i7 processor and 16Gb of RAM. For reference, the runtime for the Monte Carlo simulation is also shown in the figure. It can be seen that at lower degrees the Taylor basis performs better, and at a degree of 5 for both bases the RMSE flattens out and no significant gains are obtained if the polynomial expansion degree is increased. The maximum error does seem to improve slightly if the degree is higher. This does come at the cost of a significant increase in runtime between a degree 4 and degree 5 polynomial compared to the increase in accuracy. However, if then figure 3.4 is observed, it can be seen that earlier in the propagation, the RMSE of the degree 5 polynomial is much lower and only becomes comparable with the degree 4 polynomial towards the end of the simulation.

As was mentioned in section 3.1.1, a good estimation of the range  $I$  of the expansion is needed to estimate the elementary functions. The fastest method for this is to take the sum and subtraction of all the coefficients to obtain the maximum and minimum, respectively, for each state variable. In [117] it was shown that this method can lead to large overestimation errors. Thus another method is tested here, where the range

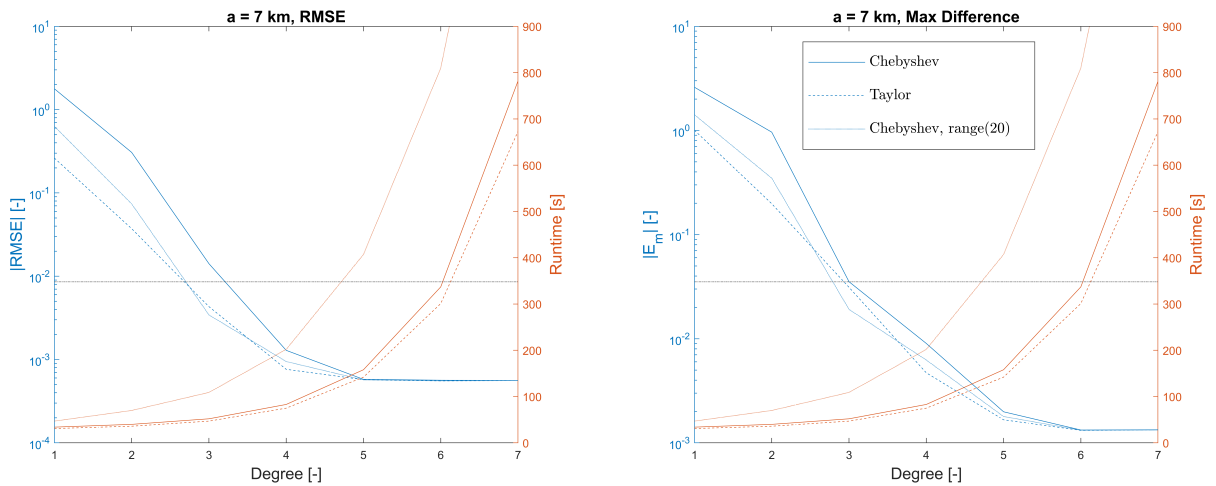


Figure 3.3: The accuracy after 10 days of propagation for different polynomial degree expansions and coefficient range estimation algorithms. The horizontal line represent the MC runtime.

is obtained by randomly selecting  $n$  samples and evaluating them using the expansion. From this, the maximum and minimum values are then saved and used as the range. Figure 3.3 and 3.4 both show how these methods give different results when using 20 samples. It can be seen that the sample based method requires a significantly longer runtime, but at lower degrees produces a much better result. However, at a degree of 5 and higher, the sample based method does not seem to result in much improvement compared to the coefficient based method. If the evolution of the accuracy is observed in figure 3.4, then for a polynomial degree of 4 the increase in accuracy at earlier times is clearly visible. However, for a polynomial degree of 5, it can be clearly seen that a maximum accuracy has already been reached and that changing the range estimation function does not influence the accuracy much. For the coming results, a polynomial of degree 5 will be considered with normal coefficient based range estimation, unless stated otherwise.

Now, the influence of choosing different uncertainty values (represented in GIPA by the size of the to be propagated set) and orbital parameters is discussed. First, a range of possible initial set sizes is investigated for the state variables. The relative set size is considered, where the sizes are determined as a percentage of the initial semi-major axes

### Chapter 3. Uncertainty Propagation and Quantification

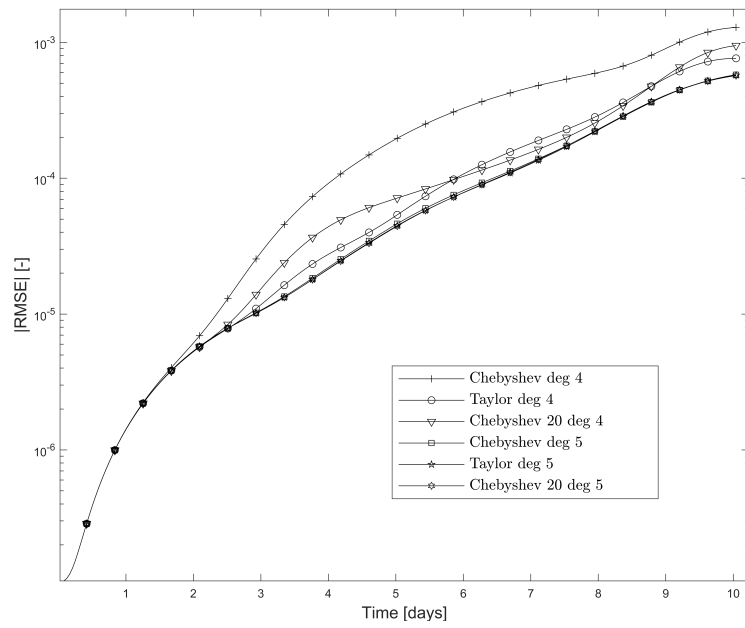


Figure 3.4: The change in accuracy over time for various GIPA settings.

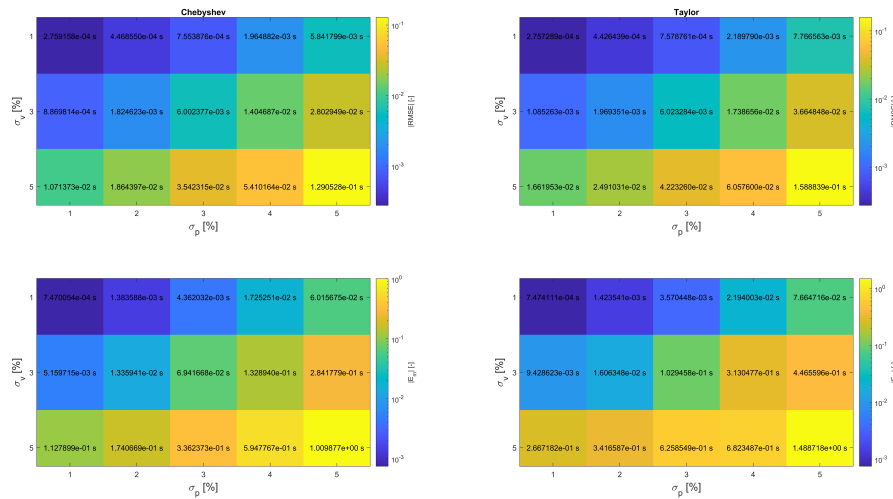


Figure 3.5: Grid of several initial set sizes and the corresponding RMSE and maximum error (norm over whole state vector) at the final time.

and orbital velocity for the position and velocity state variable respectively, i.e.  $x_i \pm \sigma_p a$  and  $v_i \pm \sigma_v \sqrt{\mu/a}$ . A grid of relative set sizes with values  $\sigma_p = [1\%, 2\%, 3\%, 4\%, 5\%]$ ,  $\sigma_v = [1\%, 3\%, 5\%]$  is taken, where  $\sigma$  represents the radius of the uncertainty ellipsoid.

The results of the accuracy at the final time for the whole grid for both the Taylor and Chebyshev bases are shown in figure 3.5. It can be seen that the difference in accuracy between the (1%, 1%) size and the (5%, 5%) (corresponding to (70m, 7mm/s) and (350m, 3.5cm/s) respectively) differs two to three orders of magnitude in both RMSE and maximum error. There is, furthermore, no clear distinction in sensitivity to either the position or velocity state variables with respect to an increase in RMSE. For lower sizes, the difference in accuracy between the bases is small. However, when increasing the set size, the relative difference between the accuracy of both bases shows that the Chebyshev basis performs better. This is due to the fact that the Taylor polynomial loses accuracy further from the central expansion point, whereas the Chebyshev uniformly converges over the whole set. For the results discussed afterwards, a set size of (1%, 1%) is chosen. The conclusions taken there still hold for larger set sizes, as only the absolute accuracy shown might differ.

Two other dynamical parameters that have a large influence on the dynamics are discussed here: the initial semi-major axis  $a$  and eccentricity  $e$ . Figure 3.6 shows the influence of changing the initial  $a$ . There, it can be seen that there is clear trend between the accuracy and the altitude. As the altitude decreases, the dynamics become more complex and the accuracy of the GIPA decreases. Except for slight variations at earlier times, the performance of both bases is comparable at all values of  $a$ .

In figure 3.7,  $a$  is fixed at 7km and the eccentricity is increased in 5 steps. For higher eccentricity values it can be seen that the accuracy significantly decrease as the spacecraft moves closer to periapsis. For smaller values of the eccentricity, it can be seen that after crossing periapsis the accuracy increases again. This is shown in more detail in 3 dimensions in figure 3.8 for  $e = 0.3$ . The RMSE initially increases before approaching and reaching the peak when at the periapsis. Here it can be seen in figure 3.8 that the accuracy, especially at the ends of the set, is relatively low compared to previous steps. However, instead of remaining at the same RMSE or increasing RMSE

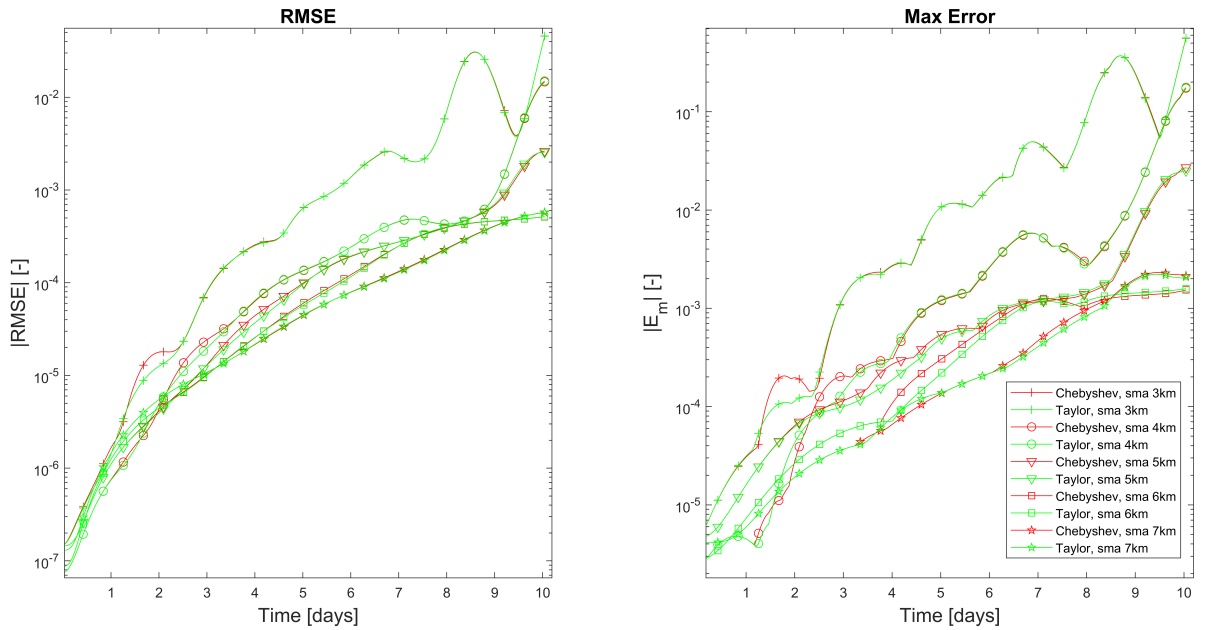


Figure 3.6: The influence of the starting semi-major axis on the accuracy development over time. The green lines are for the Taylor basis and the red lines for the Chebyshev basis.

afterwards, the RMSE decreases again when approaching apoapsis. This shows clearly that the accuracy is highly dependent on the complexity of the dynamics, which is higher near the bodies. Compared with the influence of  $a$ , the two bases show much more difference in their performance. Before approaching the periapsis, the performance is similar, however the Taylor polynomial retains much more accuracy after periapsis passage compared to the Chebyshev basis. This could be due to the fact that the Chebyshev basis builds up overestimation error over time, which it cannot lose again after periapsis. For the Chebyshev basis at  $e = 0.5$  and  $e = 0.7$ , a jump in RMSE and maximum error happens after a period of time. This happens as the large eccentricity causes the uncertainty set to wrap around the body and thus cause the range of the Cartesian coordinates to intersect the center of Didymos. This causes a numerical divergence and significantly increases the error. If these high eccentricity orbits are used, this problem can be resolved by changing the used state variables as was done in [134] using the generalised equinoctial elements.

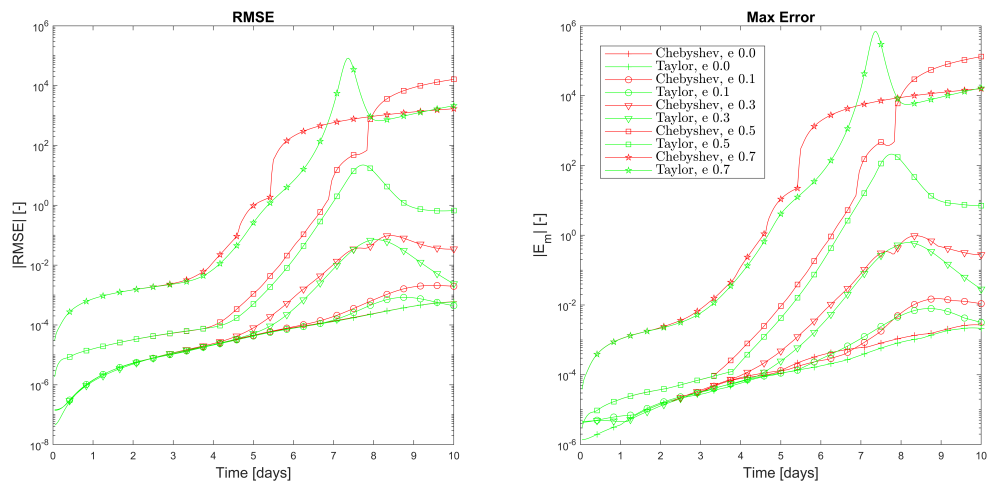


Figure 3.7: The influence of the starting eccentricity on the accuracy development over time at a semi-major axis of 7 km.

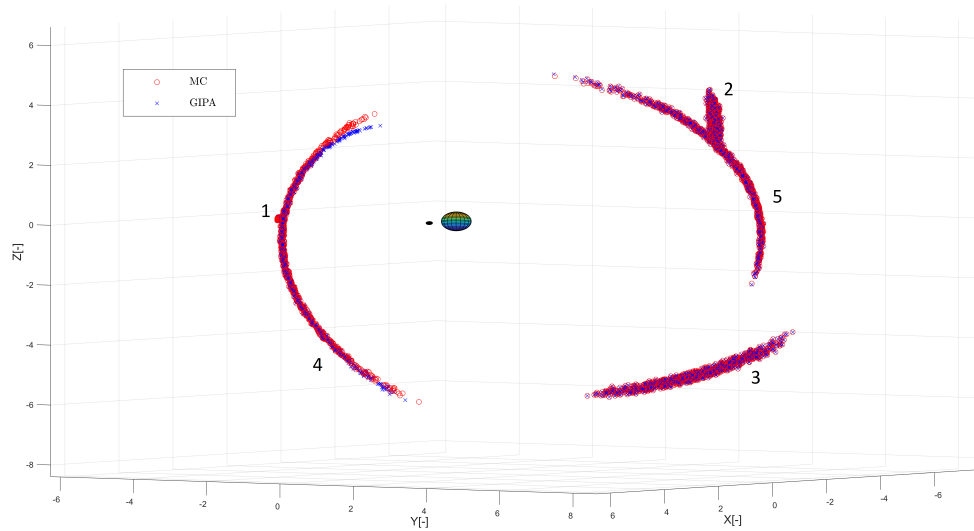


Figure 3.8: Monte Carlo versus Taylor basis GIPA of the  $e = 0.3$  orbit for 5 points in time. The order in time for the different steps is represented by the number next to it.

### 3.1.3.2 NCI

To show the effect of different sampling approaches on the accuracy of the coefficients obtained from inverting Eq. (3.16), an analysis is done on a typical landing trajectory where there is a ballistic flight phase, and a landing and surface motion phase. The complexity in the dynamics stemming from the moment of landing can be particularly difficult on the approximation. The accuracy is measured by taking a set of uniformly sampled points and comparing the samples at different times along the trajectory between a MC approach and the polynomial expansion of Eq. (3.4). Both the RMSE and maximum error over all samples are calculated. As a comparison against the Smolyak sparse grid, the Latin Hypercube Sampling (LHS) method is used. The LHS method divides the sampling space into several uniformly spaced subspaces in which a random sample is taken for each individual subspace. The resulting RMSE and maximum error along the trajectory is given in figure 3.9, where the CR3BP with SH gravitational model is used. Both methods show relatively equal accuracy during the ballistic phase. However, the sparse grid method handles the landing much better compared to the LHS method for which a large jump in RMSE and max error happens.

## 3.2 Uncertainty Quantification

The final propagated set given by Eq. (3.4) provides a surrogate dynamical system which propagates samples from the uncertain set at the initial time to the final time. This surrogate dynamical system can be efficiently evaluated and is fully defined by its coefficients. These two properties allow for different types of analyses to be performed on the uncertain dynamical system.

First, the uncertain dynamics indicators are defined, which are a set of dynamical indicators specifically designed for the analysis of uncertain systems. The first two indicators, the variance indicator and the  $n + 1$  indicator are original to this thesis, whereas the pseudo-diffusion indicator was developed in Ref. [124]. Afterwards, the different approaches for the estimation of the moments of (a subset of) the uncertainty sets are discussed.

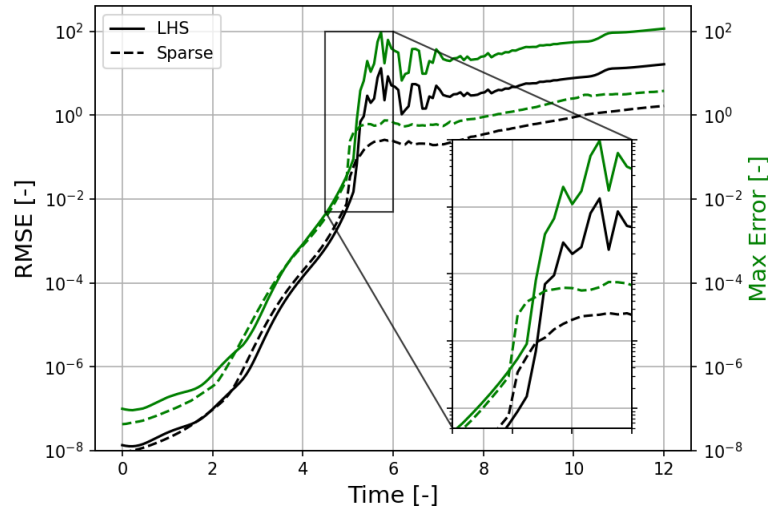


Figure 3.9: LHS sampling accuracy compared against the Smolyak sparse grid accuracy. The RMSE and max error are taken of the norm of the full state. The zoomed in part of the figure is the time epoch when the landing occurs. Both the RMSE and max error are given in the dimensionless values of the CR3BP.

### 3.2.1 Uncertain Dynamics Indicators

Dynamics indicators like the FLI and the FTLE quantify the difference, in phase space, between trajectories that start from nearby initial conditions. However, they intrinsically assume the dynamics to be deterministic. Hence, if the dynamics is uncertain, commonly used deterministic dynamics indicators would have different values for each realisation of the uncertain quantities. In order to fully analyse the system in question, the deterministic indicators would need to be re-computed for a sufficiently large amount of different realisations (or sampling) of the uncertain quantities. This can quickly become computationally expensive, especially as the dimensionality of the uncertain space increases. Therefore, for dynamical systems affected by uncertainty, different types of indicators are needed that can quantify the effect of the uncertainty in the dynamics without an extensive sampling of the uncertainty space. To this end, in [135] and [124] the authors proposed a pseudo-diffusion indicator and a stochastic version of the FTLE. Here we propose two alternative indicators that capture two aspects of the effect of uncertainty on the evolution of non-linear dynamical systems.

In the following we will develop scalar indicators that capture the evolution of  $\Omega_{\mathbf{x}t}$  and will show how the value of these indicators gives an indication of the level of sensitivity to uncertainties. The indicators are derived from the propagation of the uncertainties through the dynamics.

### 3.2.1.1 Variance Indicator

For each realisation of the uncertain quantities  $\boldsymbol{\xi}$  the dynamical system can follow a different trajectory, even for exactly the same initial conditions. Thus multiple realisations correspond to an ensemble of trajectories.

**Definition 3.2.1.** We define the diffusion of the ensemble of trajectories induced by the uncertainty  $\boldsymbol{\xi}$  in the dynamics as the evolution, over time, of the relative separation among the trajectories in the ensemble. More formally, we want to measure the expected difference between a trajectory in the ensemble  $\mathbf{x}(t)$  and the expected trajectory  $\bar{\mathbf{x}}(t)$  or:

$$\sigma^2(t) = \mathbb{E}[(\mathbf{x}(t) - \bar{\mathbf{x}}(t))^2] \quad (3.23)$$

for  $t > T$  and  $\bar{\mathbf{x}}(t) = \int_{\Omega_{\boldsymbol{\xi}}} \mathbf{x}(t) \rho(\boldsymbol{\xi}) d\boldsymbol{\xi}$ .

Thus we can measure the degree of diffusion by following the time variation of the variance  $\sigma^2(t)$  of the trajectories in the ensemble.

Diffusion in celestial mechanics has been studied before for several different types of processes, see e.g. [136] and [137]. The idea of a variance indicator comes from the fact that in dynamical systems subject to a diffusive random process, like a random-walk, the mean square displacement is proportional to  $t^\gamma$  where  $\gamma$  is the diffusion exponent [138]. In one dimension, this can be expressed in the following form:

$$\mathbb{E}[(x(t) - \bar{x})^2] \approx K_\gamma t^\gamma, \quad (3.24)$$

where  $K_\gamma$  is the diffusion coefficient and  $\bar{x}$  is a reference position. In normal diffusive processes, like Brownian motion,  $\gamma = 1$  and (3.24) reduces to the Einstein and Smoluchowski, linear time relationship  $\mathbb{E}[(x(t) - \bar{x})^2] \approx 2Dt$ , with  $D$  the diffusion coefficient,  $\bar{x}$  the mean of a Gaussian distribution, from which one can calculate the variance

$\sigma^2 = \mathbb{E}[(x(t) - \bar{x})^2]$ . Thus if one takes an ensemble of trajectories the variance of the state vector at a given time  $t$  can be written as:

$$\sigma^2 = \mathbb{E}[(x(t) - \bar{x}(t))^2] \approx K_\gamma t^\gamma, \quad (3.25)$$

Given (3.25), in the following we propose the direct use of  $\sigma^2$  to measure the degree of diffusion induced by an uncertainty in initial conditions and dynamic model parameters.

The quantity  $\sigma^2$  gives an indication of the separation of two trajectories over time due to the uncertainty in the initial conditions and dynamics. If this separation is induced by an uncertainty in a static parameter of the dynamic model, it implies that without an exact knowledge of that parameter, the true trajectory can diverge from the expected one. If the uncertainty is due to a time-dependent diffusive stochastic process,  $\sigma^2$  would measure the degree of diffusion induced by this process at a given point in time. In [139] it was also observed that if the uncertainty is parametric and the dynamics is chaotic, the variance can present a rapid increase locally even if the process is not diffusive on the long term. If the uncertainty is in the initial conditions or a combination of initial conditions and model parameters, chaotic diffusion can cause an increase in the variance. However, as also observed in [139], chaotic attractors only cause diffusion in a local, bounded, region of phase space as the trajectories remain bound to the surface of this attractor. Thus, chaotic dynamics does not necessarily imply long term diffusion.

We now observe that when the uncertainty set is approximated with an expansion in polynomials  $H_i(\boldsymbol{\xi})$  that are orthogonal with respect to a weight function  $\rho(\boldsymbol{\xi})$ , the variance is a function of the sum of the square of the coefficient of the polynomial. In fact:

$$\bar{x}(t) = \mathbb{E}[x(t)] \approx \mathbb{E}[P_{n,d}(\boldsymbol{\xi})] = \int_{\Omega_\xi} \left( \sum_{i, |i| \leq n} c_i(t) H_i(\boldsymbol{\xi}) \right) \rho(\boldsymbol{\xi}) d\xi = c_0, \quad (3.26)$$

where the fact that  $H_0 = 1$  and  $\mathbb{E}[H_i] = 0, \forall i \neq \mathbf{0}$  is used to obtain the final

relation. With this result, the second moment, or the variance, is obtained:

$$\sigma^2 = \mathbb{E}[(x(t) - \bar{x}(t))^2] \quad (3.27)$$

$$\approx \int_{\Omega_{\xi}} \left( \sum_{i, |i| \neq 0} c_i(t) H_i(\xi) \right) \cdot \left( \sum_{i, |i| \neq 0} c_i(t) H_i(\xi) \right) \rho(\xi) d\xi \quad (3.28)$$

$$= \sum_{i, |i| \neq 0} \langle H_i, H_i \rangle c_i^2(t). \quad (3.29)$$

As the monomial basis used in the GIPA method is not an orthogonal basis, the polynomial in Eq. (3.4) has to be transformed into an expansion in an orthogonal basis. If one uses a Hermite basis, the conversion from one basis to the other is given by the expression [140]:

$$\xi^n = n! \sum_{m=0}^{n/2} \frac{1}{2^m m! (n-2m)!} H_{n-2m}(\xi), \quad (3.30)$$

where  $H$  is the probabilistic Hermite polynomial. The Hermite polynomials are orthogonal under a weight function  $\rho(\xi) = e^{-\frac{\xi^2}{2}}$  and are defined as follow:

$$\langle H_n, H_m \rangle = \int_{-\infty}^{\infty} H_n(\xi) H_m(\xi) \rho(\xi) d\xi = n! \sqrt{2\pi} \delta_{nm}, \quad (3.31)$$

where  $\delta_{nm}$  is the Kronecker delta function. The statistical moments of the quantity described by the orthogonal polynomials (in this case the set  $\Omega_{\xi}$ ) can be calculated using the definitions of the moments.

Thus, by using the results from Eq. (3.29) and Eq. (3.31), the variance can be obtained from summing the square of the non-zeroth order coefficients and adding a constant factor  $\langle H_i, H_i \rangle = |i|! \sqrt{2\pi}$ . From Eq. (3.24) and Eq. (3.29), it can be seen that the coefficients of the orthogonal polynomial expansion can be used as an effective indicator of the diffusion for different initial conditions. As the relative value of the variance between different initial conditions is considered, the factor  $|i|! \sqrt{2\pi}$  remains constant, while the sum of the squared coefficients changes in value. Therefore, this factor can be ignored and simply the sum of the square of the coefficients is used.

In multiple dimensions the mean square displacement is defined as the sum of the mean square displacements along each dimension. Here, the maximum value of  $\eta_\sigma$  over all state variables is taken to represent the maximum degree of diffusion, leading to the indicator:

$$\eta_\sigma = \max_j \sigma_j^2, \quad j = 1, 2, \dots, d \quad (3.32)$$

The variance of Eq. (3.29) is based on the variance of the Cartesian state variables. However, it can be generalised to a state vector containing different representations of the state. The Keplerian orbital elements, i.e. the semi-major axis  $a$ , eccentricity  $e$ , inclination  $i$ , argument of perigee  $\omega$ , and right ascension of the ascending node  $\Omega$ , can give an intuitive view of the geometry of an orbit around the system. From the mission design perspective, having an orbit with these elements staying relatively bounded over time and are not sensitive to off-nominal conditions is important as this allows for predictable behaviour and low chances of impact or escape. However, in a highly non-linear and uncertain system, like the one considered here, this is not always the case and the variance of the possible orbital elements can grow quickly over time. Therefore, it is important to look at the evolution of these orbital elements and determine if they remain relatively bounded over time. Specifically, the  $a$  and  $e$  have a large effect on the shape of the orbit and are thus important elements that need to stay relatively constant over time.

Using the same principle as the coefficient based variance for a general state vector, the diffusion of  $a$  and  $e$  can be calculated. Using the operations defined by the GIPA method, the polynomial approximations of the state variables can be converted to polynomial approximations of  $a$  and  $e$  using the well-known conversions [78]:

$$a = \frac{1}{\frac{2}{r} - \frac{v^2}{\mu}} \quad (3.33)$$

$$\mathbf{e} = \frac{\mathbf{v} \times \mathbf{h}}{\mu} - \frac{\mathbf{r}}{r}, \quad (3.34)$$

where  $\mu$  is the gravitational parameter of the central body (Didymos) and  $\mathbf{h} = \mathbf{r} \times \mathbf{v}$  is the angular momentum. The eccentricity can then be obtained by taking the vector norm of Eq. (3.34). However, a problem arises when the norm is taken of  $\mathbf{e}$  when the final orbit is close to circular, as a Taylor approximation of a square root around zero diverges. Thus instead the squared eccentricity,  $|\mathbf{e}|^2 = e_1^2 + e_2^2 + e_3^2$  is used instead. Using Eq. (3.29), the variance in  $a$  and  $e^2$  can then be calculated, representing the diffusion of the shape-based orbital elements.

In this work, the pseudo-diffusion indicator developed in [124] is used to characterise the dynamics of ballistic landings on Dimorphos. This indicator is selected as it measures the rate of growth of the uncertainty set over time, which in the case of a (partial) landing of the uncertainty set should be very low compared to uncertainty sets which have bounced away from the body and are moving around the system. Therefore, this indicator should allow for the identification of these different dynamical regimes.

The pseudo-diffusion indicator is based on the characterisation of diffusive processes given by Eq. (3.24). Using the fact that the state is expanded using the polynomial of Eq. (3.4) and that for any polynomial with orthogonal basis the variance can be given by Eq. (3.29), the following expression can be derived:

$$\sum_{i, |i| \neq 0} \kappa_i c_i^2(t) = K_\gamma t^\gamma, \quad (3.35)$$

where  $\kappa_i = \langle \mathbf{H}_i, \mathbf{H}_i \rangle$ , which is equal to  $|\mathbf{i}|! \sqrt{2\pi}$  in the case of a Hermite basis. Assuming large  $t$ ,  $\gamma$  can be approximately found using the following expression:

$$\gamma \approx \tilde{\gamma} = \frac{\log(\sum_{i, |i| \neq 0} \kappa_i c_i^2(t) + 1)}{\log t} \quad (3.36)$$

Where  $\tilde{\gamma}$  is called the pseudo-diffusion exponent. In the multivariate case, the covariance matrix of the polynomial expansion can be found using Eq. (3.37):

$$\Sigma_x(t) \approx \int_{\Omega_\xi} \left( \sum_{i, |i| \neq 0} \mathbf{c}_i(t) \mathbf{H}_i(\xi) \right) \cdot \left( \sum_{i, |i| \neq 0} \mathbf{c}_i(t) \mathbf{H}_i(\xi) \right) \rho(\xi) d\xi = \sum_{i, i \neq \mathbf{0}} \kappa_i \mathbf{c}_i(t) \mathbf{c}_i^T(t). \quad (3.37)$$

From this expression and Eq. (3.36), a definition for the general pseudo-diffusion indicator can be given as follows [124]:

$$\tilde{\gamma} = \frac{\log(\sqrt{\max_i \lambda_i(\mathbf{c}(t))} + 1)}{\log t}, \quad (3.38)$$

where  $\lambda_i$  is the  $i$ th eigenvalue of the covariance matrix  $\Sigma_{\mathbf{x}}(t)$ . This equation for  $\tilde{\gamma}$  is again fully defined by the coefficients of the polynomial approximation of the dynamics and its relation with the diffusive process of Eq. (3.24). In the case of  $\tilde{\gamma}$ , it specifically indicates the expansion of the set over time.

### 3.2.1.2 $n + 1$ Coefficient Indicator

The accuracy of the Taylor approximation of the dynamics depends on several characteristics of the system. In [114], it was found that an increase in the size of the uncertainty set over time leads to a less accurate polynomial approximation of the set, due to the truncation of the polynomial at a certain degree. Note that this observation not only holds for Taylor expansions but can be shown to also hold for Chebyshev polynomials [141], although this is not as straight forward as for the Taylor polynomial. In the rest of this thesis this indicator is only calculated using the Taylor approximation, hence this discussion can be limited to just this case.

Given a degree  $n$  Taylor approximation  $P_{n,d}(\mathbf{x})$  of the function  $f$  around the origin, where  $f$  is  $n + 1$  times differentiable and the  $(n + 1)$ th derivative of  $f$  is bounded as follows:  $f(\mathbf{a})^{(n+1)} \leq M$ ,  $\mathbf{a} \in (0, \mathbf{x})$ , the error bound in the approximation because of the truncation at degree  $n$  can be obtained as follows:

$$|f(\mathbf{x}) - P_{n,d}(\mathbf{x})| \leq \frac{M}{(n + 1)!} \mathbf{x}^{n+1} = c_{n+1} \cdot \mathbf{x}^{n+1}. \quad (3.39)$$

As  $f$  represents the dynamics of the system, and the  $n + 1$  coefficient is related to the  $(n + 1)$ th derivative of  $f$  in the region over which the Taylor approximation is performed, the specific value of this coefficient can give information on the dynamical behaviour in that region. The specific value of  $c_{n+1}$  can be affected by several different factors, e.g. the propagation time, initial uncertainty size, and the non-linearity of

the system [114]. It can be seen that for a Taylor approximation with a high  $c_{n+1}$ , trajectories that start close together in the domain of the Taylor approximation can have significantly different behaviours.

An example illustration of this effect is shown in figure 3.10. Two sets, A and B, are propagated through two different dynamics (this can be two different dynamical systems or two different regions in phase space of the same system). At  $t_f$ , the shape of set A has been significantly deformed because of the non-linearity of the dynamics. Set B has grown larger compared to set A but has been deformed less, due to the more linear dynamics which can only cause a rotation and expansion (or contraction) of the set. Hence, a low degree  $n$  polynomial can accurately approximate set B as there are no higher order, non-linear effects, which causes  $c_{n+1}$  to be small. If the same order  $n$  is used for the approximation of set A, the error in the approximation would be high as higher order terms are needed to capture the non-linear effects that cause this deformation. This leads to a high value of  $c_{n+1}$  in this case. Therefore, fixing the degree  $n$  of the polynomial approximations (keeping the degree high enough to accurately approximate most of the phase space) and comparing the values of  $c_{n+1}$  for different regions of phase space gives the relative non-linearity of those regions.

The extent of non-linearity that is measured by the  $n + 1$  coefficient can be an indication of diffusion or chaos. On the other hand, a high value of the  $n + 1$  coefficient can indicate that the trajectories, in an ensemble induced by the uncertain quantities, behave very differently, but are not necessarily diffusing. This would be the case of a system that is chaotic but all trajectories remain confined in a region of state space. Vice versa, trajectories subject to a linear dynamics can diverge exponentially. For example, two trajectories with different initial conditions of the linear dynamics  $dx/dt = x$  will diverge exponentially over time. Thus the concepts of diffusion and non-linearity are only linked for certain cases and measuring them both can give different insights into the dynamics.

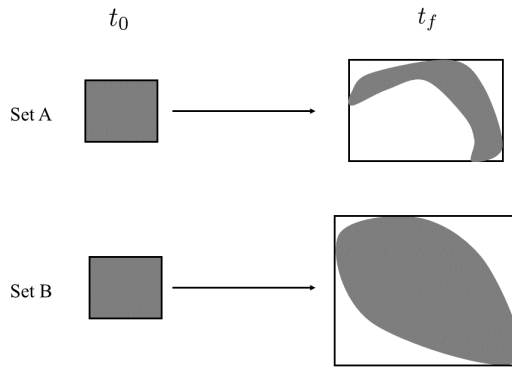


Figure 3.10: Diagram showing two sets being propagated. The gray shaded area is where the actual trajectories are located and the black square represents the range of the set. Set A represent the propagation through more non-linear dynamics while set B has larger variance but is less non-linear.

In [123], the maximum initial set size for a Taylor approximation was calculated using the estimated truncation error, and used as a dynamics indicator for the circular restricted three body problem. Furthermore, in [122] a Taylor algebra with a truncation error based domain splitting technique was used as an indicator of the stability of certain orbits under uncertainties, by measuring the amount of splits at a specific location in phase space. In this work a similar approach is used, namely the size of the  $n + 1$  degree coefficients is used as an indicator to determine suitable initial conditions for robust stable orbits. This method avoids the use of methods like automatic domain splitting, which decreases the efficiency and ease-of-use of GIPA.

The size of the  $n + 1$  degree coefficients is calculated as follows. First, a set of initial conditions and model parameters is propagated using the GIPA method. Second, from the resulting polynomial approximation, the size of the coefficients of a specific degree  $i$  are calculated, up to polynomial degree  $n$  as follows:

$$S_i = \sum_{|i|=i} c_i. \quad (3.40)$$

Using the values of  $S_i$  for all the different degrees up to and including  $n$ , a least-squares fit algorithm is used to get an analytical expression for the size of the coefficients

for a specific degree. To improve the accuracy and efficiency of the fitting procedure, a linear fit is performed using the equation as follows:

$$\log S_i = \log A - B \cdot i, \quad (3.41)$$

where  $A$  and  $B$  are constants estimated using the least squares algorithm. Finally, using Eq. (3.41), the value for the  $n + 1$  degree coefficient size,  $S_{n+1}$ , can be estimated.

As the  $S_{n+1,j}$  represents the  $n + 1$  coefficient size for each different state variable, the direction of maximum non-linearity can be found by taking the maximum value of  $S_{n+1,j}$  over all state variables. This value is then used as the indicator as follows:

$$\eta_{n+1} = \max_j S_{n+1,j}, \quad j = 1, 2, \dots, d \quad (3.42)$$

### 3.2.1.3 Duffing Oscillator Tests

The main focus of this research is on the use of these derived indicators for the analysis of the dynamics of a third body around the near-Earth binary asteroid system Didymos. However, to validate the indicators, a dynamical system with a well studied behaviour, called the Duffing oscillator, is used. As the pseudo-diffusion indicator has already been verified in Ref. [124], the focus in this section will be on the variance and  $n + 1$  indicator.

The Duffing oscillator is a two-dimensional non-linear dynamical system which models a damped and driven oscillator. The system is defined in equation (3.43).

$$\begin{cases} \dot{x} &= v_x, \\ \dot{v}_x &= A \cos \omega t - \delta v_x - \alpha x - \beta x^3. \end{cases} \quad (3.43)$$

The two state variables are  $x$  and  $v_x$ , the driving force is oscillatory described by amplitude  $A$  and frequency  $\omega$ . The damping of the system, the linear stiffness, and the non-linearity are given by  $\delta$ ,  $\alpha$ , and  $\beta$ , respectively.

Chaotic behaviour can appear in this system for specific sets of model parameters

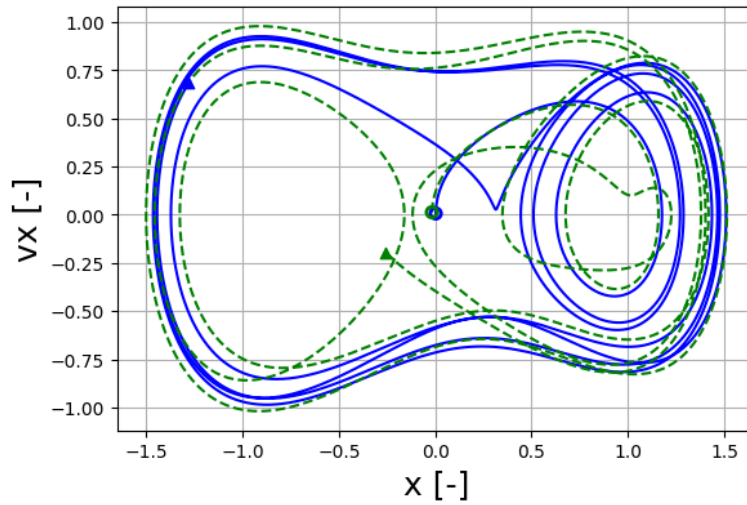


Figure 3.11: Phase plot of two trajectories (dashed green and solid blue lines) for the Duffing oscillator with slightly different initial conditions. The system parameters are as follows:  $\gamma = 0.4$ ,  $\omega = 1.0$ ,  $\delta = 0.25$ ,  $\alpha = -1.0$ ,  $\beta = 1.0$ .

and initial conditions. An example of this is shown in figure 3.11, where two trajectories are plotted with slightly different initial conditions around the origin that are represented with a blue and green dot. It can be seen that for a short amount of time the two trajectories remain close but diverge rapidly afterwards, as indicated by the two triangles marking the final states. The amount of divergence depends on the initial conditions and the time window over which the system is analysed, due to the non-autonomous behaviour caused by the driving force [103]. Therefore, it is important to determine the initial conditions that lead to more regular behaviour.

For the Duffing oscillator, the goal is to validate the performance of the indicators by comparing the results with the known dynamical structure. In [123], a Taylor polynomial algebra based method (using only state uncertainty) to determine the Lagrangian Coherent Structures (LCS) was compared with results using an FTLE indicator. It was found that both these methods give similar results. Therefore, in this research the Duffing oscillator is analysed using just state uncertainties and compared with the FTLE results from previous analyses (e.g. [103]).

A grid of a 100 by 100 initial conditions is taken in the range of  $x = [-1.5, 1.5]$  and  $v_x = [-1.5, 1.5]$ . For each of these initial conditions, an initial uncertainty set with

a range of 0.03 is defined for both coordinates, corresponding to the size between the points in the initial conditions grid. This set is then propagated to  $T = 8$ , where both the indicators are calculated, using a Taylor basis setup for the GIPA method.

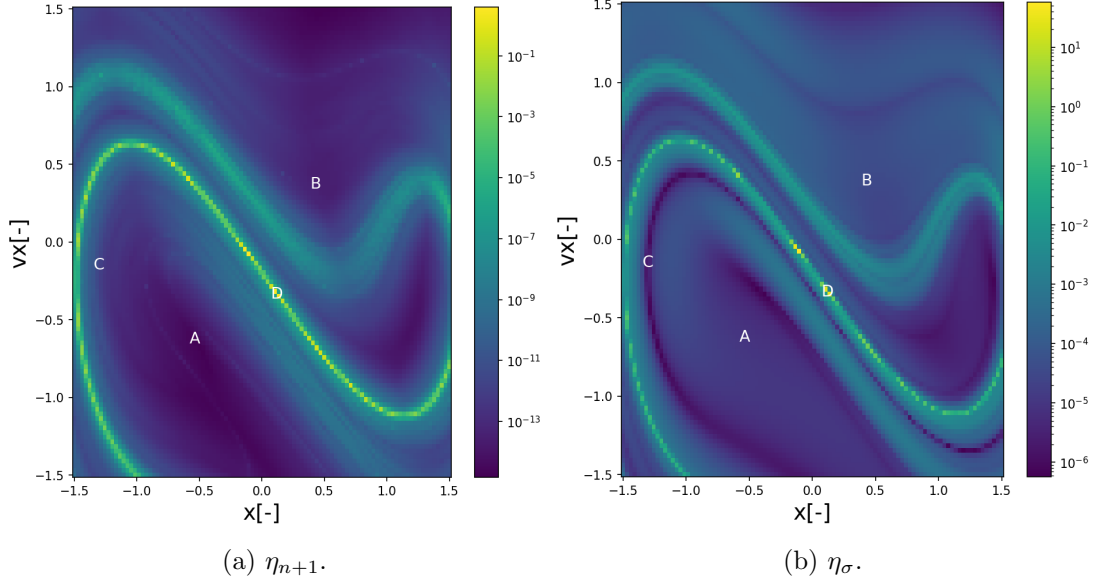


Figure 3.12: The uncertain dynamics indicators maps for the Duffing oscillator with state uncertainty at  $T = 8$ . The letters in the maps correspond to several sample trajectories shown in figure 3.13.

The grids for both the  $\eta_{n+1}$  indicator from Eq. (3.42) and the  $\eta_\sigma$  indicator from Eq. (3.32) are obtained and displayed in figure 3.12. The structure of the maps from both indicators can be compared to find the differences between the two indicators. The regions of irregular or diffusive motion (green to yellow, i.e. higher indicator value) are similar between the two maps. Showing that the effect of high diffusion on both the  $\eta_{n+1}$  and  $\eta_\sigma$  indicator is similar. However, there are more differences found when observing the areas of regular motion (dark blue, i.e. lower indicator value). Regions showing the lowest indicator values for  $\eta_\sigma$  do not correspond to the minimum  $\eta_{n+1}$  regions, and vice versa. As the  $\eta_{n+1}$  indicator measures the non-linearity, which is affected by other factors besides the divergence of trajectories as well, these regions are likely affected more by the non-linearity due to non-diffusive effects compared to the regions of lower  $\eta_{n+1}$  values.

A Monte Carlo analysis for a set of sample initial conditions for a longer integration

time ( $T = 16$ ,  $N = 500$ ) is shown in figure 3.13. Trajectories C ( $\eta_{n+1} = 4.58e-12$ ,  $\eta_\sigma = 2.09e-6$ ) and D ( $\eta_{n+1} = 2.07$ ,  $\eta_\sigma = 32.64$ ) show clearly the non-diffusive and diffusive behaviour respectively. Both trajectory A ( $\eta_{n+1} = 2.12e-15$ ,  $\eta_\sigma = 9.03e-6$ ) and B ( $\eta_{n+1} = 3.11e-14$ ,  $\eta_\sigma = 3.55e-5$ ) can be seen in figure 3.13 to have slightly more diffusion than C, but remain much closer together than trajectory D. However, comparing the values of the  $\eta_{n+1}$  indicator shows that trajectory A has the lowest value instead of C. To determine further what is the cause, the coefficients and a set of samples taken from the polynomial at the final epoch are shown in figure 3.14 and figure 3.15, respectively. The main influence on the lower value of  $\eta_{n+1}$  for A comes from the higher degree coefficients, which have a lower value compared to those of C. As  $\eta_\sigma$  is mainly influenced by the first couple of degrees, which are similar between A and C, this difference does not have as large an effect on the variance. The shape of the final sets from a number of samples is shown in figure 3.15. Even though the diffusion of A is larger than that of C, the higher non-linearity of C, shown by the difference in shape between the two sets, increases its value of  $\eta_{n+1}$ . Therefore, showing that  $\eta_{n+1}$  is affected by the non-linearity in general, and not only the diffusion.

The  $\eta_\sigma$  indicator map has a clear physical interpretation, where high values indicate a high amount of diffusion, or a large divergence of trajectories. As previously discussed, the  $\eta_{n+1}$  indicator map demonstrates the difference of the non-linearity between different regions in phase space due to the difference of the size of higher order terms in the polynomial approximation. The physical consequence of this is that trajectories that start close together can have significantly different behaviours. For high  $\eta_{n+1}$ , this non-linearity and diffusion are linked (case D), whereas for low  $\eta_{n+1}$  the trajectories can still diverge though with smaller non-linearity (see case A).

Comparing to previous analyses of the dynamical structure (e.g. [103]) from the FTLE indicator, figure 3.12 shows similar structures by using the uncertain dynamics indicators. The advantage of the uncertain dynamics indicators is that the uncertainties can also be considered for the model parameters, which is demonstrated by applying them to the Didymos system in chapter 4.

Chapter 3. Uncertainty Propagation and Quantification

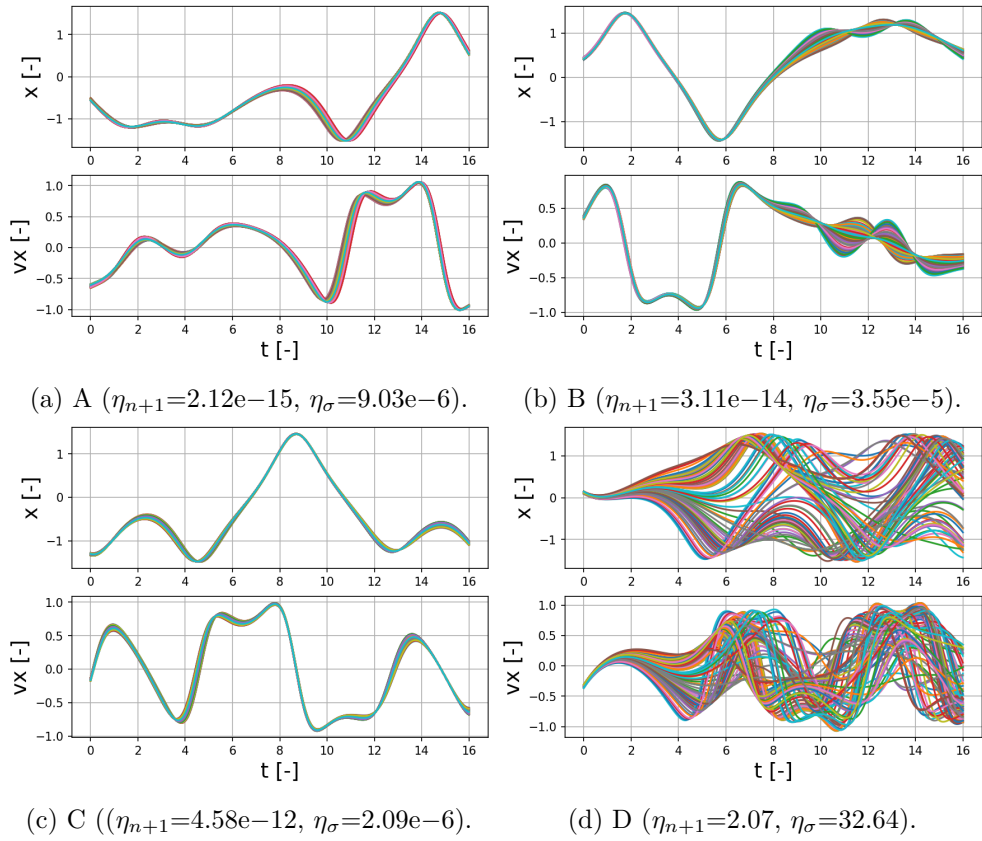


Figure 3.13: Sample trajectories from the uncertain dynamics indicator maps propagated until  $T = 16$  for the Duffing oscillator.

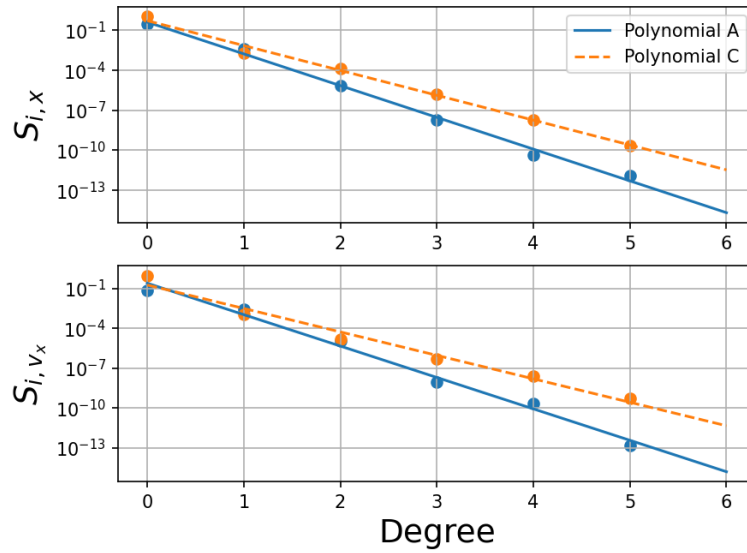


Figure 3.14: The polynomial coefficients at the final epoch from test trajectories A and C.

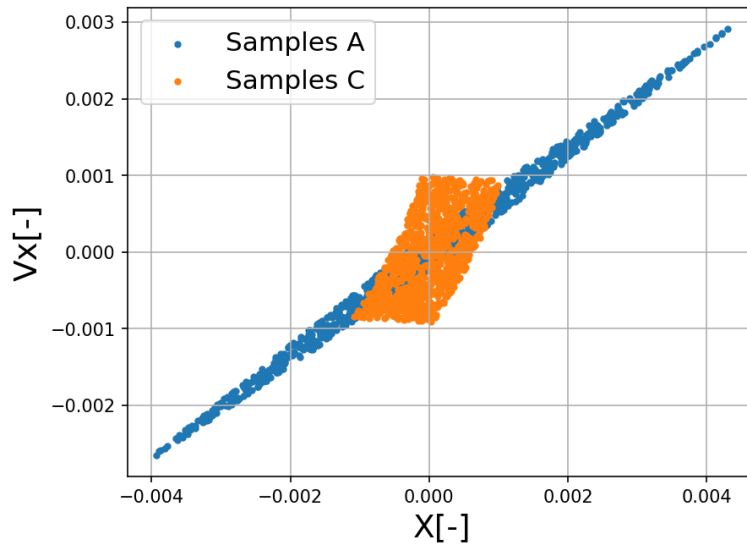


Figure 3.15: Samples taken from the resulting polynomial and translated to be centered around (0, 0) for initial conditions A and C at the final epoch.

### 3.2.2 Expectation Estimation

Another way of analysing and quantifying the uncertainties is by estimating the moments of the PDF over time. As was shown in Eqs. (3.26) and (3.37), the moments of the uncertainty set can be estimated using the coefficients of the polynomial expansion. In Ref. [142] it was shown that using the Polynomial Chaos technique for any polynomial basis where the weight function represents a PDF, e.g. the Hermite polynomials represent a Gaussian distribution through the weight function  $\rho(x) = e^{-\frac{x^2}{2}}$ , then the polynomial expansion converges to this PDF and the moments of this PDF are given by Eqs. (3.26) and (3.37). Thus, by converting to the proper basis one can obtain the moments analytically after the polynomial expansion has been performed.

As will be shown in chapter 6, sometimes only the moments for parts of the uncertainty set need to be estimated. In this case one needs different methods. A simple MC approach where  $N$  samples are taken to estimate these moments is the most straightforward approach. However, the accuracy of this method converges slowly and again a large amount of samples need to be taken. If this needs to be done a large amount of times, this can become numerically intensive even for polynomial evaluations. Another approach is to use an Unscented Transform [119], where the first two moments of a

Gaussian distribution can be estimated by properly selecting the samples to be taken. This is more efficient, however the accuracy is fixed and if a higher accuracy is needed there is no way to tune this method. Therefore, another method is used here based on sparse grids and Hermite-Gauss quadrature.

The propagation of Normally distributed variables in general requires integrating the following types of equation:

$$1/\sqrt{\pi^d|\Sigma|} \int_{-\infty}^{\infty} e^{-\frac{1}{2}(\mathbf{x}-\boldsymbol{\mu})^T\Sigma^{-1}(\mathbf{x}-\boldsymbol{\mu})} f(\mathbf{x})d\mathbf{x}, \quad (3.44)$$

where  $\boldsymbol{\mu}$  are the means and  $\Sigma$  the covariance matrix.  $f(\mathbf{x})$  can be various functions, e.g.  $f(\mathbf{x}) = \mathbf{x}$  for the mean and  $f(\mathbf{x}) = (\mathbf{x} - \boldsymbol{\mu})^T(\mathbf{x} - \boldsymbol{\mu})$  for the covariance. These integrals can be solved numerically using Gauss-Hermite quadrature and a change of variables ( $\mathbf{x} = \sqrt{2}L\mathbf{y} + \boldsymbol{\mu}$ , where  $\Sigma = LL^T$  and  $L$  is determined using Cholesky decomposition), as follows [143]:

$$1/\sqrt{\pi^d} \int_{-\infty}^{\infty} e^{-\mathbf{y}^T\mathbf{y}} f(\sqrt{2}L\mathbf{y} + \boldsymbol{\mu})d\mathbf{y} \quad (3.45)$$

$$\approx \sum_{i=0}^N \frac{w_i}{\sqrt{\pi^d}} f(\sqrt{2}L\boldsymbol{\zeta}_i + \boldsymbol{\mu}), \quad (3.46)$$

where  $w_i$  are the Gauss-Hermite weights and  $\boldsymbol{\zeta}_i$  the roots of the Hermite polynomial. The accuracy of the integration can be tuned by increasing the number of quadrature points. In case of propagating a set of Gaussian variables, e.g. the state knowledge, from time  $t_k$  to  $t_{k+1}$ , a large number of quadrature samples would need to be numerically integrated. However, as a polynomial approximation is used, instead of a numerical integration only a polynomial evaluation is needed for each quadrature point, significantly reducing the computation time. For example, the mean of the state at time  $t_{k+1}$  can be calculated as follows:

$$\boldsymbol{\mu}_{\mathbf{x}_{k+1}} \approx \sum_{i=0}^N \frac{w_i}{\sqrt{\pi^d}} \tilde{\Omega}_{t_{k+1}}(\sqrt{2}L\boldsymbol{\zeta}_i + \boldsymbol{\mu}). \quad (3.47)$$

Normally, the multivariate quadrature points are constructed as a Cartesian prod-

ucts of univariate ones. This method suffers from the curse of dimensionality in  $d$ , thus here a similar approach to the NCI method is used where a sparse grid is constructed instead.

### 3.3 Chapter Summary

In this chapter the different approaches that will be used for uncertainty propagation and quantification are discussed.

For propagation, the GIPA method is shown to work well for orbital motion around the Didymos system. The choice of Chebyshev basis works well when the uncertainties are large as it provides more uniform convergence across the expansion domain. However, certain cases, namely the highly eccentricity orbits, show bad performance in terms of accuracy as the uncertainty set starts to include the dynamical singularity at the centre of the body. The Taylor basis does not have this problem and is more efficient compared to the Chebyshev basis, at the cost of lower accuracy for large uncertainties. The NCI method works well with complex dynamical systems with possible discontinuities in the equations of motion.

The resulting propagated state is now expanded using a polynomial, which is fully defined by its coefficients. Two dynamical indicators are developed which can measure the sensitivity of the state to the uncertainties in both the initial state and model parameters. The variance indicator uses the fact that for orthogonal polynomial bases the variance of the set can be found analytically, which relates directly to the degree of diffusion of neighbouring trajectories. The  $n + 1$  indicator measures the truncation error, which is argued to be higher for more sensitive initial conditions. A test is performed using the Duffing oscillator to see how these indicators perform. It is found that both these indicators perform well, and furthermore they both measure slightly different dynamical structures. The  $n + 1$  indicator directly measures the non-linearity of a certain initial condition, which is not strictly affected by the sensitivity to the uncertainties. Thus these two indicators can together measure various characteristics of uncertain dynamical systems.

Quantifying the uncertainties can be further performed by determining the evolution

### Chapter 3. Uncertainty Propagation and Quantification

of the moments of the uncertain state over time. Several methods are discussed here, namely the MC sampling approach, the coefficient based approach, and the Gaussian-Hermite quadrature (GHQ) based approach. The GHQ uses an efficient sampling technique, and is thus the preferred approach over the MC approach when the moments of small subsets of the uncertainty set need to be determined. Whereas the coefficient based method is the most efficient if the moments of the full uncertainty set needs to be estimated.

## Chapter 4

# Uncertainty Dynamical Maps of Orbital Motion around Didymos

This chapter is based on the work published in:

Fodde, I., Feng, J., Riccardi, A., & Vasile, M. (2023). Robust stability and mission performance of a CubeSat orbiting the didymos binary asteroid system. *Acta Astronautica*, 203, 577-591. <https://doi.org/10.1016/j.actaastro.2022.12.021>

Fodde, I., Feng, J., & Vasile, M. (2022). Uncertainty maps for motion around binary asteroids. *Celestial Mechanics and Dynamical Astronomy*, 134(5), [41]. <https://doi.org/10.1007/s10569-022-10096-2>

Fodde, I., Feng, J., & Vasile, M. (2021). Uncertainty propagation for orbital motion around an asteroid using generalized intrusive polynomial algebra: application to didymos system. Paper presented at 8th International Conference on Astrodynamics Tools and Techniques.

Due to the complex dynamics around a binary asteroid system, it is important to find specific orbits that remain stable for longer periods of time, as this can significantly reduce the amount of station-keeping manoeuvres and reduce the risk of an impact or escape from the system in case of failures.

In previous studies (see e.g. [144], [89], [79]), only the nominal system was investigated, or only after the nominal design was performed were the uncertainties included. This is more time intensive, and for larger uncertainties it can affect which orbits are

determined to be stable [89]. In this chapter, a novel methodology is used to efficiently include the uncertainties in the orbit design, without decoupling these two processes. This is done using the GIPA uncertainty propagation method of section 3.1.1 and the uncertain dynamics indicators of section 3.2.1. It is shown how using the methodology presented here the uncertainties can be directly included in the analysis of the close proximity motion, and therefore improving the understanding of the uncertain dynamics of the system and aiding in the design of robust and stable orbits for spacecrafts orbiting this system.

## 4.1 Didymos Mass Uncertainty

Measuring the sensitivity of the very close proximity motion near Didymos to uncertainties in the parameters describing the dynamics using the uncertain dynamics indicators is important to both validate the indicators themselves and to investigate the changing dynamical structure around Didymos. This is especially important for both the design of extreme close proximity motion of a spacecraft around the asteroids, and for the investigation of the regions where dust and ejected particles might reside. The CR3BP model of section 2.3.2 is used as this allows for validation (by comparing to other works investigating this system, e.g. [123]) and because the Jacobi constant can be used to reduce the dimensions of the system (this process will be discussed later in this section). A second degree and order spherical harmonics field is used as the gravitational model, this combined model will be called the spherical harmonics CR3BP (SH-CR3BP) here, to separate it from the standard CR3BP where a point mass gravity is used. In this analysis, it is assumed that the primary rotates at the same rate as the binary orbit period. This makes the system easier to analyse as it becomes an autonomous system in the synodic reference frame (rotating together with the orbit of the secondary), even considering non-spherical gravity. The uncertainties in the mass variables of both bodies are taken, as they are fairly large (in the order of 10 percent) as can be seen from table 2.1.

The Didymos dynamical system is a 3 degree of freedom (DOF) system with 6 state

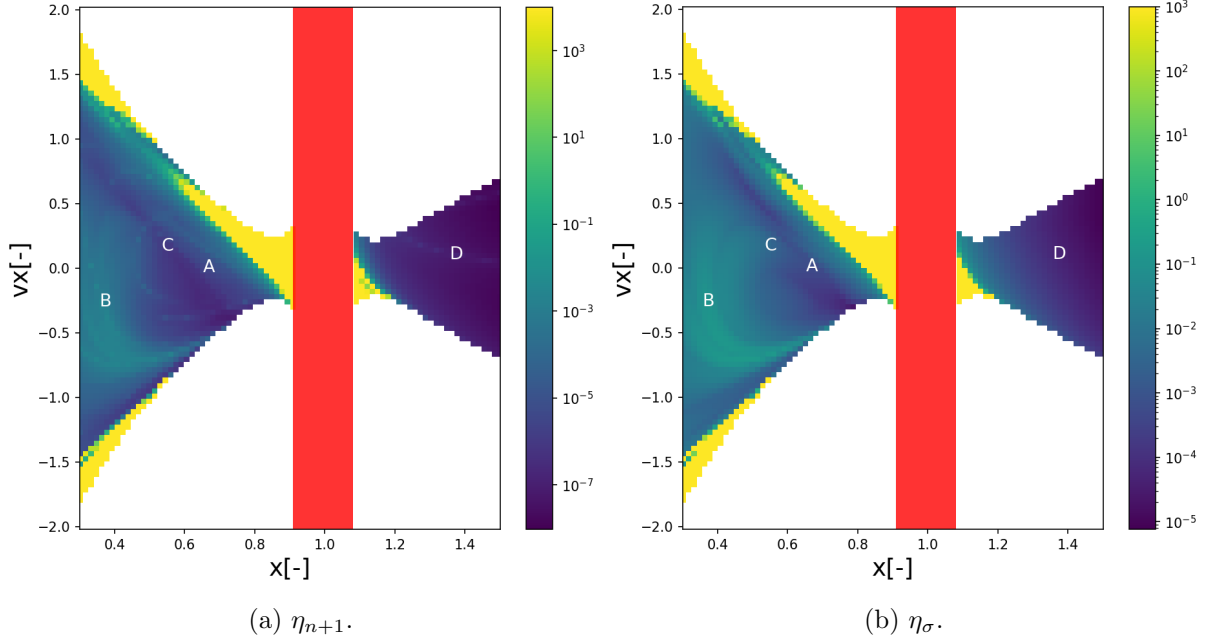


Figure 4.1: The maps of the uncertain dynamics indicator for the SH-CR3BP with model uncertainties at  $T = 3$  with  $C = 3.1$ . The red area contains the secondary, therefore no initial conditions appear there.

variables, while the Duffing oscillator (used to test the uncertain dynamics indicators in section 3.2.1) has one DOF with 2 state variables. To reduce the dimensionality of the problem, only the planar case ( $z = 0$  and  $v_z = 0$ ) is considered, as the motion then remains constrained to this plane during the integration. Furthermore, the initial  $y$ -coordinate can be set to zero and then the initial  $v_y$ -coordinate can be found according to a pre-determined Jacobi constant  $C$ , using Eq. (2.32).

A similar grid as with the Duffing oscillator can be constructed, using the range of  $x = [0.3, 1.5]$  and  $v_x = [-2, 2]$  for 100 by 100 grid points. The lower  $x$ -values are not taken into account here due to the presence of the primary. Additionally, the region where the secondary is located is removed from the grid. As was mentioned before, an uncertainty of 10 percent in the masses of the two bodies is used.

A polynomial degree of 5 is chosen for the Didymos system as this keeps the RMSE sufficiently low, below  $10^{-6}$  for the specific case considered in Figure 3.3, and the runtime manageable for the larger grids.

The maps, representing the  $\eta_{n+1}$  and  $\eta_\sigma$  indicators, are shown in figure 4.1. For all

maps, the white areas represent the regions where no initial condition with the selected value of  $C$  is possible. For the  $\eta_\sigma$  indicator, a maximum variance of  $10^{-3}$  was set.

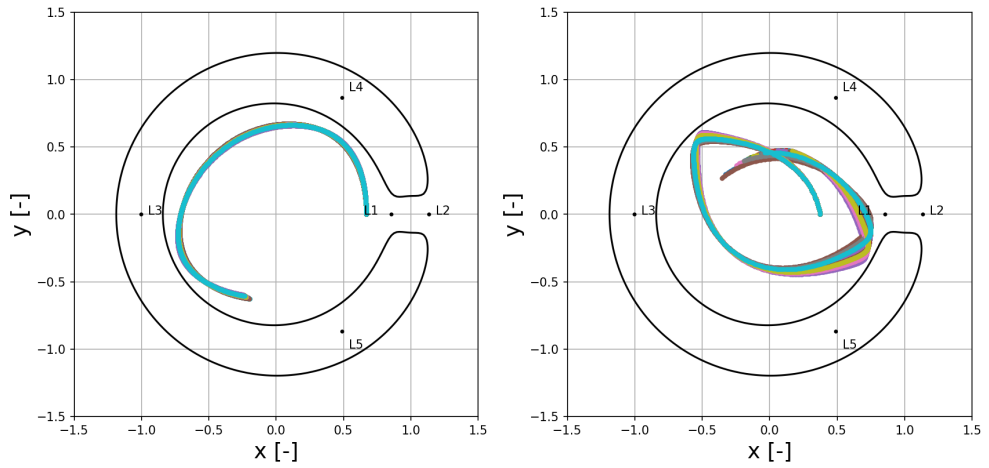
For both maps, there are several regions, indicated by a bright yellow colour, where the indicators are at the maximum value or show noisy behaviour. These regions are where the polynomial approximation intersects the center of either the primary or the secondary at some point during the integration, as was also observed in the high eccentricity orbits analysed in section 3.1.1. This causes the polynomial approximation to diverge as the gravitational dynamical model includes a  $1/r$  term. If  $r = c_0 + n(r)$ , where  $n(r)$  are the higher order terms of the polynomial approximation, the inverse can be written as follows:

$$\frac{1}{r} = \frac{1}{c_0} \cdot \frac{1}{1 + \frac{n(r)}{c_0}}. \quad (4.1)$$

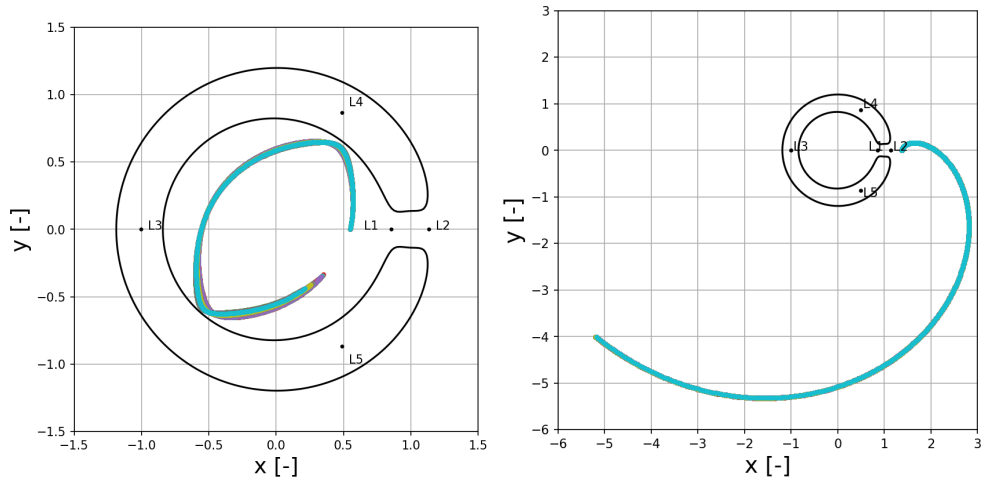
As for a Taylor polynomial  $c_0$  represents the central reference point, if the central point of the position uncertainty set approaches either of the bodies, the inverse of Eq. (4.1) will become (close to) singular and the approximation diverges. As part of the trajectories in the set impact with one of the bodies in this case and cause a singularity with a high likelihood, they are considered as infeasible trajectories.

Analysing the maps from figure 4.1 further, several regions of low diffusion (dark blue) can be found. Motion outside the system ( $x > 1 - \mu$ ) is found to have mainly low diffusion. The inner region ( $x < 1 - \mu$ ) shows various different structures, where a clear diagonal line of low diffusion can be found, showing that there are inner regions where the uncertainty of the masses of the primary and secondary has less of an influence on the motion of a third body. This line is slightly shifted when compared between the two indicators. As for the Duffing oscillator, this difference is likely due to the non-diffusive effects that affect the non-linearity more for certain regions. The more diffusive regions do correspond between the two different indicators.

To validate the dynamical structures from the uncertain dynamics indicator maps from figure 4.1, four initial conditions have been chosen from figure 4.1a and 4.1b. A Monte Carlo analysis was performed with double the total propagation time of the map. The four different results are shown in figure 4.2. Trajectory A ( $\eta_{n+1} = 4.51 \cdot 10^{-6}$ ,



(a) A ( $\eta_{m+1} = 4.51 \cdot 10^{-6}$ ,  $\eta_{\sigma} = 5.68 \cdot 10^{-4}$ ). (b) B ( $\eta_{m+1} = 1.02 \cdot 10^{-3}$ ,  $\eta_{\sigma} = 0.10$ ).



(c) C ( $\eta_{m+1} = 9.79 \cdot 10^{-7}$ ,  $\eta_{\sigma} = 4.11 \cdot 10^{-3}$ ). (d) D. ( $\eta_{m+1} = 1.62 \cdot 10^{-7}$ ,  $\eta_{\sigma} = 4.78 \cdot 10^{-5}$ ).

Figure 4.2: Sample trajectories from the uncertain dynamics indicator maps propagated until  $T = 6$ . The ZVS are shown from the nominal system parameters.

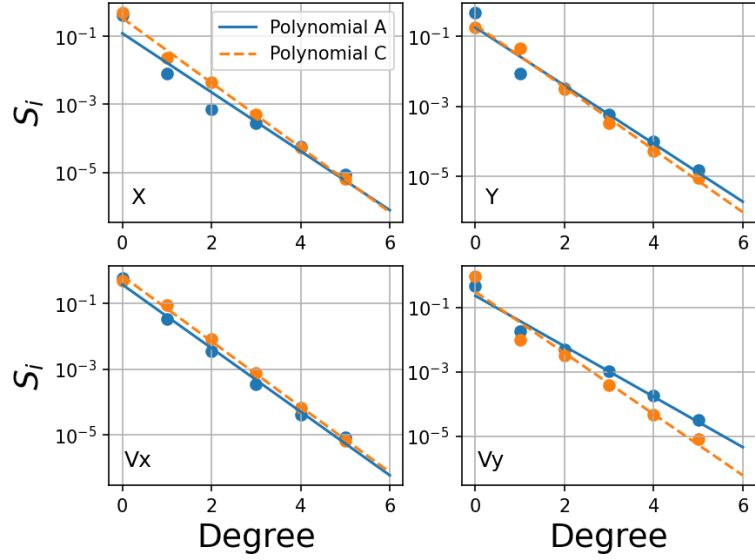


Figure 4.3: The polynomial coefficients at the final epoch from test trajectories A and C from figure 4.1a.

$\eta_\sigma = 5.68 \cdot 10^{-4}$ ) is taken from the low  $\eta_\sigma$  area and trajectory C ( $\eta_{n+1} = 9.79 \cdot 10^{-7}$ ,  $\eta_\sigma = 4.11 \cdot 10^{-3}$ ) is taken from the low  $\eta_{n+1}$  area. A small difference is observed in terms of the diffusion of the trajectories, where A shows lower diffusion compared to C. Similar with the Duffing oscillator case, this is likely due to the higher non-diffusive component of the measured non-linearity for A. Indeed, the coefficients and polynomial samples shown in figures 4.3 and 4.4 show this similar effect for the Didymos grid. The polynomial of A has lower  $S_i$  compared to that of C for lower degree coefficients, which decreases the value of  $\eta_\sigma$ . However, the higher degree coefficients are larger in size, hence increasing the value of  $\eta_{n+1}$ . The samples of figure 4.4 show as well that the diffusion (and therefore  $\eta_\sigma$ ) is larger for C, while the deformation of A is larger due to the higher non-linearity (and thus higher  $\eta_{n+1}$ ). Trajectory B ( $\eta_{n+1} = 1.02 \cdot 10^{-3}$ ,  $\eta_\sigma = 0.10$ ) shows high diffusion and non-linearity, as both  $\eta_\sigma$  and  $\eta_{n+1}$  are large, and trajectory D ( $\eta_{n+1} = 1.62 \cdot 10^{-7}$ ,  $\eta_\sigma = 4.78 \cdot 10^{-5}$ ) shows the low diffusion and non-linearity behaviour for the outer region, confirmed by the low value of both indicators.

In addition to the dynamical structure of the inner region for different  $v_x$ , a second set of initial conditions is investigated. For these maps, both the  $x$  and  $y$  velocities are set to zero and a set of values for  $x$  and  $y$  are selected. A grid of a 100 by 100 points is

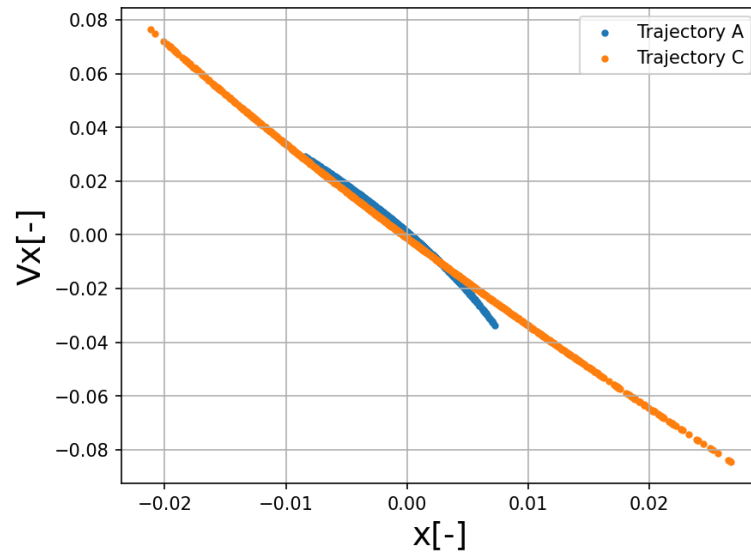


Figure 4.4: Samples taken from the resulting polynomial and translated to be centered around  $(0, 0)$  for initial conditions A and C at the final epoch for figure 4.1a.

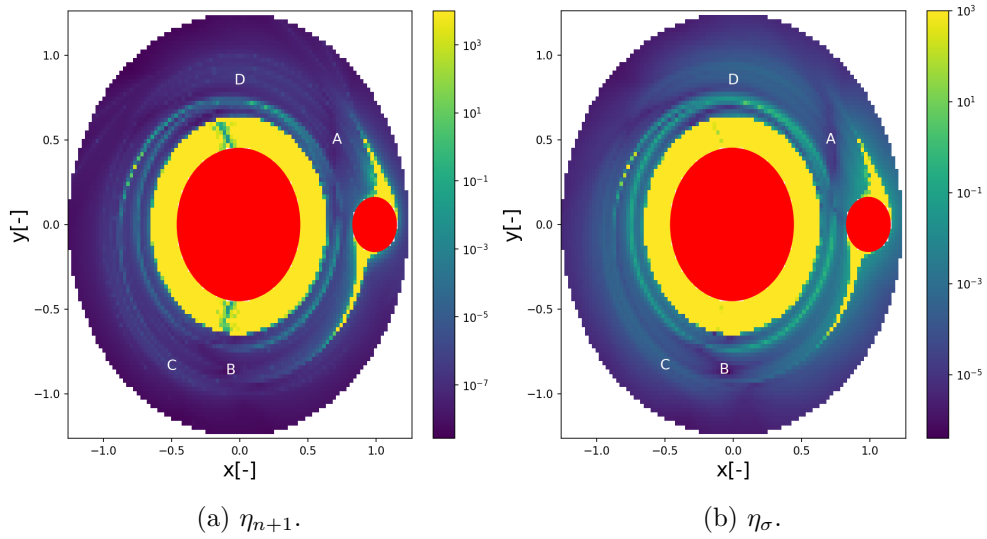


Figure 4.5: The uncertain dynamics indicator maps for the SH-CR3BP with model uncertainty at  $T = 3$  with velocities set to zero.

taken for  $x = y = [-1.25, 1.25]$ , where the points further than 1.25 from the barycentre are removed as they correspond to generally low values of the indicators. Furthermore, orbits inside the Brillouin sphere of both bodies, together with a small region around the surface of the bodies, are also removed as they generally impact with the bodies at some point.

The maps for the zero velocity motion are shown in figure 4.5. Contrary to previous maps, the  $\eta_{m+1}$  maps and the  $\eta_\sigma$  indicator maps show mostly similar results. This indicates that for these initial conditions, the largest part of the non-linearity is caused by the divergence of the trajectories. There are two distinct areas with low indicator values that are of interest. The first is located in front of the secondary in the direction of its motion and the second around the bottom of the primary. These regions can allow motion close to the bodies which is not sensitive to off-nominal conditions, and thus can be of interest for a spacecraft observing the system.

Four sample trajectories from the maps in figure 4.5a and figure 4.5b are propagated to validate the dynamical structures, which are demonstrated in figure 4.6. Figure 4.6a and 4.6b show trajectories from two areas with low values for the indicators. As expected from the maps, all trajectories here remain close together. The test trajectories from figure 4.6c and 4.6d show trajectories from regions with high values for the uncertain dynamics indicators. These test trajectories show more spread in the different trajectories, which indicates that they are more sensitive to the mass uncertainties of the Didymos system.

## 4.2 Didymos High-Fidelity Model

In section 4.1 the focus was more on the characterization of a specific regime of the dynamics, namely the very close proximity motion with just environment uncertainties, and on giving an example of how the uncertain dynamics indicators can be used for these types of systems. Now, the goal is to apply the different techniques discussed in chapter 3 to a realistic mission scenario. In this case the design of the close proximity orbits for a spacecraft around Didymos, specifically for the Hera mission. Two CubeSats (called

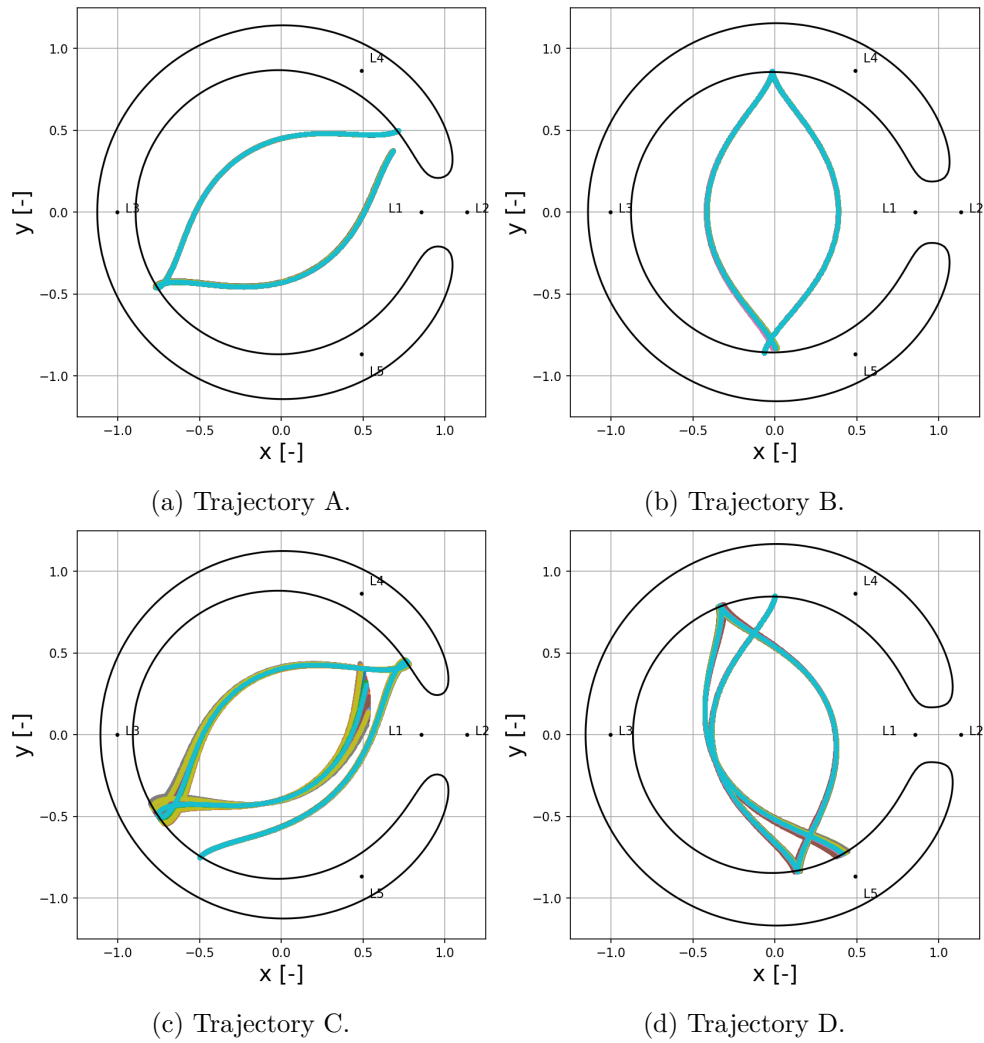


Figure 4.6: Sample trajectories from the uncertain dynamics indicator maps of the zero velocity initial conditions propagated until  $T = 6$ .

Milani [30] and Juventas [31]) will be released into orbits around the system besides the Hera spacecraft. The Hera spacecraft plans to follow hyperbolic arcs around the system, while the CubeSats will use the natural dynamics of the system to orbit more closely to the bodies (for Milani, this only holds for the final phase of the mission as mainly it will also use hyperbolic arcs). Therefore, the full dynamics as described by the generalised inertial form is used.

Here, a spherical harmonics model of Didymos is considered to calculate the force due to its non-spherical shape. For the main purpose of trajectory design, the spherical harmonics terms up to and including the fourth order need to be considered [145]. In the case of Didymos, the  $C_{20}$  and  $C_{22}$  terms are at least one order of magnitude larger than the higher order terms of the gravity field. As a large uncertainty of about 10 percent is considered in these second order coefficients, the higher order terms will have a significantly lower impact on the gravitational acceleration compared to the effect of the large uncertainties in  $C_{20}$  and  $C_{22}$ . Therefore, the spherical harmonics acceleration is truncated at the second order and degree. Similarly, higher fidelity models based on the current polyhedron shape of Didymos (e.g. see [146]) would increase the accuracy of the calculated trajectories for the deterministic case, but for the uncertain case the accuracy improvement is less significant due to the uncertainties in the physical parameters considered for these models.

As the orbits considered are at a minimum distance of 2 km from the Didymos centre, the secondary is considered to have a point mass gravity field, as was shown to be sufficiently accurate for these dynamical regimes in [79]. The gravitation of the Sun is assumed to be described by a point mass as well, due to the large distance between the asteroids and the Sun.

For the SRP acceleration, a cannonball radiation pressure model is used. As was discussed in chapter 2, the relative position of Didymos with respect to the Sun remains constant for the timescales discussed here, and is located at a distance of 1.831 AU (the distance on July 2027, which is during the operational phase of the two CubeSats [147]). In this SRP model the specific difference in reference areas between the different sides of the CubeSat are not taken into account, as the uncertainties in the reference area

considered in this work include these differences. The analysis of the effect of the (uncertain) attitude on the SRP force, similar to [148], is left for future work. The nominal value for the mass-to-area ratio of the CubeSat is taken as  $25.86 \text{ kg/m}^2$  (The mass-to-area ratio of Juventas [31]).

#### 4.2.1 Robust Stability

The variation of the volume of the uncertainty set and its shape over time are a measure of the evolution of an ensemble of trajectories induced by multiple realisations of  $\boldsymbol{\xi}$ . If the trajectories are moving apart over time one would expect an increase in the volume of the set. On the other hand the set can stretch in one particular direction without increasing its volume. If the trajectories in the ensemble grow apart, whether increasing the volume of the set or just by stretching it in some directions, we call the process diffusive. The degree to which the trajectories in the ensemble grow apart is a function of the level of uncertainty and of the dynamics governing the evolution of each trajectory.

We can now provide a definition of robust stability.

**Definition 4.2.1** (Robust Stability). Given the uncertainty set  $\Omega_{\boldsymbol{\xi}}$ , the initial bounded set  $\Omega_{\boldsymbol{x}_0}$  and propagated states (3.3), consider a restriction  $\Omega_{\boldsymbol{y}_t}$  of  $\Omega_{\boldsymbol{x}_t}$  to the subspace defined by only some of the components  $\boldsymbol{y}_t$  of  $\boldsymbol{x}_t$ . A robust stable motion is such that for every realisation of  $\boldsymbol{\xi} \in \Omega_{\boldsymbol{\xi}}$  every restriction  $\Omega_{\boldsymbol{y}_t}$  is such that  $\int_{\Omega_{\boldsymbol{y}_t}} d\boldsymbol{y}_t < \varepsilon_y, \forall t > 0$ , for a sufficiently small phase space volume  $\varepsilon_y$ . In other words the motion remains bounded over time in all directions.

Following the definition of diffusion of an ensemble of trajectories, this means that if the diffusion remains low when parametric uncertainties are also considered, the orbit is defined to be robust stable. A robust stable orbit around an asteroid thus shows that the spacecraft will be stable, even if the true environment is different from the nominal dynamical model. Comparing the measure of robust stability between different initial conditions allows for the comparison of different regions in phase space against each other to determine regions of less sensitive motion.

Table 4.1: The initial conditions for the three different maps.

Parameter	Grid 1	Grid 2	Grid 3
$a$ [km]	[2 - 6]	[2 - 6]	3
$e$ [-]	0	[0 - 0.4]	0
$i$ [°]	[0 - 180]	85	[0 - 180]
$\Omega$ [°]	90	90	[0 - 180]
$\omega$ [°]	-90	-90	-90
$\nu$ [°]	0	0	0

The uncertain dynamics are investigated for a set of initial conditions that are generated from a range of Kepler orbital elements. As this is a highly perturbed environment, these orbital elements will quickly diverge from the classical two-body values (or their original values) and thus are only used to generate a set of interpretable initial conditions and to understand the evolution of the shape of the orbit over time. The initial orbital elements are converted to Cartesian coordinates to perform the integration. Three grids of 80 by 80 points are constructed from the different initial conditions. For each grid two orbital elements vary and the other orbital elements remain constant. The specific initial conditions for each grid are shown in table 4.1. The first grid investigates the effect of  $a$  and  $i$  for circular orbits facing the Sun. The second grids focuses specifically on the terminator orbits and the effect of  $e$ . Finally, for a fixed  $a$  the orbital plane is varied with a grid in  $i$  and  $\Omega$ .

Each point on the three different grids is propagated for five orbital periods (calculated from the initial  $a$ ), using a Runge-Kutta 4 numerical integrator. Uncertainties are considered in the initial state (position and velocity),  $C_{20}$ ,  $C_{22}$ , and the spacecraft SRP force. The SRP uncertainty stems from both uncertainty in the parameters and inaccurate modelling of this force. However, GIPA works with individual uncertain variables, hence only parameter  $1/B$  is considered to have an uncertainty in this case, and the inaccurate modelling is not considered for this analysis. The uncertainty of the parameter  $1/B$  is directly proportional to the uncertainty in the final acceleration for the Cannonball SRP model, and can thus represent the total uncertainty in the SRP force. The state uncertainties are set to a value of 1 percent to be able to determine

the effect of small perturbations in the state. The model parameters, i.e.  $C_{20}$ ,  $C_{22}$ , and  $B$  will have a larger uncertainty of 10 percent, representing the possible values these parameters can take. Furthermore, a polynomial degree of 5 is selected as this has previously been shown to be a good trade-off between speed and accuracy [149]. All values used during propagation are adimensionalized and scaled by dividing them by the position and period of Dimorphos with respect to Didymos, based on their respective units. This improves the numerical efficiency of the integration. Hence, all the indicator values do not have a unit as well. As the indicators are mainly used in maps to compare their relative values and find regions of relatively robust stability, their absolute values are of less significance.

Figure 4.7 shows the result for the  $\eta_{n+1}$  indicator and the  $\eta_\sigma$  indicator for grid 1. Where the Cartesian state is considered for the  $\eta_\sigma$  indicator. The colors in the two plots represent the values of the variance  $\eta_\sigma$  and non-linearity  $\eta_{n+1}$  indicator. Lower values of both these indicators means in general that those initial conditions are less sensitive to changes in both the initial conditions and dynamical parameters, and thus these trajectories remain more closely bounded. Hence, they can generally be viewed as being more robust stable than regions with higher values of the indicators, according to the definition given in Section 4.2.1.

Compared to the results for the SH-CR3BP, the  $\eta_{n+1}$  and  $\eta_\sigma$  maps here are very similar in terms of relative values within the map. Thus, it can be concluded that the effect mainly driving the absolute value of the  $\eta_{n+1}$  indicator is similar to the diffusion that the  $\eta_\sigma$  is measuring.

Several general regions of interest can be found in these maps. First, the prograde and retrograde orbits ( $<\sim 90^\circ$  and  $>\sim 90^\circ$  respectively) at larger  $a$  show unstable behaviour. For these regions, the SRP is of a similar order with the gravitational force and therefore has a significant destabilizing effect on these orbits. Due to this sensitivity to the SRP, the uncertainty in the  $B$  parameter increases the diffusion of these trajectories as well. Closer to the system, the retrograde orbits become more stable as the SRP force becomes less significant compared to the gravity of both bodies. However, the prograde orbits remain relatively unstable compared to the retrograde

ones. The retrograde orbits experience less influence from the non-spherical gravity contributions due to the high relative velocities with respect to the asteroid. This also means that the uncertainties in the  $C_{20}$  and the  $C_{22}$  value have less of an influence on these trajectories. Closer to the body, the influences of both the resonances with the spin of the primary and the orbital motion of the secondary can be observed in the maps (2:1 mean motion resonance at 2.1 km and the 3:1 orbital resonance at 2.475 km). These resonances in combination with the uncertainties in the gravity field can be seen to cause both stable and unstable behaviour. The most stable behaviour can be found around the terminator orbit, which corresponds to previously found results, e.g. [76], showing that these orbits are robust against uncertainties in the gravity field and SRP force.

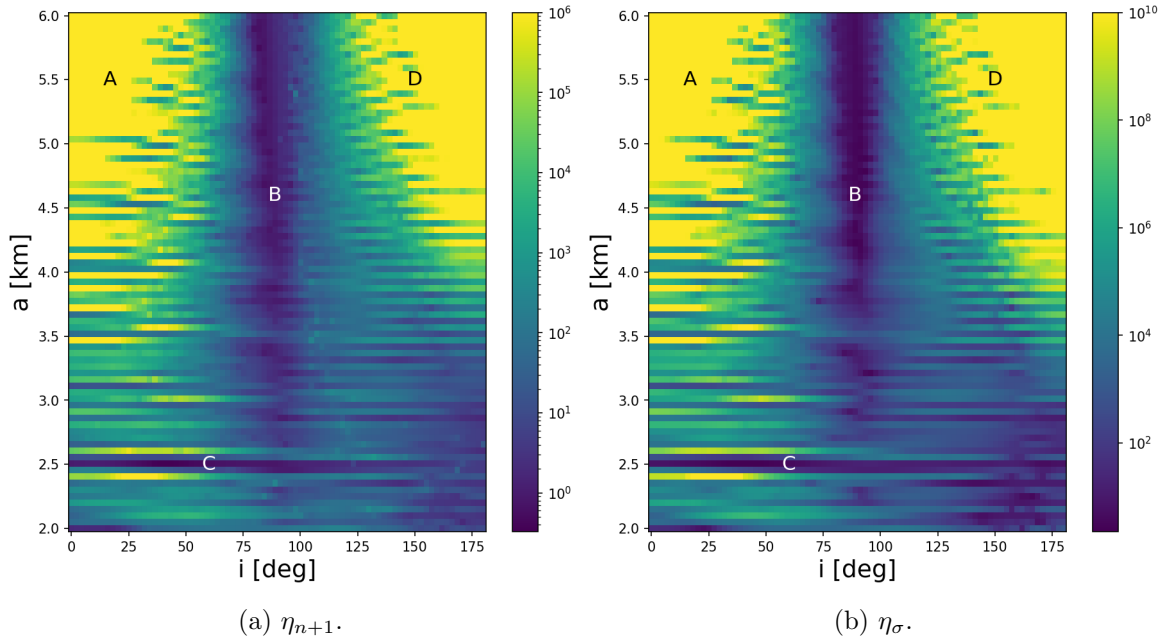
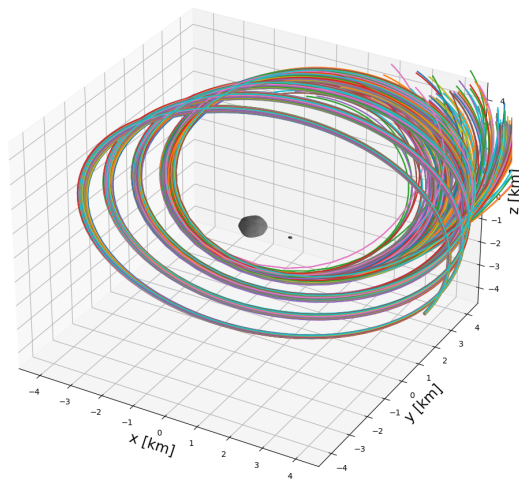


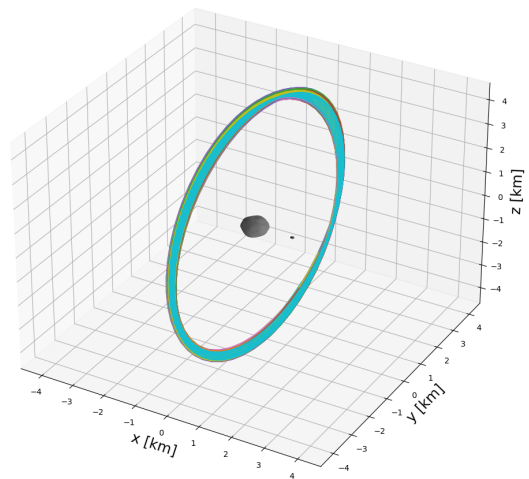
Figure 4.7: The uncertain dynamics indicators for grid 1. The colormaps represent the value of the respective indicator, thus the amount of variance and non-linearity. The letters indicate the set of sample orbits that are used to verify this grid, which are shown in Figure 4.8.

To validate the map of grid 1, a Monte Carlo analysis with 1000 samples for a longer period of time of 8 orbital periods of the spacecraft is performed for four different initial conditions shown in figure 4.7. The resulting trajectories are shown in figure

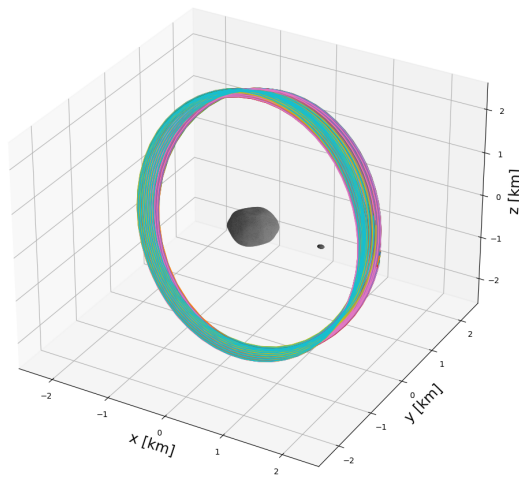
4.8 using different colours for the different Monte Carlo samples. From the robust stability grids, the two trajectories A and D are expected to be unstable, which is proven by the diffusive behaviour among the different sample trajectories and by the rapid change of the eccentricity and semi-major axis over time of most sample trajectories. Furthermore, the two stable trajectories B and C have significantly less diffusion and remain close to the initial orbit.



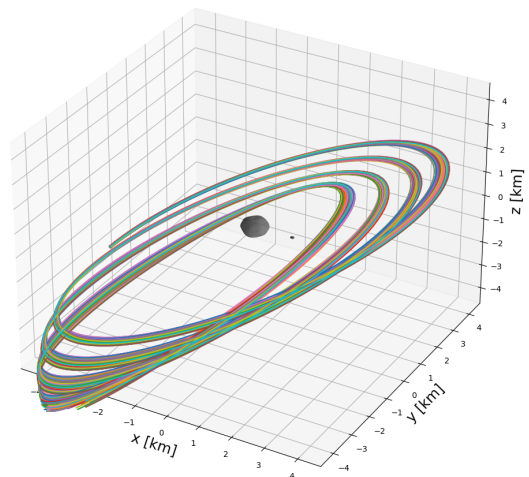
(a) Sample orbits A.



(b) Sample orbits B.



(c) Sample orbits C.



(d) Sample orbits D.

Figure 4.8: Sample trajectories from the uncertain dynamics indicator maps propagated until  $t_f = 8$  periods.

For grid 2, the effect of  $e$  on the terminator orbits (see  $i = 90^\circ$  from figure 4.7) is investigated. The results are shown in figure 4.9. The eccentricity can be seen to have a significant effect on the robust stability of an orbit. For higher semi-major axes, the eccentricity can be increased and the orbit remains relatively stable. While for low semi-major axes, small initial eccentricities can already lead to unstable orbits. Small values of  $e$  result in close approaches to the asteroid system in the case of low  $a$ , which results in destabilizing effects due to the higher gravitational acceleration.

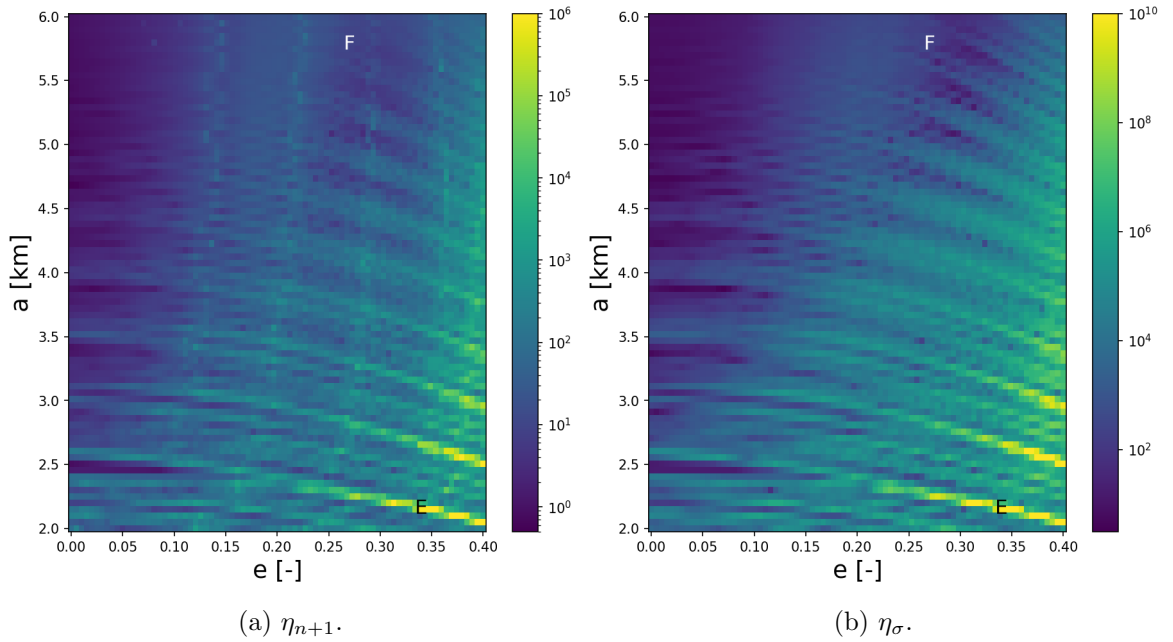
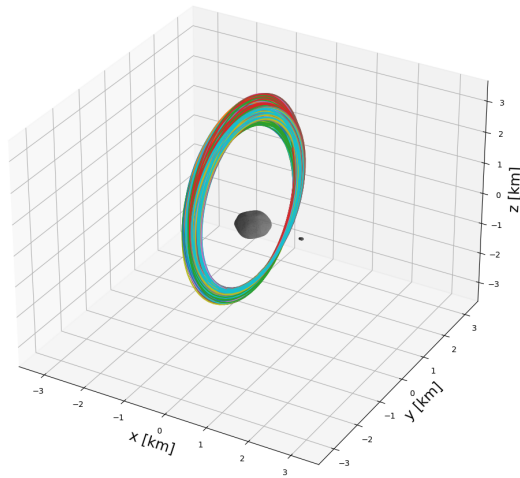
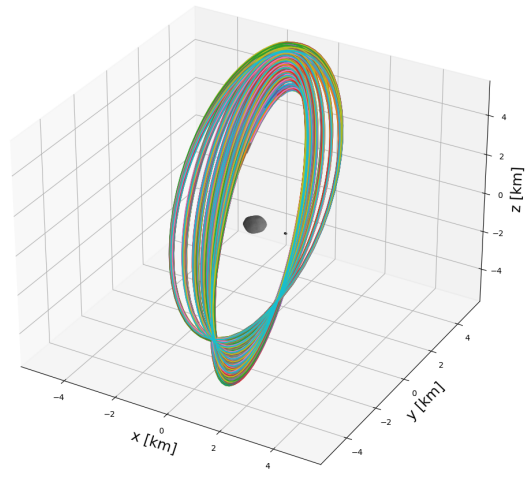


Figure 4.9: The uncertain dynamics indicators for grid 2. The colormaps represent the value of the respective indicator, thus the amount of variance and non-linearity.

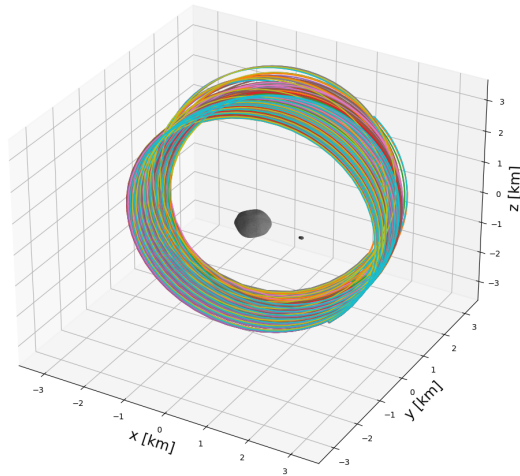
A set of sample trajectories from a similar Monte Carlo analysis as before are also plotted in figures 4.10a and 4.10b. From these figures it seems as if trajectories from E are more stable than expected compared to F. However, from the evolution of the distance from the centre of Didymos and the velocity, seen in figure 4.11, it can be seen that the amplitude for both variables are decreasing over time for F. Whereas for E these are slightly increasing over time.



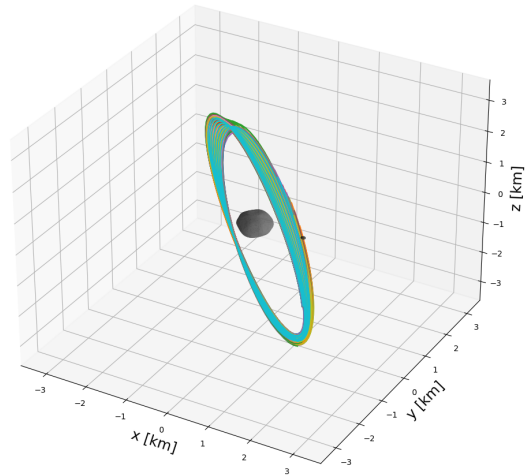
(a) Sample orbits E.



(b) Sample orbits F.



(c) Sample orbits G.



(d) Sample orbits H.

Figure 4.10: Sample trajectories from the uncertain dynamics indicator maps propagated until  $t_f = 8$  periods for grid 2 and 3.

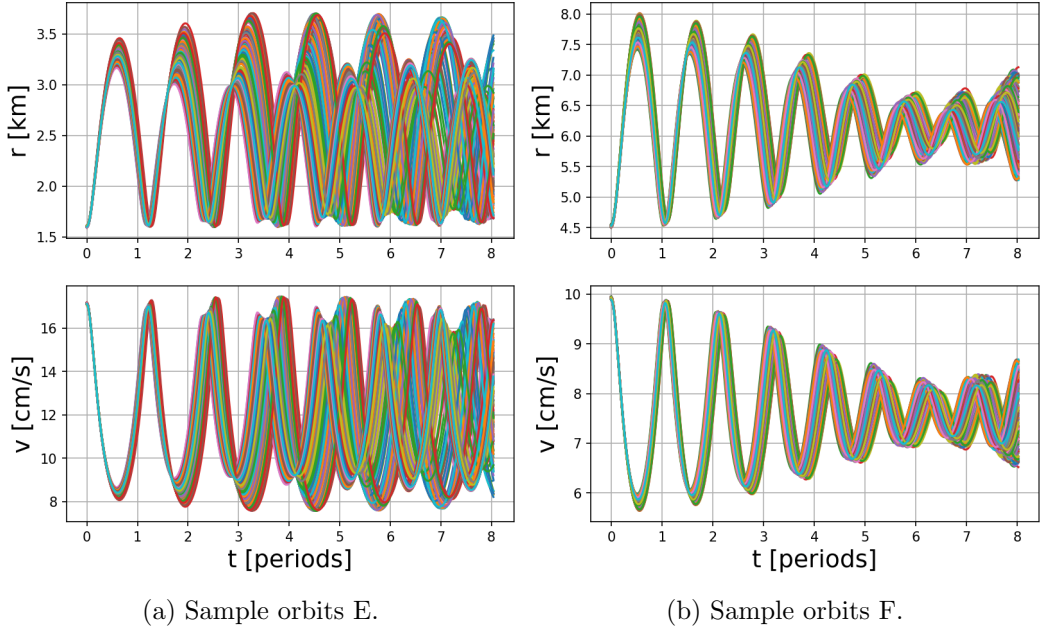


Figure 4.11: The distance  $r$  from the centre of Didymos and velocity  $v$  of different trajectories over time for sample orbits E and F.

Finally, the results for grid 3 can be seen in figure 4.12. For these maps there is a more clear difference between the  $\eta_{n+1}$  and  $\eta_{\sigma}$  indicators, as there are several regions and structures in the  $\eta_{n+1}$  map which do not appear in the  $\eta_{\sigma}$  map. From the discussion in section 3.2.1.2, it is observed that  $\eta_{n+1}$  is an indicator of the non-linearity, which is not strictly affected by the diffusion. Hence, it is possible that these factors increase the  $\eta_{n+1}$  more for these regions and structures, therefore changing the relative value.

The two main regions of unstable motion are similar between the two indicators. They can be found in the range of  $i \approx [20^{\circ} - 70^{\circ}]$ ,  $\Omega \approx [40^{\circ} - 90^{\circ}]$  and for  $i \approx [0^{\circ} - 20^{\circ}]$ ,  $\Omega \approx [125^{\circ} - 175^{\circ}]$ . Various robust stable structures can be found in these maps. As can be seen from figure 4.7, the value of  $a$  used for this map is close to the transition where the SRP force becomes less dominant and the non-spherical shape become more dominant, as the retrograde orbits go from unstable to stable. This leads to various different robust stable combinations of  $i$  and  $\Omega$ .

Two sample initial conditions, G and H, are taken from the two maps and analysed using a Monte Carlo analysis. The results can be seen in figures 4.10c and 4.10d. These

analyses match with the expected robust stability as around G the trajectories diffuse more compared to H.

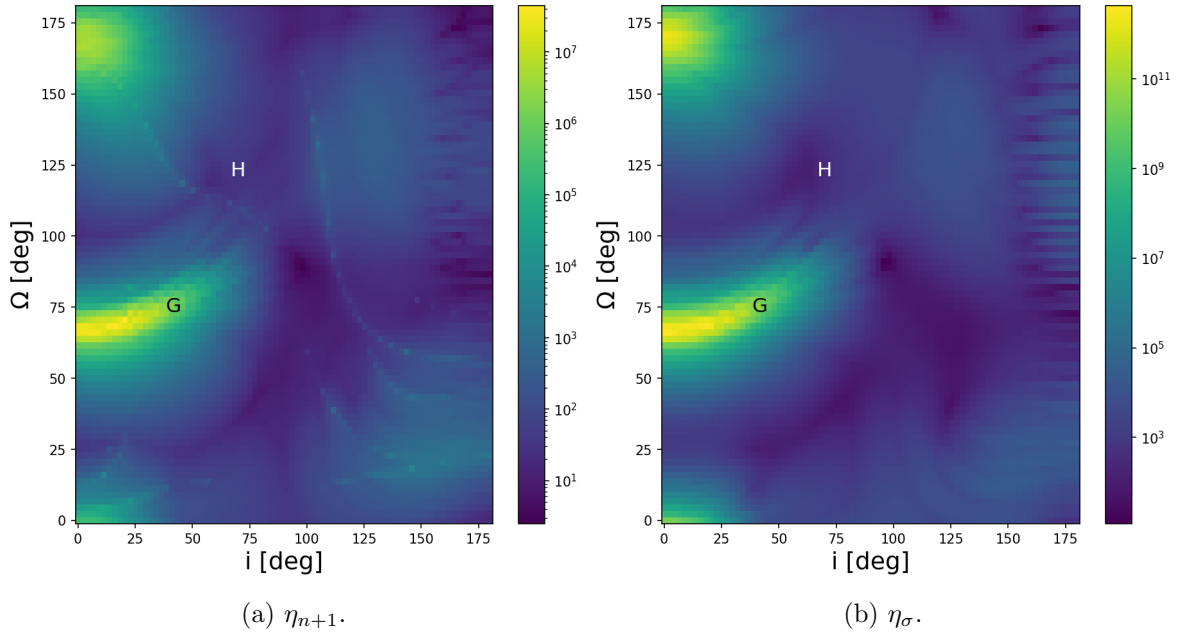


Figure 4.12: The uncertain dynamics indicators for grid 3. The colormaps represent the value of the respective indicator, thus the amount of variance and non-linearity.

Besides the  $\eta_\sigma$  indicator for the variance in the Cartesian state, the variance in  $a$  and  $e$  is also measured. These indicators are shown for grid 1 in figure 4.13. These maps show how the bounds of the orbital elements evolve over time due to sensitivity to the state and model parameters. It can be seen that in general these results agree with the robust stability indicators from figure 4.7. The orbital elements  $a$  and  $e$  remain the most bounded for terminator orbits and close ( $< 3\text{km}$ ) retrograde orbits, whereas the orbits with a high influence of the SRP show high variance.

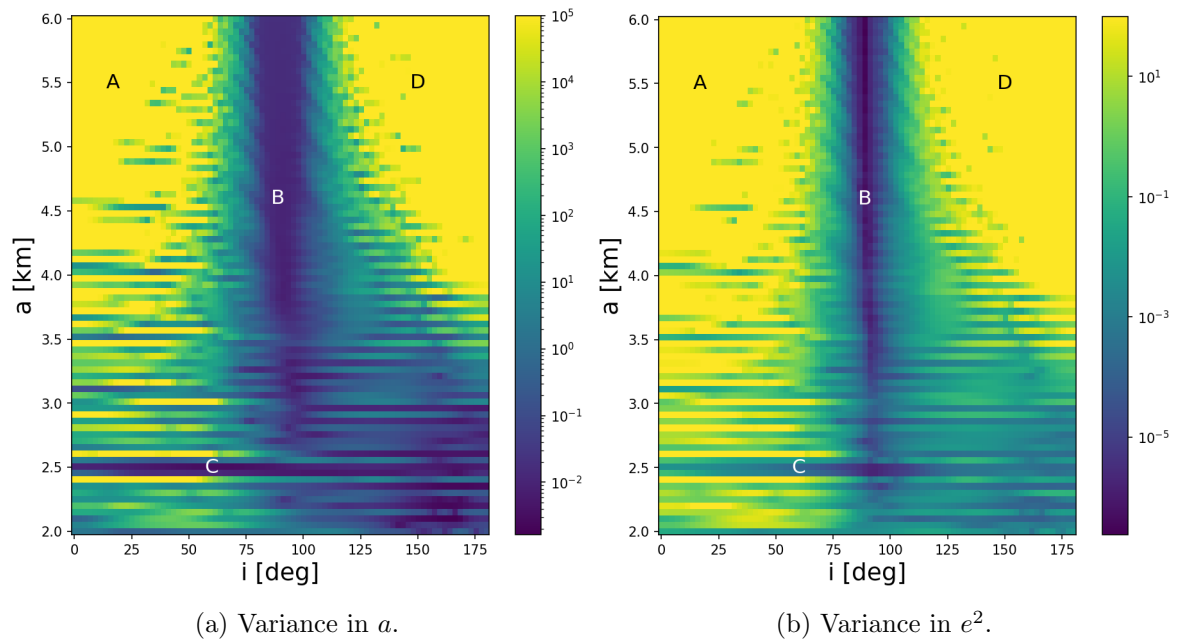


Figure 4.13: The variance in the semi-major axis  $a$  and squared orbital eccentricity  $e^2$  at the final time for grid 1. The letters indicate the set of sample orbits that are used to verify this grid, which are shown in Figure 4.8.

The results from figure 4.13 can be verified using a similar MC method as was discussed before. The same sample points, A to D, are used (see figure 4.13) and the spread and evolution of the trajectories from the Monte Carlo analysis are investigated in more detail. The bounds of the orbital elements for the four sample regions are shown in figure 4.14a. As expected, the bounds of  $a$  and  $e$  for A and D are both increasing over time, whereas for B and C these remain much more constant. For C (around the 3:1 orbital resonance), the bounds of  $a$  seem to shrink until 3 orbital periods is reached after which the bounds increase again as can be seen in figure 4.14b. These results agree with what is expected from the maps developed in figure 4.13.

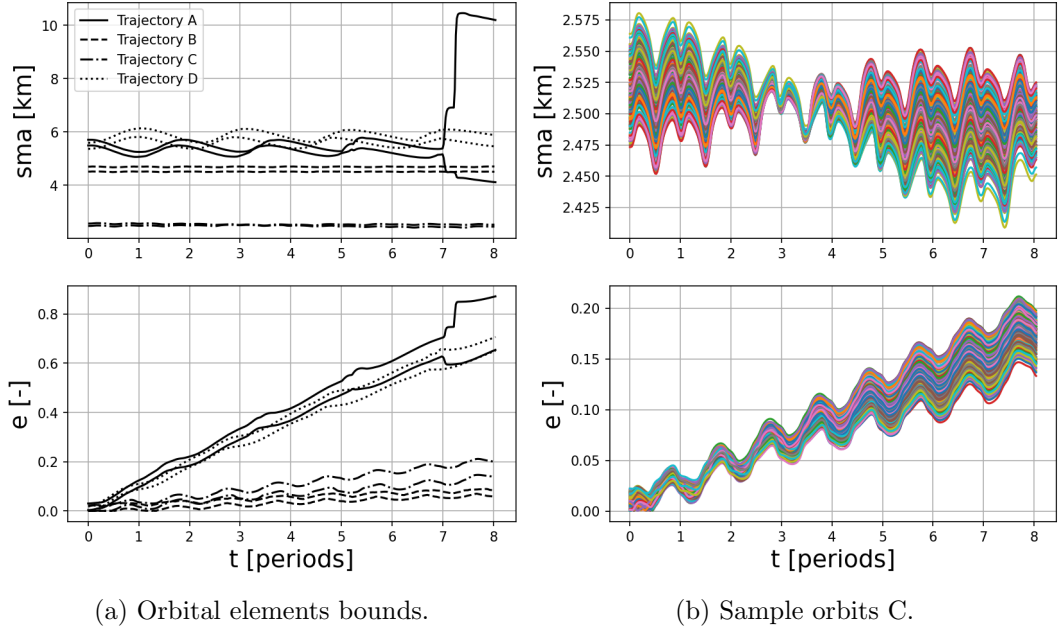


Figure 4.14: Maximum and minimum values for the semi-major axis and eccentricity of the different initial conditions and the sample orbits shown for C.

The same similarity between the robust stability indicators and the variance in  $a$  and  $e$  of grid 1 can be found for grid 2 in figure 4.15. The main difference in the variance maps is that the contrast for regions of high and low robust stability is greater for the orbital elements maps compared to the Cartesian maps. This shows the sensitivity of the orbital bounds to the effect of the uncertain dynamics in different regions of initial conditions. In [76], an analytical estimate of the eccentricity as a function of semi-major axis for a stable terminator orbit conditions was derived as:

$$e = \cos \Lambda, \quad (4.2)$$

$$\tan \Lambda = \frac{3(1 + \kappa_s)P_0}{2B} \sqrt{\frac{a}{\mu_{did}\mu_{Sun}a_H(1 - e_H^2)}}, \quad (4.3)$$

where  $a_H$  and  $e_H$  are the heliocentric semi-major axis and eccentricity. This function is shown in the maps of Figure 4.15 as a white dotted line. It can be seen that for a larger  $a$ , this theoretical value is located in the region with the low  $\eta_\sigma$  and low  $\eta_{n+1}$  region, thus it still is able to predict the stable  $e$  values well. As the orbit gets closer to the system, other unmodelled perturbations like the gravity of Dimorphos reduce the

accuracy of Eq. (4.2) and thus show more unstable behaviour.

The orbital element bounds for sample orbits from E and F are shown in figure 4.16. The stable region F has relatively constant bounds and also has a decreasing mean value for  $e$ . In contrast, the bounds for E are growing slowly. Furthermore, due to the orbital resonance around this initial condition, an empty region is found after around 4 periods. This resonance alters the orbits around this region to form two different groups.

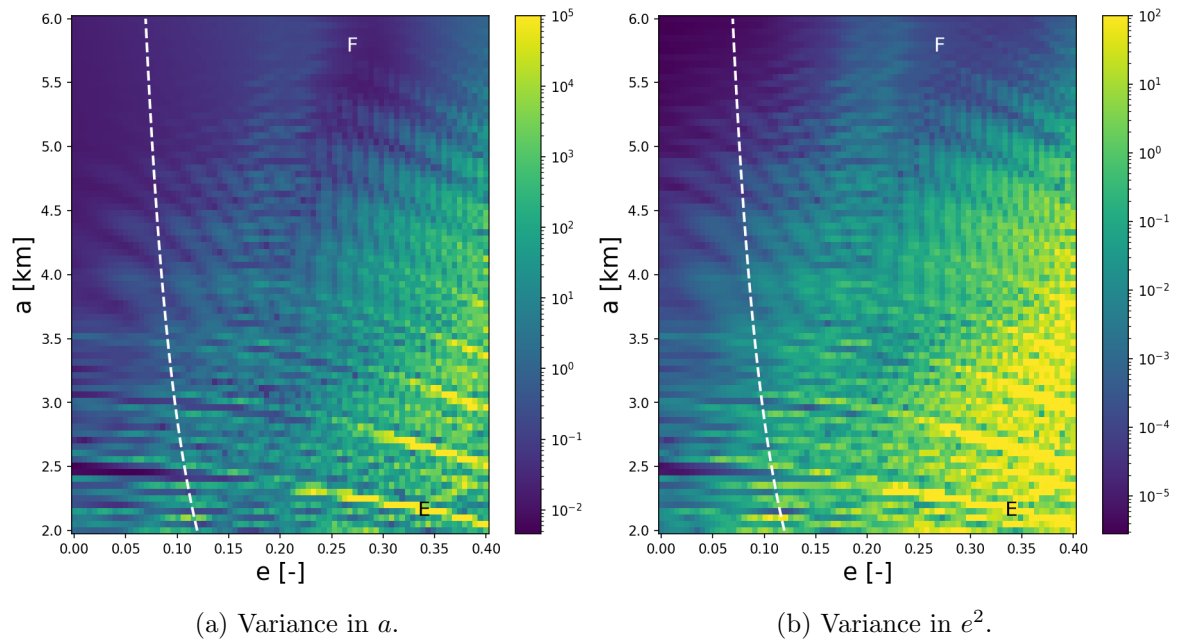


Figure 4.15: The variance in the semi-major axis  $a$  and squared orbital eccentricity  $e^2$  at the final time for grid 2. The dotted line represents the theoretical frozen orbit condition from Eq. (4.2)

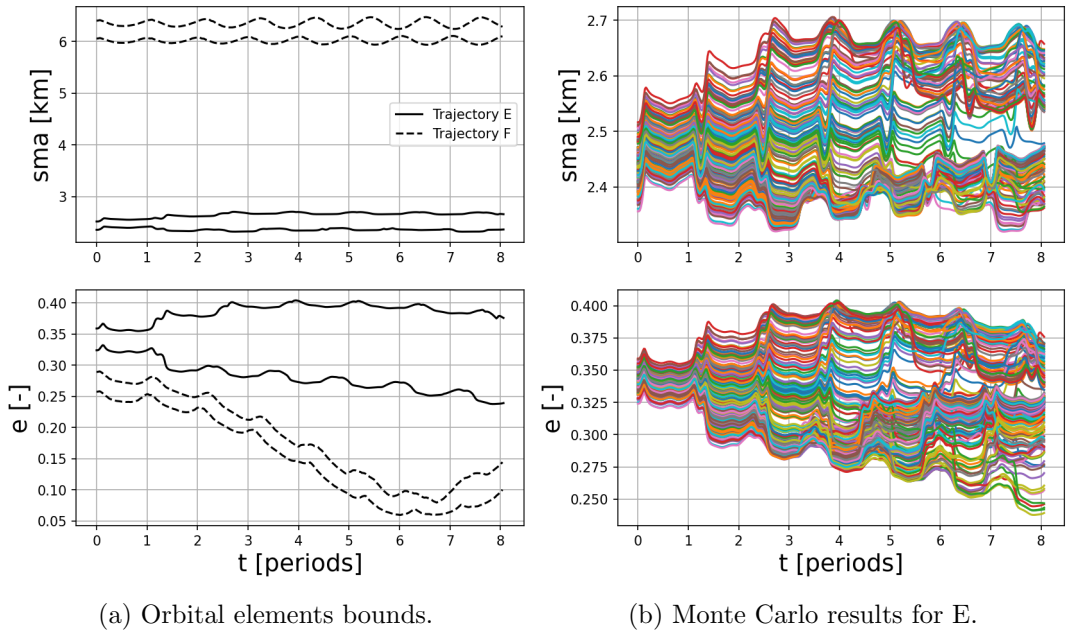


Figure 4.16: The orbital elements over time for two different test trajectories from grid 2. In 4.16a the bounds are shown, and in 4.16b the results for E are shown in more detail.

For grid 3, the results are shown in figure 4.17. The highest values for the variance of  $a$  are lower compared to the previous maps, showing some more structure in both the unstable and stable regions. It can be seen that there are several structures of stable behaviour within the unstable regions. Furthermore, the region around  $i = 180^\circ$  shows the lowest variance in the orbital elements, representing regions of bounded motion.

The bounds for the sample orbits in figure 4.18 show again the difference between the stable and unstable region. The difference is relatively small for  $a$ . However, for  $e$  it can be seen that the difference in both the growth of the mean and variance is larger. The maps show as well that the effect of  $\Omega$  is more significant for the prograde motion, where more regions of high variance are found.

The analysis performed using the indicators in this section does not directly measure the safety against impact, as the time period over which the polynomial propagation is performed is not long enough to find impact trajectories. However, for Monte Carlo analyses of several unstable orbits for longer periods of time (e.g. figure 4.8a), several orbits were found to impact with one of the asteroids in the system. Therefore, it is

implied here that orbits from regions of high indicator values of the robust stability maps have a higher risk in terms of possible impacts. A more quantitative analysis of this impact risk is left for future work.

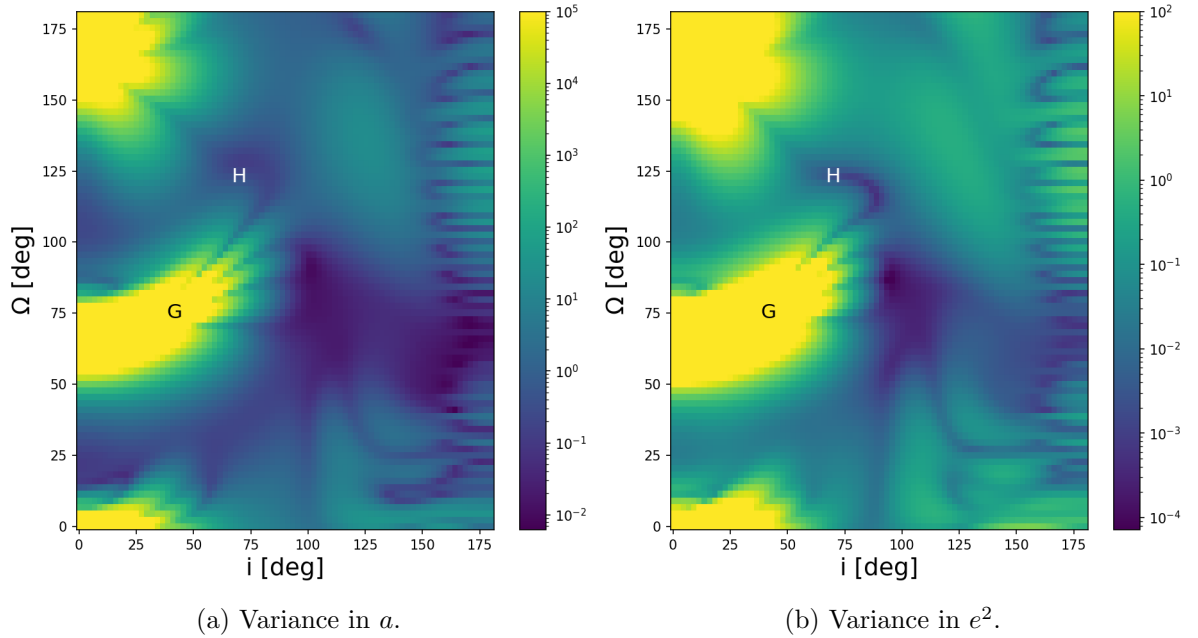


Figure 4.17: The variance in the semi-major axis  $a$  and squared orbital eccentricity  $e$  at the final time for grid 3.

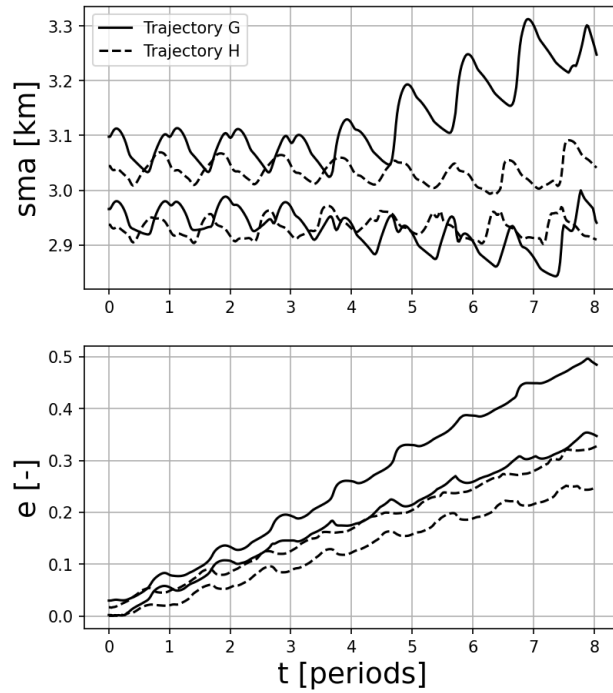


Figure 4.18: Maximum and minimum values for the semi-major axis and eccentricity of the sample orbits from grid 3.

#### 4.2.2 Mission Performance

From the perspective of mission operations, the robust stability discussed in section 4.2.1 is an important factor in the selection of an orbit for a spacecraft as it shows how frequent adjustments need to be made to the trajectory to keep it within the desired bounds. In addition, the spacecraft needs to fulfill a certain set of operational and scientific requirements that are influenced by the specific orbit the spacecraft is in. In previous studies ([31], [79], [150]) the different constraints and requirements for the trajectory design of the different spacecraft orbiting Didymos and observe Dimorphos are discussed. One of the main important factors that is discussed is the observability of Dimorphos in terms of lighting for the passive instruments (e.g. optical cameras).

To determine the observability of Dimorphos, several key factors need to be taken into account [151]. These factors are all related to the illumination and geometry of the system. It is required for several instruments on-board the spacecraft to observe the body with sufficient illumination to determine all the necessary features. First, the

angle between the lines connecting the Sun and Dimorphos, and the spacecraft and Dimorphos is calculated (i.e. the phase angle). If this angle is smaller than 90 degrees, the illumination is sufficient. Second, it is determined whether Dimorphos is located in the shadow of Didymos, where the shape of the shadow is taken to be conical. Finally, it is determined whether Dimorphos is not located behind Didymos with respect to the position of the spacecraft. At all evaluation points in an orbit, these three factors are calculated. If they are all shown to be favourable (i.e. Sun angle less than 90 degrees, not in shadow, and Didymos is not blocking Dimorphos), then at that time Dimorphos is deemed observable. If any of these factors are determined to be false, then Dimorphos is not observable. At the end of a simulation run, the percentage of time Dimorphos is observable is calculated. This measure of observability is similar to the one used for the trajectory design of the close proximity phase of the Hera spacecraft [5].

To test the ability of this method to analyse the mission parameters and performance, the observability for the three grids is measured.

The upper and lower bounds for the observability is shown in figure 4.19 for grid 1. The stability of the region around the terminator orbit makes the bounds of the observability lie close together (30 - 50 percent). The unstable regions allow for both lower minimal values (higher chance of bad observability conditions), but also higher maximum values (higher chance of good observability). This is caused by the diffusion of trajectories allowing for a wider spread of trajectories with different geometries. Part of these trajectories allow for better observability conditions. Therefore, from these plots a trade-off can be made among the robust stability and boundedness shown in figures 4.7 and 4.13, and the observability of the secondary in figure 4.19.

The same effect can be seen for grid 2 in figure 4.20. However, there is a much larger difference between the uncertain dynamics maps and the observability maps for grid 3, as is shown in figure 4.21. The terminator orbit is again shown here to have much smaller difference between the maximum and minimum bounds, indicating that the geometry for these orbits is less sensitive to state and model parameter uncertainties. Due to these small bounds, the terminator orbits minimize the worst case scenario observability while also lowering the maximum possible observability. The coverage

of Dimorphos was not taken into account for this analysis, however it is noted here that the terminator orbits tend to observe the same face of the asteroid, reducing the coverage of the body from these orbits [5].

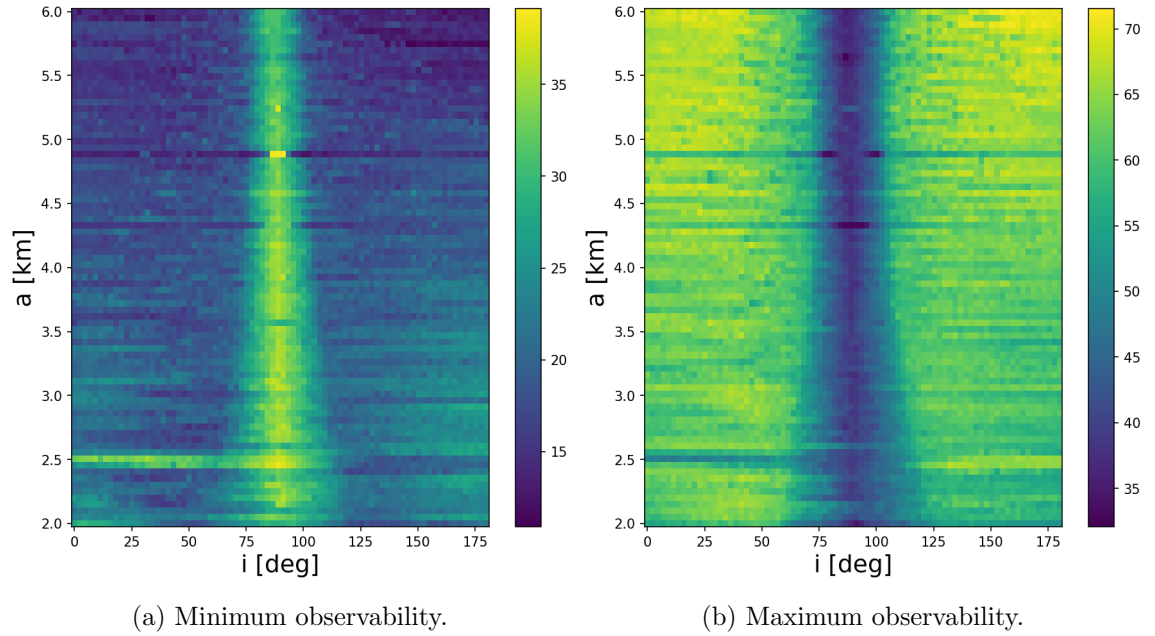


Figure 4.19: Minimum and maximum observability, shown in percentage of the trajectory for which Dimorphos is observable for grid 1.

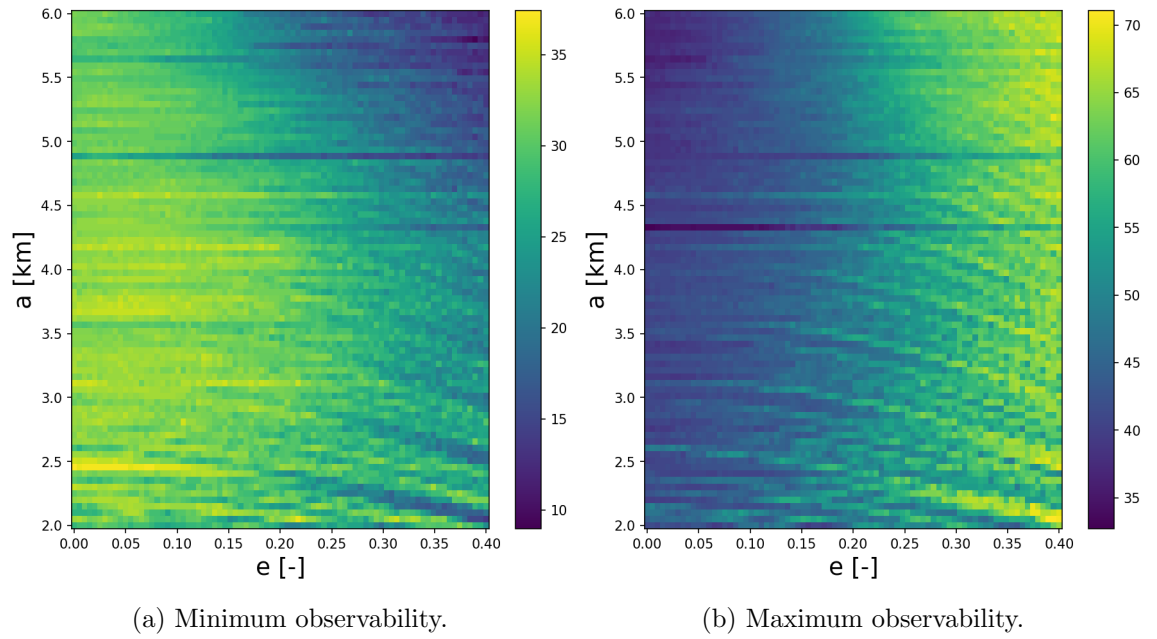


Figure 4.20: Minimum and maximum observability, shown in percentage of the trajectory for which Dimorphos is observable for grid 2.

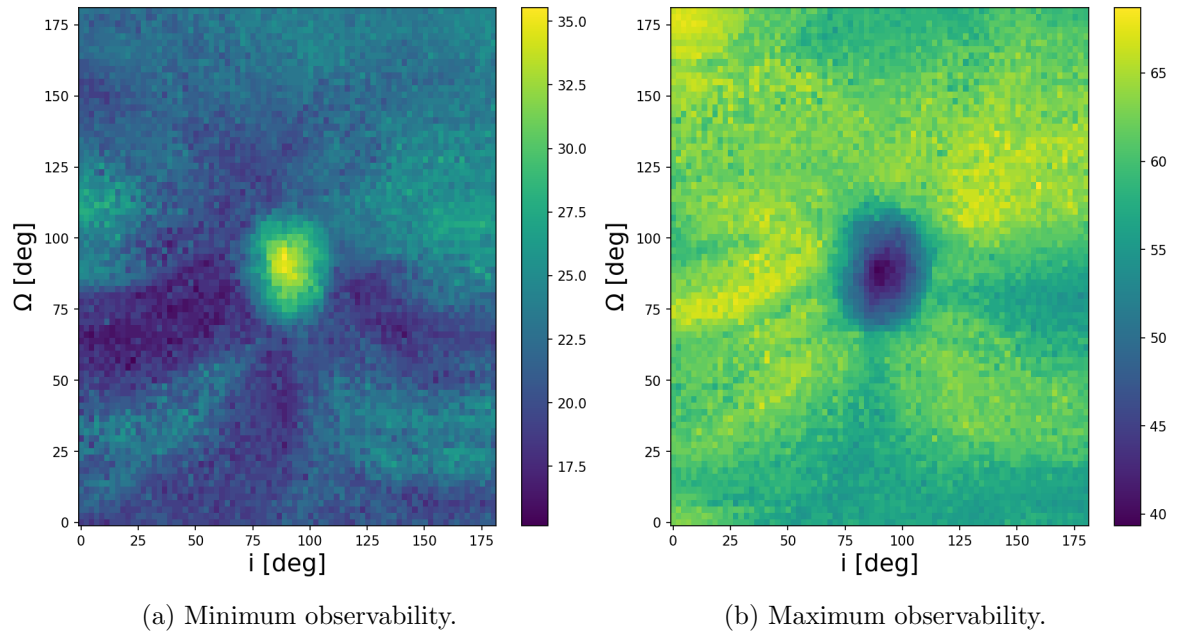


Figure 4.21: Minimum and maximum observability, shown in percentage of the trajectory for which Dimorphos is observable for grid 3.

### 4.3 Chapter Summary

This chapter presents a methodology of how the GIPA method and the uncertain dynamics indicators can be used in the characterisation of the dynamics and the design of close proximity orbits that are both stable and robust against uncertainties.

First, the methodology was applied to Didymos system, modeled using the CR3BP with spherical harmonics gravitational models. The effect of just the uncertainty in the gravitational parameter was analysed using the variance and  $n + 1$  indicator for extremely close proximity motion (interior to the system). The variance indicator shows that there are possible regions of low diffusion, i.e. initial conditions for which the trajectories that originate from these conditions remain together even if the gravitational parameter is different. The  $n + 1$  indicator on the other hand showed the influence of non-linearities on the evolution of trajectories, specifically showing that the regions of low diffusion and low non-linearity are not always the same.

This analysis gave a first indication of how the indicators can be used to characterise the uncertain dynamics. The next step is to apply these indicators to a high-fidelity model and analyse the effect of both the state and model uncertainties, defining that if an orbit that has a low sensitivity to both these uncertainties, that it is robust stable. The classical orbits that are determined to be stable like the terminator orbits are found to be generally also robust stable. However, this stability breaks down closer to the bodies and the resonances with the orbit of Dimorphos show to have large influences on the stability of certain regions in phase space. Other combinations of orbital parameters were also found to be robust stable, allowing for various options for mission designers.

The polynomial algebra is then used to investigate the effect of uncertainties on the parameters that determine the performance of the mission, like the observability of Dimorphos. This analysis shows that the robust stable orbits found by applying the uncertain indicators to the Cartesian or Kepler elements do not always correspond to the highest performing orbits in terms of observability. Hence, it is important to consider both these factors when selecting mission orbits.

## Chapter 5

# Ballistic Landing Trajectory Design under Uncertainty

This chapter is based on the work published in:

Fodde, I., Feng, J., Vasile, M., & Gil-Fernández, J. (2023). Design and Analysis of Robust Ballistic Landings on the Secondary of a Binary Asteroid. *Journal of Guidance, Control, and Dynamics*. In-review.

Fodde, I., Feng, J., Gil-Fernández, J., & Vasile, M. (2022). Binary asteroid landing trajectory design from a self-stabilized terminator orbit considering parametric uncertainties. Paper presented at 73rd International Astronautical Congress 2022, Paris, France.

Fodde, I., Feng, J., & Vasile, M. (2022). Landing area analysis for ballistic landing trajectories on the secondary of a binary asteroid. Paper presented at AAS/AIAA Astrodynamics Specialist Conference 2022, Charlotte, United States.

Fodde, I., Feng, J., & Vasile, M. L. (2022). Robust trajectory design for ballistic landings on Dimorphos. Paper presented at American Institute of Aeronautics and Astronauts SCITECH 2022 Forum, San Diego, United States. <https://doi.org/10.2514/6.2022-1476>

Landings on the surface of asteroids are incredibly valuable in terms of scientific return as the spacecraft-surface interaction provides direct information on the internal structure and material properties of the asteroid while their instruments can do some in-situ measurements to characterize the asteroid in more depth. Various previous

missions performed landings or surface touchdowns, among them the Hayabusa mission [152], Rosetta [51], Hayabusa 2 [153], and OSIRIS-REx [24]. Precise landings require a complex and precise guidance, navigation, and control (GNC) system, increasing the complexity of the spacecraft. As the Hera CubeSats have a limited size and mass budget, a dedicated landing GNC system might not be feasible. Therefore, ballistic landings, i.e. with no closed-loop control of the translational state during descent, are good options for the landing manoeuvre. The main drawback of ballistic landings are their sensitivity to errors in the deployment manoeuvre and uncertainties in the dynamical parameters [154]. Therefore, when designing ballistic landing trajectories, the impact of uncertainties needs to be taken into account.

The complex dynamics due to the large influence of the primary, the non-spherical shape of both bodies, and the low gravitational forces make the landing trajectory design difficult. Previous work has focused on using the hyperbolic manifolds around the  $L_2$  point to find trajectories that intersect with the surface of the secondary [81], [155], [156], [82], [157]. These types of trajectories are very efficient and robust, however often require deployment from close to the  $L_2$  point and do not guarantee favourable landing conditions (e.g. large touchdown velocity and/or shallow impact angle). Other approaches involving bisection based methods to find minimum touchdown velocity landing trajectories for any landing location on the body have also been investigated in [154] and [158]. These methods give insight into what dynamically is the minimum touchdown velocity of a certain location, but it cannot consider any additional constraints on the trajectory itself. The bouncing and surface motion of landers has also been investigated in detail in [159], [160], [161], [162], and [163]. These studies highlight the importance of implementing accurate and efficient models for the dynamics of this phase of the landing trajectory design as well as it can have a large influence on to the lander settling location and success of the landing itself.

Besides the complex dynamics, another problem in the trajectory design process is the highly uncertain environment in which the spacecraft needs to operate, as ground based observations are not able to determine the asteroid's property with a high degree of accuracy [40]. Often, these uncertainties are only included in the analysis after a

nominal trajectory has been designed to check the sensitivity of the trajectory to them. This decoupling is inefficient and can lead to worse performances as conservative safety margins are added [65]. Furthermore, conventional methods for this process like linear covariance analysis require the dynamics to be close to linear and/or the uncertainties to be small. More accurate techniques like the Monte Carlo method, on the other hand, requires a large amount of samples to be propagated through the dynamics (error is roughly proportional to  $1/\sqrt{N}$  where  $N$  is the amount of samples) [164]. Hence, this technique is not numerically efficient enough to be used in applications like determining phase space structures or trajectory optimization algorithms, which require large amount of initial conditions to be investigated and thus need more efficient uncertainty propagation and quantification techniques.

This section introduces a novel methodology for the analysis and design of ballistic landing trajectories, which takes into account the uncertainties present in the system throughout the full process. The proposed method first uses non-intrusive Chebyshev interpolation (NCI) to propagate the uncertain state of the lander for a large amount of landing conditions (velocity magnitude and direction). For each landing condition, the rate of growth of the uncertain state is then determined using the pseudo-diffusion indicator of section 3.2.1.1. This information allows for the discovery of conditions that lead to a high probability of a successful landing, which is then used to design the final ballistic landing trajectory. This trajectory is again designed with the uncertainties taken into account, by applying NCI inside the trajectory optimization transcription and minimizing the final variance of the state.

## 5.1 Surface Motion

The motion of the spacecraft during touchdown and the phase after landing where it can bounce and move around the surface is mainly defined by the shape of the surface, the characteristic of the surface material to dissipate the energy of the spacecraft, and the presence of surface features like rocks and/or craters. Previous research has investigated the surface motion for a large range of fidelity, from simple point mass models with no rocks on the surface (e.g. [159]) to full polyhedron models of the spacecraft and

asteroid surface (e.g. [162]). It was shown previously in [160], [161], and [163] that the shape of the lander has a significant impact on its surface motion. Considering the spacecraft shape allows the effects like frictional torque and rolling resistance to be modeled, however it also requires an accurate shape of the body to be implemented. In the case of a preliminary analysis of the landing manoeuvre, the surface properties like the local slope, rock sizes and distribution, and surface composition will only be known with a high degree of uncertainty. Therefore, this work focuses more on the implementation and analysis of uncertainties within the dynamical models (in this case, the energy damping coefficient of the surface and the local normal vector) and apply a relatively simple point mass model for the surface motion. Future work, when the surface properties of the post-impact Dimorphos are better known, should incorporate higher fidelity dynamical models and determine the impact of them on the analyses presented here.

### 5.1.1 Surface Impact

The spacecraft is assumed here to be a point mass, while Dimorphos is modelled as a triaxial ellipsoid. Therefore, Dimorphos can be parametrized using the previously defined ellipsoidal axes of Table 2.1 as follows:

$$E(x, y, z) = \frac{x^2}{a^2} + \frac{y^2}{b^2} + \frac{z^2}{c^2} = 1, \quad (5.1)$$

where the  $x$ ,  $y$ , and  $z$  coordinates are with respect to the ellipsoid centre. This significantly simplifies the condition of when an impact occurs to:

$$E(x, y, z) \leq 1, \quad (5.2)$$

and the normal at any point along the surface can be found through the gradient operator:

$$\hat{\mathbf{n}}(x, y, z) = \nabla E(x, y, z) = 2[x/a^2, y/b^2, z/c^2]^T. \quad (5.3)$$

The surface of a small body can often be modeled as either a hard rock type surface

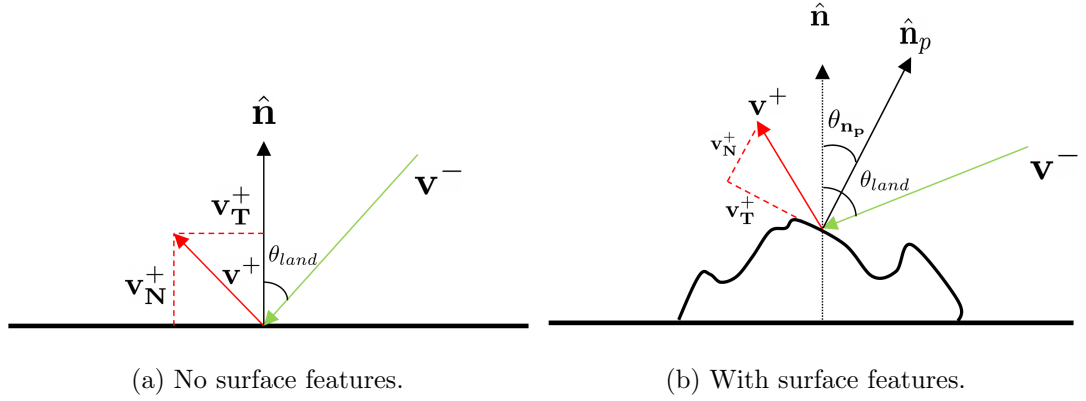


Figure 5.1: 2D representation of the geometry during landing.

or a soft regolith type surface [165]. During its multiple impacts, Philae encountered both of these types of surfaces [166], showing the importance of both of these types of models. For the soft surface case, a numerically expensive discrete element method (DEM) is usually used, which also requires a good knowledge of the surface conditions and parameters. Hence, it is less useful for this type of analysis.

The energy dissipation during an impact is characterised using the coefficient of restitution (CoR)  $0 \leq \epsilon \leq 1$ , which is defined here as follows:

$$\epsilon = \frac{v_N^+}{v_N^-}, \quad (5.4)$$

where the plus and minus sign indicate the post- and pre-impact velocity respectively, and the  $N$  subscript represents the normal component of the vector. Using the geometry of the impact shown in figure 5.1a, the post-impact velocity vector can be calculated as follows:

$$\mathbf{v}^+ = \mathbf{v}_T^+ + \mathbf{v}_N^+ \quad (5.5)$$

$$\mathbf{v}_N^+ = -\epsilon(\hat{\mathbf{n}} \cdot \mathbf{v}^-)\hat{\mathbf{n}} \quad (5.6)$$

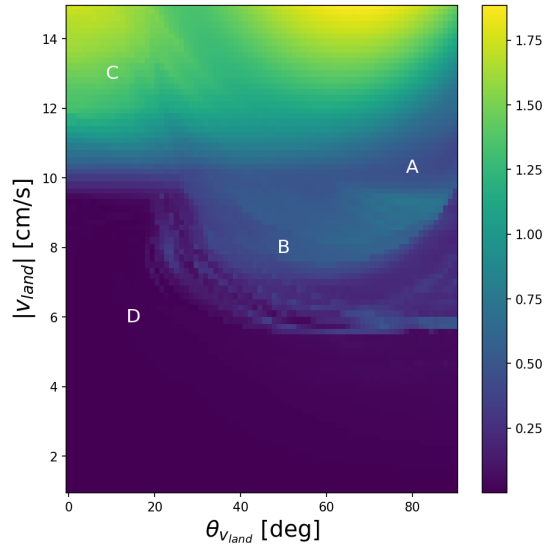
$$\mathbf{v}_T^+ = \mathbf{v}^- - (\hat{\mathbf{n}} \cdot \mathbf{v}^-)\hat{\mathbf{n}}. \quad (5.7)$$

Thus, given an impact point and impact velocity, the post-impact velocity can be

calculated and used to initialise the following arc of ballistic flight that is propagated using the dynamics described in section 4.1 (i.e. the SH-CR3BP).

For the design of landing trajectories, it is important to study which landing conditions lead to the highest probability of a successful landing, which is defined as having the spacecraft remain on the surface of Dimorphos. In this case, the important uncertain dynamical parameters that govern this probability are  $\epsilon$  and the uncertainties in the gravitational field given here by the spherical harmonics coefficients. To find the range of landing conditions that give a high probability of success, a large number of landing velocities  $|\mathbf{v}_{land}|$  and landing angles  $\theta_{land}$  (defined as the angle between the local normal and the incoming velocity vector, see figure 5.1a) are taken and used to calculate the initial post-impact velocity vector. From there, based on the sampling method discussed in section 3.1.2, a set of samples are propagated. Each time if one sample is determined to impact with Dimorphos, the post-impact vector is calculated again. Once enough time has passed (defined here to be 12 hours), the pseudo-diffusion indicator is calculated. From various previous studies, the range of possible values for  $\epsilon$  are taken to be  $[0.55, 0.85]$  (see e.g. [167], [168], [169], [60], [170]), and the  $C_{20}$ ,  $C_{22}$ , and  $C_{40}$  are all taken to be in the range of their nominal value with ten percent uncertainty, which is close to the uncertainties given for most parameters in the Didymos reference model [3]. The surface location on Dimorphos has a large influence on the results. In this case, the landing location is taken to be the crater made by the DART impact, located at 90 degrees longitude facing the direction of motion of Dimorphos. The results of  $\tilde{\gamma}$  are shown in the map in figure 5.2.

As is explained in section 3.2.1.1, low  $\tilde{\gamma}$  indicates regions of low diffusion, i.e. where trajectories that have slightly different initial conditions or dynamical parameters still behave similarly and stay close to each other. In the case of a spacecraft landing scenario, the lowest diffusion happens when all realisations of the uncertainties result in the remaining of the spacecraft on the surface of Dimorphos. When part or all of the realisations result in the spacecraft bouncing away from the surface into prolonged ballistic flight, the diffusion will likely increase as during the ballistic flight the trajectories can move away from each other due to the different environmental parameters and initial

Figure 5.2:  $\tilde{\gamma}$  for CoR only model at DART crater location.

conditions. Therefore, the regions of low  $\tilde{\gamma}$  correspond to landing conditions that allow the spacecraft landing on Dimorphos with a high likelihood, which is defined here as a successful landing condition. It can be seen that this happens for most conditions with the  $|\mathbf{v}_{land}| < 10$  cm/s and  $\theta_{land} < 20$  degrees. As the landing velocity decreases until around 6 cm/s, successful landings become more likely for higher  $\theta_{land}$ . After that, the direction of impact does not have any significant impact on the  $\tilde{\gamma}$  value. For most of the landing velocities above 10 cm/s,  $\tilde{\gamma}$  is much higher and thus there is a low likelihood of having a successful landing. The transition region between these two limits (i.e. the region between 5 cm/s and 10 cm/s for larger impact angles) shows many interesting structures which result in part of the trajectories landing on Dimorphos and part of them going into bounded motion around both the primary and secondary.

To validate this map and show the relationship between the value of  $\tilde{\gamma}$  and the size of the resulting uncertainty sets, the MC analyses of a set of sample are performed for certain initial conditions, corresponding to the letters A, B, C and D shown in figure 5.2. The resulting trajectories, plotted in the synodic reference frame in all three dimensions, are illustrated in figure 5.3. The final positions of all the sample trajectories can also be seen in figure 5.4. The two cases in the transition region, A and B, have part of the trajectories landed on Dimorphos and part of them in a bounded

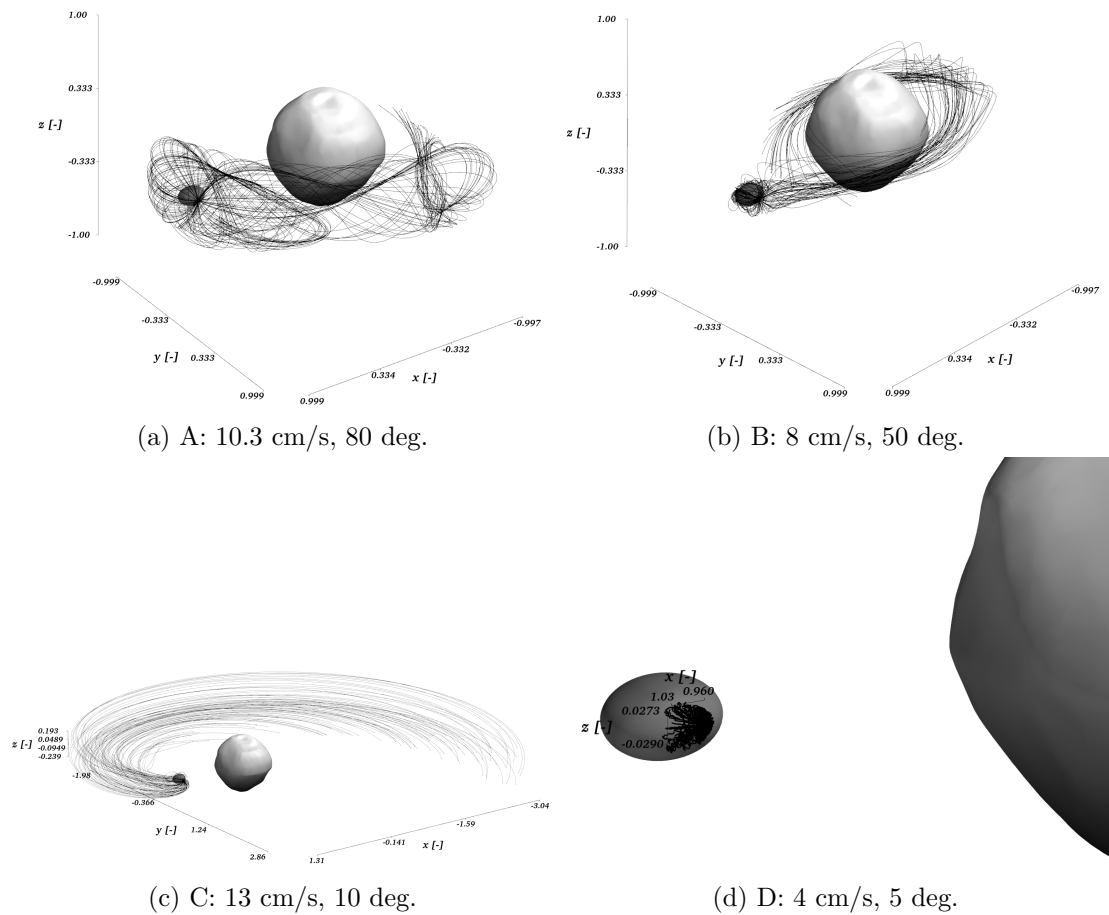


Figure 5.3: A set of the trajectories plotted from the example MC analyses performed for the case of an uncertainty in the CoR and spherical harmonics coefficients only.

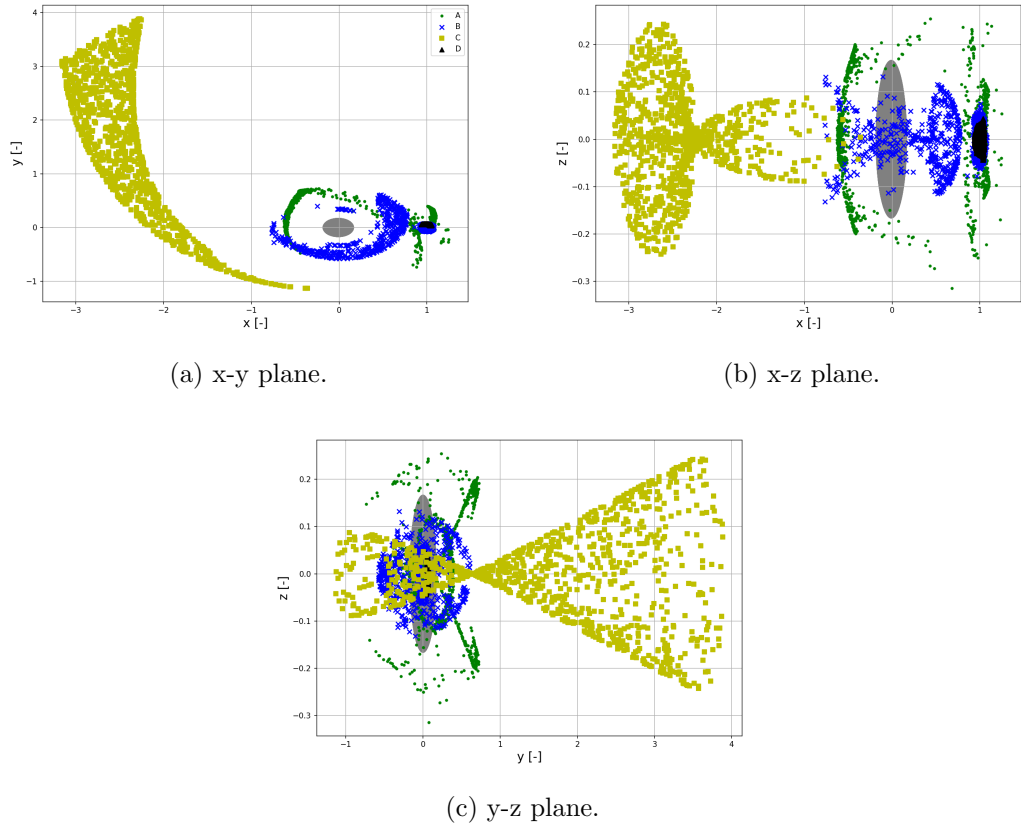


Figure 5.4: Distribution of the final locations of the MC analyses performed for the case of an uncertainty in the CoR and spherical harmonics coefficients only.

trajectory around the system. For the case of C with high  $\tilde{\gamma}$ , it can be clearly seen that all samples are escaped from the surface of Dimorphos and moving away from both bodies. Whereas for D with low  $\tilde{\gamma}$ , all trajectories remain on the surface of Dimorphos, some bouncing several times before going stationary.

### 5.1.2 Surface Rocks

In the previous section, the only parameter that influences the post-impact bounce velocity is the coefficient of restitution  $\epsilon$ , where the normal vector is calculated assuming a smooth ellipsoid as the shape of Dimorphos. This does not necessarily correspond to the real shape of Dimorphos, due to the likely presence of surface features like boulders and craters. Therefore, these features need to be implemented to ensure

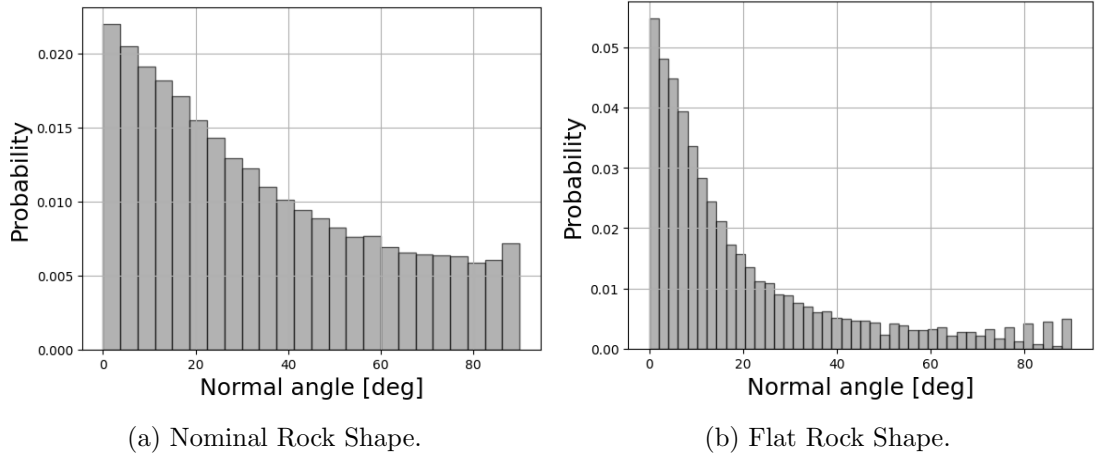
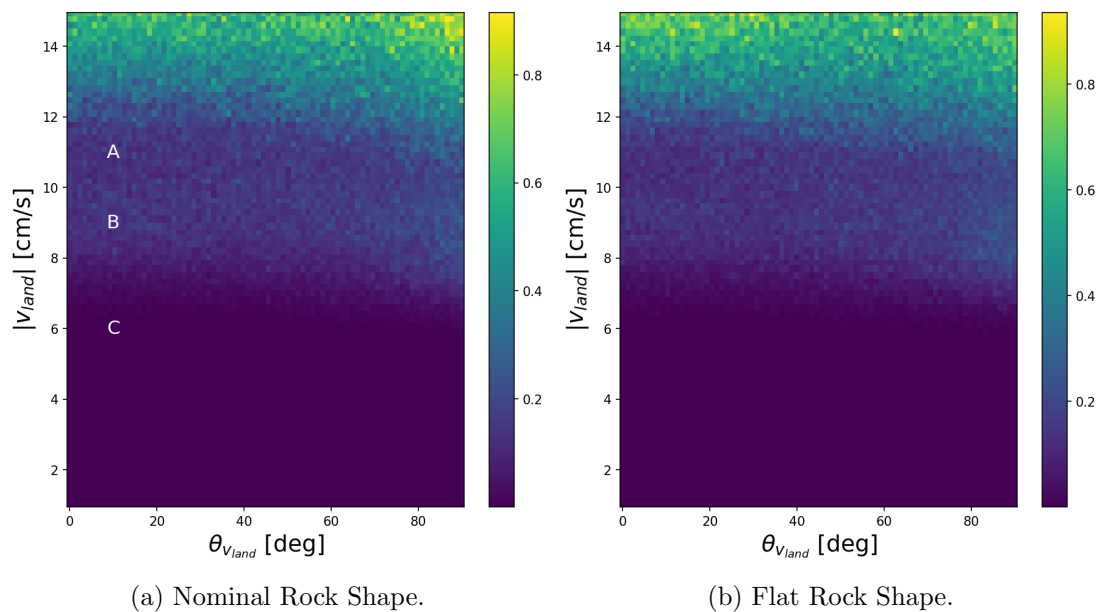


Figure 5.5: Distribution of the angles with respect to the local surface normal for different rock shapes.

proper modelling of the surface motion of the lander.

The high-fidelity modelling of the landing on the surface of Dimorphos can be achieved by using polyhedral models of the spacecraft, surface topography, and rock shapes (see e.g. [161] and [162]). In this work, the main focus is on the effect of the uncertain landing conditions, including uncertainty in the local surface features, on the motion of the spacecraft. Therefore, the use of accurate shape models is not as beneficial and models that more easily incorporate the uncertain nature of the problem are preferred. Therefore, the rocks are modelled here as a stochastic perturbation on the normal vector  $\hat{\mathbf{n}}$ , used in Eq. (5.6) and (5.7). This model has some drawbacks, such as the bias of the lander towards low slope areas and the failure to register grazing impacts [160], but is numerically efficient and allows for easy implementation of the knowledge of the distribution of the shape and size of rocks. The model considered here is thus not only uncertain in terms of the parameters describing the model anymore, but now as well stochastic due to the "noisy" normal vector.

The distribution of the normal vector perturbation is taken from observations of previous rubble pile asteroids like Ryugu. It was found that when the boulders from images of the spacecraft are fitted to ellipsoidal shapes, the mean values of  $b/a$  and  $c/a$  were found to be around 0.7 and 0.44, respectively [171]. This can then be converted to a distribution of normal angles  $\theta_{\hat{\mathbf{n}}_p}$  of the perturbed normal vector  $\hat{\mathbf{n}}_p$  w.r.t.  $\hat{\mathbf{n}}$ , where

Figure 5.6:  $\tilde{\gamma}$  for different rock models at DART crater location.

the different variables are explained graphically in figure 5.1b. The found distribution is shown in figure 5.5a. This distribution is then fitted to a Beta probability distribution function and implemented in the dynamical model. To determine the influence of different shapes, a more flat shaped rock ( $b/a = 0.9$  and  $c/a = 0.2$ ) was implemented as well, as is shown in figure 5.5b. If increased fidelity is needed, the same procedure can be used to combine various different rock shapes to create a single distribution of normal angles. However, for a first analysis, here a single rock shape is used for each simulation.

The  $\tilde{\gamma}$  map of the new dynamical system with the distribution taken from both the nominal rocks (left) and the flat rocks (right) can be found in figure 5.6. First, it can be seen that the difference between the two rock distributions is minimal, thus showing that the shape of the rocks has less of an effect on the large scale distribution of the final states. If compared with the results without rocks, the main difference is that the impact angle has less impact on the results than that of the landing velocity. It can be seen that now the main driver is that the landing velocity should be below around 8 cm/s to ensure a high probability of landing. The impact angle should still be low, as there still is a slight slope on the boundary between the low and higher diffusion areas,

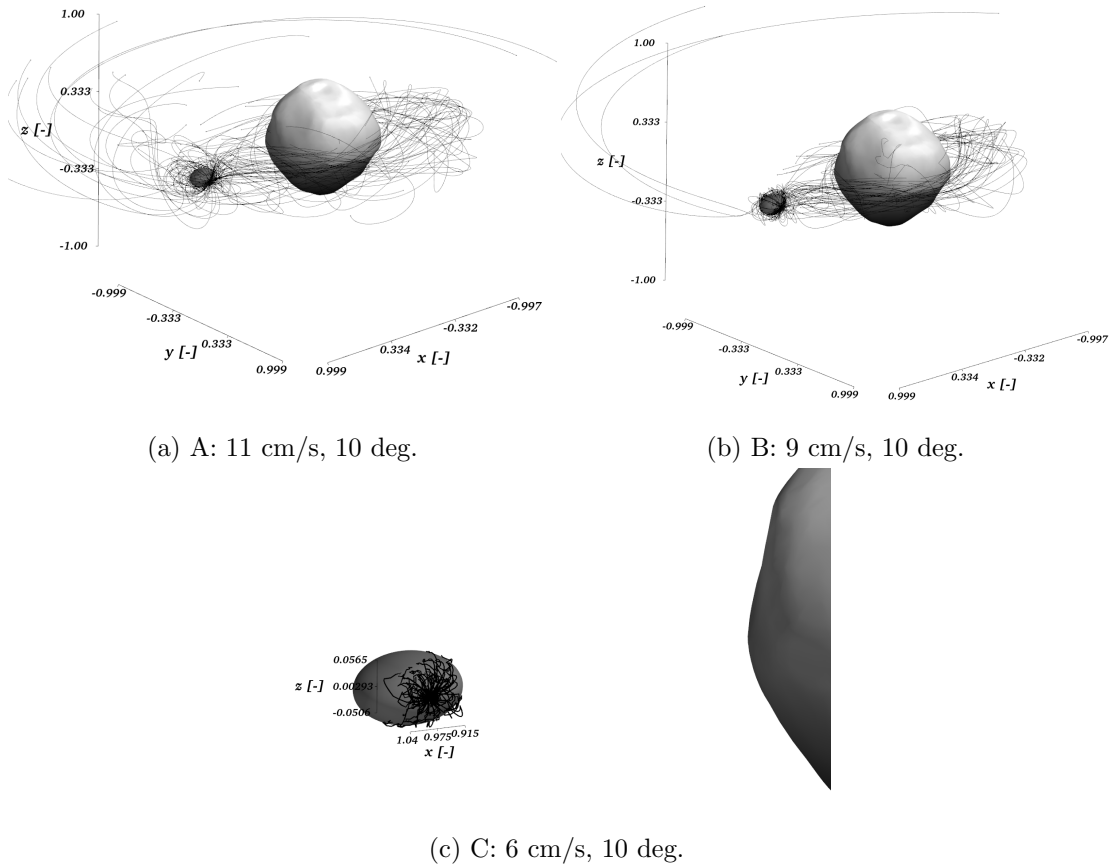


Figure 5.7: A set of the trajectories plotted from the example MC analyses performed for the case of an uncertainty in the CoR, spherical harmonics coefficients, and with stochastic perturbation of the normal vector.

but this slope is much less significant compared to figure 5.2. Another feature to note is that as the impact velocity increases, the diffusion increases as expected. However, there is another band of lower diffusion between 10 and 12 cm/s, after which for higher velocities the diffusion increases again.

Three different example MC analyses are performed again to analyse these different regions, where each one is taken with a similar impact angle but landing velocity taken from the different regions discussed before. The results can be seen in figure 5.7 and 5.8. As expected, C shows that most of the trajectories remain bounded on the surface of Dimorphos. The difference between A and B is seen more clearly in the distribution of final positions of figure 5.8, where it is shown that even though the higher landing

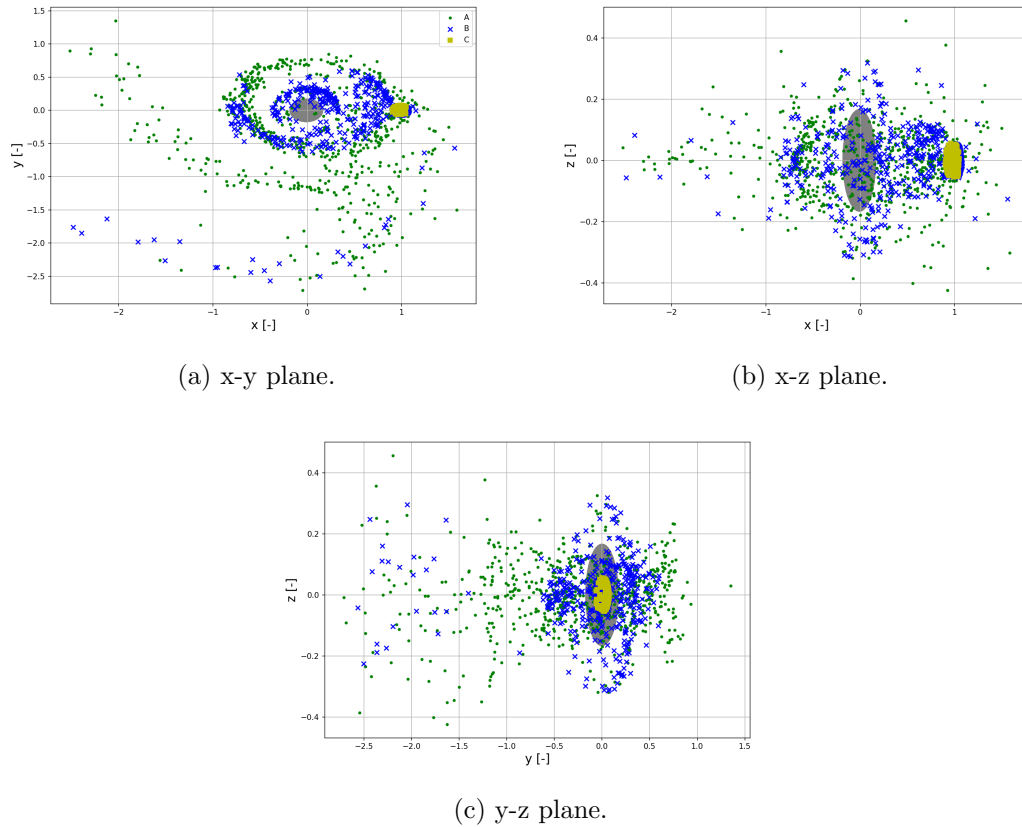


Figure 5.8: Distribution of the final locations of the MC analyses performed for the case of an uncertainty in the CoR, spherical harmonics coefficients, and with stochastic perturbation of the normal vector.

velocity of A results in more trajectories going in far orbits around the system, the lower velocity of B between 8 and 10 cm/s have small chances of some trajectories being captured into far orbits which increases the diffusion.

## 5.2 Minimum Touchdown Velocity

During the proximity operations at Didymos, the spacecraft will move slowly towards the bodies over time. During the final phase, when it is the closest to the system, the manoeuver to put it on the landing trajectory towards Dimorphos will be executed. As mentioned before, for this study it is assumed that the translational state is not continuously controlled during descent. Hence, the minimum possible landing velocity

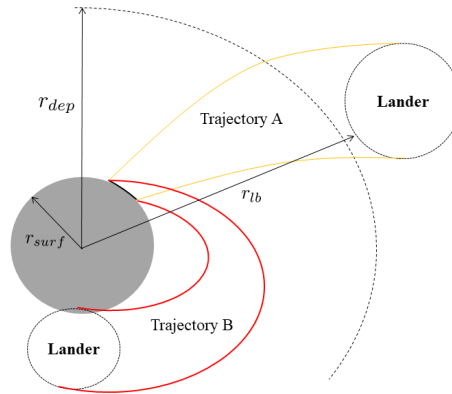


Figure 5.9: Diagram showing the process of finding the minimum landing velocity when considering uncertainties.

cannot be controlled and is determined by the natural dynamics of the system.

This minimum landing velocity for Dimorphos is determined as follows. For the nominal case, [172] developed a bisection method to determine the minimum touchdown velocity for ballistic landings on asteroid surfaces. This was then further extended in [158] to use uncertainty propagation methods to include state and dynamical uncertainties in the process. This method is used here to determine the touchdown velocity, considering the current, pre-arrival uncertainties in the total mass of the system and the mass distribution of Dimorphos. For the sake of completeness, this method is explained here as well.

The method starts by selecting a landing location and initialising an upper and lower bound for the landing velocity,  $v_l$  and  $v_u$  respectively. For each iteration of the algorithm, the landing velocity  $v_c$  is taken to be the middle point of these bounds, i.e.  $v_c = (v_u + v_l)/2$ . As was shown in section 5.1, the highest probability of the spacecraft remaining on the surface of Dimorphos after bouncing is when the landing happens perpendicular to the surface. Therefore, the impact angle is taken to be 0 degree, and the landing state can be seen as a point located at the desired landing location with the velocity vector pointing towards the center of Dimorphos. The trajectory is then propagated backwards in time, until either the spacecraft reaches a pre-determined

deployment distance  $r_{dep}$  (which can be either the distance at which a mothercraft is orbiting at deployment, or the previous operational orbit of the spacecraft before starting the landing manoeuvre), the spacecraft lands back on Dimorphos, or the flight time of 12 hours is reached. If  $r_{dep}$  is reached, the landing velocity might be too large, thus the upper bound of the next iteration is lowered to the  $v_c$  of the current iteration. For the other possibilities (flight time larger than 12 hours or re-impact on the surface),  $v_c$  is too low and thus the lower bound of the landing velocity for the next iteration is set to  $v_c$  of the current iteration. A maximum flight time of 12 hours is selected for operational purposes and to minimize the maximal growth of the set of states. This process is repeated until the difference between  $v_l$  and  $v_u$  reaches a set tolerance, taken here to be  $1 \cdot 10^{-8}$ .

In the case that uncertainties are also considered, the process remains relatively similar except for the fact that the state is now an uncertain set, which needs to be propagated using the NCI method discussed in section 3.1.2. Furthermore, determining how to adjust the velocity bounds is now done according to the value of the minimum distance between the set of lander states and Dimorphos. The method is shown graphically in figure 5.9, where case A shows the scenario where the full set of lander states reaches the deployment distance and case B where the landing velocity is not high enough to reach the deployment distance. Additionally, a summary of the method is shown in algorithm 1.

---

**Algorithm 1** Robust trajectory design algorithm
 

---

```

Set  $v_{lb}, v_{ub}$ 
Set  $\mu_p \pm \sigma_{\mu_p}, \mu_s \pm \sigma_{\mu_s}$ 
Set  $C_{20,s} \pm \sigma_{C_{20,s}}, C_{22,s} \pm \sigma_{C_{22,s}}$ 
while  $|v_{ub} - v_{lb}| < TOL$  do
   $v_l = (v_{ub} + v_{lb})/2$ 
  Propagate  $\tilde{\Omega}_{x_f} \rightarrow \tilde{\Omega}_{x_0}$ 
  if  $r_{lb} < r_{surf}$  then
     $v_{lb} = v_l$ 
  else if  $r_{lb} > r_{dep}$  then
     $v_{ub} = v_l$ 
  else
     $v_{lb} = v_l$ 
  end if
end while

```

---

Figure 5.10 shows the results for Dimorphos, with  $r_{dep} = 2.0$  km (the final orbital distance of Juventas) and the uncertainties at 10 percent of their nominal values. The surface of Dimorphos can be divided into two different regions, the side facing away from Didymos (longitude between  $-90$  and  $90$  degrees) and the side facing towards Didymos (longitude between  $-90$  and  $-180$  degrees and between  $90$  and  $180$  degrees). The latter region shows in general high landing velocities as it needs to travel further to reach the deployment distance and to avoid Didymos. Only for high latitudes can lower touchdown velocities be reached, as Didymos can be avoided more easily from these landing locations. In general, the landing velocities in this region are too high to be feasible for a ballistic landing strategy. For the region facing away from Didymos, the lowest touchdown velocities are near the  $(0, 0)$  degrees latitude and longitude point, where velocities around  $5$  cm/s can be found. Moving towards the desired landing location at the DART crater (i.e.  $(0, 90)$  degrees latitude and longitude), the velocity increases again, reaching around  $38$  cm/s. As determined in section 5.1, this landing velocity does not guarantee that the spacecraft remains on the surface of Dimorphos after touchdown (for both the cases of rocks and no rocks). Therefore, either the assumption of landing perpendicular to the surface needs to be relaxed, or a braking manoeuvre needs to be added to the landing trajectory to reduce the speed of the spacecraft before touchdown.

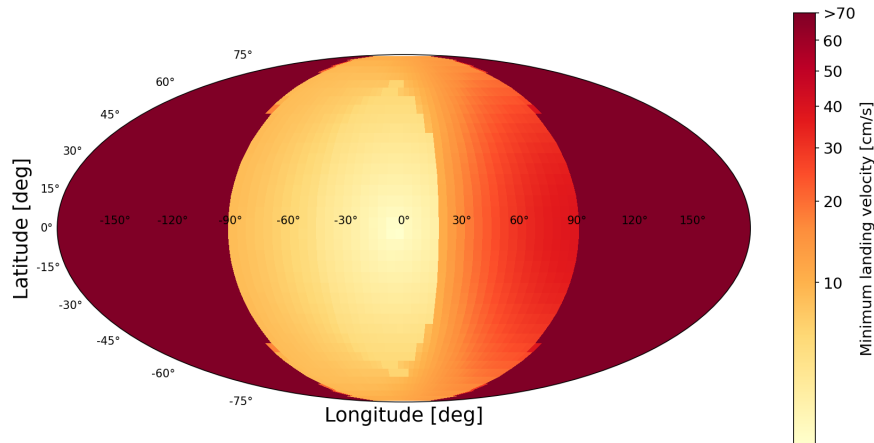


Figure 5.10: Minimum landing velocity for different landing areas, considering also uncertainty in the mass of both bodies and the  $C_{20}$  and  $C_{22}$  coefficients of Dimorphos. It is important to note that the colors are plotted according to a power law to allow for more detail in the low velocity areas.

Figure 5.11 shows the influence of the incoming velocity direction on the minimum landing velocity. The angle  $\theta_{v_{land}}$  corresponds to the impact angle discussed in section 5.1 and the azimuth is the angle of the landing velocity vector with respect to the negative x-axis of the synodic frame. As can be seen from figure 5.11, there are options for low velocity landings (between 7 and 10 cm/s) with a very shallow impact angle around 180 degrees azimuth, corresponding to the velocity vector pointing away from the barycentre of the system. However, even for the lower velocities found there, the very shallow impact angle will significantly increase the likelihood of the spacecraft bouncing away from the surface again as was shown in section 5.1. Therefore, if the goal is to land in or near the DART impact crater, a braking manoeuvre closer to the surface is the only option to have a high probability of a successful landing.

### 5.3 Robust Trajectory Optimization

After finding the target conditions of the lander at the surface in section 5.1, the goal now is to design a trajectory that can ensure that the spacecraft can reach these conditions reliably. As mentioned in section 5.2, the minimum touchdown velocity at the DART crater for a direct deployment from  $r_{dep} = 2.0$  km is around  $38$  cm/s, whereas

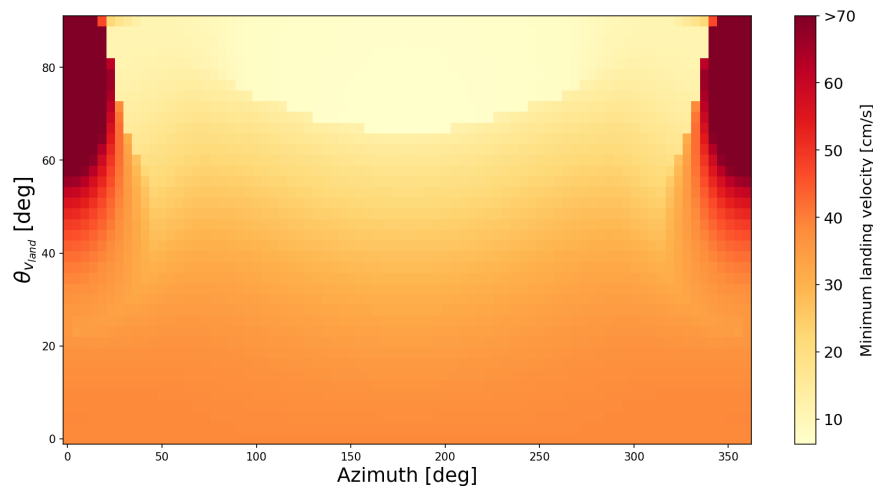


Figure 5.11: Minimum landing velocity for different landing vector orientations at the DART impact crater, considering also uncertainty in the mass of both bodies and the  $C_{20}$  and  $C_{22}$  coefficients of Dimorphos.

from the  $\tilde{\gamma}$  maps of section 5.1 it was found that the touchdown velocity should be below  $10 \text{ cm/s}$ , preferably below  $7 \text{ cm/s}$  if a rocky environment is found, to ensure a high probability of settling on the surface of Dimorphos. Therefore, a braking manoeuvre is needed between the deployment manoeuvre and the time of landing.

For the ballistic landing considered here there is no dedicated navigation system that is capable of estimating the state and correcting for off-nominal conditions, hence the braking manoeuvre is performed open-loop using a pre-calculated  $\Delta V$  manoeuvre. As the spacecraft has no capabilities to correct for the uncertainties in the state of the spacecraft stemming from manoeuvre errors and dynamical model uncertainties, both the deployment and braking manoeuvre needs to be generated such that the landing success percentage is the highest. Normally, this is done by first designing a nominal trajectory, then doing a sensitivity analysis (often using a MC method) to assess the impact of uncertainties, and finally altering the nominal trajectory based on the found sensitivities. This process often needs multiple iterations and is thus time consuming and can result in worse trajectories with added safety margins [65]. In this section, the NCI uncertainty propagation technique is used to generate landing trajectories that directly take into account all the different uncertainties and minimize its sensitivity to them.

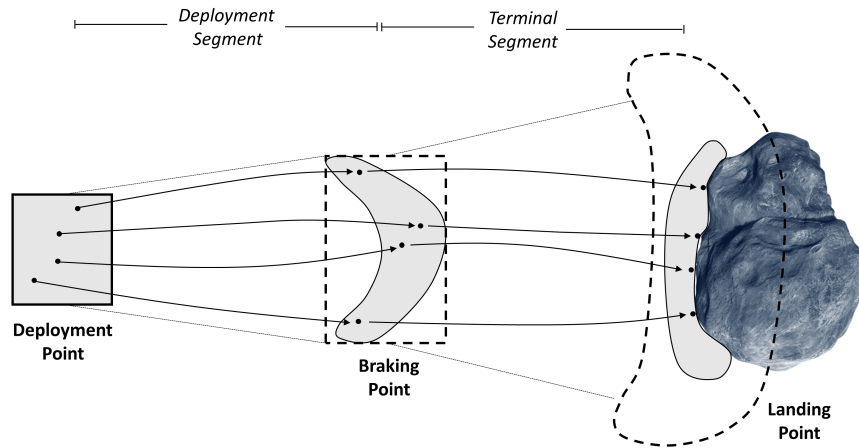


Figure 5.12: Diagram explaining how the robust landing trajectory optimization works using the NCI uncertainty propagation method. The grey areas represent the actual area which the trajectories occupy whereas the squares represent the total propagated area using NCI.

The approach taken here is based on the direct multiple shooting method developed in [173]. The landing trajectory is divided into two segments: the deployment segment spanning from the deployment point to the braking point, and the terminal segment stemming from the braking point to the landing point. A Non-Linear Programming (NLP) solver is then used to find the optimal values of the decision variables  $\mathbf{u}$ , which consist of the deployment velocity vector  $\mathbf{v}_{dep}$ , the braking manoeuvre  $\Delta\mathbf{v}$ , and the time of the braking manoeuvre  $t_{\Delta v}$ . The trajectory is then propagated using the selected  $\mathbf{u}$  after which the different objectives and constraints are evaluated and used to select a new  $\mathbf{u}$ . When considering uncertainties, this point-wise propagation of the state is substituted by the propagation of the uncertainty set, which is performed here using the NCI method. In principle, the full trajectory can be propagated in one go obtaining one polynomial representation of the landing trajectory under uncertainty. However, both the required polynomial degree and number of samples increases quickly as the number of uncertain variables increases. Therefore, it is more efficient to separate the polynomial for the two different segments. The continuity between the two segments is guaranteed using a re-initialisation approach, which is shown graphically in figure 5.12. First, the uncertainty set at the deployment point is propagated using NCI to

Table 5.1: The results of the optimization of the landing trajectory.

Variable	Point	Robust
$v_{dep}$	40.9 cm/s	29.6 cm/s
$\phi_{dep}$	186.3 °	182.7 °
$\theta_{dep}$	93.7 °	98.1 °
$\Delta v$	39.9 cm/s	26.3 cm/s
$\phi_{\Delta v}$	185.3 °	162.6 °
$\theta_{\Delta v}$	84.7 °	78.3 °
$t_{\Delta v}$	7.071 hours	7.070 hours
Landing success	74.3 %	94.7 %
Landing Latitude (mean, 1- $\sigma$ )	2.49 ± 26.5 °	9.46 ± 26.9 °
Landing Longitude (mean, 1- $\sigma$ )	77.9 ± 41.5 °	18.2 ± 27.5 °
$\theta_{land}$ (mean, 1- $\sigma$ )	35.9 ± 19.4 °	41.4 ± 17.9 °
$v_{land}$ (mean, 1- $\sigma$ )	8.68 ± 0.46 cm/s	7.12 ± 0.71 cm/s

the braking point, shown as the grey areas in the left side of figure 5.12. The initial uncertainty range for the terminal segment needs to be represented by an upper and lower bound of the various state variables, i.e. a hypercube in phase space. This means that the shape of the final set of states at the braking point, which is often shaped very differently from a hypercube, cannot be used directly as an input for the initial state uncertainties of the terminal phase. Hence, the uncertainty set at the braking point is re-initialised as a hypercube that conservatively bounds the set (the dashed box). This hypercube can be used as the input for the following phase, and is then propagated through the terminal segment until the time of landing. As the resulting hypercube is an overestimation of the actual uncertainty set, a set of samples are first propagated using the deployment segment polynomial and then used as an input for the terminal segment polynomial to obtain the actual distribution at the landing point, see figure 5.12. This distribution is then used to obtain the necessary objective and constraint values that are formulated as part of the NLP, which are now functions of the distribution of landing trajectories.

The robust optimization problem considered here is formulated as follows:

$$\min_{\mathbf{u}} \max(\text{diag}(\Sigma_{\mathbf{r},\text{land}})), \quad (5.8)$$

$$\text{s.t. } \mathbf{x}_{k+1} = \tilde{\Omega}_{t_{k+1}}(\boldsymbol{\xi}_k), k = 0, 1 \quad (5.9)$$

$$\mathbb{E}[\mathbf{r}_{\text{land}}] - \mathbf{r}_{\text{crater}} < 100m \quad (5.10)$$

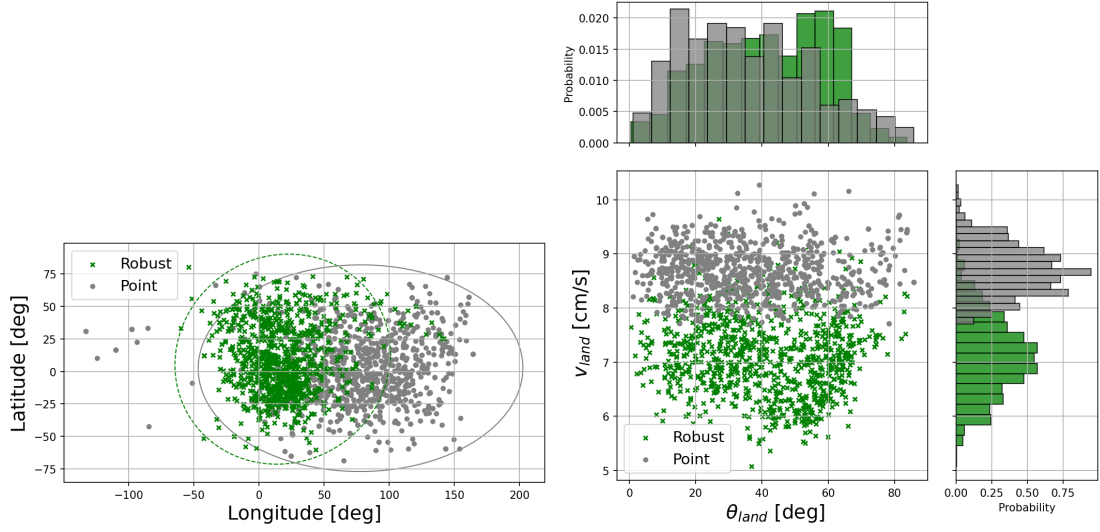
$$\mathbb{E}[|\mathbf{v}_{\text{land}}|] < 10cm/s \quad (5.11)$$

$$\mathbb{E}[\theta_{\text{land}}] < 25^\circ \quad (5.12)$$

The maximum variance of the state at the final time is selected as the cost function that needs to be minimized. Using this objective will desensitize the landing trajectory to the uncertainties and thus reduce the landing footprint. To ensure that the spacecraft will land mostly in the DART crater hemisphere, constraint (5.10) is added to ensure that the mean landing state should be within 100 meters of the DART crater location. Constraints (5.11) and (5.12) are derived from the  $\tilde{\gamma}$  maps for the case of a smooth surface, where landings below these two values have sufficiently low  $\tilde{\gamma}$  such that the probability of settling on the surface is high. For the rocky case, the  $\theta_{\text{land}}$  constraint can be relaxed whereas the  $|\mathbf{v}_{\text{land}}|$  constraint needs to be lowered to 7 cm/s. However, it will be shown that the result with the constraints set for the smooth surface case also work well for the rocky case, thus this setup is kept for now.

Initially, a point-wise propagated trajectory is found using a simple single shooting approach, where the trajectory is propagated backwards from the estimated DART crater location to the final time, minimizing the difference between the actual final position and the desired deployment location (assumed here to be located on the x-axis of the synodic frame at 2.0 km away from the barycentre). This trajectory is then used as both a comparison against the robust method discussed here and as an initial guess for the NLP solver. The uncertainties considered here are: 100 meters (3- $\sigma$ ) in the deployment position, 5 percent (3- $\sigma$ ) in the velocity magnitude of the deployment and braking manoeuver, and 3 degrees (3- $\sigma$ ) in the pointing of the deployment and braking manoeuver. The specific solver used here is the WORHP algorithm [174].

The results of a MC analysis of both the point-wise and robust approach are sum-



(a) Landing location distribution and  $3\text{-}\sigma$  ellipse.

(b) Landing geometry distribution.

Figure 5.13: The distributions of landing location and geometry of both the robust optimization method and the nominal point-wise method.

marised in table 5.1. The main result is the large increase in trajectories landing on Dimorphos, going from 74.3 % to 94.7 %. This is done by significantly reducing the magnitude of the manoeuvres and at the same time changing the pointing slightly while keeping the braking time almost the same as for the point-wise result. This results in a smaller uncertainty set due to the proportionality of the  $\Delta v$  error and thus results in a significantly smaller landing ellipse, as can be seen in figure 5.13, and in significantly reducing the landing velocities, as shown in figure 5.13b. However, this does come at the cost of moving the mean landing location more away from the estimated crater location and also increasing the mean impact angle (see table 5.1).

To determine how these results relate to the desired landing conditions found in section 5.1, the MC results are projected on the  $\tilde{\gamma}$  maps in figure 5.14. It can be seen that for both cases the trajectories of the robust solution are located in lower  $\tilde{\gamma}$  regions compared to the point-wise solution. For the smooth case in figure 5.14a, the higher impact angle does result in a significant part of the trajectories from the robust solution residing in the transition region and therefore not necessarily all settling on the surface. However, for the rocky case the decreased sensitivity to this angle and the fact that the

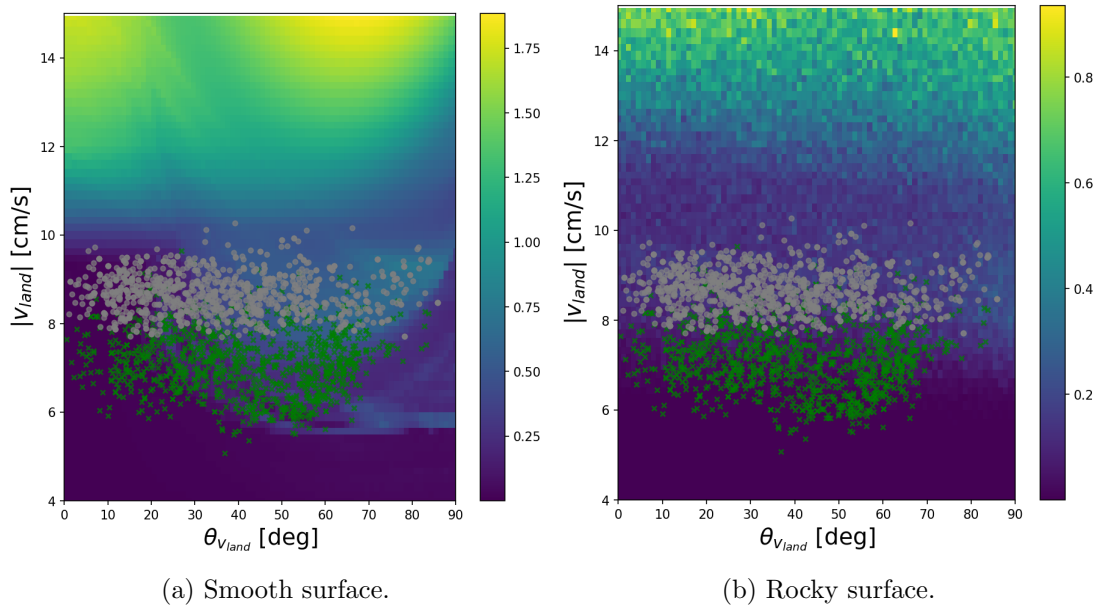


Figure 5.14: The distributions of landing geometry of both the robust optimization method and the nominal point-wise method projected on the  $\tilde{\gamma}$  maps.

mean touchdown velocity is much lower, results in the most of the MC samples for the robust solution residing in low  $\tilde{\gamma}$  regions, which directly relates to a high probability of a successful landing.

## 5.4 Chapter Summary

This chapter introduces a novel methodology for the design and analysis of ballistic landing trajectories on the secondary of a binary asteroid. The methodology shows how efficient uncertainty propagation and quantification tools, specifically Non-Intrusive Chebyshev Interpolation (NCI) and the pseudo-diffusion indicator, can be used to analyse the uncertain dynamics and design a robust landing trajectory.

It is shown how the pseudo-diffusion indicator can be used to determine constraints on the landing geometry and touchdown velocity that ensure high probability of the spacecraft settling on the surface of the asteroid. For the model where a smooth surface of the asteroid was assumed, a maximum touchdown velocity of 10 cm/s was found and a maximum impact angle of 20 degrees. As the touchdown velocity decreases, the

maximum allowable impact angle also increases, where for around 6 cm/s almost all impact angles result in settling on the surface. A transition region also appears for touchdown velocities between 10 and 6 cm/s and high impact angles, where part of the trajectories settle on Dimorphos' surface and part go into an orbit around the system. When the dynamics are altered to model surface features like rocks and craters using a stochastic perturbation on the local surface normal, the dependency on the impact angle is less significant and the maximum touchdown velocity decreases to around 8 cm/s.

Using a NCI based bisection method, it was then found that if a landing location in the DART crater hemisphere is considered with a deployment point 2 km away from the system, the necessary minimum touchdown velocity would be much higher than what is required for settling on the surface. Thus an extra braking manoeuvre is needed along the trajectory to reduce the touchdown velocity.

The deployment  $\Delta v$ , braking  $\Delta v$ , and time of the braking  $\Delta v$  were then determined using a novel method which incorporates the NCI uncertainty propagation method into the trajectory optimization transcription. This method was able to find a trajectory which increase the landing success percentage from 74.3% to 94.7% compared to a trajectory designed without considering the uncertainties. Furthermore, the landing footprint on Dimorphos was also significantly reduced together with lowering the mean touchdown velocity. This comes at the cost of increasing the mean impact angle and moving the mean landing longitude away from the desired location. However, even with these changes the robust trajectory was found to be much more desirable.

## Chapter 6

# Robust Crater Fly-by Trajectory Design

This chapter is based on the work published in:

Fodde, I., Feng, J., Vasile, M., & Gil-Fernández, J. (2023). Chance-Constrained Trajectory Design for Hera's Experimental Phase using Polynomial Algebra. In-development.

Fodde, I., Feng, J., Gil-Fernández, J., & Vasile, M. (2023). Combined Trajectory Design and Navigation Analysis for Hera's Very-Close Flyby of Dimorphos. Paper presented at 74th International Astronautical Congress 2023, Baku, Azerbaijan.

The final nominal phase of Hera is the experimental phase, where the highest resolution images of the impact crater will be taken. As during this phase the closest fly-bys of Dimorphos will take place, it is important to ensure the safety of the spacecraft and minimise the risk of impact. Therefore, the trajectory design of these fly-bys needs to consider the performance of the navigation system, and the possible execution errors of the  $\Delta V$  manoeuvres.

This is mostly tackled by performing a so-called navigation analysis after the nominal design is done. This analysis determines the sensitivity of the trajectory to perturbations, navigation and control system performances, and system uncertainties. Based on this analysis, the nominal design is updated by adding margins, implementing large

amounts of trajectory correction manoeuvres, and/or increasing distances with respect to the body [64] [65] [66]. These factors reduce the scientific gain of the mission, complicate the design, and as this cycle is often repeated, the development time is also significantly increased.

Within the trajectory optimization field, there has been a focus on solving this by incorporating uncertainties into the trajectory optimization process, which allows for solving problems with so-called chance constraints [175], and controlling the state covariance along the vehicle's path [176]. Within asteroid missions, various previous works have focused on robust trajectory design under uncertainties. An optimization approach for minimizing the covariance in orbital transfers was proposed in [177], using linear dynamics for the covariance. In [178], a soft landing trajectory was found using a robust optimization technique where the landing area dispersion was minimised. Similarly, [179] designed a landing trajectory using a reliability assessment involving a Monte Carlo analysis. These approaches use either linearization or Monte Carlo methods to propagate the uncertainties. As the uncertainties can be quite large in this case, the linearization technique is not accurate enough. A Monte Carlo approach is more accurate, but its convergence is slow and most problems require large amounts of samples to be propagated, hence this can become inefficient. More efficient uncertainty propagation (UP) methods have also been investigated. In [180] and [181] an Unscented Transform was used to propagate the first two moments of normally distributed state variables and design a robust guidance policy. The authors of [182] and [173] applied polynomial algebra based UP techniques to general trajectory optimization problems. Recently, several works have focused on introducing the measurement process and closed-loop control within the trajectory optimization process. These types of systems are called partially observable Markov decision processes (POMDP), which is a decision-making system within a stochastic environment in which the state is not perfectly known [183]. This was applied to spacecraft trajectory design in [130], using non-intrusive polynomial interpolation and a multiple-shooting type transcription.

The approach introduced in this chapter starts from the method described in [130], and applies it to the design of the very-close fly-bys (VCFB) of asteroid Dimorphos

for the Hera mission, combining the trajectory design and navigation assessment to produce more robust solutions. This requires altering the method for the use with the autonomous optical navigation system of Hera. Furthermore, the Generalised Intrusive Polynomial Algebra (GIPA) method will be used instead of the original non-intrusive method for the uncertainty propagation, as it is generally more efficient compared to its non-intrusive counterpart.

## 6.1 Experimental Phase

The mission and trajectory design of Hera is similar to Rosetta, where mostly hyperbolic arcs are flown around the system [21]. The mission has various phases, each one having different observational requirements and arc geometries. Between each phase the distance to the system is decreased, as the observations made during the previous phases reduces the uncertainties regarding the physical parameters of the two bodies, and thus the trajectories can be predicted with more accuracy. The final nominal close-proximity operations phase of Hera is the experimental phase (EXP). The main goal of the EXP is the detailed characterization of the crater made by the DART impact.

This section details the requirements associated with the EXP, the nominal trajectory design, and the basic guidance, navigation, and control (GNC) algorithms used.

### 6.1.1 Nominal Trajectory Design

The EXP consists of three hyperbolic arcs: one approach arc, one fly-by arc, and one return arc connecting again to the start of the approach arc. The geometry of the EXP can be seen in more detail in figure 6.1.

During the fly-by arc, also known as the very-close fly-by (VCFB), the spacecraft will try to image the crater at extremely close distances. This arc starts with a completely open-loop manoeuvre, computed on-ground and uploaded during the previous arcs. Two additional manoeuvres are planned during the VCFB, which have two different purposes: sequentially reduce the periapsis of the VCFB, and correct for off-nominal conditions using an autonomous GNC system. Reducing the periapsis sequentially al-

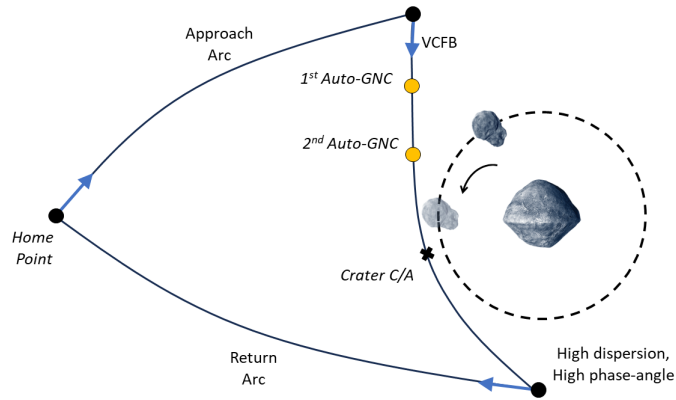


Figure 6.1: A diagram of Hera's experimental phase.

lows for a more robust design as any missed thrust event will result in a relatively high flyby periapsis, reducing the risk of impact. Furthermore, the autonomous GNC system can significantly reduce the dispersion at close-approach (C/A).

After the C/A, the dispersion of the spacecraft will increase and once it is sufficiently far away from the system another pre-computed manoeuvre will put the spacecraft on the return arc. During this arc, ground based orbit determination will be performed and using a manoeuvre at the home point the difference with respect to the nominal trajectory will be corrected for.

This phase consists of several technology demonstration objectives, mainly related to optical navigation and autonomous operations [32]. The main scientific goal is related to the close observation of the DART impact crater. For the observation of the crater at C/A there are several requirements [5]:

1. Crater imaged with a resolution of  $< 10$  cm/pixel.
2. Spacecraft elevation angle ( $\epsilon_{s/c}$ ) between 20 and 70 degrees.
3. Sun elevation angle ( $\epsilon_{\odot}$ ) between 25 and 75 degrees.
4. Phase angle ( $\phi$ ) between 5 and 90 degrees.

The definition of these angles can be seen in figure 6.2, where  $\hat{n}_c$  is the crater normal,  $\mathbf{r}_{s/c}$  the spacecraft position with respect to the crater, and  $\mathbf{r}_{\odot}$  the position of the Sun

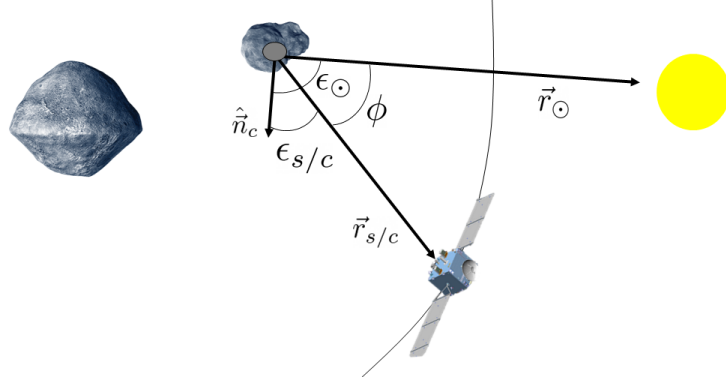


Figure 6.2: Definition of the various angles that influence the lighting conditions during close approach.

with respect to the crater. Requirements 2 - 4, related to the lighting conditions of the crater, are especially important as when these angles are outside their respective bounds, the quality of the observation is significantly reduced.

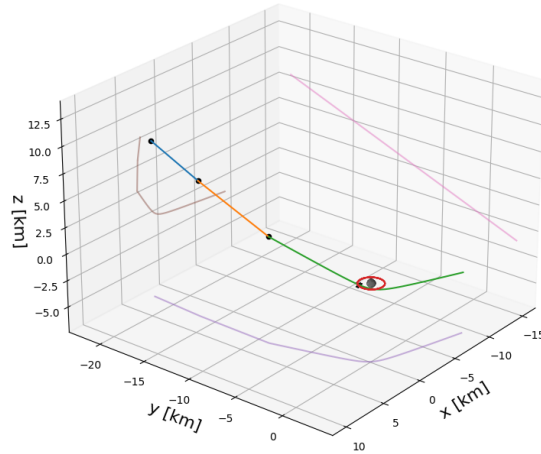
An important operational requirement is to have a certain velocity margin  $C$ , i.e. an excess velocity above the escape velocity  $v_{esc}$ , during the various arcs. This velocity margin is defined as follows:

$$V_{s/c} = (1 + C)\sqrt{\frac{2\mu}{r}} = (1 + C)v_{esc}. \quad (6.1)$$

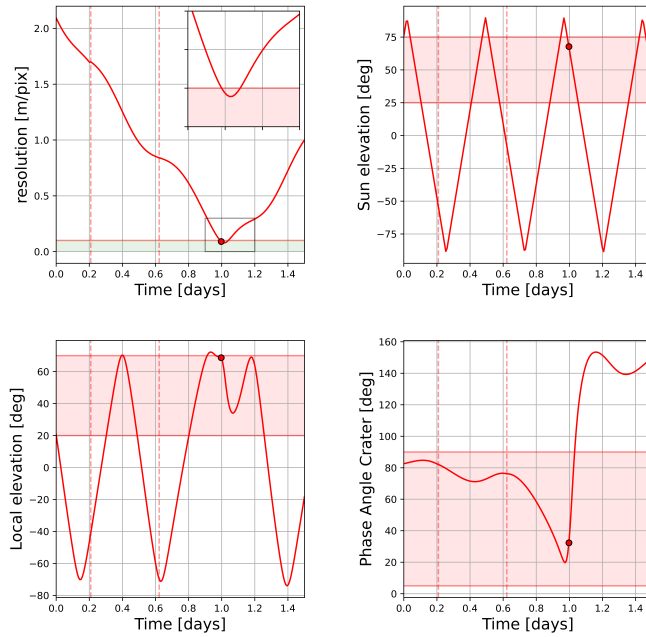
Here, the value required for  $C$  is 0.4 or above, i.e. the velocity is always 1.4 times the escape velocity. This is to ensure that if a thruster failure or missed thrust event happens, the spacecraft will escape the system on a collision free trajectory.

The trajectory design of the VCFB consists of selecting the following variables: the position of the initial open-loop point, the initial open-loop manoeuvre, the open-loop  $\Delta\mathbf{v}$  and time of the first auto-GNC point, and the open-loop  $\Delta\mathbf{v}$ , time of the second auto-GNC point. The true anomaly of Dimorphos' orbit around Didymos at the start of the VCFB, i.e. the timing of the first manoeuvre, is selected to ensure optimal C/A observation conditions, especially related to  $\epsilon_{\odot}$  as this parameter is independent of the spacecraft location, instead only relating to the true anomaly of Dimorphos at C/A.

In this work, the nominal trajectory for the VCFB is obtained semi-analytically. A two-body system is initially assumed, which allows for the use of several simple



(a) Trajectory from semi-analytic method.



(b) Observation parameters.

Figure 6.3: The semi-analytically designed nominal VCFB trajectory and its observation parameters given over time. The time of closest approach with respect to the crater is given by the black cross, and the shaded regions in the observation parameter plots are the desired constraint regions. Furthermore, the vertical dashed lines show when the periapsis lowering manoeuvres are executed.

equations to obtain the final trajectory. First, the desired sequence of pericentre radii (with respect to the system) are selected, in this case:  $r_p = \{4, 3, 1.5\}$  km. Then, for the first arc a velocity margin is also selected, which allows for the calculation of the pericentre velocity using Eq. (6.1). Using these values the semi-major axis  $a$ , eccentricity  $e$ , and semi-latus rectum  $p$  of the first arc are calculated using the vis-viva equation and other common two-body equations (see e.g. [78]). For the following arc the desired pericentre radius is taken from the previously selected sequence. Then, the corresponding velocity margin can be selected to give the desired characteristics of the following arc. However, this velocity margin cannot be freely selected as the two arcs must intersect at some point. The possible second velocity margin is found by taking a set of possible manoeuvre times  $t_{\Delta v}$ , and for each  $t_{\Delta v}$  use the following procedure to determine for what margin the arcs intersect:

1. Calculate the true anomaly of the initial arc,  $\nu_i$ , corresponding to the current  $t_{\Delta v}$ .
2. Take a possible  $C_{i+1}$ , and calculate  $a_{i+1}$ ,  $e_{i+1}$ ,  $p_{i+1}$ , and  $\nu_{i+1}$ .
3. Calculate the difference in distance:

$$\Delta r_{t_{\Delta v}} = \frac{p_i}{1 + e_i \cos \nu_i} - \frac{p_{i+1}}{1 + e_{i+1} \cos \nu_{i+1}}. \quad (6.2)$$

4. Repeat steps 2 and 3 using new guess for  $C_{i+1}$  until  $\Delta r_{t_{\Delta v}} < tol$ , where  $tol$  can be set to a desired accuracy, here taken to be  $1 \cdot 10^{-8}$ .

Solving for  $\Delta r_{t_{\Delta v}}$  in steps 2 - 4 is done using a root-finding algorithm, e.g. the Newton-Raphson method. After this procedure, the desired  $C_{i+1}$  can be obtained by selecting the corresponding  $t_{\Delta v}$  which minimizes  $\Delta r_{t_{\Delta v}}$  for that  $C_{i+1}$ . This process is repeated for all three arcs of the VCFB to obtain the trajectory for the two-body system, which is then tested in a "full" dynamical system including separate gravitational influences for Didymos and Dimorphos (where Dimorphos is moving around Didymos), and including the Solar Radiation Pressure (SRP) effect (see [79] for an overview of the relative importance of the different accelerations in the Didymos environment). The C/A timing is set such that Dimorphos is located exactly along its orbit where the

Sun elevation with respect to the crater will be 45 degrees. The resulting trajectory is shown in figure 6.3, where the evolution of the various observation parameters is also shown. It can be seen that at C/A, all the observation parameters are located within the desired bounds, and that a minimum resolution below 10 cm/pixel is achieved.

### 6.1.2 GNC System Design

The presence of dispersion in position and velocity at the initial time of the VCFB, together with imperfect manoeuvre execution, will result in the actual trajectory not following the one previously designed. If this initial dispersion is not corrected for, there is a large chance that the observation constraints will not be met, or in the worst-case scenario there will be a collision with one of the bodies. Therefore, besides the previously calculated open-loop manoeuvres that lower the periapsis distance, these manoeuvres will also correct for the off-nominal conditions using the GNC system. As these manoeuvres happen within several hours of each other, there is little time to collect sufficient observations, downlink navigation data, perform orbit determination, calculate the desired correction manoeuvre, and uplink the desired new manoeuvre. Therefore, the GNC system has to perform this process autonomously.

The two so-called auto-GNC manoeuvres now consist of three parts:

$$\Delta \mathbf{V} = \Delta \mathbf{V}_{OL} + \delta \Delta \mathbf{v} + \epsilon_{\Delta \mathbf{V}}, \quad (6.3)$$

where  $\Delta \mathbf{V}_{OL}$  is the open-loop manoeuvre calculated in section 6.1,  $\delta \Delta \mathbf{v}$  the closed-loop manoeuvre that is used to bring the true trajectory back to the nominal trajectory, and  $\epsilon_{\Delta \mathbf{V}}$  the execution error which cannot be controlled. The execution error is modelled using spherical coordinates, where there is a proportional error in the magnitude and a fixed error in the angles. For the closed-loop manoeuvre, a simple linear targeting approach is used, which calculates the manoeuvre using the linearized dynamics around the nominal trajectory given by  $\Phi$  as follows:

$$\begin{pmatrix} \delta \mathbf{r}_f \\ \delta \mathbf{v}_f \end{pmatrix} = \Phi \begin{pmatrix} \delta \mathbf{r}_0 \\ \delta \mathbf{v}_0 + \delta \Delta \mathbf{v}_0 \end{pmatrix} \quad (6.4)$$

$$= \begin{pmatrix} \Phi_{1,1} & \Phi_{1,2} \\ \Phi_{2,1} & \Phi_{2,2} \end{pmatrix} \begin{pmatrix} \delta \mathbf{r}_0 \\ \delta \mathbf{v}_0 + \delta \Delta \mathbf{v}_0 \end{pmatrix}, \quad (6.5)$$

where  $\delta \mathbf{r}$  and  $\delta \mathbf{v}$  are the differences in position and velocity with respect to the nominal values, and  $\delta \Delta \mathbf{v}_0$  is the closed-loop manoeuvre. Eq. (6.5) can then be inverted to obtain  $\delta \Delta \mathbf{v}_0$ :

$$\delta \Delta \mathbf{v}_0 = -\Phi_{1,2}^{-1} \begin{pmatrix} \Phi_{1,1} & \Phi_{1,2} \end{pmatrix} \begin{pmatrix} \delta \mathbf{r}_0 \\ \delta \mathbf{v}_0 \end{pmatrix} \quad (6.6)$$

This linear targeting controller requires an estimate of the state at the time of  $\Delta V$  execution. This estimate comes from the navigation system of Hera which uses images of Dimorphos to measure its relative state. Dimorphos is used for optical navigation as during large parts of the VCFB, Didymos will not fit within the field-of-view of the on-board camera. Observables like the centre of brightness are extracted from these images and fed into a navigation filter to obtain an estimate of the position and velocity together with their covariance, also known as the state knowledge distribution. The image processing pipeline that is used to obtain these observables is out of the scope of this work, readers are referred to [110], [184], and [185] for more in-dept information. As it is important to measure the influence of the performance of the navigation system, this work uses an analytical approximation of the evolution of the state knowledge, which is based on the actual performance of the optical navigation system. This is to reduce the complexity of the implementation and improve the numerical efficiency when implemented in a trajectory optimization context, which is discussed in more detail in section 6.2. The analytical model is given as follows:

$$\boldsymbol{\sigma}_{\tilde{\mathbf{r}}} = \begin{cases} \boldsymbol{\sigma}_{0,\tilde{\mathbf{r}}} + \boldsymbol{\epsilon}_{\Delta V} \cdot (t - t_{\Delta V}) & t < t_1 \\ (\boldsymbol{\sigma}_{0,\tilde{\mathbf{r}}} + \boldsymbol{\epsilon}_{\Delta V} \cdot (t - t_{\Delta V})) \cdot e^{-(t-t_1)/\tau} & t_1 \leq t < t_2 \\ \boldsymbol{\sigma}_{ss,\tilde{\mathbf{r}}} & t_2 \leq t \end{cases} \quad (6.7)$$

$$\sigma_{\tilde{v}} = \begin{cases} \sigma_{0,\tilde{v}} + \epsilon_{\Delta V} & t < t_1 \\ (\sigma_{0,\tilde{v}} + \epsilon_{\Delta V}) \cdot e^{-(t-t_1)/\tau} & t_1 \leq t < t_3, \\ \sigma_{ss,\tilde{v}} = \sigma_{ss,\tilde{r}}/\tau & t_3 \leq t \end{cases}, \quad (6.8)$$

where  $\sigma$  represents the standard deviations,  $\sigma_0$  the standard deviations at the start of the current arc,  $\epsilon_{\Delta V} = 2.5\% \cdot \Delta v$  the expected error in the initial manoeuvre which influences the initialization of the filter,  $t_{\Delta V}$  is the time of the initial manoeuvre,  $\tau$  the characteristic time representing the performance of the optical navigation equal to a sixth of the orbital period of Dimorphos ( $T$ ), and  $t_1 = T/10$ . The navigation reaches a steady-state error after a certain amount of time, which is calculated as follows:

$$\sigma_{ss,\tilde{r}} = \sqrt{\left(\frac{R}{5}\right)^2 + \sigma_{ephem}^2}, \quad (6.9)$$

where  $R$  is the radius of Dimorphos and  $\sigma_{ephem}$  is the error in the ephemeris of Dimorphos, estimated to be 10 meters at the time of the VCFB. The time of steady-state is then calculated by solving the following equation for time:

$$(\sigma_{0,v} + \epsilon_{\Delta V}) \cdot e^{-(t_{2/3}-t_1)/\tau} = \sigma_{ss,r/v}. \quad (6.10)$$

As Dimorphos is the target body for optical navigation, the observability of Dimorphos also needs to be taken into account. Dimorphos will not be observable during both the period of its orbit when it is in the shadow of Didymos, and when Didymos is blocking the view of Dimorphos relative to the spacecraft (occultation). During these times, the position knowledge error increase is calculated simply using:  $\sigma_{i+1} = B\sigma_i$ , where  $B = \begin{pmatrix} I_{3 \times 3} & \Delta t I_{3 \times 3} \\ I_{3 \times 3}/\Delta t & I_{3 \times 3} \end{pmatrix}$ . The evolution of the position variance for this model is shown in figure 6.4.

For the design of the VCFB trajectory, there are several sources of uncertainties and errors that need to be taken into account. First, the initial state of the spacecraft at the start of the VCFB will be uncertain due to execution errors from previous manoeuvres to get to that point. Second, the commanded  $\Delta V$  will not be exactly the same as the executed  $\Delta V$  due to imperfect pointing and thruster performance. Finally,

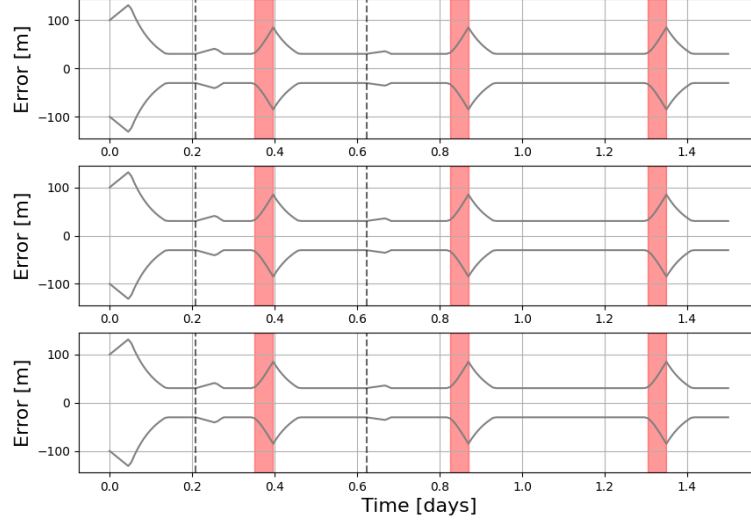


Figure 6.4: The evolution of the position knowledge variance based on the analytical model. The red areas are the blackout periods where Dimorphos is not visible.

the knowledge of the state required for the linear targeting controller is not perfect, making the executed  $\Delta V$  different from the desired one corresponding to the true state of the spacecraft. The values for these uncertainties used throughout this work are summarised in table 6.1.

Source	Magnitude ( $1\text{-}\sigma$ )
Initial position dispersion	700 m
Initial velocity dispersion	10 mm/s
Initial position knowledge	100 m
Initial velocity knowledge	0.5 mm/s
$\Delta V$ magnitude	0.33 %
$\Delta V$ angle	$1.0^\circ$

Table 6.1: Uncertainties considered for the VCFB, taken from [5].

The performance of this GNC system is simulated using a Monte Carlo (MC) method, and presented in figure 6.5. Even though the GNC system is able to reduce some of the dispersion, there is still a significant probability of impact with Didymos, i.e. roughly 3 percent, as can be seen in figure 6.5a where the impact plane, also known as the B-plane, is shown for the flyby of Didymos which occurs after the flyby

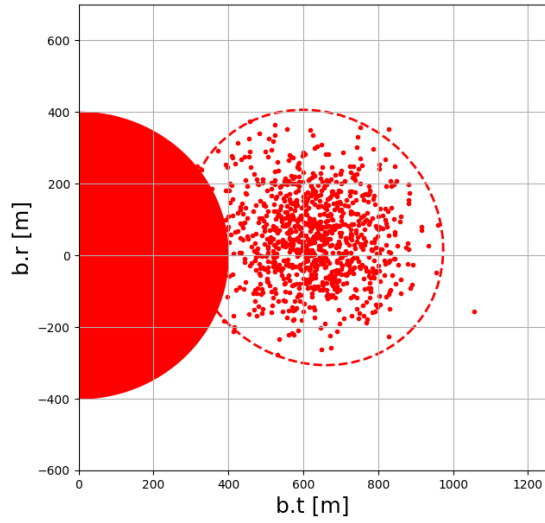
of Dimorphos. In most cases, an iterative process will be used where the MC results are used to change the semi-analytical trajectory by for example increasing the pericentre radii or changing the velocity margins. Often, the semi-analytical trajectory is numerically optimized as well using some sort of trajectory optimization scheme, with heuristically obtained constraints to improve the safety of the trajectory [64]. This decoupled method, where the nominal trajectory design is separated from the uncertainty analysis, can reduce the scientific gain of the mission, complicate the design, and as this cycle is often repeated, the development time is also significantly increased. Section 6.2 will present a novel methodology where the nominal design is combined with the uncertainty analysis.

## 6.2 Trajectory Optimization under Uncertainty

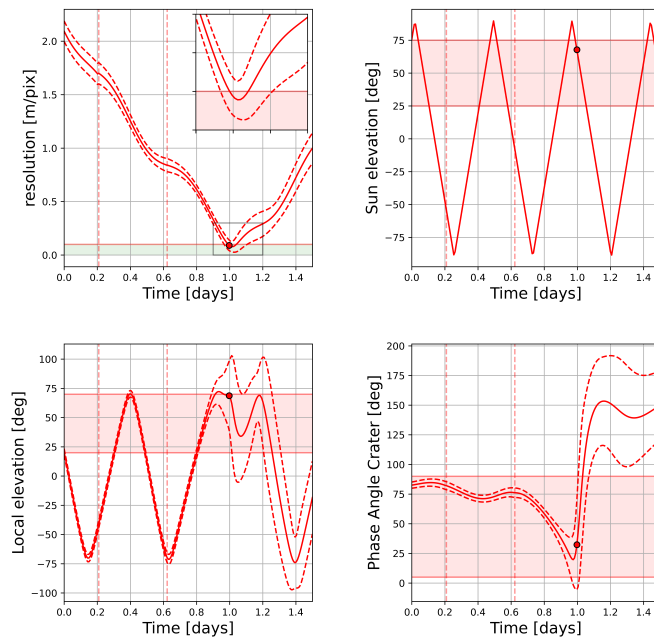
For the deterministic trajectory design case, first an optimal control problem is formulated, which is then transcribed into a non-linear programming problem, which in turn is solved using an optimization algorithm. There are several methods like multiple shooting or orthogonal collocation that are usually used for the transcription. However, to transcribe the problem considered here, other methods need to be used as both uncertainties and state measurements need to be taken into account. This work uses transcription method developed in [130], which was applied to design the Clipper flyby of Jupiter's moon Europa. However, there ground-based radiometric navigation was considered. Furthermore, a non-intrusive uncertainty propagation method was used, which can be more computationally expensive compared to intrusive methods. Thus, here this method is adapted for use with Generalised Intrusive Polynomial Algebra (GIPA) [117], and for use with autonomous optical navigation.

### 6.2.1 Problem Definition

In the deterministic case, an optimal control problem (OCP) can be formulated to obtain an optimal control law  $\mathbf{u}^*(t) \in U$ , where  $\mathbf{u}$  are the control variables and  $U$  the set of admissible control values, which minimizes the cost function  $J$  under a set of



(a) B-plane of Didymos flyby.



(b)  $3\text{-}\sigma$  evolution of observation parameters.

Figure 6.5: The results for the Monte Carlo analysis of the semi-analytically determined trajectory. The B-plane distribution for Didymos is shown on the left, where the ellipse is the  $3\text{-}\sigma$  region. And the evolution of the different observation parameter mean (solid line) and  $3\text{-}\sigma$  region (dotted lines) on the right.

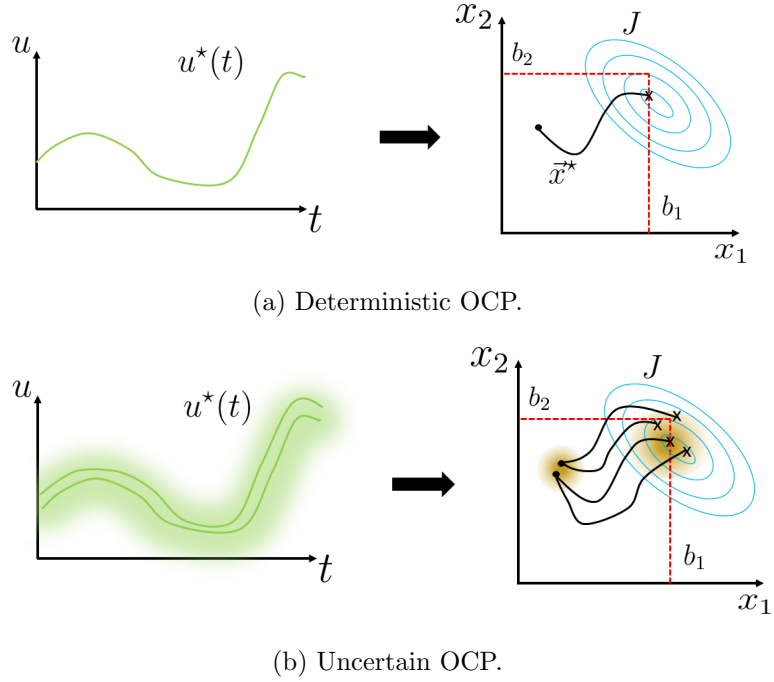


Figure 6.6: Diagram showing an example two-variable system in the case of a deterministic OCP (above) and an uncertain OCP (below). The shaded green areas represent the probability distribution of  $u^*$  and  $\mathbf{x}_0$ , and in 6.6b the solid lines represent realisations of the uncertainties.

path and boundary constraints. This can be formulated as follows:

$$\min_{\mathbf{u} \in U} J = \phi(t_0, \mathbf{x}_0, t_f, \mathbf{x}_f) + \int_{t_0}^{t_f} L(\tau, \mathbf{x}, \mathbf{u}) d\tau, \quad (6.11a)$$

$$\text{s.t. } \dot{\mathbf{x}} = f(\mathbf{x}, \mathbf{u}, \boldsymbol{\beta}, t) \quad (6.11b)$$

$$\mathbf{b}(t_0, \mathbf{x}_0, t_f, \mathbf{x}_f) \in B \quad (6.11c)$$

$$\mathbf{g}(t, \mathbf{x}, \mathbf{u}) \in G \quad (6.11d)$$

where  $\phi$  are the boundary objectives and  $L$  the path objectives,  $f(\mathbf{x}, \mathbf{u}, \boldsymbol{\beta}, t)$  are the system dynamics with  $\boldsymbol{\beta}$  a set of model parameters,  $\mathbf{b}$  are the boundary variables with constraint region  $B$ , and  $\mathbf{g}$  are the path variables with constraint region  $G$ .

If any uncertainties are introduced in  $\mathbf{x}_0$ ,  $\mathbf{u}$ , and/or  $\boldsymbol{\beta}$ , any found optimal control

law  $\mathbf{u}^*$  does not lead any more to a single trajectory  $\mathbf{x}(t)$ , but to a set of trajectories that together results in a distribution of the objective  $J$ , and constraints  $b$  and  $g$ . A simple example of this is shown in figure 6.6. For this example, a two dimensional state with a single control variable is shown, where a cost function is used that is only dependent on the final state, with a simple boundary inequality constraint:  $\{x_1(t_f) < b_1, x_1(t_f) < b_2\}$ . Figure 6.6a shows the deterministic case where an optimal control law  $\mathbf{u}^*(t)$  is found that brings the state from its initial state  $\mathbf{x}_0$  to the minimum cost function value at  $t_f$ , while abiding by the boundary constraints. However, if  $\mathbf{u}^*(t)$  and/or  $\mathbf{x}_0$  is uncertain, e.g. due to imperfect actuation and/or state estimation errors, the true control law and trajectory might differ from the desired ones, resulting in a set of possible trajectories. This case is shown in figure 6.6b, where the shaded areas are the probability distributions of the now random variables  $\mathbf{u}^*(t)$  and  $\mathbf{x}_0$ . This results in both the final cost and constraint values becoming random variables as well. Figure 6.6b shows two samples taken from both the distribution of  $\mathbf{u}^*(t)$  and  $\mathbf{x}_0$ , which result in four different trajectories with increased cost values with respect to the nominal case and possible violated constraints.

To determine an optimal control law which is robust against these uncertainties, the deterministic OCP needs to be reformulated. An uncertain parameter vector  $\boldsymbol{\xi} = [\mathbf{x}_0, \mathbf{u}]$  is defined which contains all the uncertain parameters, which has a probability distribution  $p(\boldsymbol{\xi})$  and sample space  $\Omega_{\boldsymbol{\xi}}$ . For the uncertainty propagation process it is assumed that  $\Omega_{\boldsymbol{\xi}}$  is bounded. In the case that  $\boldsymbol{\xi}$  has a probability distribution  $p(\boldsymbol{\xi})$  with infinite support,  $\Omega_{\boldsymbol{\xi}}$  can be taken such that  $\int_{\Omega_{\boldsymbol{\xi}}} \rho(\boldsymbol{\xi}) d\boldsymbol{\xi} < \varepsilon$  with  $\varepsilon$  a given percentile. Obtaining the evolution of the state probability distribution  $p(\mathbf{x}(t))$  can be a significant challenge, and becomes especially complex once the state measurement updates need to be incorporated as well [33]. Besides estimating  $p(\mathbf{x}(t))$ , the formulation of the objectives and constraints is also a non-trivial task [175]. Various statistical measures can be used for the cost function, e.g. the mean, variance, conditional value-at-risk, etc. And for the constraints either an expected value formulation or chance formulation can be used. The chance constraints can also be calculated using the expectation of the indicator function, however here these types of constraints are separated as this way of

calculating the chance constraints can create discontinuities in the gradient and in some cases other methods exist to calculate the probability [186]. This will be discussed in more detail for the specific case considered here in section 6.3. In general, the uncertain OCP can be formulated as follows:

$$\min_{\mathbf{u} \in \mathcal{U}} \mathbb{E}[\phi_J(t, \mathcal{X}, \mathcal{U}, \mathcal{B})], \quad (6.12a)$$

$$\text{s.t.} \quad \begin{cases} \dot{\mathbf{X}} = f(\mathbf{X}, \mathbf{U}, \mathcal{B}, t) \\ \mathcal{X}^+ = H(\mathcal{X}^-, t) \end{cases} \quad (6.12b)$$

$$\mathbb{E}[\phi_{\mathbf{b}}(t_0, \mathcal{X}_0, t_f, \mathcal{X}_f)] \in B \quad (6.12c)$$

$$\mathbb{E}[\phi_{\mathbf{g}}(t, \mathcal{X}, \mathcal{U})] \in G \quad (6.12d)$$

$$Pr[\mathbf{b}(t_0, \mathcal{X}_0, t_f, \mathcal{X}_f) \in B] < \epsilon_b \quad (6.12e)$$

$$Pr[\mathbf{g}(t, \mathcal{X}, \mathcal{U}) \in G] < \epsilon_g \quad (6.12f)$$

where the capital letters  $\mathcal{X}$ ,  $\mathcal{U}$ , and  $\mathcal{B}$  are the uncertain variables corresponding to  $\mathbf{x}$ ,  $\mathbf{u}$ , and  $\boldsymbol{\beta}$  respectively. Besides the uncertain dynamics equation for  $\dot{\mathbf{X}}$  in Eq. (6.12b), the measurement update equation  $H$  is also present for the uncertain case. Furthermore,  $\phi$  here represents the specific statistical function used, e.g. for the mean cost  $\phi_J = J$  which leads to  $\mathbb{E}[\phi_J] = \mathbb{E}[J] = \bar{J}$ , and for the variance  $\phi_J = (J - \bar{J})(J - \bar{J})$ . The expectation operator  $\mathbb{E}$  itself is defined as follows (where  $Z$  is a generic random variable):

$$\mathbb{E}[\phi(Z)] = \int_{\Omega_{\xi}} \phi(\boldsymbol{\xi}) p(\boldsymbol{\xi}) d\boldsymbol{\xi} \quad (6.13)$$

Finally,  $Pr$  is the probability operator, where  $\epsilon$  represents the desired percentile. As there are many types of problems where the chance of a certain event happening needs to be constrained, this type of trajectory optimization problem is also known as a chance-constrained problem [175].

As in most cases this problem can only be solved numerically, the following sections

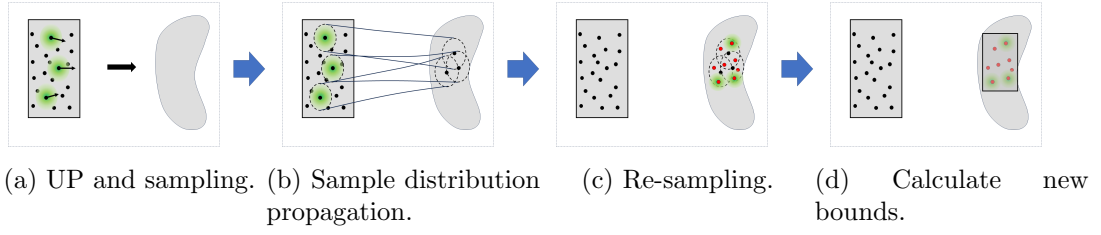


Figure 6.7: The different steps that are performed at each segments to solve the UOCP. In figure 6.7a and 6.7c a large number of samples are shown, however the knowledge distribution and its propagation is only shown for a subset of points for clarity. Thus, it is important to keep in mind that these steps are performed for all points.

will go over this process in more depth.

### 6.2.2 Transcription Method

Similar to a multiple shooting scheme used to solve a deterministic OCP, for solving the UOCP of Eqs. (6.12a) - (6.12f), the trajectory will be discretised into several segments. As in the case considered here the control consists of impulsive manoeuvres:

$$\mathbf{u}(t) = \sum_{i=0}^{N_{\Delta v}} \delta(t - t_i) \Delta \mathbf{v}_i, \quad (6.14)$$

the trajectory is discretised into the various segments between control points. In [130], specific segments for the ground-based observation windows were considered. However, the autonomous navigation system considered in this work is constantly running, even during blackout periods where the knowledge is decreasing. Thus, only the impulsive segments are considered, requiring the optimizer to find the optimal timing of the manoeuvres considering the evolution of the state knowledge during each segment.

For the VCFB, there are three distinct segments of the trajectory, which begin and end with an impulsive manoeuvre. For the transcription of the UOCP, there are several steps that are in general repeated for each segment. The general process is shown in figure 6.7. The process starts with taking the state dispersion of the previous segment, or if it is the initial segment, the initial dispersion of the state, which is represented by the grey rectangle in figure 6.7a. Then, using GIPA, this dispersion is propagated from the start time of the segment  $t_i$  until the end time  $t_{i+1}$ , which provides a polynomial

model  $P_{n,d}(\boldsymbol{\xi})$  for efficiently propagating any realisation of the uncertainty vector  $\boldsymbol{\xi}$  at time  $t_i$ .

Once the polynomial model is generated, a set of  $M$  sample state observations are taken from  $\Omega_{\boldsymbol{\xi}}$ , denoted by  $y_i^k$ , where  $k = 1, \dots, M$ , which are represented by the black dots in figure 6.7a. Each of these observation samples have an associated knowledge distribution, given by:

$$\mathcal{X}_i^k = p(\mathbf{x}_i | \mathbf{y}_{1:i}^k), \quad (6.15)$$

which are represented by the green areas around the observations in figure 6.7.

For each  $\mathcal{X}_i^k$ , a  $\Delta \mathbf{v}$  is calculated, which can either consist of the execution error component and either only the open-loop component, or of both open- and closed-loop components. In the latter case, the closed-loop  $\Delta \mathbf{v}$  is calculated based on the mean state observation value. Each knowledge distribution  $\mathcal{X}_i^k$ , which can now be seen as a dispersion for which the  $\Delta \mathbf{v}$  is applied to the whole distribution, is propagated to  $t_{i+1}$ . This process is shown in figure 6.7b. For a generic type of distribution, there are several different types of methods that can be used to propagate the distribution, e.g. importance sampling [130]. However, here it is assumed that these distributions are Gaussian, and can hence be characterised by their first two moments: the mean  $\boldsymbol{\mu}$  and covariance  $\boldsymbol{\Sigma}$ . After propagation, this distribution might not be Gaussian anymore as non-linear effects can change the nature of the distribution [115]. However, as is done with most types of filters like the Extended and Unscented Kalman filter, it is assumed that the propagated distribution can be sufficiently characterised using just the first two moments.

The propagation of Normally distributed variables in general requires integrating the following types of equation:

$$\mathbb{E}[f(\mathbf{x})] = 1/\sqrt{\pi^d |\boldsymbol{\Sigma}|} \int_{-\infty}^{\infty} e^{-\frac{1}{2}(\mathbf{x}-\boldsymbol{\mu})^T \boldsymbol{\Sigma}^{-1}(\mathbf{x}-\boldsymbol{\mu})} f(\mathbf{x}) d\mathbf{x}. \quad (6.16)$$

These integrals can be solved numerically using Gauss-Hermite quadrature and a change of variables ( $\mathbf{x} = \sqrt{2}L\mathbf{y} + \boldsymbol{\mu}$ , where  $\boldsymbol{\Sigma} = LL^T$  and  $L$  is determined using Cholesky

decomposition), as follows [143]:

$$\mathbb{E}[f(\mathbf{x})] = 1/\sqrt{\pi^d} \int_{-\infty}^{\infty} e^{-\mathbf{y}^T \mathbf{y}} f(\sqrt{2}L\mathbf{y} + \boldsymbol{\mu}) d\mathbf{y} \quad (6.17)$$

$$\approx \sum_{j=0}^N \frac{w_j}{\sqrt{\pi^d}} f(\sqrt{2}L\boldsymbol{\zeta}_j + \boldsymbol{\mu}), \quad (6.18)$$

where  $w_j$  are the Gauss-Hermite quadrature weights and  $\boldsymbol{\zeta}_j$  the roots of the Hermite polynomial. The accuracy of the integration can be tuned by increasing the number of quadrature points. For our purpose of propagating a Gaussian distribution, i.e.  $\mathcal{X}_i^k$ , from time  $t_i$  to  $t_{i+1}$ , a large number of quadrature samples would need to be numerically integrated. However, as a polynomial approximation is used, instead of a numerical integration only a polynomial evaluation is needed for each quadrature point, significantly reducing the computation time. In this sense, the mean of the distribution at time  $t_{i+1}$  can be calculated as follows:

$$\mu_{\mathcal{X}_{i+1}}^k \approx \sum_{j=0}^N \frac{w_j^k}{\sqrt{\pi^d}} \tilde{\Omega}_{x_{i+1}} \left( \sqrt{2}L_{x_i} \boldsymbol{\zeta}_j^k + \boldsymbol{\mu}_{x_i} \right), \quad (6.19)$$

and the covariance using:

$$\Sigma_{\mathcal{X}_{i+1}}^k \approx \sum_{j=0}^N \frac{w_j^k}{\sqrt{\pi^d}} \left[ \tilde{\Omega}_{x_{i+1}} \left( \sqrt{2}L_{x_i} \boldsymbol{\zeta}_j^k + \boldsymbol{\mu}_{x_i} \right) - \mu_{\mathcal{X}_{i+1}}^k \right] \cdot \left[ \tilde{\Omega}_{x_{i+1}} \left( \sqrt{2}L_{x_i} \boldsymbol{\zeta}_j^k + \boldsymbol{\mu}_{x_i} \right) - \mu_{\mathcal{X}_{i+1}}^k \right]^T. \quad (6.20)$$

Normally, the multivariate quadrature points are constructed as a Cartesian products of univariate ones. This method suffers from the curse of dimensionality in  $d$ , thus here a another sampling approach is used, called a Smolyak sparse grid. The Smolyak sparse grid was developed in [131], and selects a set of points based on the extrema of Chebyshev polynomials. An important aspect is that they do not suffer the curse of dimensionality, as the number of points grow polynomially with the dimension of the problem instead of exponentially. A more in depth explanation of this method for uncertainty propagation is given in [126].

Once the distributions at time  $t_{k+1}$  are available, it is possible to update these

distributions with the navigation solution, obtaining the final updated distributions for the next segment. However, this can lead to an exponential increase of sample points as for the next segment  $M$  new observations would need to be sampled from each individual propagated distribution, increasing the amount of trajectories, navigation solutions, and control laws calculated significantly over time. Hence, a step needs to be incorporated which combines the different distributions at time  $t_{i+1}$ . This is performed by combining the different  $\mathcal{X}_{i+1}^k$  into a Gaussian Mixture Model (GMM), given by:

$$\mathcal{X}_{i+1}^- = \sum_{k=1}^M b^k \mathcal{X}_{i+1}^k = \sum_{k=1}^M b^k \mathcal{N}(\mathbf{x}_{k+1} | \mu_{\mathcal{X}_{i+1}}^k, \Sigma_{\mathcal{X}_{i+1}}^k), \quad (6.21)$$

$$\sum_{k=1}^M b^k = 1 \quad (6.22)$$

where  $b^k$  are the mixture weights, and  $\mathcal{N}$  represents a single Gaussian distribution. This distribution can then be re-sampled to obtain  $M$  new observation samples at time  $t_{i+1}$ , for which the covariance is obtained through the navigation process simulated from time  $t_i$  to  $t_{i+1}$ . If the full measurement and filtering process needs to be simulated, before sampling the GMM from Eq. (6.21) the individual knowledge distribution can be updated using the simulated measurements and the corresponding calculated Kalman gain [130]. This increases the fidelity of the navigation simulation, but also decreases the efficiency of the method. Therefore, it is left for future work. The re-initialisation process is shown in figure 6.7c. The expected value of any function, e.g. the objectives and constraints can also be calculated from the GMM, using the quadrature rule from Eq. (6.18):

$$\mathbb{E}[f(\mathbf{x}_i) | \mathbf{y}_{1:i}] = \sum_{k=1}^M b^k \sum_{j=0}^N \frac{w_j^k}{\sqrt{\pi^d}} f(\sqrt{2}L^k \boldsymbol{\zeta}_j^k + \boldsymbol{\mu}^k). \quad (6.23)$$

The final step of the transcription is to calculate the initial manoeuvre for the next segment for each individual sample. Then, using the sample state observations, their distribution, and their respective  $\Delta \mathbf{v}$  manoeuvre, the new state and manoeuvre bounds are calculated and the polynomial for the following section is re-initialized using those

bounds. This process is shown in figure 6.7d. The next segment uses the samples and manoeuvres calculated during this final step of the current segment, to start the process again for the following segment. This re-initialization process is similar to what is done in [173], and guarantees continuity between the segments, which for normal multiple shooting schemes needs to be added as a constraint.

### 6.3 Results

A combined trajectory design and navigation analysis can now be performed for the Hera VCFB, where probabilistic objectives and constraints are included. The GNC system discussed in section 6.1.2 is modelled, and the nominal semi-analytic trajectory from section 6.1 is used as an initial guess and comparison with respect to the trajectory found using the methods discussed in section 6.2. The uncertainties shown in table 6.1 are used within the optimization process as well.

The final NLP problem for this trajectory is given as follows:

$$\min_{\mathbf{u} \in \mathcal{U}} \mathbb{E}[r(t_{C/A,dim})], \quad (6.24a)$$

$$\text{s.t.} \quad \begin{cases} \mathcal{X}_{i+1}^- = F(\mathcal{X}_i, \mathbf{u}_i) \\ \mathcal{X}_{i+1}^+ = H(\mathcal{X}_{i+1}^-) \end{cases}, i = \{0, 1, 2\} \quad (6.24b)$$

$$Pr[\mathbf{x}(t_{C/A,dim}) \in B_{dim}] < 0.1\% \quad (6.24c)$$

$$Pr[\mathbf{x}(t_{C/A,did}) \in B_{did}] < 0.1\% \quad (6.24d)$$

$$\mathbb{E}[C_{marg}(\mathbf{x}, t)] > 0.4 \quad (6.24e)$$

$$\mathbb{E}[\boldsymbol{\theta}(t_{C/A,dim})] \in \Theta \quad (6.24f)$$

The objective is the expected value of the flyby altitude of Dimorphos, as the goal of the EXP phase is to have high resolution images of the DART crater. The dynamics equation, Eq. (6.24b), consists of both the creation of the polynomial model of Eq. (3.4) using GIPA, and its use to propagate the distributions  $\mathcal{X}_i$  and create the GMM

$\mathcal{X}_{i+1}^-$  of Eq. (6.21).

The chance constraints (6.24c) and (6.24d) are referring to the probability of impact with either one of the bodies, where here  $B$  represents the space occupied by either Didymos or Dimorphos. As mentioned before, the calculation done in Eq. (6.23) can also give the probability of an event by having  $f = \mathbb{1}_A$ , where  $\mathbb{1}_A$  is the indicator function, given by:

$$\mathbb{1}_A(\mathbf{x}) = \begin{cases} 1 & \text{if } \mathbf{x} \in A \\ 0 & \text{otherwise} \end{cases} \quad (6.25)$$

The probability is then calculated by:  $Pr(\mathbf{x} \in A) = \mathbb{E}[\mathbb{1}_A(\mathbf{x})]$ . The problem with this formulation is that the indicator function is discontinuous, and thus for use in a gradient based solver it needs to be smoothed, which decreases its accuracy. For the case here, another approach is used. First, the first two moments of the uncertain height at  $C/A$ ,  $\mathcal{H}_{C/A}$ , are calculated using Eq. (6.23) with for the mean  $f(\mathbf{x}) = h(\mathbf{x}) = \sqrt{x^2 + y^2 + z^2}$ , and for the variance  $f(\mathbf{x}) = (h(\mathbf{x}) - \bar{h})^2$ . This is done for each observation to create  $M$  height distributions  $\mathcal{H}^k$ . Then, it can be observed that the GMM of Eq. (6.21) can also give the mixture model for the cumulative distribution function (CDF)  $\Phi$  by replacing  $\mathcal{N}^k$  with the CDF of each observation:

$$\Phi_{\mathcal{H}}(h) = \sum_{k=1}^M b^k \Phi(h | \mu_{\mathcal{H}}^k, \sigma_{\mathcal{H}}^k). \quad (6.26)$$

Then, the probability of impact can be formulated as:

$$Pr(h(t_{C/A}) < r_b) = \Phi_{\mathcal{H}}(r_b). \quad (6.27)$$

The two expectation constraints pertain to the velocity margin constraints, (6.24e), and the observation angles of figure 6.2, which are combined into a single vector  $\boldsymbol{\theta} = [\phi, \epsilon_{s/c}, \epsilon_{\odot}]$  in constraint (6.24f), with  $\Theta$  the desired observation values.

The NLP problem of (6.24) is solved here using the IPOPT algorithm [187]. At each iteration the same number of samples are used, and throughout the optimization process their spacing within the bounds are kept constant in order to remove sampling

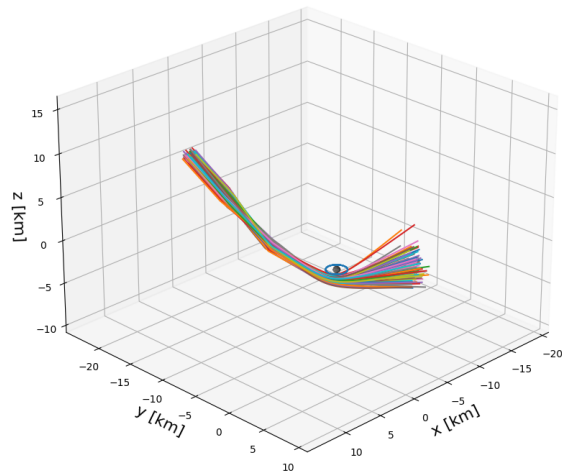
based changes in the objective and constraint values when calculating the gradient. The UP step is done using a Taylor polynomial basis with degree 3.

### 6.3.1 Optimised Trajectory

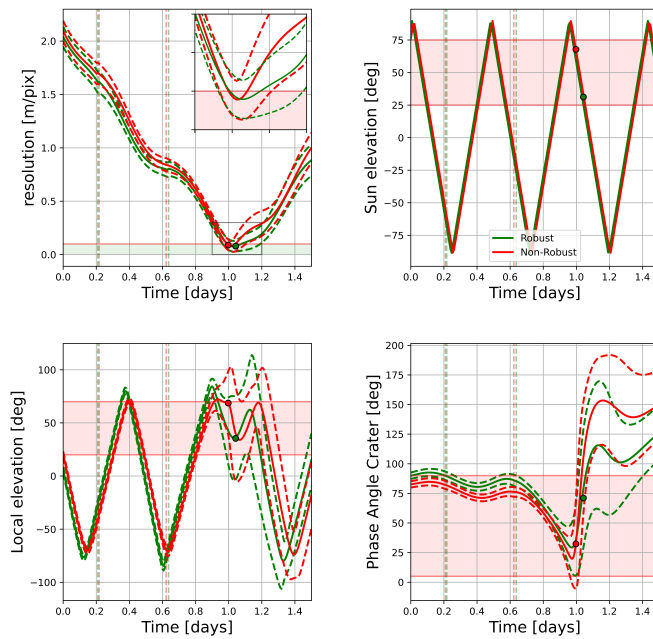
The resulting trajectory found by IPOPT is shown in figure 6.8, where a MC analysis was performed using 1000 samples. The original semi-analytical trajectory, which will be called the non-robust trajectory here, is also shown as a reference. It can be seen that the mean crater C/A distance, i.e. obtained resolution, of both the robust and non-robust method is similar. Hence, to increase the robustness of the trajectory does not necessarily result in a decrease in performance. Furthermore, the observation parameters all fall well into the requirement region resulting in good expected performance with respect to observation.

The main problem found with the original semi-analytic, non-robust, trajectory is the high probability of impact (PoI) with Didymos. The found trajectory significantly reduces this probability as can be seen in figure 6.9, where the b-plane parameters of both the non-robust and robust method are shown. The confidence region of the robust solution does not intersect the red region, representing Didymos, suggesting a very low PoI. This is achieved by having a slacker trajectory entering the C/A of the crater. As can be seen in the resolution in figure 6.8b, after C/A of the crater the resolution remains lower for longer periods of time. This results in a trajectory which does not immediately turn towards Didymos and thus decreases the PoI.

Finally, the most important performance indicator of the trajectory is the time spent during the trajectory in good observation conditions, which are defined here according to the requirements stated in section 6.1. The distribution of these times for both trajectories is shown in figure 6.10, where it can be clearly seen that the robust trajectory has much better performance. The robust solution averages about 1.5 hours with cases of up to roughly 3 hours, where the non-robust trajectory only goes to around 0.5 - 0.75 hours on average. This increase in performance comes from both the slacker trajectory as mentioned before, and from considering the distribution of observation angles inside the optimization problem.



(a) Trajectory from uncertain optimization method.



(b) Observation parameters.

Figure 6.8: The trajectory obtained from the uncertain optimization procedure, for which the NLP is given by (6.24). The MC results for this trajectory in Cartesian space is given on the left and the observation parameter mean and  $3\text{-}\sigma$  regions are given on the right.

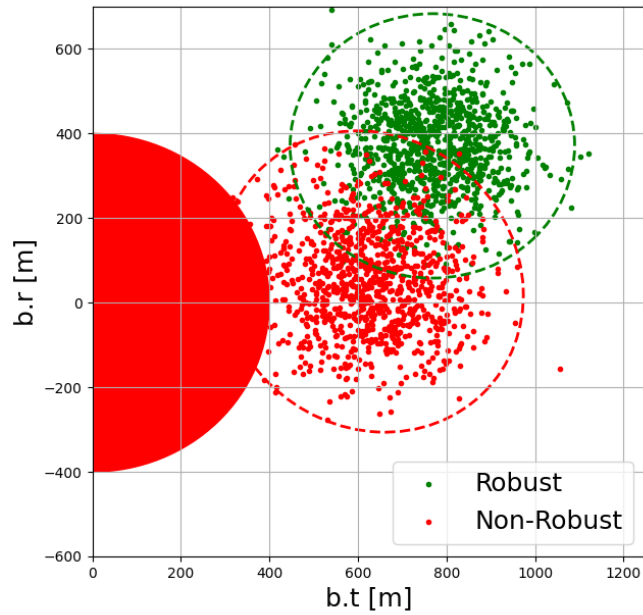


Figure 6.9: The B-plane distribution of both the semi-analytical and robust trajectory for the Didymos flyby section.

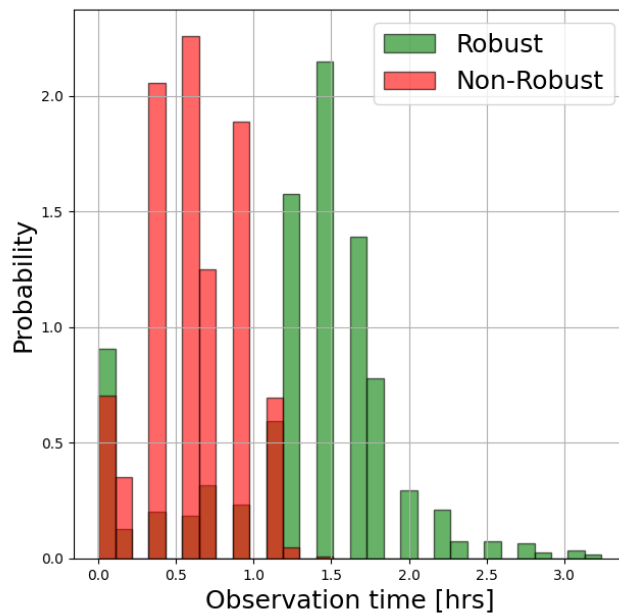


Figure 6.10: The distribution of observation times, which is defined to be the time spent within the observation parameter requirements, including resolutions higher than 10 cm/pixel.

## 6.4 Chapter Summary

In this chapter the trajectory design of the experimental phase (EXP) of Hera is performed. For this phase, a very-close flyby of Dimorphos needs to happen to image the crater with high levels of details, leading to stringent requirements on both observation conditions and safety. Using the conventional method of designing a nominal trajectory without considering uncertainty and GNC performance, however the trajectory was also shown to have a high probability of impact.

To solve this, a novel method based on uncertainty propagation using Generalised Intrusive Polynomial Algebra (GIPA) combined with knowledge distribution propagation is derived. This method is able to performance trajectory optimization considering chance-based and expectation-based constraints, while also taking into account the performance of the GNC system.

A novel trajectory is found with a significantly reduced probability of impact and equal, even in some cases improved, performance. These results show the need to taken uncertainties into account, and how this is done for a real-life scenario.

# Chapter 7

## Conclusion

In the introduction of this thesis, an overall thesis statement was made and several objectives were formulated which in turn can support this statement if fulfilled. In this chapter, using these objectives a summary is made of the work in this thesis, and the contributions of that work towards the objectives are highlighted. Then, the limitations of this thesis are addressed and recommendations on future work are given that could improve the findings in this thesis.

### 7.1 Summary and Contributions

The different objectives formulated in section 1.3.2 are repeated here for convenience. For each objective a summary is given of the work done and the main findings are presented.

**Objective 1: Determine the applicability and efficiency of different uncertainty propagation techniques for trajectories around a binary asteroid, and develop an indicator that can be used to quantify the sensitivity of a trajectory to the uncertainties present in the system.**

In chapter 3, the Generalised Intrusive Polynomial Algebra (GIPA) method for uncertainty propagation was introduced and applied to orbital motion around binary asteroid system Didymos. It was found that a Chebyshev basis performed better with respect to a Taylor basis for larger uncertainties. However, in highly eccentric cases the

Chebyshev basis showed some numerical problems, leading to divergence. For the case of landing on either of the bodies, the non-intrusive Chebyshev interpolation (NCI) method was tested, which handled the discontinuous dynamics well when using a sparse sampling method.

Additionally, two novel dynamics indicators were introduced, named the variance indicator  $\eta_\sigma$  and the  $n+1$  indicator  $\eta_{n+1}$  (defined in Eqs. (3.32) and (3.42) respectively). The theory and motivation behind them is discussed in depth in section 3.2.1. Then, in chapter 4, they were combined with the GIPA method to study the motion around a binary asteroid system under uncertainty in model parameters and initial conditions.

It was shown how to use these indicators to create a map, in phase space, of the evolution of ensembles of trajectories starting from the same initial conditions.

The  $\eta_{n+1}$  indicator was shown to provide slightly different results compared to the  $\eta_\sigma$  indicator. It was found that the  $\eta_{n+1}$  is more sensitive to the deformation of the set of propagated states rather than the diffusion of the ensemble of trajectories. This was confirmed by observing the differences between the polynomial coefficient values of different sample trajectories. On the other hand, the  $\eta_\sigma$  is more geared, by its own nature, towards capturing the diffusion of the ensemble regardless of the non-linearities.

Compared to deterministic indicators, the  $\eta_\sigma$  and  $\eta_{n+1}$  indicators allow one to directly quantify the effect of parametric uncertainties in the dynamical system without the need of a Monte Carlo analysis for the variation of deterministic indicators. Since in many real world applications, the parameters of the dynamical model are not completely known a priori, the  $\eta_\sigma$  and  $\eta_{n+1}$  indicators can give a better understanding of the effect of the uncertainty on the evolution of the dynamics.

When the two indicators were applied to the dynamics around Didymos, several regions of robust motion were found, both for the inner region of the system and for motions around the two bodies. These regions of low diffusion and non-linearity are less sensitive to parametric uncertainties. Therefore, under the assumption that the dynamical model used in this work is only affected by parametric uncertainty in the mass of the two primaries, a trajectory that starts from these regions would be less affected by differences in the masses of the two bodies compared to others.

In conclusion, this research demonstrates that the two defined indicators are capable of detecting regions of diffusion and non-linearity around binary asteroid system Didymos considering model uncertainties.

**Objective 2: Use the previously developed indicators to determine robust stable orbits around the asteroid system considering the full dynamical model.**

Chapter 4, also showed a novel method of determining the robust stability of orbital motion. This was more broadly applied to study the dynamics under uncertainties of a spacecraft around the Didymos system.

Using the variance and  $n + 1$  indicators, it is shown that the terminator and close retrograde orbits show robust stable behaviour. This corresponds with previous results (e.g. [148]) which also found that these types of orbits are stable. This verifies the ability of the indicators to find robust stable orbits, and thus allows for the further study of other features of the uncertain dynamics. When the motion is close to the body, the stability of the terminator orbit is not guaranteed as the dynamical structure becomes more complex due to the effect of the non-spherical gravity, the uncertainties in  $C_{20}$  and  $C_{22}$ , and the presence of resonances with Dimorphos' orbit. Furthermore, slightly eccentric terminator orbits show stable behaviour for higher semi-major axes (corresponding to previous analytical predictions [76]), but the range of stable eccentricities decrease if the semi-major axis decreases. Finally, several different stable regions besides the terminator plane were found when changing the ascending node and inclination, allowing for different options when the terminator orbit is not desirable.

Additionally, the performance of certain orbits in terms of the observability of Dimorphos are analysed. It is found that in general the stable regions show smaller bounds for the observability, minimizing the worst case scenario but also not allowing the maximum observability to become larger compared to other initial conditions. This is especially the case for the terminator orbits, showing less favourable geometry for the maximum observability.

This study thus shows that the robust stability of the orbital motion around Didymos can be analysed using the uncertain dynamics indicators developed in this thesis,

considering the full, complex, dynamical model of the system. Using GIPA it is also shown that other parameters, like the observability of Dimorphos, can also be analysed efficiently.

**Objective 3: Design ballistic landing trajectories on an asteroid that are reliable and have low sensitivity to uncertainties in both the landing conditions and deployment execution.**

Chapter 5 introduces a novel methodology for the design and analysis of ballistic landing trajectories on the secondary of Didymos, i.e. Dimorphos. The methodology shows how efficient uncertainty propagation and quantification tools, specifically Non-Intrusive Chebyshev Interpolation (NCI) and the pseudo-diffusion indicator, can be used to analyse the uncertain dynamics and design a robust landing trajectory.

It was shown how the pseudo-diffusion indicator can be used to determine constraints on the landing geometry and touchdown velocity that ensure high probability of the spacecraft settling on the surface of the asteroid. For the model where a smooth surface of the asteroid was assumed, a maximum touchdown velocity of 10 cm/s was found and a maximum impact angle of 20 degrees. As the touchdown velocity decreases, the maximum allowable impact angle also increases, where for around 6 cm/s almost all impact angles result in settling on the surface. A transition region also appears for touchdown velocities between 10 and 6 cm/s and high impact angles, where part of the trajectories settle on Dimorphos' surface and part go into an orbit around the system. When the dynamics are altered to model surface features like rocks and craters using a stochastic perturbation on the local surface normal, the dependency on the impact angle is less significant and the maximum touchdown velocity decreases to around 8 cm/s.

Using a NCI based bisection method, it was then found that if a landing location in the DART crater hemisphere is considered with a deployment point 2 km away from the system, the necessary minimum touchdown velocity would be much higher than what is required for settling on the surface. Thus an extra braking manoeuvre is needed along the trajectory to reduce the touchdown velocity.

The deployment  $\Delta v$ , braking  $\Delta v$ , and time of the braking  $\Delta v$  were then determined

using a novel method which incorporates the NCI uncertainty propagation method into the trajectory optimization transcription. This method was able to find a trajectory which increase the landing success percentage from 74.3% to 94.7% compared to a trajectory designed without considering the uncertainties. Furthermore, the landing footprint on Dimorphos was also significantly reduced together with lowering the mean touchdown velocity. This comes at the cost of increasing the mean impact angle and moving the mean landing longitude away from the desired location. However, even with these changes the robust trajectory was found to be much more desirable.

These results show the potential of this methodology for the design of a ballistic landing on Dimorphos. The increased knowledge about the uncertain and stochastic dynamics gained through the NCI and pseudo-diffusion indicator techniques increase the robustness and performance of these types of missions and thus it is important to use them in the mission design process.

**Objective 4: Develop a method to combine the navigation analysis and nominal trajectory design to obtain robust trajectories for the very close flyby of an asteroid.**

Chapter 6 shows that a polynomial surrogate model of the uncertain dynamics, generated by the GIPA method, can be used in the context of uncertain optimal control problems to perform combined trajectory design and navigation analysis. The specific method discussed is able to find trajectories that optimally consider the uncertainties stemming from the GNC system and thus generate a robust, high performance, trajectory.

The EXP phase of Hera is considered, where first a nominal trajectory is constructed based on a two-body approximation. An autonomous GNC system was also developed and implemented to correct for the off-nominal conditions. A navigation analysis is performed for this trajectory, which shows that even though the scientific objectives are met, the probability of impact is significantly high, which renders this trajectory infeasible.

A methodology is discussed in Chapter 6 that is able to immediately take into account the uncertainties and GNC performance, and subsequently is able to consider

chance-constrained problems, like the one presented here. Using this method, a new trajectory is found that is able to both improve upon the performance of the original trajectory, as the time in favourable observation conditions is increased, and reduce the probability of impact to much more desirable values below 0.1%.

This thus shows that this methodology can produce effective and risk-reduced trajectories, which are produced with the performance of the autonomous GNC system in mind.

## 7.2 Limitations and Future Work

**Investigate more in-depth the numerical issues found for the Chebyshev basis.**

Chapter 3 showed the potential of using GIPA with a Chebyshev basis, as the uniform convergence property overcomes some of the Taylor basis' shortcomings. However, its numerical issues and slightly worse runtime led to the selection of a Taylor basis for large parts of the results. Future research should focus on the Chebyshev basis and how it can be adapted to improve efficiency and numerical performance. On-going research is focusing on how changing the state-representation can already overcome some of these issues, e.g. [134].

**Add more test cases for the uncertain dynamics indicators regarding stochastic forces.**

In testing GIPA and the uncertain dynamics indicators, the main focus was on parametric uncertainties as this allows for less complex test cases to show the applicability and performance of the indicators. The use of these indicators in case of stochastic forces was then introduced for the surface motion after landing in 5. Stochastic dynamics are important cases for the uncertain dynamics indicators, as it is not possible to use variational based chaos indicators for these systems. As there are several cases where stochastic forces are encountered in spaceflight dynamics, this should be explored more in future work. The stochastic coupling between SRP and rotational state, translational components of de-saturation manoeuvres, impacts due to clouds of asteroid ejecta and/or space debris, and unmodelled accelerations are all important dynamical

components and cannot currently be used within the framework of deterministic indicators. Hence, analysing these models using uncertain dynamics indicators can be beneficial.

**Determine the applicability of these methods to autonomous mission architectures.**

Section 1.3.2 mentioned that both robust mission design and autonomy are solutions for the problems currently found with mission performance under large uncertainties. The largest potential gains can be found when combining these two techniques. This requires both the application of these uncertainty propagation techniques on-board the spacecraft [188], and investigating the different ways these techniques can be used to improve the robustness of autonomous systems.

**Implement higher fidelity models of the autonomous GNC system.**

Chapter 6 introduced a technique that allows for the incorporation of a navigation system inside the trajectory optimization process. An analytical model of the optical navigation was used for efficiency reasons. Incorporating the simulation of optical measurements and the state estimation filter would increase the fidelity and improve the final performance of the found trajectory. Thus, this is an important point for future research.

**Incorporate both aleatoric and epistemic uncertainties.**

Epistemic uncertainties were not considered in this thesis, as additional methods would need to be developed. However, it is of importance that these types of uncertainties are also considered in the UP process as they represent an important class of uncertainties that affect space missions. GIPA and NCI have been shown to lend themselves well to the incorporation of epistemic uncertainties in [173] and [130]. Thus, future research should focus on incorporating this to the uncertain dynamics indicators developed here.

# Bibliography

- [1] I de Pater and J J. Lissauer. *Planetary Sciences*. Cambridge University Press, 2010.
- [2] Patrick Michel, Michael Küppers, Adriano Campo Bagatin, Benoit Carry, Sébastien Charnoz, et al. The ESA Hera Mission: Detailed Characterization of the DART Impact Outcome and of the Binary Asteroid (65803) Didymos. *The Planetary Science Journal*, 3(7):160, 7 2022.
- [3] Hera Didymos Reference Model Issue 5. Technical report, ESA, 2020.
- [4] Andrew F. Cheng, Harrison F. Agrusa, Brent W. Barbee, Alex J. Meyer, Tony L. Farnham, et al. Momentum transfer from the DART mission kinetic impact on asteroid Dimorphos. *Nature*, 616(7957):457–460, 3 2023.
- [5] HERA: Proximity Operations Guidelines Issue 6 Rev 3. Technical report, European Space Agency, Noordwijk, The Netherlands, 2020.
- [6] Patrick Michel, Michael Küppers, and Hera Investigation Team. The science return of the ESA Hera mission to the binary asteroid Didymos. *43rd COSPAR Scientific Assembly*, 43:275, 2 2021.
- [7] Yasuhiro Oba, Yoshinori Takano, Jason P. Dworkin, and Hiroshi Naraoka. Ryugu asteroid sample return provides a natural laboratory for primordial chemical evolution. *Nature Communications 2023 14:1*, 14(1):1–5, 5 2023.

## Bibliography

- [8] Peter Schulte, Laia Alegret, Ignacio Arenillas, José A. Arz, Penny J. Barton, et al. The chicxulub asteroid impact and mass extinction at the cretaceous-paleogene boundary. *Science*, 327(5970):1214–1218, 3 2010.
- [9] M. Pajola, O. S. Barnouin, A. Lucchetti, M. Hirabayashi, R.-L. Ballouz, et al. Anticipated Geological Assessment of the (65803) Didymos–Dimorphos System, Target of the DART–LICIACube Mission. *The Planetary Science Journal*, 3(9):210, 9 2022.
- [10] Andreas M. Hein, Robert Matheson, and Dan Fries. A Techno-Economic Analysis of Asteroid Mining. *Acta Astronautica*, 168:104–115, 10 2018.
- [11] Kevin J. Walsh. Rubble Pile Asteroids. *Annual Review of Astronomy and Astrophysics*, 56:593–624, 9 2018.
- [12] Fred Jourdan, Nicholas E. Timms, Tomoki Nakamura, William D.A. Rickard, Celia Mayers, et al. Rubble pile asteroids are forever. *Proceedings of the National Academy of Sciences of the United States of America*, 120(5):e2214353120, 1 2023.
- [13] F. Ferrari and E. M. Alessi. A new method for identifying dynamical transitions in rubble-pile asteroid scenarios. *Astronomy & Astrophysics*, 672:A35, 4 2023.
- [14] Daniel J. Scheeres. *Orbital Motion in Strongly Perturbed Environments*. Springer, Berlin Heidelberg, 2012.
- [15] L. Prockter, S. Murchie, A. Cheng, S. Krimigis, R. Farquhar, et al. The NEAR shoemaker mission to asteroid 433 eros. In *Acta Astronautica*, volume 51, pages 491–500. Pergamon, 7 2002.
- [16] P Antreasian, S Chesley, James Miller, J Bordi, and Bobby Williams. The design and navigation of the near Shoemaker landing on Eros. In *Advances in the Astronautical Sciences*, volume 109, 2001.
- [17] Bobby G. Williams and Bobby G. Technical challenges and results for navigation of NEAR Shoemaker. *Johns Hopkins APL Technical Digest*, 23(1):34–45, 2002.

## Bibliography

- [18] M. Yoshikawa, A. Fujiwara, and J. Kawaguchi. The nature of asteroid Itokawa revealed by Hayabusa. In *Proceedings of the International Astronomical Union*, volume 2, pages 401–416, 8 2006.
- [19] Jun'ichiro Kawaguchi, Akira Fujiwara, and Tono Uesugi. Hayabusa (MUSES-C) - Rendezvous and proximity operation. In *International Astronautical Federation - 56th International Astronautical Congress 2005*, volume 2, pages 941–951, Reston, Virginia, 10 2005. American Institute of Aeronautics and Astronautics.
- [20] S. Watanabe, M. Hirabayashi, N. Hirata, N. Hirata, R. Noguchi, et al. Hayabusa2 arrives at the carbonaceous asteroid 162173 Ryugu-A spinning top-shaped rubble pile. *Science*, 364(6437):268–272, 4 2019.
- [21] Andrea Accomazzo, Paolo Ferri, Sylvain Lodiot, Jose Luis Pellon-Bailon, Armelle Hubault, et al. Rosetta operations at the comet. *Acta Astronautica*, 115:434–441, 7 2015.
- [22] M. G.G.T. Taylor, N. Altobelli, B. J. Buratti, and M. Choukroun. The Rosetta mission orbiter science overview: The comet phase. *Philosophical Transactions of the Royal Society A: Mathematical, Physical and Engineering Sciences*, 375(2097), 7 2017.
- [23] C. T. Russell and C. A. Raymond. The Dawn mission to Vesta and Ceres. *Space Science Reviews*, 163(1-4):3–23, 12 2011.
- [24] D. S. Laretta, S. S. Balram-Knutson, E. Beshore, W. V. Boynton, C. Drouet d'Aubigny, et al. OSIRIS-REx: Sample Return from Asteroid (101955) Bennu, 10 2017.
- [25] D Scheeres, B M Sutter, and Aaron Rosengren. Design, dynamics and stability of the OSIRIS-REx sun-terminator orbits. *Advances in the Astronautical Sciences*, 148:3263–3282, 2013.

## Bibliography

- [26] R. Terik Daly, Carolyn M. Ernst, Olivier S. Barnouin, Nancy L. Chabot, Andrew S. Rivkin, et al. Successful kinetic impact into an asteroid for planetary defence. *Nature 2023 616:7957*, 616(7957):443–447, 3 2023.
- [27] Cristina A. Thomas, Shantanu P. Naidu, Peter Scheirich, Nicholas A. Moskovitz, Petr Pravec, et al. Orbital period change of Dimorphos due to the DART kinetic impact. *Nature*, 616(7957):448–451, 3 2023.
- [28] David Jewitt, Yoonyoung Kim, Jing Li, and Max Mutchler. The Dimorphos Boulder Swarm. *The Astrophysical Journal Letters*, 952(1):L12, 7 2023.
- [29] Jian Yang Li, Masatoshi Hirabayashi, Tony L. Farnham, Jessica M. Sunshine, Matthew M. Knight, et al. Ejecta from the DART-produced active asteroid Dimorphos. *Nature 2023 616:7957*, 616(7957):452–456, 3 2023.
- [30] Fabio Ferrari, Vittorio Franzese, Mattia Pugliatti, Carmine Giordano, and Francesco Topputo. Preliminary mission profile of Hera’s Milani CubeSat. *Advances in Space Research*, 67(6):2010–2029, 3 2021.
- [31] Hannah Goldberg, özgür Karatekin, Birgit Ritter, Alain Herique, Paolo Tortora, et al. The Juventas CubeSat in Support of ESA’s Hera Mission to the Asteroid Didymos. *Small Satellite Conference*, 8 2019.
- [32] Jesus Gil-Fernandez, M Casasco, I Carnelli, P Martino, and M Küppers. HERA autonomous Guidance, Navigation and Control experiments: enabling better asteroid science & future missions. *8th European Conference for Aeronautics and Space Sciences (EUCASS)*, 2019.
- [33] Ya zhong Luo and Zhen Yang. A review of uncertainty propagation in orbital mechanics. *Progress in Aerospace Sciences*, 89:23–39, 2 2017.
- [34] H. Peter, A. Jäggi, J. Fernández, D. Escobar, F. Ayuga, et al. Sentinel-1A – First precise orbit determination results. *Advances in Space Research*, 60(5):879–892, 9 2017.

## Bibliography

- [35] Zicong An, Kai Shao, Defeng Gu, Chunbo Wei, Zheyu Xu, et al. Precise Orbit Determination and Accuracy Analysis for BDS-3 Satellites Using SLR Observations. *Remote Sensing 2023, Vol. 15, Page 1833*, 15(7):1833, 3 2023.
- [36] Huang Pu, Wen Guangwei, Cai Yingkai, and Wang Zhaokui. Reduction of Space Debris Collision Prediction Uncertainty Based on Q-Sat Precise Orbit. *Space: Science and Technology (United States)*, 3, 2 2023.
- [37] G. Tommei, A. Milani, and A. Rossi. Orbit determination of space debris: Admissible regions. *Celestial Mechanics and Dynamical Astronomy*, 97(4):289–304, 4 2007.
- [38] Oliver Montenbruck and Eberhard Gill. *Satellite Orbits: Models, Methods and Applications*. Springer Berlin Heidelberg, 2000.
- [39] Charles D. Bussy-Virat, Aaron J. Ridley, and Joel W. Getchius. Effects of Uncertainties in the Atmospheric Density on the Probability of Collision Between Space Objects. *Space Weather*, 16(5):519–537, 5 2018.
- [40] Jinglang Feng, Xiyun Hou, and Roberto Armellin. Survey on studies about model uncertainties in small body explorations, 10 2019.
- [41] J. K. Miller, B. G. Williams, W. E. Bollman, R. P. Davis, C. E. Helfrich, et al. Navigation analysis for Eros rendezvous and orbital phases. *Journal of the Astronautical Sciences*, 43(4):453–476, 10 1995.
- [42] Steven J. Ostro, Lance A.M. Benner, Michael C. Nolan, Christopher Magri, Jon D. Giorgini, et al. Radar observations of asteroid 25143 Itokawa (1998 SF36). *Meteoritics and Planetary Science*, 39(3):407–424, 3 2004.
- [43] Yu Takahashi and D. J. Scheeres. Small-body postrendezvous characterization via slow hyperbolic flybys. In *Journal of Guidance, Control, and Dynamics*, volume 34, pages 1815–1827. American Institute of Aeronautics and Astronautics Inc., 5 2011.

## Bibliography

- [44] A. S. Konopliv, S. W. Asmar, R. S. Park, B. G. Bills, F. Centinello, et al. The Vesta gravity field, spin pole and rotation period, landmark positions, and ephemeris from the Dawn tracking and optical data. *Icarus*, 240:103–117, 9 2014.
- [45] Michael K. Shepard, James Richardson, Patrick A. Taylor, Linda A. Rodriguez-Ford, Al Conrad, et al. Radar observations and shape model of asteroid 16 Psyche. *Icarus*, 281:388–403, 1 2017.
- [46] Paolo Panicucci, Benjamin Bercovici, Emmanuel Zenou, Jay McMahon, Michel Delpech, et al. Uncertainties in the gravity spherical harmonics coefficients arising from a stochastic polyhedral shape. *Celestial Mechanics and Dynamical Astronomy*, 132(4):23, 4 2020.
- [47] Siamak G. Hesar, Daniel J. Scheeres, and Jay W. McMahon. Precise Solar Radiation Pressure Models for Small-Body Orbiters: Applications to OSIRIS-REx Spacecraft. *Journal of Guidance, Control, and Dynamics*, 40(7):1638–1650, 7 2017.
- [48] Takahiro Kato and Jozef C. Van Der Ha. Precise modelling of solar and thermal accelerations on Rosetta. *Acta Astronautica*, 72:165–177, 3 2012.
- [49] Mark Moretto and Jay McMahon. Evolution of orbits about comets with arbitrary comae. *Celestial Mechanics and Dynamical Astronomy*, 132(6-7), 6 2020.
- [50] N. Fougere, K. Altwegg, J.-J. Berthelier, A. Bieler, D. Bockelée-Morvan, et al. Three-dimensional direct simulation Monte-Carlo modeling of the coma of comet 67P/Churyumov-Gerasimenko observed by the VIRTIS and ROSINA instruments on board Rosetta. *Astronomy & Astrophysics*, 588:A134, 4 2016.
- [51] Pablo Muñoz, Frank Budnik, Vicente Companys, Bernard Godard, Carlos M Casas, et al. Rosetta navigation during lander delivery phase and reconstruction of Philae descent trajectory and rebound. In *25th International Symposium on Space Flight Dynamics*, 2015.

## Bibliography

- [52] Peter G. Antreasian, Michael C. Moreau, Coralie D. Adam, Andrew French, Jeroen Geeraert, et al. Early navigation performance of the OSIRIS-REx approach to Bennu. In *Advances in the Astronautical Sciences*, volume 169, pages 141–160. Univelt Inc., 2019.
- [53] B. Williams, P. Antreasian, E. Carranza, C. Jackman, J. Leonard, et al. OSIRIS-REx Flight Dynamics and Navigation Design, 6 2018.
- [54] Bernard Godard, Frank Budnik, Pablo Muñoz, Trevor Morley, and Vishnu Janarthanan. Orbit determination of Rosetta around comet 67P/Churyumov-Gerasimenko. In *Proceedings 25th International Symposium on Space Flight Dynamics–25th ISSFD*, Munich, 2015.
- [55] E. M. Alessi, S. Cicalò, A. Milani, and G. Tommei. Desaturation manoeuvres and precise orbit determination for the BepiColombo mission. *Monthly Notices of the Royal Astronomical Society*, 423(3):2270–2278, 7 2012.
- [56] J. K. Miller, A. S. Konopliv, P. G. Antreasian, J. J. Bordi, S. Chesley, et al. Determination of shape, gravity, and rotational state of asteroid 433 Eros. *Icarus*, 155(1):3–17, 1 2002.
- [57] Hitoshi Ikeda, Naru Hirata, Ryosuke Nakamura, Yuichi Tsuda, Takahiro Iwata, et al. Preliminary Analysis of Small-body Gravity Estimation in the Hayabusa-2 Mission. In *the 24th JAXA Workshop on Astrodynamics and Flight Mechanics*, 2014.
- [58] M. Pätzold, T. Andert, M. Hahn, S. W. Asmar, J. P. Barriot, et al. A homogeneous nucleus for comet 67P/Churyumov-Gerasimenko from its gravity field. *Nature*, 530(7588):63–65, 2 2016.
- [59] D. J. Scheeres, J. W. McMahon, A. S. French, D. N. Brack, S. R. Chesley, et al. The dynamic geophysical environment of (101955) Bennu based on OSIRIS-REx measurements. *Nature Astronomy*, 3(4):352–361, 4 2019.

## Bibliography

- [60] S. R. Chesley, A. S. French, A. B. Davis, R. A. Jacobson, M. Brozović, et al. Trajectory Estimation for Particles Observed in the Vicinity of (101955) Bennu. *Journal of Geophysical Research: Planets*, 125(9):e2019JE006363, 9 2020.
- [61] Tiffany Russell Lockett, Julie Castillo-Rogez, Les Johnson, Joe Matus, Jack Lightholder, et al. Near-Earth Asteroid Scout Flight Mission. *IEEE Aerospace and Electronic Systems Magazine*, 35(3):20–29, 3 2020.
- [62] Roger Walker, David Binns, Cristina Bramanti, Massimo Casasco, Paolo Concari, et al. Deep-space CubeSats: Thinking inside the box. *Astronomy & Geophysics*, 59:24–5, 2018.
- [63] Ben Malphrus, Anthony Freeman, Robert Staehle, Andrew Klesh, and Roger Walker. Interplanetary CubeSat missions. In *Cubesat Mission Handbook: From Mission Design to Operations*, page 85. Elsevier B.V., 2020.
- [64] Marc D. Rayman and Steven N. Williams. Design of the First Interplanetary Solar Electric Propulsion Mission. <https://doi.org/10.2514/2.3848>, 39(4):589–595, 5 2012.
- [65] Cristian Greco and Massimiliano Vasile. Closing the Loop Between Mission Design and Navigation Analysis. In *71th International Astronautical Congress (IAC 2020)*, 3 2020.
- [66] Claudio Bottiglieri, Felice Piccolo, Carmine Giordano, and Francesco Topputo. Applied Trajectory Design for close-proximity operations of Asteroid CubeSat Mission. 7 2022.
- [67] David A. Surovik and Daniel J. Scheeres. Reactive and robust paradigms for autonomous mission design at small bodies. *Journal of Guidance, Control, and Dynamics*, 40(2):333–343, 12 2017.
- [68] Derek C. Richardson, Harrison F. Agrusa, Brent Barbee, William F. Bottke, Andrew F. Cheng, et al. Predictions for the Dynamical States of the Didymos

## Bibliography

- System before and after the Planned DART Impact. *The Planetary Science Journal*, 3(7):157, 7 2022.
- [69] William M. Kaula. *Theory of satellite geodesy : applications of satellites to geodesy*. Dover Publications, Waltham, MA: Blaisdell, 1966.
- [70] Georges Balmino. Gravitational potential harmonics from the shape of an homogeneous body. *Celestial Mechanics & Dynamical Astronomy*, 60(3):331–364, 11 1994.
- [71] Leland E. Cunningham. On the computation of the spherical harmonic terms needed during the numerical integration of the orbital motion of an artificial satellite. *Celestial Mechanics*, 2(2):207–216, 6 1970.
- [72] Robert A. Werner. The gravitational potential of a homogeneous polyhedron or don't cut corners. *Celestial Mechanics & Dynamical Astronomy*, 59(3):253–278, 7 1994.
- [73] Simon Tardivel. The limits of the mascons approximation of the homogeneous polyhedron. In *AIAA/AAS Astrodynamics Specialist Conference*. American Institute of Aeronautics and Astronautics Inc, AIAA, 2016.
- [74] Patrick T Wittick and Ryan P Russell. Mixed-model gravity representations for small celestial bodies using mascons and spherical harmonics. *Celestial Mechanics and Dynamical Astronomy*, 131(7):31, 2019.
- [75] Sean McArdle and Ryan P. Russell. Point Mascon Global Lunar Gravity Models. *Journal of Guidance, Control, and Dynamics*, 45(5):815–829, 1 2022.
- [76] D. J. Scheeres. Orbit mechanics about asteroids and comets. *Journal of Guidance, Control, and Dynamics*, 35(3):987–997, 8 2012.
- [77] Dario Izzo and Pablo Gómez. Geodesy of irregular small bodies via neural density fields. *Nature Communications Engineering*, 1(1):1–12, 12 2022.
- [78] Karel Wakker. *Fundamentals of Astrodynamics*. Institutional Repository Delft University of Technology, Delft, 1 2015.

## Bibliography

- [79] Fabio Ferrari, Vittorio Franzese, Mattia Pugliatti, Carmine Giordano, and Francesco Topputo. Trajectory Options for Hera’s Milani CubeSat Around (65803) Didymos. *The Journal of the Astronautical Sciences*, pages 1–22, 9 2021.
- [80] Shane Ross, Wang Koon, Martin Lo, and Jerrold Marsden. *Dynamical Systems, the Three-Body Problem, and Space Mission Design*, volume 1.2. 6 2011.
- [81] Simon Tardivel and Daniel J. Scheeres. Ballistic deployment of science packages on binary asteroids. *Journal of Guidance, Control, and Dynamics*, 36(3):700–709, 4 2013.
- [82] Fabio Ferrari and Michèle Lavagna. Ballistic landing design on binary asteroids: The AIM case study. *Advances in Space Research*, 62(8):2245–2260, 10 2018.
- [83] Peter S. Maybeck. Stochastic models, estimation and control. 3:291, 1982.
- [84] Jay W. McMahon, Daniel J. Scheeres, Steven R. Chesley, Andrew French, Daniel Brack, et al. Dynamical Evolution of Simulated Particles Ejected From Asteroid Bennu. *Journal of Geophysical Research: Planets*, 125(8):e2019JE006229, 8 2020.
- [85] Siamak G. Hesar, Daniel J. Scheeres, and Jay W. McMahon. Sensitivity Analysis of the OSIRIS-REx Terminator Orbits to Maneuver Errors. *Journal of Guidance, Control, and Dynamics*, 40(1):81–95, 1 2017.
- [86] Stefania Soldini, Saiki Takanao, Hitoshi Ikeda, Koji Wada, Tsuda Yuichi, et al. A generalised methodology for analytic construction of 1:1 resonances around irregular bodies: Application to the asteroid Ryugu’s ejecta dynamics. *Planetary and Space Science*, 180:104740, 1 2020.
- [87] Jinglang Feng. *Orbital dynamics in the vicinity of contact binary asteroid systems*. PhD thesis, Delft University of Technology, 2016.
- [88] Hassan K. Khalil. *Nonlinear Systems*. Pearson, 3rd edition, 12 2001.
- [89] L. Dell’Elce, N. Baresi, S. P. Naidu, L. A.M. Benner, and D. J. Scheeres. Numerical investigation of the dynamical environment of 65803 Didymos. *Advances in Space Research*, 59(5):1304–1320, 3 2017.

## Bibliography

- [90] D. J. Scheeres. Orbital mechanics about small bodies. *Acta Astronautica*, 72:1–14, 3 2012.
- [91] Nicola Baresi and D Scheeres. Quasi-periodic Invariant Tori of Time-periodic Dynamical Systems: Applications to Small Body Exploration. In *67th International Astronautical Congress*, Guadalajara, 8 2016.
- [92] Stephen B. Broschart, Gregory Lantoine, and Daniel J. Grebow. Quasi-terminator orbits near primitive bodies. *Celestial Mechanics and Dynamical Astronomy*, 120(2):195–215, 8 2014.
- [93] D. J. Scheeres. Satellite Dynamics About Asteroids: Computing Poincaré Maps for the General Case. In *Hamiltonian Systems with Three or More Degrees of Freedom*, pages 554–557. Springer Netherlands, 1999.
- [94] Shota Kikuchi, Yusuke Oki, and Yuichi Tsuda. Frozen orbits under radiation pressure and zonal gravity perturbations. *Journal of Guidance, Control, and Dynamics*, 44(11):1924–1946, 9 2021.
- [95] N. P. Maffione, L. A. Darriba, P. M. Cincotta, and C. M. Giordano. A comparison of different indicators of chaos based on the deviation vectors. Application to symplectic mappings. *Celestial Mechanics and Dynamical Astronomy*, 111(3):285–307, 8 2011.
- [96] A. Bazzani, M. Giovannozzi, C. E. Montanari, and G. Turchetti. Performance analysis of indicators of chaos for nonlinear dynamical systems. *Physical Review E*, 107(6):064209, 6 2023.
- [97] Massimiliano Guzzo, Elena Lega, and Claude Froeschlé. On the numerical detection of the effective stability of chaotic motions in quasi-integrable systems. *Physica D: Nonlinear Phenomena*, 163(1-2):1–25, 3 2002.
- [98] Elena Lega, Massimiliano Guzzo, and Claude Froeschlé. Theory and Applications of the Fast Lyapunov Indicator (FLI) Method. In *Chaos Detection and Predictability*, volume 915, pages 35–54. 6 2016.

## Bibliography

- [99] Claude Froeschlé, Elena Lega, and Robert Gonczi. Fast Lyapunov indicators. Application to asteroidal motion. *Celestial Mechanics and Dynamical Astronomy*, 67(1):41–62, 1997.
- [100] Benjamin Villac and Stephen Broschart. Applications of Chaoticity Indicators to Stability Analysis around Small Bodies. In *Advances in the Astronautical Sciences*, volume 134, 1 2009.
- [101] P. M. Cincotta and C. Simó. Simple tools to study global dynamics in non-axisymmetric galactic potentials - I. *Astronomy and Astrophysics Supplement*, 147(2):205–228, 12 2000.
- [102] Martín Mestre Citrinovitz, Pablo Cincotta, and C Giordano. Analytical relation between two chaos indicators: FLI and MEGNO. *Monthly Notices of the Royal Astronomical Society: Letters*, 414:L100 – L103, 6 2011.
- [103] George Haller and Themistoklis Sapsis. Lagrangian coherent structures and the smallest finite-time Lyapunov exponent. *Chaos: An Interdisciplinary Journal of Nonlinear Science*, 21(2):023115, 5 2011.
- [104] Ana M. Mancho, Stephen Wiggins, Jezabel Curbelo, and Carolina Mendoza. Lagrangian descriptors: A method for revealing phase space structures of general time dependent dynamical systems. *Communications in Nonlinear Science and Numerical Simulation*, 18(12):3530–3557, 12 2013.
- [105] Jacques Laskar. Frequency analysis for multi-dimensional systems. Global dynamics and diffusion. *Physica D: Nonlinear Phenomena*, 67(1-3):257–281, 8 1993.
- [106] Alireza Hadjighasem, Mohammad Farazmand, Daniel Blazevski, Gary Froyland, and George Haller. A critical comparison of Lagrangian methods for coherent structure detection. *Chaos*, 27(5), 5 2017.
- [107] Sebastiano Raffa, Gianmario Merisio, and Francesco Topputo. Finding regions of bounded motion in binary asteroid environment using Lagrangian descriptors.

## Bibliography

- Communications in Nonlinear Science and Numerical Simulation*, 121:107198, 6 2023.
- [108] D. J. Scheeres, F. Y. Hsiao, R. S. Park, B. F. Villac, and J. M. Maruskin. Fundamental limits on spacecraft orbit uncertainty and distribution propagation. *Journal of the Astronautical Sciences*, 54(3-4):505–523, 8 2006.
- [109] S. P. Naidu, L. A.M. Benner, M. Brozovic, M. C. Nolan, S. J. Ostro, et al. Radar observations and a physical model of binary near-Earth asteroid 65803 Didymos, target of the DART mission. *Icarus*, 348:113777, 9 2020.
- [110] Jesus Gil-Fernandez and Guillermo Ortega-Hernando. Autonomous vision-based navigation for proximity operations around binary asteroids. *CEAS Space Journal*, 10(2):287–294, 6 2018.
- [111] Hannes Risken. *Fokker-Planck Equation*, pages 63–95. Springer Berlin Heidelberg, Berlin, Heidelberg, 1996.
- [112] Igor A. Tanski. Two simple solutions of nonlinear fokker - planck equation for incompressible fluid, 2009.
- [113] Giacomo Acciarini, Cristian Greco, and Massimiliano Vasile. Uncertainty propagation in orbital dynamics via galerkin projection of the fokker-planck equation. *Advances in Space Research*, 73(1):53–63, 2024.
- [114] Alexander Wittig, Pierluigi Di Lizia, Roberto Armellin, Kyoko Makino, Franco Bernelli-Zazzera, and Martin Berz. Propagation of large uncertainty sets in orbital dynamics by automatic domain splitting. *Celestial Mechanics and Dynamical Astronomy*, 122(3):239–261, 7 2015.
- [115] Ryan S. Park and Daniel J. Scheeres. Nonlinear mapping of Gaussian statistics: Theory and applications to spacecraft trajectory design. *Journal of Guidance, Control, and Dynamics*, 29(6):1367–1375, 2006.

## Bibliography

- [116] M. Valli, R. Armellin, P. Di Lizia, and M. R. Lavagna. Nonlinear mapping of uncertainties in celestial mechanics. *Journal of Guidance, Control, and Dynamics*, 36(1):48–63, 1 2013.
- [117] Massimiliano Vasile, Carlos Ortega Absil, and Annalisa Riccardi. Set propagation in dynamical systems with generalised polynomial algebra and its computational complexity. *Communications in Nonlinear Science and Numerical Simulation*, 75:22–49, 8 2019.
- [118] Norbert Wiener. The Homogeneous Chaos. *American Journal of Mathematics*, 60(4):897, 10 1938.
- [119] E. A. Wan and R. Van Der Merwe. The unscented Kalman filter for nonlinear estimation. In *IEEE 2000 Adaptive Systems for Signal Processing, Communications, and Control Symposium, AS-SPCC 2000*, pages 153–158. Institute of Electrical and Electronics Engineers Inc., 2000.
- [120] Brandon A. Jones, Alireza Doostan, and George H. Born. Nonlinear propagation of orbit uncertainty using non-intrusive polynomial chaos. *Journal of Guidance, Control, and Dynamics*, 36(2):430–444, 3 2013.
- [121] Jinglang Feng, Xiyun Hou, Pierluigi Di Lizia, Roberto Armellin, and Daniele Antonio Santeramo. Sensitivity analysis of the orbital motion around 469219 Kamo’oalewa (2016 HO3) to uncertainties on asteroid mass and solar radiation pressure. *Advances in Space Research*, 12 2021.
- [122] Jinglang Feng, Danielle Santeramo, Pierluigi Di Lizia, Roberto Armellin, and Xiyun Hou. Stability indicator of orbital motion around asteroids with automatic domain splitting. In *Proceedings of the International Astronautical Congress, IAC*, volume 2019-Octob, 10 2019.
- [123] Daniel Pérez-Palau, Josep J. Masdemont, and Gerard Gómez. Tools to detect structures in dynamical systems using Jet Transport. *Celestial Mechanics and Dynamical Astronomy*, 123(3):239–262, 11 2015.

## Bibliography

- [124] Massimiliano Vasile and Matteo Manzi. Polynomial Stochastic Dynamic Indicators. *Celestial Mechanics and Dynamical Astronomy*, 2022.
- [125] Antonio Giorgilli and Marco Sansottera. Methods of algebraic manipulation in perturbation theory. *Third La Plata International School on Astronomy and Geophysics.*, pages 147–183, 3 2013.
- [126] Annalisa Riccardi, Chiara Tardioli, and Massimiliano Vasile. An intrusive approach to uncertainty propagation in orbital mechanics based on tchebycheff polynomial algebra. In *Advances in the Astronautical Sciences*, volume 156, pages 707–722, Vail, 2016. Univelt Inc.
- [127] Nicolas Brisebarre and Mioara Joldeş. Chebyshev interpolation polynomial-based tools for rigorous computing. In *Proceedings of the International Symposium on Symbolic and Algebraic Computation, ISSAC*, pages 147–154, New York, New York, USA, 2010. Association for Computing Machinery (ACM).
- [128] Carlos Ortega Absil, Romain Serra, Annalisa Riccardi, and Massimiliano Vasile. De-orbiting and re-entry analysis with generalised intrusive polynomial expansions. In *67th International Astronautical Congress*, Guadalajara, 9 2016. International Astronautical Federation.
- [129] Carlos Ortega Absil, Annalisa Riccardi, Massimiliano Vasile, and Chiara Tardioli. SMART-UQ: uncertainty quantification toolbox for generalised intrusive and non intrusive polynomial algebra. In *6th International Conference on Astrodynamics Tools and Techniques*, Darmstadt, Germany, 3 2016.
- [130] Cristian Greco, Stefano Campagnola, and Massimiliano Vasile. Robust Space Trajectory Design Using Belief Optimal Control. *Journal of Guidance, Control, and Dynamics*, 45(6), 6 2022.
- [131] Sergei Abramovich Smolyak. Quadrature and interpolation formulas for tensor products of certain classes of functions. *Doklady Akademii Nauk SSSR*, 148(5):1042–1045, 1963.

## Bibliography

- [132] D Scheeres. Satellite Dynamics about Small Bodies: Averaged Solar Radiation Pressure Effects. *Journal of the Astronautical Sciences*, 47, 1999.
- [133] Hera Proximity Operations Guidelines. Issue 6, revision 3. Technical report, European Space Agency, Noordwijk, 10 2020.
- [134] Max Hallgarten La Casta, Davide Amato, and Massimiliano Vasile. Polynomial Algebra for Uncertainty Propagation in Generalised Equinoctial Orbital Elements. In *International Astronautical Congress*, 2022.
- [135] Massimiliano Vasile. Fast Chaos Expansions of Diffusive and Sub-Diffusive Processes in Orbital Mechanics. In *72nd International Astronautical Congress (IAC)*, 2021.
- [136] Shambhu N. Sharma and H. Parthasarathy. Dynamics of a stochastically perturbed two-body problem. *Proceedings of the Royal Society A: Mathematical, Physical and Engineering Sciences*, 463(2080):979–1003, 4 2007.
- [137] Frédéric Pierret. Stochastic Gauss Equations. *Celestial Mechanics and Dynamical Astronomy*, 124(2):109–126, 2 2014.
- [138] Samuel B. Alves, Gilson F. De Oliveira, Luimar C. De Oliveira, Thierry Passerat De Silans, Martine Chevrollier, et al. Characterization of diffusion processes: Normal and anomalous regimes. *Physica A: Statistical Mechanics and its Applications*, 447:392–401, 4 2016.
- [139] Matteo Manzi and Massimiliano Vasile. Analysis of Stochastic Nearly-integrable Dynamical Systems using Polynomial Chaos Expansions. In *2020 AAS/AIAA Astrodynamics Specialist Conference*, South Lake Tahoe, 2020.
- [140] Frank Olver, Daniel Lozier, Ronald Boisvert, and Charles Clark. *NIST Handbook of Mathematical Functions*. Cambridge University Press, 1 2010.
- [141] Lloyd Trefethen. *Approximation Theory and Approximation Practice*. SIAM, 2013.

## Bibliography

- [142] Dongbin Xiu and George Em Karniadakis. The Wiener-Askey Polynomial Chaos for Stochastic Differential Equations. *SIAM Journal on Scientific Computing*, 24(2):619–644, 7 2006.
- [143] William H Press, Saul A Teukolsky, William T Vetterling, and Brian P Flannery. *Numerical Recipes 3rd Edition: The Art of Scientific Computing*. Cambridge University Press, USA, 3 edition, 2007.
- [144] Friedrich Damme, Hauke Hussmann, and Jürgen Oberst. Spacecraft orbit lifetime within two binary near-Earth asteroid systems. *Planetary and Space Science*, 146:1–9, 10 2017.
- [145] Xiyun Hou, Daniel J. Scheeres, and Xiaosheng Xin. Mutual potential between two rigid bodies with arbitrary shapes and mass distributions. *Celestial Mechanics and Dynamical Astronomy*, 127(3):369–395, 3 2017.
- [146] I. Jean, A. K. Misra, and A. Ng. Controlled Spacecraft Trajectories in the Context of a Mission to a Binary Asteroid System. *Journal of the Astronautical Sciences*, 68(1):38–70, 3 2021.
- [147] Claudio Bottiglieri, Felice Piccolo, Antonio Rizza, Carmine Giordano, Mattia Pugliatti, et al. Trajectory design and orbit determination of Hera’s Milani Cube-Sat. In *AAS/AIAA Astrodynamics Specialist Conference*, 1 2021.
- [148] Shota Kikuchi, Yuichi Tsuda, Makoto Yoshikawa, and Kawaguchi Jun’ichiro. Stability analysis of coupled orbit-attitude dynamics around asteroids using finite-time Lyapunov exponents. *Journal of Guidance, Control, and Dynamics*, 42(6):1289–1305, 3 2019.
- [149] Iosto Fodde, Jinglang Feng, and Massimiliano Vasile. Uncertainty Propagation for Orbital Motion Around an Asteroid Using Generalized Intrusive Polynomial Algebra: Application to Didymos System. In *8th International Conference on Astrodynamics Tools and Techniques - Virtual*, 6 2021.

## Bibliography

- [150] Andrea Capannolo, Fabio Ferrari, and Michèle Lavagna. Families of Bounded Orbits near Binary Asteroid 65803 Didymos. *Journal of Guidance, Control, and Dynamics*, 42(1):189–198, 1 2019.
- [151] David A. Surovik and Daniel J. Scheeres. Autonomous maneuver planning at small bodies via mission objective reachability analysis. In *AIAA/AAS Astrodynamics Specialist Conference 2014*. American Institute of Aeronautics and Astronautics Inc., 2014.
- [152] Jun'ichiro Kawaguchi. Hayabusa, summary of guidance, navigation and control achievement in its proximity phase. In *Collection of Technical Papers - AIAA/AAS Astrodynamics Specialist Conference, 2006*, volume 2, pages 1334–1341. American Institute of Aeronautics and Astronautics Inc., 2006.
- [153] Yuichi Tsuda, Takanao Saiki, Fuyuto Terui, Satoru Nakazawa, Makoto Yoshikawa, and Sei ichiro Watanabe. Hayabusa2 mission status: Landing, roving and cratering on asteroid Ryugu. *Acta Astronautica*, 171:42–54, 6 2020.
- [154] Onur Çelik, Ozgur Karatekin, Birgit Ritter, and Joan-Pau Sánchez. Reliability Analysis of Ballistic Landing in Binary Asteroid 65803 (1996GT) Didymos under Uncertainty and GNC Error Considerations. In *26th International Symposium on Spaceflight Dynamics*, 2017.
- [155] Simon Tardivel, Patrick Michel, and Daniel J. Scheeres. Deployment of a lander on the binary asteroid (175706) 1996 FG3, potential target of the european MarcoPolo-R sample return mission. *Acta Astronautica*, 89:60–70, 8 2013.
- [156] E. Herrera-Sucarrat, P. L. Palmer, and R. M. Roberts. Asteroid Observation and Landing Trajectories Using Invariant Manifolds. *Journal of Guidance Control and Dynamics*, 37(3):907–920, 2014.
- [157] Daniel Villegas Pinto, D Hestroffer, Elisabet Canalias, and Francesco Capolupo. Deployment of small-body landers from terminator orbits in perturbed environments. In *AAS/AIAA Astrodynamics Specialist Conference*, Virtual Lake Tahoe, 4 2020.

## Bibliography

- [158] Iosto Fodde, Jinglang Feng, and Massimiliano Vasile. Robust Trajectory Design for Ballistic Landings on Dimorphos. *AIAA Science and Technology Forum and Exposition, AIAA SciTech Forum 2022*, 2022.
- [159] Shujiro Sawai, Jun'ichiro Kawaguchi, Daniel Scheeres, Naoki Yoshizawa, and Masahiro Ogasawara. Development of a Target Marker for Landing on Asteroids. *Journal of Spacecraft and Rockets*, 38(4):601–608, 5 2012.
- [160] Stefaan Van Wal, Simon Tardivel, and Daniel Scheeres. Parametric Study of Ballistic Lander Deployment to Small Bodies. *Journal of Spacecraft and Rockets*, 54(6):1330–1355, 11 2017.
- [161] Stefaan Van Wal, Robert G. Reid, and Daniel J. Scheeres. Simulation of Non-spherical Asteroid Landers: Contact Modeling and Shape Effects on Bouncing. <https://doi.org/10.2514/1.A34573>, 57(1):109–130, 11 2019.
- [162] Martina Rusconi, Fabio Ferrari, and Francesco Topputo. The effect of a rocky terrain for CubeSat landing on asteroid surfaces. *Advances in Space Research*, 11 2022.
- [163] X. Y. Zeng, Z. W. Li, T. G. Wen, and Y. L. Zhang. Influence of the Lander Size and Shape on the Ballistic Landing Motion. *Earth and Space Science*, 9(2):e2021EA001952, 2 2022.
- [164] Jianping Luo, Qiqi Liu, Yun Yang, Xia Li, Min-Rong Chen, and Wenming Cao. An artificial bee colony algorithm for multi-objective optimisation. *Applied Soft Computing Journal*, 50:235–251, 2017.
- [165] Onur Çelik, Nicola Baresi, Ronald Louis Ballouz, Kazunori Ogawa, Koji Wada, and Yasuhiro Kawakatsu. Ballistic deployment from quasi-satellite orbits around Phobos under realistic dynamical and surface environment constraints. *Planetary and Space Science*, 178, 11 2019.

## Bibliography

- [166] Jens Biele, Stephan Ulamec, Michael Maibaum, Reinhard Roll, Lars Witte, et al. The landing(s) of Philae and inferences about comet surface mechanical properties. *Science*, 349(6247), 7 2015.
- [167] Hajime Yano, T. Kubota, H. Miyamoto, T. Okada, D. Scheeres, et al. Touchdown of the Hayabusa Spacecraft at the Muses Sea on Itokawa. *Science*, 312(5778):1350–1353, 6 2006.
- [168] Jens Biele, Lars Kessler, Christian D. Grimm, Silvio Schröder, Olaf Mierheim, et al. Experimental Determination of the Structural Coefficient of Restitution of a Bouncing Asteroid Lander. 5 2017.
- [169] F. Scholten, F. Preusker, S. Elgner, K. D. Matz, R. Jaumann, et al. The descent and bouncing path of the Hayabusa2 lander MASCOT at asteroid (162173) Ryugu. *Astronomy & Astrophysics*, 632:L3, 12 2019.
- [170] Florian Thuillet, Yun Zhang, Patrick Michel, Jens Biele, Shingo Kameda, et al. Numerical modeling of lander interaction with a low-gravity asteroid regolith surface - II. Interpreting the successful landing of Hayabusa2 MASCOT. *Astronomy & Astrophysics*, 648:A56, 4 2021.
- [171] Tatsuhiro Michikami, Chikatoshi Honda, Hideaki Miyamoto, Masatoshi Hirabayashi, Axel Hagermann, et al. Boulder size and shape distributions on asteroid Ryugu. *Icarus*, 331:179–191, 10 2019.
- [172] Onur Çelik and Joan Pau Sánchez. Opportunities for ballistic soft landing in binary asteroids. *Journal of Guidance, Control, and Dynamics*, 40(6):1390–1402, 4 2017.
- [173] Cristian Greco, Marilena Di Carlo, Massimiliano Vasile, and Richard Epenoy. Direct multiple shooting transcription with polynomial algebra for optimal control problems under uncertainty. *Acta Astronautica*, 170:224–234, 5 2020.

## Bibliography

- [174] Christof Büskens and Dennis Wassel. The ESA NLP Solver WORHP. In Giorgio Fasano and János D Pintér, editors, *Modeling and Optimization in Space Engineering*, volume 73, pages 85–110. Springer New York, 2013.
- [175] Marcello Farina, Luca Giulioni, and Riccardo Scattolini. Stochastic linear Model Predictive Control with chance constraints – A review. *Journal of Process Control*, 44:53–67, 8 2016.
- [176] Kazuhide Okamoto and Panagiotis Tsiotras. Optimal Stochastic Vehicle Path Planning Using Covariance Steering. *IEEE Robotics and Automation Letters*, 4(3):2276–2281, 7 2019.
- [177] Erica L. Jenson and Daniel J. Scheeres. Multi-Objective Optimization of Covariance and Energy for Asteroid Transfers. *Journal of Guidance, Control, and Dynamics*, 44(7):1253–1265, 7 2021.
- [178] Haijing Hu, Shengying Zhu, and Pingyuan Cui. Desensitized optimal trajectory for landing on small bodies with reduced landing error. *Aerospace Science and Technology*, 48:178–185, 1 2016.
- [179] Yuan Ren and Jinjun Shan. Reliability-Based Soft Landing Trajectory Optimization near Asteroid with Uncertain Gravitational Field. *Journal of Guidance, Control, and Dynamics*, 38(9):1810–1820, 7 2015.
- [180] Kenshiro Oguri and Jay W. McMahon. Robust Spacecraft Guidance Around Small Bodies Under Uncertainty: Stochastic Optimal Control Approach. *Journal of Guidance, Control, and Dynamics*, 44(7):1295–1313, 4 2021.
- [181] Naoya Ozaki, Stefano Campagnola, and Ryu Funase. Tube stochastic optimal control for nonlinear constrained trajectory optimization problems. *Journal of Guidance, Control, and Dynamics*, 43(4):645–655, 2020.
- [182] P. Di Lizia, R. Armellin, F. Bernelli-Zazzera, and M. Berz. High order optimal control of space trajectories with uncertain boundary conditions. *Acta Astronautica*, 93:217–229, 1 2014.

## Bibliography

- [183] Leslie Pack Kaelbling, Michael L. Littman, and Anthony R. Cassandra. Planning and acting in partially observable stochastic domains. *Artificial Intelligence*, 101(1-2):99–134, 5 1998.
- [184] Aurelio Kaluthantrige, Jinglang Feng, and Jesús Gil-Fernández. CNN-based Image Processing algorithm for autonomous optical navigation of Hera mission to the binary asteroid Didymos. *Acta Astronautica*, 211:60–75, 10 2023.
- [185] M. Pugliatti, F. Piccolo, A. Rizza, V. Franzese, and F. Topputo. The vision-based guidance, navigation, and control system of Hera’s Milani CubeSat. *Acta Astronautica*, 210:14–28, 9 2023.
- [186] Peng Chen and Omar Ghattas. Taylor approximation for chance constrained optimization problems governed by partial differential equations with high-dimensional random parameters. *SIAM-ASA Journal on Uncertainty Quantification*, 9(4):1381–1410, 11 2020.
- [187] Andreas Wächter and Lorenz T. Biegler. On the implementation of an interior-point filter line-search algorithm for large-scale nonlinear programming. *Mathematical Programming*, 106(1):25–57, 5 2006.
- [188] Mauro Massari, Pierluigi Di Lizia, Francesco Cavenago, and Alexander Wittig. Differential Algebra software library with automatic code generation for space embedded applications. *AIAA Information Systems-AIAA Infotech at Aerospace, 2018*, 1 2018.